COMPUTATIONAL MODELING OF THE AERODYNAMIC CHARACTERISTICS AND FLIGHT MECHANICS AND CONTROL OF AN UNMANNED AERIAL VEHICLE

SUBMITTED BY

TAN CHOON SENG LEON MARK

SCHOOL OF MECHANICAL AND AEROSPACE ENGINEERING

A thesis

Submitted to the

Nanyang Technological University

in partial fulfillment of the

requirements for the

Degree of Master of Engineering

2007/2008

Abstract

This thesis outlines the effort in developing an integrated simulation framework for assessing the stability and control characteristics of an Unmanned Aerial Vehicle (UAV). The objectives are to understand flight instabilities experienced by the UAV and to propose solutions for the flight stability and control problems via an integrated modeling framework. The basic core of the framework involves the incorporation and integration of the UAV aerodynamic characteristics, flight stability derivatives and digital flight control system, into a six degree-of-freedom flight simulation model, the outputs of which are visualized graphically. To support the development of the simulation model, a comprehensive aerodynamic database for the UAV is required. Empirical aerodynamic estimation software such as *USAF Digital Datcom* and computational flow simulation software suites such as *FLUENT* and *SolidWorks FloWorks* have been used to estimate the aerodynamic force and moments as well as stability and control derivatives of the UAV. By combining these estimates with wind tunnel data, a comprehensive aerodynamic characteristics model is constructed for augmenting the flight dynamics model of the UAV. Initially, a de-coupled longitudinal and lateral stability analysis based on the small disturbance theory has been developed to understand the stability modes of the UAV. A coupled longitudinal and lateral stability analysis was then developed to study the effects of the aerodynamic coupling caused by the single propulsion system to the stability and control characteristics. The model is created within the programmable software environments of *Matlab®*, *Simulink®* and *Aerospace Blockset®* which are used to construct the six-degree-of-freedom model for the dynamical motion of the UAV. The inputs to the model include the aerodynamic information based on the aerodynamic characteristics, stability derivatives, engine characteristics, flight variables and atmospheric disturbances. The outputs from this model are the responses of the flight variables depicting lateral, longitudinal and directional stability characteristics of the flight vehicle. Virtual Reality based systems such as the *Flight Gear* software has been used as a graphical interface for displaying the UAV trajectory, the orientation of the vehicle and the stability and control characteristics of the UAV based on the outputs from the model. With this framework, it is possible to assess the impact of flight control system and its modifications on the stability and control of the UAV.

Acknowledgement

The author would like to take this opportunity to express his appreciation to his project supervisor, Associate Professor Dr. Damodaran Murali. Without his kind guidance and technical knowledge on the subject matter, the study would not have been conducted smoothly. His advice and feedback have been invaluable and assisted the author greatly in the execution of this study.

This project is funded by a grant from Defence Science and Technology Agency (DSTA), Ministry of Defence (MINDEF), Singapore. The author would also like to thank Mr. Lek Ngak Yong previously Section Head, Aerodynamic Branch and Mr. Melvin Wong, Staff Officer, Aerodynamic Branch, HQ Air Logistics, Republic of Singapore Air Force, MINDEF for their interactions, technical advice and data inputs to facilitate this investigation.

Finally, the author would like to thank all his family and friends and whoever had in one way or another assisted him in the execution of this project.

Table of Contents

List of Tables

List of Figures

Chapter 1
Introduction

Unmanned Aerial Vehicle (UAV) is defined by the Department of Defense in The United States of America in the article by Blazakis [1] as a powered, aerial vehicle that do not carry a human operator, uses aerodynamic forces to provide vehicle lift, can fly autonomously or be piloted remotely, can be expendable or recoverable, and carry a lethal or non lethal payload. The application of Unmanned Aerial Vehicles (UAVs) has grown drastically in many fields over the past few years. UAVs can perform a large variety of missions including surveillance, communication relay, ships decoy and detection of biological, chemical or nuclear materials.

UAVs first took flight during World War I from 1914 to 1918 and were primarily deployed for military purposes. It was mainly developed for reconnaissance and exploration to gather information. During World War II in 1940s, Nazi Germany's innovative V-1 as shown in Figure 1.1(a) demonstrated the formidable threats a UAV could pose in combat. America's attempts to eliminate the V-1 laid the groundwork for post-war UAVs development around the world.

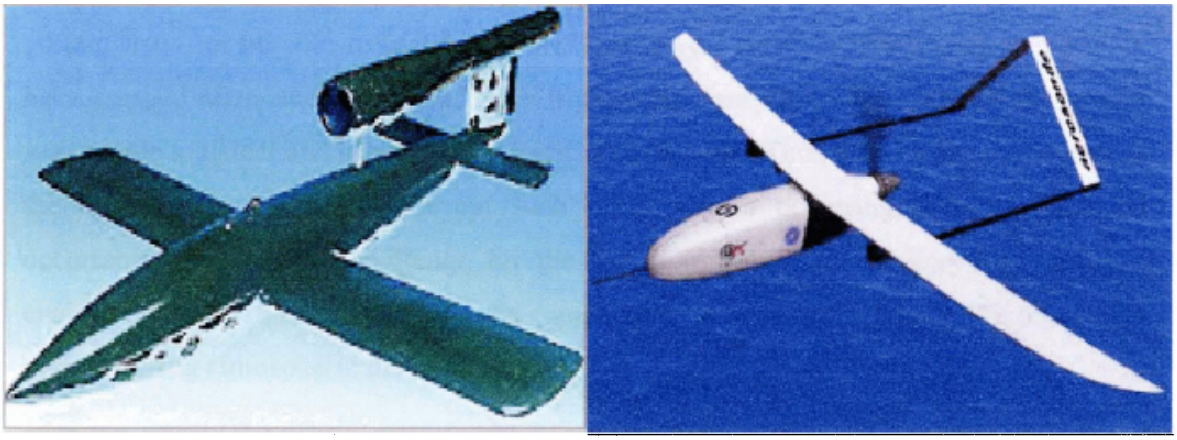

(a) Germany V-1 (b) The Aerosonde

Figure 1.1: Unmanned Aerial Vehicles

Source of photos: http://www.pbs.org/wgbh/nova/spiesfly/uavs.html

It was only during the 1970s and 1980s, that modern UAVs were developed extensively. The employments of UAVs gradually increase as flight missions become more complex and involve a high degree of risk. They are also deployed for long missions that may exceed the pilot's physical capabilities. During 1990s, UAVs grew in prominence in military operations all over the world, from the United States and Europe to Asia and even in the Middle East. They play an important role in military campaigns and are pivotal in their operations. There are thousands of UAVs flying today, and the diversity of applications to which they are being applied is continually expanding. Besides being used for military applications, UAVs are also beginning to play peaceful roles such as monitoring of our Earth's environment or patrolling hilly areas to detect forest fires. An example of such a UAV is the Aerosonde UAV as shown in Figure 1.1(b). This UAV was developed and operated globally by Aerosonde Pte. Ltd. (AePL) and Aerosonde North America (AeNA) and has been undertaking various operations worldwide for the past 10 years. It was also the first UAV to cross the Atlantic Ocean in 1998.

However, UAVs have their own limitations. UAVs are generally small and light weight compared to conventional aircraft, thus their performance is affected by atmospheric disturbance. With the absence of real time pilot inputs during such circumstances of changing environment flight conditions during flight, the operator on ground may not be able to rectify the problem in real time. In many instances, UAVs have crashed after entering into adverse flight conditions which the operator on ground was unable to detect and subsequently rectify the problem. Thus it is beyond the means of the operator on ground to prevent such crashes from occurring. In view of such occurrences, the biggest challenge for the future would be to develop a system that enables the UAV to stabilize itself via a comprehensive instrumentation and flight control system during atmospheric disturbance.

1.1 Stability and Control Analysis and Flight Control Systems

The design process of UAV is similar to that of a conventional aircraft. There are several essential disciplines that need to be considered in the development of an aircraft. These can be broadly categorized into four main disciplines, namely aerodynamic, stability and control system, structures and propulsion system. The aerodynamic and stability and control system form the backbone of the aircraft, while the propulsion system acts as the key driving force. These sit in the structures component which holds the whole aircraft together. Stability and control system determines how well the aircraft can fly and how well it can be maneuvered. Over the years, it is one of the key characteristics that have grown in interest to researchers. There are many problems that need to be addressed during the design process. The design process can be costly and time consuming; however, with the development of computer systems in the industry, pre-flight simulation provides an effective method in solving such problems. Flight simulation is a tool for the aircraft designer to analyze potential problems and to visualize the responses of the aircraft with various disturbance and inputs.

The aeronautical community has began researching and solving many technical problems for achieving powered flight of heavier than air aircraft since the beginning of the 20th Century. Albert Zahm [2] was the first person to outline correctly the requirements for static stability in a paper presented in 1893. Prior to the Wright brothers' successful flight, many individuals in the United States and Europe were working with gliders and unpiloted powered modes. Through their research and study of others works, the Wright brothers were convinced that the major obstacle to achieving power flight was the lack of sufficient control. Thus, they seek to improve control capabilities.

The approach taken by aviation pioneers like Lilenthal, Chanute and Langley [3] was to design an aircraft that was inherently stable, leaving the pilot with no other duty except to steer the vehicle. The price paid for this stability was the lack of maneuverability and susceptibility to atmospheric disturbance. Although the Wright brothers aircraft was statically unstable, it was quite maneuverable. This design was similar to the current design of the world renowned F-16. The lack of stability made the control very difficult but it also allowed the plane to perform more maneuvers. This

characteristic introduced by the Wright brothers naturally made the pilot's job more difficult and challenging. Therefore, there is a need to design an aircraft with a balance between the stability and maneuverability. This has hastened the development of flight control acting as automatic system to relieve the human pilot of some of the duties.

There are many inherent stability characteristics which can be found in today's aircraft. The main purpose of the early autopilot was to stabilize the aircraft and return it to the desired flight attitude after any disturbance. It is worthy to note that merely after 11 years after Wright brother's historical flight, an auto pilot, using gyros to sense the deviation of the aircraft from the desired attitude and servo motors to activate the elevators and ailerons, was developed and built by the Sperry Gyroscope Company of New York under the direction of Dr. Sperry [4]. The apparatus called the "Sperry Aeroplane Stabilizer", installed in the Glenn H. Curtis flying boat, won prominence on the eighteenth of June 1914. The pilot Lawrence Sperry was walking back and forth the wing during a demonstration while flying close to the ground with the automatic control activated, thus winning the award of the most stable plane of that era.

Many types of flight control systems (FCS) also commonly known as autopilot system were developed over the years. They were initially developed to maintain the attitude and heading of an aircraft. However with the introduction of high performance jet aircraft, new systems has to be developed to solve the complex problems faced by these aircraft. Only in recent years, unmanned and autonomous flight has grown in prominence and new systems have to be introduced. Therefore there is a need for the development of a more sophisticated flight control system to aid the pilot in his control of the aircraft during flight. Regardless of its role, control systems generally respond faster and more accurately but with less reliability than human controllers as control systems are unable to exercise judgment in the decision model. The goal of the control system engineer is to optimize the performance of the system to meet the specified design requirements. The first step in the design procedure stated in Blakelock [5] is the determination of the system purpose and overall system requirements, such as the mission phases and operational requirements; the second step is the determination of the characteristics of the vehicle, control surface actuators and feedback sensors. The proposed systems are then

analyzed to determine if any stability problem exist which would require system modification to correct. The designed system is then evaluated by developing a hybrid or digital simulation of the complete system with the possibility of including actual hardware in the loop.

After defining the initial requirements, the stability and control characteristics of an aircraft which are referred to as the vehicle's handling or flying qualities are calculated based on the requirements. Aircraft with poor handling qualities are unsafe and hazardous for the pilot to fly. Hence, the design and performance of the control system is an integral part for the stability and control of the aircraft. Aircraft stability and control determine the conditions that make an aircraft stable and determine the design of control systems for good handling qualities. Handling qualities of conventional aircraft are readily available through FAR standards. However, the handling qualities of the UAV are not explicitly stated in standards presently and thus post a challenge for researchers in the development and design of UAVs.

The classical approach to stability and control analysis is to start with the complete equation of motion and make assumptions that enable this equation to be linearized about some equilibrium local point. The basis for such analysis, computation or simulation of the unsteady motions of a flight vehicle is the mathematical model of the vehicle and its subsystem. An aircraft in flight is a very complicated dynamic system and the foundation of the analysis of aircraft dynamic stability and response were laid by the pioneering work of Bryan [1]. His formulation was based on two principal assumptions: 1) the instantaneous aerodynamic forces and moments depend only on the instantaneous values of the motion variables and 2) the aerodynamic forces and moments vary linearly with motion variables. From his works, the development of "Stability Derivatives" is introduced to develop a mathematical model which is used to represent the aircraft in a simulation. These stability derivatives are related to the changes in the aerodynamic forces and moments acting on the aircraft caused by changes in motion, orientation or control surface motion. This mathematical model forms the fundamental framework for flight simulation.

1.1.1 Flight Simulation

Flight simulation plays an important role in flight testing today. As its name implies, the object of flight simulation is to reproduce on the behaviors of an aircraft in flight on the ground. The practical value of flight simulation can be judged by the extensive use of technique in aerospace research and development and by the fact that more than 500 flight simulators are used throughout the world for training and maintaining the skills of civilian and military aircrew. Over the years, simulators have evolved from a simple machine in its early days, as shown in Figure 1.2(a), to a more comprehensive system that mimics the actual aircraft to have enhanced pilot training, as shown in Figure 1.2 (b).

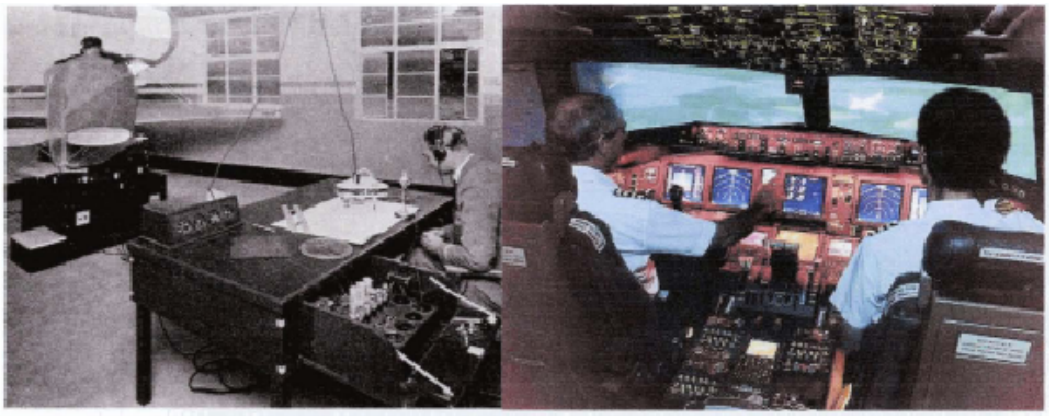

(a) Year 1938 (b) Present

Figure 1.2: Development of Flight Simulators from the early days to present
Source: http://homepage.ntlworld.com/bleep/SimHist8.html

When flight simulators are used in research, designers can explore the implications of different design options without having to incur expenses. Further delay arising from building and testing a range of prototypes can be avoided. Engineers at BAE Systems Controls in Jonhson City, New York, developed and successfully flight tested a UAV, flight avionics system and ground control station in just eight months using MathWorks tools [6]. The tools enabled the geographically separated team to design, model, and analyze control system, simulate the UAV, visualize the simulation data, perform testing and generate the autopilot code automatically, all in a single, model-

based design environment. This is an example of how flight simulation tools are used in the development of a product in the industry.

Flight simulation has provided a means of evaluating the likely behavior and consequences arising from abnormal operating configurations. Solutions to handling problems associated with deep stall, spiral descends; air turbulence and wind shear have been developed with the aid of simulators. A high fidelity simulation model can simulate the responses of an UAV under any flight conditions with disturbance from the environment as required by the operators. In a modular based design framework, the functions of the UAV can be adjusted according to the requirements and fine tuned to obtain the desired outcome. This output of the modular framework can be incorporated into graphical interface for visualization using tools from MathWorks like *VRML* or using *Simulink* [7] interfacing with *FlightGear* [8] as shown in Figure 1.3.

(a) External View (b) Cockpit View

Figure 1.3: Screenshots on UAV Flight Simulation on *FlightGear*
Source: http://www.u-dynamics.com/

Scans & Barnes [9] pointed to the fact that, while flight simulators have existed for more than half a century, most of the advantages and benefits from simulation have only been evident since the mid 1960s. The form of simulation here is the creation of a dynamic representation of the behavior of an aircraft in a manner which allows the human operator to interact with the simulation as part of the simulations. Flight simulation presents a multidisciplinary challenge to skills and ingenuity. This position has been described by former Chief Test Pilot of the British Civil Aviation Authority, Davis [10]

Flight Simulation is a fascinating and challenging field of science. It encompasses a wide field of disciplines from hydraulics and electronics to aerodynamics, performance and optics as well as massive contribution in terms of human engineering. The biggest challenge is overcoming the limitation of not being able to establish all the root equations of motions as fundamental parameters and the need to cook the system so that these compromises are not significant. In many ways working with simulators is much more demanding than working with real aircraft.

The usage technique in the development of the flight simulation is essential and important. Thus the task or set of function for which the simulation is used is constrained and elements of the real-life task may themselves have to be distorted to allow a valid solution to the aim of the simulation. Decision about the choice and content of the model and the associated device are an aspect of that facet of simulation practice which has already been described as being in some part an art. Shannon [11] emphasizes this as a key point in simulation when he says:

"The tendency is nearly always to simulate too much detail rather than too little. Thus, one should always design the model around the question to be answered rather than to imitate the real system exactly. Pareto's law says that in every group or collection, there exists a vital few and a trivial many. Nothing really significant happens unless it happens to the vital few. The tendency among systems analyst has too often been to transfer all the detailed difficulties in the real situation into the model, hoping that the computer will solve their problems. This approach is unsatisfactory not only because of the increased in difficulty of programming the model and the additional cost of longer experimental runs, but also because the truly significant aspects and relationships may get lost in all the trivial details. Therefore, the model must include only those aspects of the system relevant to the study objectives."

Clearly, Shannon's advice is directed towards those who would use simulations for research. However, in relation to the use of flight simulators for trainings his views is complemented by Prophet, Caro & Hall [12] who remarked that: *"If the aircraft is a poor learning environment, and for many flight related skills it is one of the poorest*

imaginable – then a ground based duplicate of that environment will not necessarily be a better one in which to learn."

The above advice states explicitly that not only must a thorough examination of the application be undertaken before deciding upon the simulation as the solution but also what elements to include in the simulation must be made with care. This is clearly so in this context, where the UAV have to be simplified and analyzed based on constraints and the needs for its research scope in the identification of possible problems that it will face in the specific flight conditions.

As mentioned earlier, the platform to be used for the modeling of the aircraft before the analytical process of flight control system design is the mathematical model. The mathematical model which describes the subject aircraft configuration is the heart of the analysis. Mathematical model of aircraft has existed a long time ago. However, due to limitation in calculation techniques, these models have to be simplified and usually not a good representation of the actual model. This became possibility with the development of computer systems. With the increased capability of computer over the years, two ensuing development resulted, firstly the scope and magnitude of the model could be extended, and secondly because the model was being implemented using a device which used electrical pulses, initially in analogue and subsequently in digital form, it opened the way to the development of enhancements to the implementing device.

The aircraft model is the core component of the simulation and it contains sub models representing the handling characteristics of the airframe, engines and manual and automatic control system which are placed in a simulation environment. It is possible to create detailed air and ground environments in which the aircraft model reside with the capabilities of computers.

1.2 Description of UAV Systems and Case Studies

Figure 1.4: UAV model used in study
Source: http://www.mindef.gov.sg/rsaf/main.asp

The system as defined in the manual [13] operates an UAV designed as an airborne observation platform to provide reconnaissance mission. The digital assembly controls the UAV subsystems. The major components of the system are the UAV airframe, the propulsion system, the ground control station (GCS), flight control system (FCS) and Air data Unit. The UAV is a fixed-wing, 7.65m wingspan aircraft as shown in the photograph Figure 1.4. The UAV is made of composite materials, characterized by low weight and high strength. The major components of the UAV structure are namely, a fuselage assembly, a wing assembly, a tail and boom assembly and a landing gear assembly which consist of a main landing gear, a nose landing gear and the arresting hook system.

The UAV fuselage houses the propulsion system and payload of the aircraft. Various compartments have been designed to place the various types of equipment and its system for different missions. The weight without any payload is 222.0 kg and the maximum take off weight is approximately 381.0 kg. The wing assembly has two booms that connect to the tail assembly which consists of a twin vertical tail and a horizontal platform. The pusher propulsion system is placed at the end of the aft fuselage. A geometric model of the UAV is developed using AutoCAD tools like *SolidWorks* [14]

and *Rhinoceros* [15]. The aerodynamic, stability and control characteristics of the UAV can be found in Appendix A.

The UAV basic flight control systems consist of ailerons and flaps on the wing, a twin rudder system on the vertical tail section and elevators on the horizontal tail. The flaps have three configurations, namely for taking off, cruising flight and landing. Elevators, ailerons and rudders are used for the various flight actions and they are controlled via the ground control station. The GCS is the main control unit of the system. It centralizes all commands sent to the UAV and all the reports received from the UAV. It provides the man-machine interface required by the system operators to evaluate the data received.

The FCS controls all flight functions and its block diagram can be seen in Figure 1.5. It receives commands from GCS and flight data detected by the system. It then sends a correcting signal to the servo-actuators to execute the required command. The FCS is the autopilot (AP) software module, which performs UAV guidance and stabilization. The FCS uses the sensors such as the vertical gyro unit, rate gyro unit, air data unit and flux valve unit as flight references data for the AP loop operations. The FCS program controls the UAV stabilization using sensor data and guidance commands received from the GCS or the mission control system (MCS), and controls the servo actuators that move the control surfaces.

Autopilot (AP) operates in the following configuration that transmits the information to the uplink (UPL). For the UPL Stick Control there are two modes, AP disconnect and AP normal. In AP disconnect, the UAV operator positions a switch sending a command to disconnect and bypass the AP stabilization loops. The stick command goes directly to the control surfaces and steers the UAV without stabilization. In AP normal, the stick commands are translated into position commands. Position steering commands for pitch and roll are sent to the AP stabilization loops. The UAV follows the stick position. The throttle command from the stick is send through a linearization circuit so that engine output is linear. The rudder channel also operates a yaw damper and a stick command. In the UPL hold (Knob) control the air vehicle operator uses the operator control panel knobs to select speed, altitude and roll or

direction values. The knob commands are processed by the speed, altitude, roll and direction loops. After processing, these commands are fed to the stabilization loops instead of the stick command. Operation of UAV by knobs is maintained even if one UAV sensor fails, by using the sensor backup mode. A malfunctioning sensor is backed up by other flight data sensors according to a pre-calculated estimation function by the digital central processing assembly (DCPA).

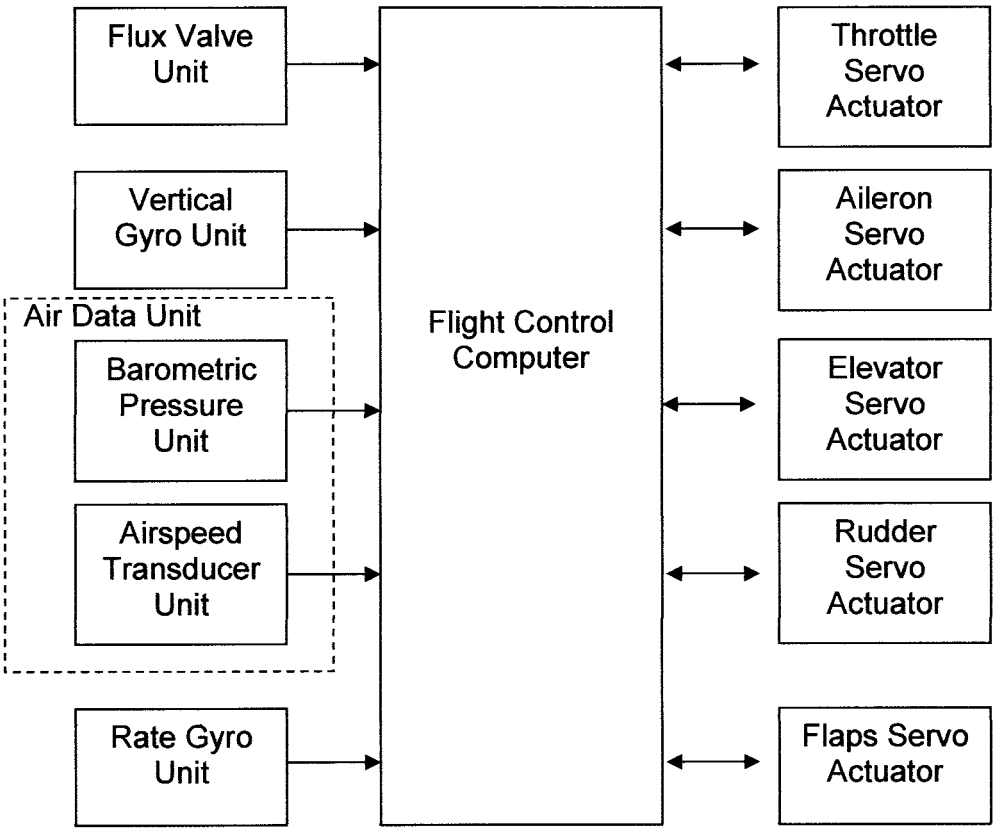

Figure 1.5: Block Diagram of Flight Control System

UAV stabilization in the longitudinal axis is performed by using five different control loops in the system. The pitch control loop is utilized to control the elevators and the airspeed control loop utilizes the pitch control loop as its inner loop to maintain the required airspeed. The throttle and altitude control functions in the same manner with the throttle control loop being used as the inner control loop. Finally there is the flap control system which controls the flap configuration. In the lateral axis, the system uses the roll

loop, heading loop and the yaw loop to stabilize the UAV. The AP receives data from the Vertical Gyro Unit (VGU) which measures the pitch and roll angles. The Air Data Unit (ADU) which consist of the airspeed transducer and the barometric pressure unit measure the indicated airspeed and altitude. The Flux Valve Unit (FVU) indicates the heading angle of the UAV while the Directional Rate Gyro Unit (RGU) measures yaw rate. The external pilot controls the UAV during the take-off and landing sequence. He takes control of the UAV when the UAV is within the field of vision from the pilot. The internal pilot operates from the Ground Control Station through the data provided by the telemetry from the Flight Control Computer.

1.2.1 Case Studies

Two separate field scenarios in which the UAV experienced an uncommanded spiral decent and an uncommanded roll oscillation is considered for modeling studies in this section.

In the first incident, the UAV cruised at 36 m/s (67 knots) as indicated by the indicated airspeed (IAS) reading at an altitude of 1067 m (3500 ft) when the internal pilot from the ground control station initiated a 20° right roll towards the north to avoid adverse weather conditions. However, instead of following the command initiated by the internal pilot via the control knob, the aircraft went into a left roll of 45° and started to descend. The crew attempted to regain control of the UAV by switching between the two configurations mode, the knob control function and the stick control function. Finally after the UAV had spiraled downwards through 3 revolutions, the control of the UAV was regained at an altitude of 304.8 m (1000 ft) which was still within the UAV flight envelope. An investigation conducted on the incident concluded that the primary cause of the incident was due to a strong tail wind. The effectiveness of the elevator controller was also identified as the secondary cause of the incident.

In the second incident, the UAV cruised at an altitude of 457.2 m (1500 ft) when the external pilot executed a left turn under crosswind conditions. The UAV experienced an excessive left roll and telemetry readings indicated an excessive roll oscillation varying from 40 degrees left to 20 degrees right on the UAV's attitude indicator. It was

concluded that the UAV had entered into a high angle of attack regime which resulted in a stall on the left wing which induced the roll oscillation.

In order to have a better understanding of the problems experienced by the operators, a thorough re-evaluation of both incidents had been carried out in the field. A summary of the telemetry and pilot input during the course of the case study are shown in Table 1.1. The data plotted in the Figure 1.6 to 1.9 is obtained from the operators. The crew attempted to regain control of the UAV by switching between different controls modes from knob control mode to stick control mode and vice versa. The plots of the time history of the control surface deflection and pitch and roll angle shown in Figures 1.6 and 1.7 respectively give an overview of the efforts made by the crew in regaining control of the UAV during the incident.

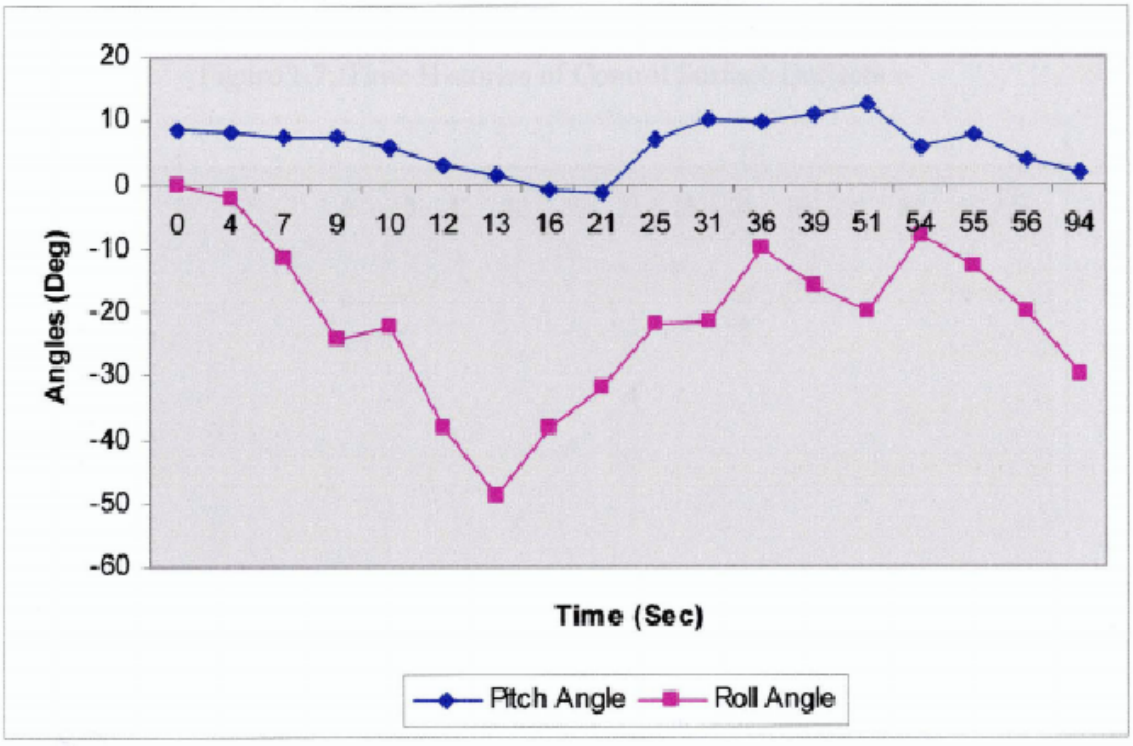

Figure 1.6: Time Histories of Pitch and Roll Angle

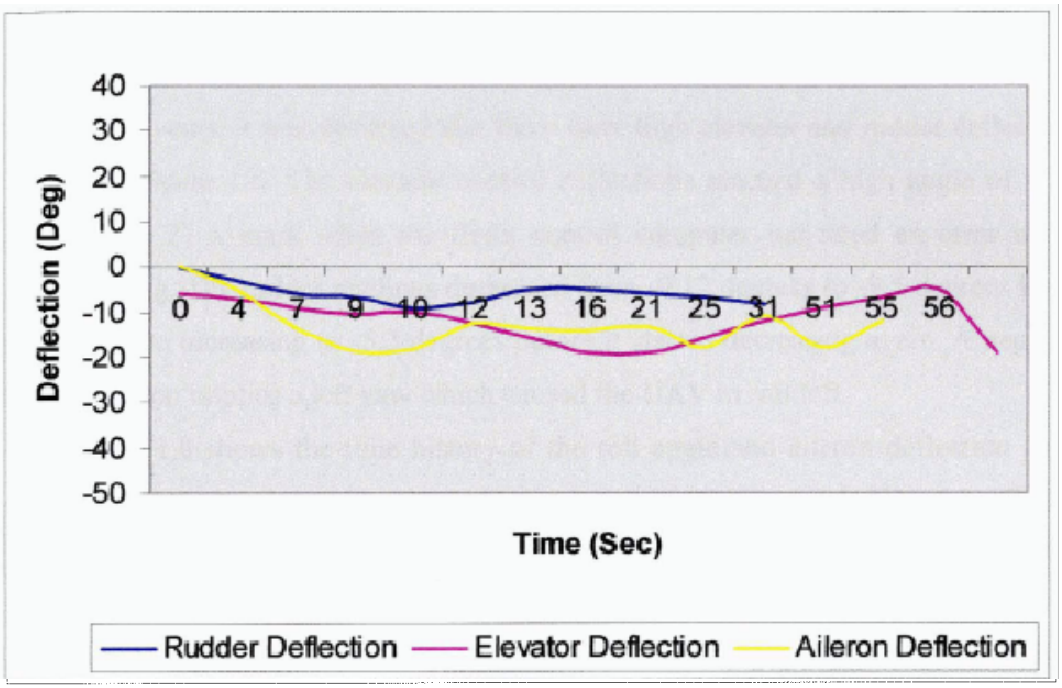

Figure 1.7: Time Histories of Control Surface Deflection

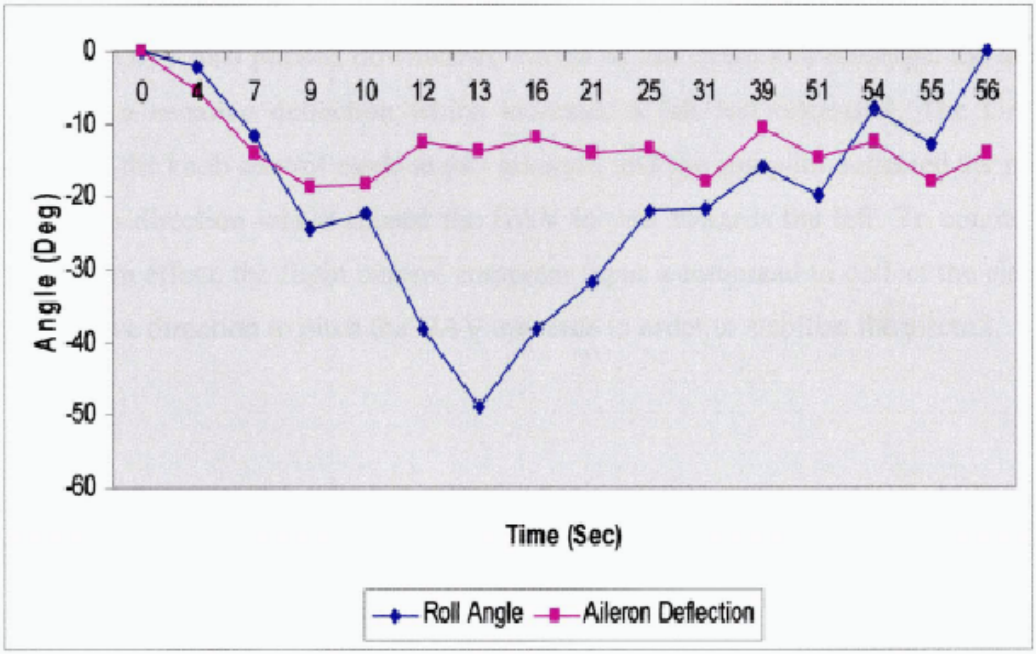

Figure 1.8: Time histories of Roll Angle and Aileron deflection

When commanded to roll right, the aileron servos responded correctly, with the left aileron deflected downwards, and the right aileron deflected upwards. During the course of the events, it was observed that there were high elevator and rudder deflections as shown in Figure 1.6. The elevator control deflections reached a high angle of -19.2 degrees at the 21 s mark when the flight control computer indicated an error in the heading reading. The rudder readings decreased from -0.12 degrees to -9.5 degrees in the first 10 s before increasing to -5.3 degrees before it started decreasing again. A negative rudder deflection implies a left yaw which caused the UAV to roll left.

Figure 1.8 shows the time history of the roll angle and aileron deflection angle over a 60 second duration when the UAV executed an uncommanded descent. By the sign convention defined in Kertesx [13], the roll angle decreased to a reading of -50 degrees, indicating a left roll during the first 13 second before reversing its direction for the later time of the incident. The aileron deflection was maintained for the whole incident between -10 degrees to -20 degrees, which represents a right roll command. It was also observed that the aileron oscillated during this motion. As the UAV began the left roll, the UAV also pitched downwards. Based on the down link readings, the aileron experienced a negative deflection which indicated a left roll command. The UAV is operating on the knob control mode at this instance, and the autopilot deflected the rudder in a negative direction which caused the UAV to yaw towards the left. To counter the pitching down effect, the flight control computer input a command to deflect the elevator in the negative direction to pitch the UAV upwards in order to stabilize the aircraft.

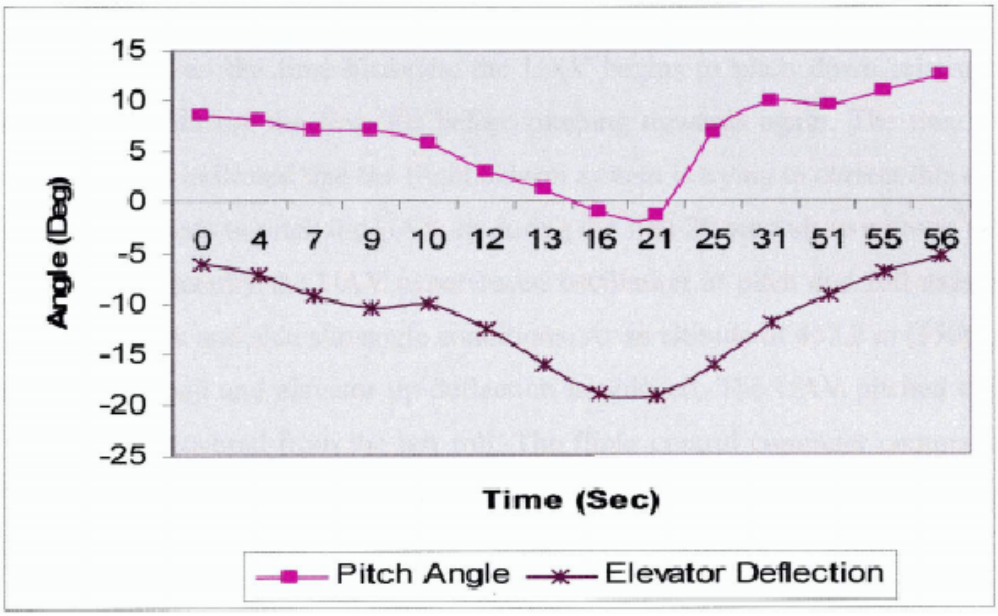

Figure 1.9: Time histories of Pitch Angle and Elevator deflection

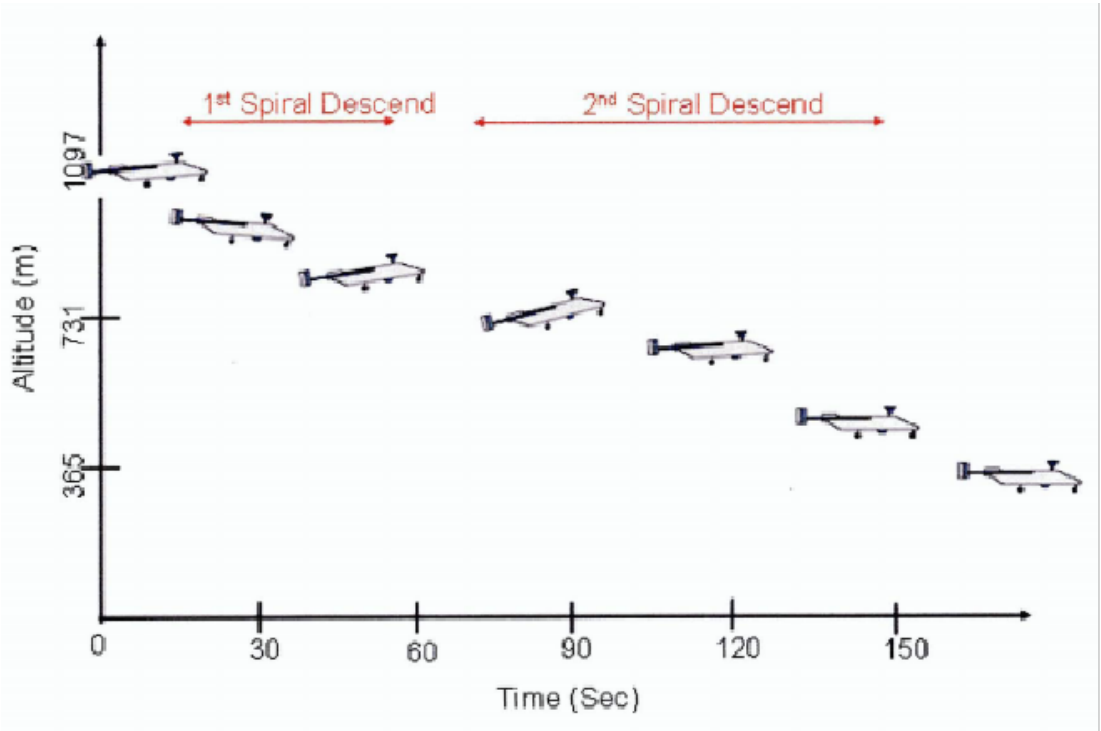

Figure 1.10: Altitude History plot of Case Study

Similarly the time histories of the pitch angle and elevator deflection are shown in Figure 1.9. Based on the time histories, the UAV begins to pitch down relative to its previous position during the first 20s before pitching upwards again. The trend of the elevator deflection indicated that the flight control system is trying to correct this error by deflecting downwards to pitch the UAV up during the first 20 seconds to recover the trim conditions. Subsequently the UAV experienced oscillation in pitch and roll axis due to high angle of attack and side slip angle conditions. At an altitude of 457.2 m (1500 ft) the IAS reading dropped and elevator up deflection is reduced. The UAV pitched down to gain speed and recovered from the left roll. The flight control computer commands the UAV based on the calculated value of the airspeed. Thus a clogged pitot tube caused an over reading of IAS by the flight control system and thus lead to an auto-pilot increasing UAV pitch/angle of attack to decrease speed when in actual fact the speed is much lower.

At an altitude of 304.8 m (1000 ft) and 4km away from the airbase, the UAV responded to the pilot inputs and started to climb. An immediate recovery was initiated and the UAV landed uneventfully. A plot of the time variation of the decent in terms of altitude is shown in Figure 1.10 from which it can be concluded that the possible causes of the incidents were elevator creep which reduced the roll control and lateral stability at high angle of attack. Elevator creep occurs when the structure of the control surface undergo severe stress due to fatigue after extensive hours of flight. Coupled with the strong tail wind conditions during the incident and the over reading of the IAS due to the clogging of the pitot tube assembly, the UAV experienced an uncommanded spiral descent. It was subsequently recommended that the UAV flight characteristics especially the high angle of attack warning system in the flight and operator's manual be reviewed. Investigators also recommended that a study on the aerodynamics and the stability and control of the UAV be investigated in order to assess how critical the environmental and atmospheric effects are on the UAV.

Table 1.1: Incident Summary

Time (in Sec)	**Pilot Input**	**Telemetry Playback**
0:00	During Straight and Level Flight, at 3500 ft (1067 m), in knob mode, IP initiated heading change via heading knob (UAV to execute right roll)	Heading command change from 187 to 263. Downlink indicates a change from 185 to 183.
0:04	UAV execute left roll High angle of attack warning (8.2 deg)	1st Spiral Descend
0:07	Descend at 7.62 m/s	Autopilot Malfunction warning lit. 2 Spiral descend. High elevator angles and rudder deflection. Elevator increases to -19.2 at 21 s mark (pitch up action) Rudder deflect at a max of -9.5 at the 10 s mark (Right yaw)
0:09		
0:10		
0:12		
0:13		
0:16		
0:21		
0:25		
0:31		
0:36	IP switch from Altitude (ALT) and heading (HDG) knob mode to Stick mode	Autopilot System disengaged, External pilot took control of the UAV.
0:39	Stick active IAS indicate 67 knots (34.5 m/s)	
0:51	Stick active 2842 ft (866.2m)	
0:54	Stick active	
0:55	Stick active	
0:56		
1:34	Heading Knob mode	
1:48	Roll mode	
1:50		
2:10		
2:16	Heading Knob mode	
2:41	Regain control	

Firstly due to the weight of the UAV, which is relatively low compared to a conventional aircraft, the UAV is subjected to a disturbance that creates an unpredictable behavior when subjected to unfavorable atmospheric conditions. Secondly with a single propulsion system, the UAV is subjected to an asymmetrical flight condition about flight path axis. Thirdly, the slipstream caused by the pusher propulsion system at the aft of the UAV will create an interference with the tail assembly. This is most apparent during sideslip condition, where the rudder control surface will fall in the slipstream and this will caused the rudder to lose its effectiveness partially.

1.3 Motivation and Objectives

Without any simulation framework to study and investigate the effects of the atmospheric disturbance and asymmetrical flight, the main aim of the proposed study is to develop a high-fidelity simulation model to simulate the different flight conditions that the UAV is experiencing. With a simulation framework, the parameters of the UAV can be modified in response to the various disturbance caused by the atmosphere. A computational model for predicting the aerodynamic and its stability and control characteristics of the UAV will first be developed. These computational predictions will be verified with the experimental data obtained from the wind tunnel model provided by the OEM of the UAV and flight data provided by the operators. The computational model for both non-linear and linear simulations will be build. The simulation model will be used to study the various flight stability and control problems experienced by the UAV at the various flight conditions and also to examine and proposed solutions to this flight stability and control problems which will provide insight into possible modifications to the existing UAV to correct these instabilities.

1.4 Overview of Study

After analyzing the case study, several steps have been taken in the investigation of the incident. Based on the experience of the operator of the UAV, the problems have to be simplified into several components to be analyzed. The mathematical model for the simulation of the UAV will be developed in chapter 2. From Newton's 2nd Law of motion, the aircraft equation of motions will be derived, and basic assumptions will be made to formulate the most appropriate model. The aircraft model is linearized by using the small disturbance theory for the conventional stability and control analysis. Longitudinal and lateral directed motion is decoupled and the six degrees of freedom equation split into two groups each describing three degree-of-freedom. However decoupled effects are based on the assumption of a symmetrical flight, and in this case the propulsion system in the UAV might create an asymmetrical flight conditions. Thus a mathematical model based on a coupled analysis will be derived to make a comparison with the decoupled analysis.

A comprehensive aerodynamic database of the UAV has to be developed for the calculation of the mathematical equations. The aerodynamic characteristics data provided by the industrial partner is incomplete. As this data is required for this study, various methods have been used to obtain the missing data and construct a more complete aerodynamic database for the flight simulation framework. The results based on empirical methods and computational fluid dynamics are discussed in Chapter 3. Within the scope of the aerodynamic analysis, the author will also study the characteristics of the UAV at high angle of attack where the author will look at the stalling and spinning effects of the UAV. After the development of the aerodynamic database the study of the natural modes of the UAV based on both the de-coupled and coupled analysis calculated using *Matlab*® [16] will be discussed, before a non linear framework of the UAV model built in *Simulink* with *Aerospace Blockset* [15] and *AeroSim* [16] interfacing with a graphical tool in *FlightGear* will be presented. The models of each of the subsystem based on the mathematical models will be discussed in this chapter. Finally recommendations to the enhancement of the operations of the UAV and the conclusion to this report can be found in Chapter 4 based on the analysis of the results found in the previous chapters.

Chapter 2
Formulation of Flight Dynamics Model

The term 'mathematical model' is growing in complexity and extent, and is also applied to other features of the aircraft such as its control system and many internal systems. For each of the feature being modeled, it is necessary to formulate the model so that the 'behavior' of the system in some sense, i.e. the response of the system to a stimulus, may be calculated. Central to this framework is a mathematical model of the aircraft which is usually referred to as the equation of motion. The equation of motion provides a complete description of response to controls, subject to the modeling limitation. The response is measured in terms of the displacement, velocity and acceleration variables. The flight conditions describes the conditions under the model is used and includes such parameters as Mach number, altitude, aircraft geometry mass and trim state. The model provides the basis for flight control system design and analysis.

The simulation space is divided into three basic elements as depicted in Figure 2.1. Starting with reality, a conceptual model, described via equations or other governing relations, is obtained by analysis. Implementation via computer programming yields a computer model which, through simulation, may be related to reality. The credibility of the conceptual model is then evaluated by procedures which test the adequacy of the model to provide an acceptable level of agreement with reality, while the computer model, in the form of an operational computer program, is confirmed as an adequate representation of the conceptual model by procedures of verification. Finally, model validation demonstrates that this computer model possesses a satisfactory range of accuracy in comparison with reality and consistent with what is required. In creating or deriving the mathematical models, it is important that the modeler (the person doing the modeling) has a clear idea of what the model is for, and that he states this together with his definition of his model. It is important as stated by Thomas H.H. [19] because the purpose of the model influences its form and quality. Many systems are strictly governed by equations which may be extremely complex but which may often simplified in the

interest of obtaining practical solutions and yet still retains sufficient realism for the task at hand.

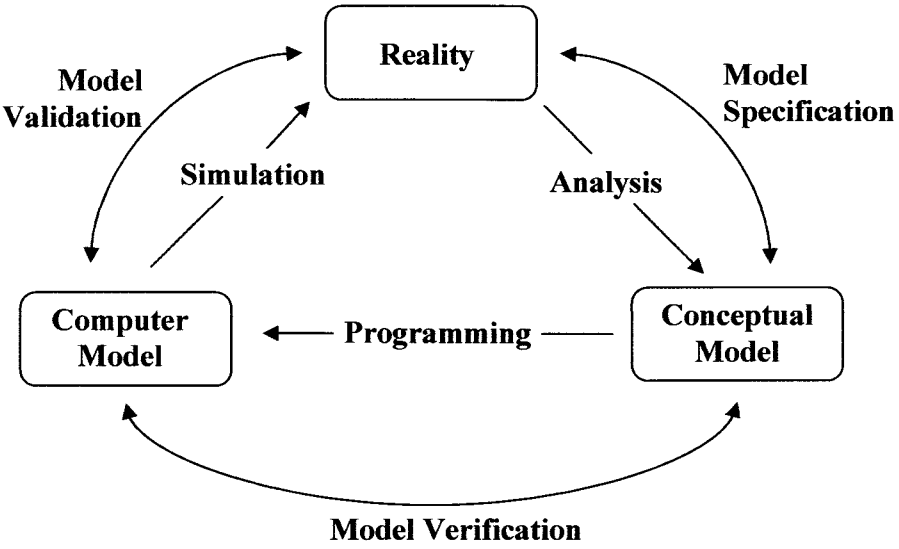

Figure 2.1: The Simulation Space and Definition of 'models'

A practical solution in the present context means one of adequate accuracy which can be achieved in real time. Real time here refers to a solution in which the calculation of a system's behavior over, say, one second of elapsed time can be achieved in one second or less of computing time. Adequate accuracy means that the real time solution yields the steady state performance of the vehicle and its transient behavior with an accuracy which is acceptable and sufficient for the role of the simulator. In aircraft flight mechanic analysis, the six-degree-of-freedom rigid-body equations are commonly linearized using the small disturbance theory. In the application of this theory, the lateral equations of this motion are usually uncoupled from the longitudinal equations motions as a result of imposing the small-disturbance theory approximation and assumptions made during the course of linearization. This is usually the case when they are linearized about a straight and level flight conditions. The equations are thus decomposed into the lateral and longitudinal equations for computation and analysis.

In reality, the actual response of a rigid aircraft subjected lateral disturbance involves six-degree-of-freedom mathematical model. Furthermore, inertia and gyroscopic

effects can produce coupling between lateral and longitudinal equations, even in the framework of small disturbance theory. Inertial coupling occurs when the aircraft are flown in an asymmetrical configuration where the aircraft mass is not symmetrical about the x-z plane. The spinning rotors associated with the aircraft power plants, i.e. turbines, compressors and propellers is another addition effect that causes cross coupling. This so called gyroscopic coupling occurs as a result of the presence of any net angular momentum associated with the rotor spinning relative to the body-fixed coordinate system. Even in the present analysis, such occurrences of the first order coupling between the lateral and longitudinal equations are not unusual. Furthermore, this coupling could prove relatively important in fields where the propulsion system rotor mass may be of a very significant fraction of the total mass. This is more significant in smaller aircraft for example UAV and MAV.

In conventional analysis of flight mechanics stated in Ekins [20] and Nelson [2], the coupled effect was not taken into considerations in the linearized aircraft stability and control analysis to simplify the calculations. Thus there is a need to develop a coupled mathematical model to investigate and analyze the linearized aircraft flight mechanics as well as its stability and control in a coupled model. This is especially so in the analysis of the UAV in this study, where the propeller effects might have significant effects in the analysis to identify the problems it faces in flight.

Decades ago, when the linearized aircraft dynamics was first developed, the longitudinal and lateral equations of motion reduce eigen problems associated with the six DOF aircraft dynamics from one of a 12 x 12 system to two 6 x 6 systems. This represented a significant reduction in computation time. In usual practice, to further reduce computation time, the 6 x 6 systems was commonly reduce to a 4 x 4 systems. The eigenvalue obtained from the 4 x 4 system are identical to those obtained from the 6 x 6 system, except that the lower-order system does not yield the trivial rigid body displacement modes. This represents no loss of information. However, there is a loss of information in the eigenvectors when the 6 x 6 systems are reduced to 4 x 4. Two components of each eigenvector are lost. This is a small price to pay for the computational savings that were realized in the early mid 20^{th} century. Today, there are

no significant computational savings to be gained by uncoupling the linearized longitudinal and lateral equation of motion. When modern computational facilities are used, the solution of a 12 x 12 eigenproblem is trivial. Thus, it is quite simple to account for longitudinal-lateral coupling in the linearized six degree of freedom aircraft dynamics.

The aim of this chapter is to develop a mathematical model for coupled and decoupled mathematical model linearized about a coordinated turn and straight and level flight conditions. Both models will later be used to evaluate initial conditions disturbance as well as step input function using *MATLAB*® to obtain results for both type of analysis to make a comparison and understand the effects it has on the longitudinal and lateral motion under similar conditions of flight. As discussed in the previous chapter, stalling and subsequently spinning might be a potential problem faced by the operators of the UAV. This mathematical model will aid the users in the understanding of such phenomenon and provide the foundation for the author to develop solutions to such occurrence.

2.1 The Rigid Body Aircraft Equations of Motion Derivation

2.1.1 Formulation

Before developing the equations of motion, it is important to understand the axis system specified. Figure 2.2 shows the body axis system fixed to the UAV and the inertial axis system that is fixed to the Earth.

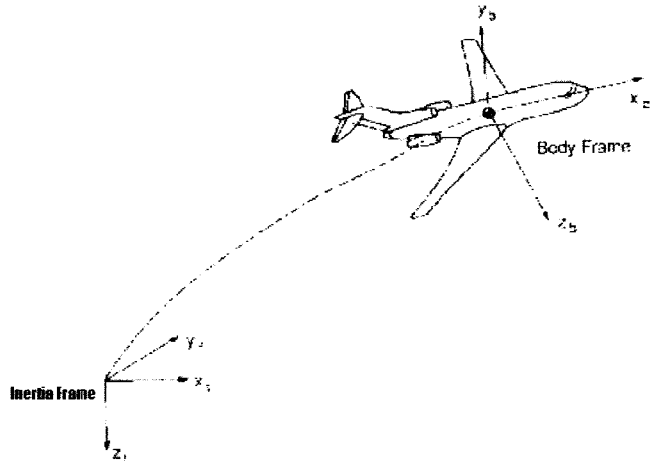

Figure 2.2: Body and Inertial axis systems

Source: Nelson, R.C., *Flight Stability and Automatic Control*, 2nd Edition

Body axis system refers to a centerline (x axis) and two orthogonal axes that are convenient references for design, construction, and operations of the aircraft, one vertical down in the mirror symmetry and another to the right (as viewed from the rear of the aircraft). The equations of motion are derived from Newton's second law. For many problems in aircraft dynamics, an axis system fixed to the Earth can be taken as an inertial reference frame. Based on Newton's second law, it can be expressed as:

$$\sum \mathbf{F} = \frac{d}{dt}(m\mathbf{v}) \tag{2.1}$$

$$\sum \mathbf{M} = \frac{d}{dt}\mathbf{H} \tag{2.2}$$

Equation (2.1) and (2.2) can be rewritten in scalar form and then contain three equations and three moments equation. The three force equation can be expressed in the following equations:

$$F_x = \frac{d}{dt}(mu) \qquad F_y = \frac{d}{dt}(mv) \qquad F_z = \frac{d}{dt}(mw) \qquad (2.3)$$

where F_x, F_y, F_z and *u, v, w* are the components of the forces and velocity along the x, y and z axes, respectively. The moment equations can be expressed in a similar way:

$$L = \frac{d}{dt}H_x \qquad M = \frac{d}{dt}H_y \qquad N = \frac{d}{dt}H_z \qquad (2.4)$$

where *L, M, N* and H_x, H_y, H_z are the components of the moment and moment of momentum along the x, y and z axes, respectively.

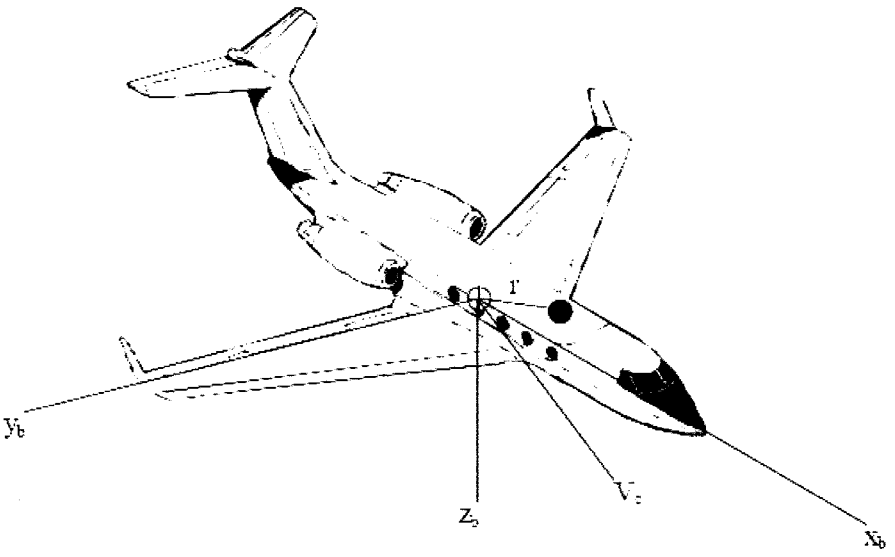

Figure 2.3: An element of mass on an aircraft

Source: Nelson, R.C., *Flight Stability and Automatic Control*, 2nd Edition

In figure (2.3), let δ_m be an element of mass of the aircraft, **v** be the elemental mass velocity relative to an absolute or inertial frame, and $\delta\mathbf{F}$ be the resulting force acting on the elemental mass. Newton's second law yields

$$\delta\mathbf{F} = \delta m \frac{dv}{dt} \tag{2.5}$$

And the total external force acting on the aircraft is found by summing all the elements of the aircraft:

$$\sum \delta\mathbf{F} = \mathbf{F} \tag{2.6}$$

The velocity of the of the differential mass δ_m is

$$\mathbf{v} = \mathbf{v}_c + \frac{d\mathbf{r}}{dt} \tag{2.7}$$

where $\mathbf{v_c}$ is the velocity of the center of mass of the aircraft and $\frac{d\mathbf{r}}{dt}$ is the velocity of the element relative to the center of mass. Substituting Equation (2.7) for velocity into Newton's second law yields

$$\sum \delta\mathbf{F} = \mathbf{F} = \frac{d}{dt}\sum(\mathbf{v}_c + \frac{d\mathbf{r}}{dt})\delta m \tag{2.8}$$

Assume the mass of the vehicle is constant; Equation (2.8) can be rewritten as

$$\mathbf{F} = m\frac{d\mathbf{v}_c}{dt} + \frac{d}{dt}\sum\frac{d\mathbf{r}}{dt}\delta m \tag{2.9}$$

or

$$\mathbf{F} = m\frac{d\mathbf{v}_c}{dt} + \frac{d^2}{dt^2}\sum\mathbf{r}\delta m \tag{2.10}$$

Because **r** is measured from the center of mass, the summation $\sum\mathbf{r}\delta m$ is equal to 0. Both Equation (2.9) and Equation (2.10) then become

$$\mathbf{F} = m\frac{d\mathbf{v}_c}{dt} \tag{2.11}$$

which relates the external force on the aircraft to the motion of the vehicle's center of mass.

Similarly, the moment equation referred to a moving center of mass can be developed. For the differential element of mass, δ_m, the moment equation can be written as

$$\delta\mathbf{M} = \frac{d}{dt}\delta\mathbf{H} = \frac{d}{dt}(\mathbf{r}\times\mathbf{v})\delta m \tag{2.12}$$

The velocity of the mass element can be separated into the velocity of the center of mass and the relative velocity of the mass element to the center of mass:

$$\mathbf{v} = \mathbf{v}_c + \frac{d\mathbf{r}}{dt} = \mathbf{v}_c + \omega\times\mathbf{r} \tag{2.13}$$

Where ω is the angular velocity of the vehicle and $\mathbf{r}$ is the position of the mass element measured from the center of mass. The total moment of the momentum is expressed as

$$\mathbf{H} = \sum\delta\mathbf{H} = \sum(\mathbf{r}\times\mathbf{v}_c)\delta m + \sum[\mathbf{r}\times(\omega\times\mathbf{r})]\delta m \tag{2.14}$$

The velocity $\mathbf{v_c}$ is constant and can be taken outside the summation sign

$$\mathbf{H} = \sum\mathbf{r}\delta m\times\mathbf{v}_c + \sum[\mathbf{r}\times(\omega\times\mathbf{r})]\delta m \tag{2.15}$$

The first term in equation (2.15) is 0 because the term $\mathbf{r}\delta m$=0. If the angular velocity and position vectors are expressed as

$$\omega = p\mathbf{i} + q\mathbf{j} + r\mathbf{k} \tag{2.16}$$

$$\mathbf{r} = x\mathbf{i} + y\mathbf{j} + z\mathbf{k} \tag{2.17}$$

then after expanding equation (2.15), $\mathbf{H}$ can be written as

$$\mathbf{H} = (p\mathbf{i} + q\mathbf{j} + r\mathbf{k})\sum(x^2 + y^2 + z^2)\delta m - \sum(x\mathbf{i} + y\mathbf{j} + z\mathbf{k})(px + qy + rz)\delta m \tag{2.18}$$

The scalar components of $\mathbf{H}$ are

$$\begin{aligned} H_x &= p\sum(y^2 + z^2)\delta m - q\sum xy\delta m - r\sum xz\delta m \\ H_y &= -p\sum xy\delta m + q\sum(x^2 + z^2)\delta m - r\sum yz\delta m \\ H_z &= -p\sum xz\delta m - q\sum yz\delta m + r\sum(x^2 + y^2)\delta m \end{aligned} \tag{2.19}$$

The summations in these equations are the mass moment and products of inertia of the aircraft and are defines as follows:

$$I_x = \iiint (y^2 + z^2)\delta m \qquad I_{xy} = \iiint xy\delta m$$
$$I_y = \iiint (x^2 + z^2)\delta m \qquad I_{xz} = \iiint xz\delta m \qquad (2.20)$$
$$I_z = \iiint (x^2 + y^2)\delta m \qquad I_{yz} = \iiint yz\delta m$$

The terms I_x, I_y, *and* I_z are the mass moments of inertia of the body about the x, y and z axes respectively. The terms with the mixed indexes are called products of inertia. The scalar equations of moment of momentum can be expressed as

$$H_x = pI_x - qI_{xy} - rI_{xz}$$
$$H_y = -pI_{xy} + qI_y - rI_{yz} \qquad (2.21)$$
$$H_z = -pI_{xz} - qI_{yz} + rI_z$$

If the reference frame is not rotating, then as the aircraft rotates the moments and the products of inertia will vary with time. To avoid the difficulty, the axis system will be fixed to the body axis system of the aircraft. It can be shown that the derivative of an arbitrary vector **A** referred to a rotating body frame having an angular velocity ω can be represented by the following vector identity

$$\left.\frac{d\mathbf{A}}{dt}\right|_I = \left.\frac{d\mathbf{A}}{dt}\right|_B + \omega \times \mathbf{A} \qquad (2.22)$$

where the subscripts *I* and *B* refer to the inertial and body fixed frames of reference. Applying the identity to the equations derived earlier yields

$$\mathbf{F} = m\left.\frac{d\mathbf{v}_c}{dt}\right|_B + m(\omega \times \mathbf{v}_c) \qquad (2.23)$$

$$\mathbf{M} = \left.\frac{d\mathbf{H}}{dt}\right|_B + \omega \times \mathbf{H} \qquad (2.24)$$

The scalar equations are

$$F_x = m(\dot{u} + qw - rv) \qquad F_y = m(\dot{v} + ru - pw) \qquad F_z = m(\dot{w} + pv - qu)$$
$$L = \dot{H}_x + qH_z - rH_y \qquad M = \dot{H}_y + rH_x - pH_z \qquad N = \dot{H}_z + pH_y - qH_x \qquad (2.25)$$

Assume the xz plane is a plane of symmetry of the aircraft, and it make the product of inertia $I_{yz} = I_{xy} = 0$. With this assumption, the moment equations can be written as

$$\begin{aligned} L &= I_x \dot{p} - I_{xz} \dot{r} + qr(I_z - I_y) - I_{xz} pq \\ M &= I_y \dot{q} + rp(I_z - I_y) - I_{xz}(p^2 - r^2) \\ N &= -I_{xz} \dot{p} + I_z \dot{r} + pq(I_y - I_x) + I_{xz} qr \end{aligned} \tag{2.26}$$

2.1.2 Transformation from Inertial Frame to Body Frame

The orientation and position of the aircraft can be defined in terms of a fixed frame of reference as shown in Figure 2.4. The orientation of the aircraft can be described by three consecutive rotations. The angular rotations are called the Euler angles. The processes to transform the orientation of the body frame to the fixed frame are described in the following manner. Imagine the aircraft to be posited so that the body axis system is parallel to the fixed frame and then apply the following rotations firstly rotate the x_f, y_f, z_f frame about the $0z_f$ through the yaw angle ψ to the frame to x_1, y_1, z_1, next rotate the x_1, y_1, z_1 frame about the $0y_1$ through the pitch angle θ bringing the frame to x_2, y_2, z_2. Finally rotate the x_2, y_2, z_2 frame about the $0x_2$ through the roll angle φ to bring the frame to x_3, y_3, z_3, the actual orientation of the body frame relative to the fixed frame.

After defining the Euler angles, the flight velocities components relative to the fixed reference frame will be determined. To accomplish this, let the velocity components along x_f, y_f, z_f frame be $\dot{x}$, $\dot{y}$, $\dot{z}$ and similarly let the subscripts 1 and 2 denote the components along x_1, y_1, z_1 and x_2, y_2, z_2, respectively. In Figure 2.4, the relationship between $\dot{x}$, $\dot{y}$, $\dot{z}$ and u_1, v_1, w_1 can be expressed as

$$\dot{x} = \frac{dx}{dt} = u_1 \cos\Psi - v_1 \sin\Psi \qquad \dot{y} = \frac{dy}{dt} = u_1 \sin\Psi + v_1 \cos\Psi \qquad \dot{z} = \frac{dw}{dt} = w_1 \tag{2.27}$$

Defining the shorthand notation $S_\Psi \equiv \sin\psi, C_\psi \equiv \cos\psi, S_\theta \equiv \sin\theta$, the equations can be simplified as shown in equation (2.28) and (2.29). In a manner similar to equation (2.27), u_1, v_1, w_1 can be expressed in terms of u_2, v_2, w_2

$$u_1 = u_2 C_\theta + w_2 S_\theta \qquad v_1 = v_2 \qquad u_1 = -u_2 S_\theta + w_2 C_\theta \tag{2.28}$$

$$u_2 = w \qquad v_2 = vC_\phi - wS_\phi \qquad w_2 = vS_\phi + wC_\phi \tag{2.29}$$

where the *u, v* and *w* are the velocity components along the body axes x_b, y_b, z_b

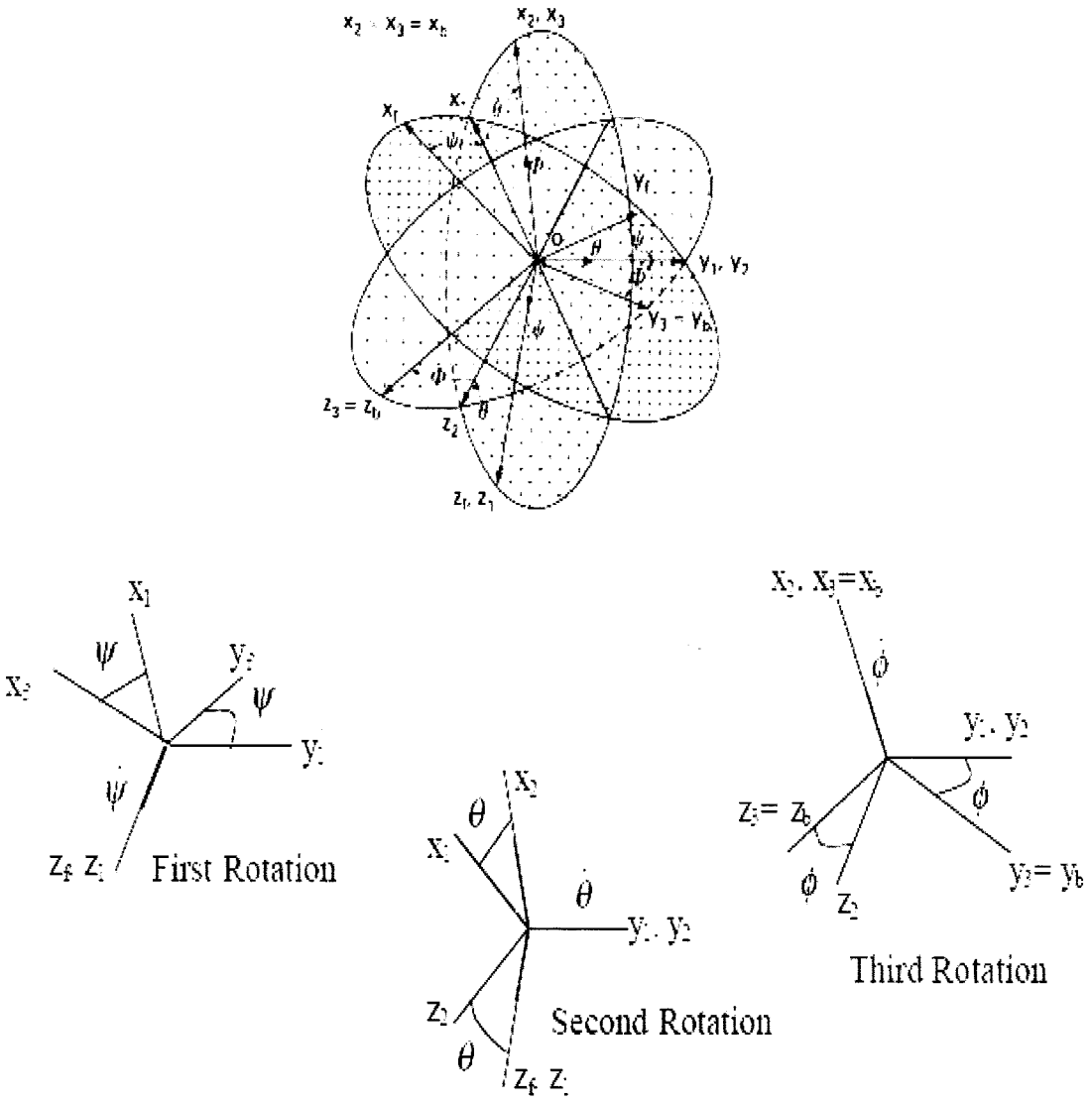

Figure 2.4: Relationship between body and inertia axes system

Source: Nelson, R.C., *Flight Stability and Automatic Control*, 2nd Edition

The absolute velocity in terms of the Euler angles and velocity components in the body frame can be determined by back-substituting the preceding equations

$$\begin{bmatrix} \frac{dx}{dt} \\ \frac{dy}{dt} \\ \frac{dz}{dt} \end{bmatrix} = \begin{bmatrix} C_\theta C_\psi & S_\phi S_\theta C_\Psi - C_\phi S_\psi & C_\phi S_\theta C_\Psi + S_\phi S_\psi \\ C_\theta S_\psi & S_\phi S_\theta S_\Psi + C_\phi C_\psi & C_\phi S_\theta S_\Psi - S_\phi C_\psi \\ -S_\theta & S_\theta C_\psi & C_\theta C_\psi \end{bmatrix} \begin{bmatrix} u \\ v \\ w \end{bmatrix} \quad (2.30)$$

The relationship between the angular velocities in the body frame (p, q and r) and the Euler rates ($\dot{\psi}, \dot{\theta}, and \dot{\phi}$) also can be determined in Figure 2.4

$$\begin{bmatrix} p \\ q \\ r \end{bmatrix} = \begin{bmatrix} 1 & 0 & -S_\theta \\ 0 & C_\phi & C_\theta S_\phi \\ 0 & -S_\phi & C_\theta C_\phi \end{bmatrix} \begin{bmatrix} \dot{\phi} \\ \dot{\theta} \\ \dot{\psi} \end{bmatrix} \quad (2.31)$$

Equation (2.31) can be solved for the Euler rates in terms of the body angular velocities

$$\begin{bmatrix} \dot{\phi} \\ \dot{\theta} \\ \dot{\psi} \end{bmatrix} = \begin{bmatrix} 1 & S_\phi \tan\theta & C_\phi \tan\theta \\ 0 & C_\phi & -S_\phi \\ 0 & S_\phi \sec\theta & C_\phi \sec\theta \end{bmatrix} \begin{bmatrix} p \\ q \\ r \end{bmatrix} \quad (2.32)$$

By integrating Equation (2.30) and (2.32), one can determine the aircraft's position relative to the fixed frame of reference and the Euler angles ψ, θ and ϕ. Table 2.1 gives a summary of the rigid body equations of motions in a matrix form.

Table 2.1 Summary of kinematics and dynamic equations

Description	**Equations**
Force Equations	$\begin{Bmatrix} X \\ Y \\ Z \end{Bmatrix} = m \begin{Bmatrix} \dot{u}+qw-rv \\ \dot{v}+ru-pw \\ \dot{w}+pv-qu \end{Bmatrix}$
Moment Equations	$\begin{Bmatrix} L \\ M \\ N \end{Bmatrix} = \begin{Bmatrix} I_x\dot{p}-I_{xz}\dot{r}+qr(I_z-I_y)-I_{xz}pq \\ I_y\dot{q}+rq(I_x-I_z)+I_{xz}(p^2-r^2) \\ -I_{xz}\dot{p}+I_z\dot{r}+pq(I_y-I_x)+I_{xz}qr \end{Bmatrix}$
Body angular Velocities in terms of Euler angles and Euler rates	$\begin{bmatrix} p \\ q \\ r \end{bmatrix} = \begin{bmatrix} 1 & 0 & -S_\theta \\ 0 & C_\phi & C_\theta S_\phi \\ 0 & -S_\phi & C_\theta C_\phi \end{bmatrix} \begin{bmatrix} \dot{\phi} \\ \dot{\theta} \\ \dot{\psi} \end{bmatrix}$
Euler rates in terms of Euler angles and body angular velocities	$\begin{Bmatrix} \dot{\phi} \\ \dot{\theta} \\ \dot{\psi} \end{Bmatrix} = \begin{bmatrix} 1 & S_\phi \tan\theta & C_\phi \tan\theta \\ 0 & C_\phi & -S_\phi \\ 0 & S_\phi \sec\theta & C_\phi \sec\theta \end{bmatrix} \begin{Bmatrix} p \\ q \\ r \end{Bmatrix}$
Velocity of aircraft in the fixed frame in terms of Euler angles and body velocity components	$\begin{bmatrix} \frac{dx}{dt} \\ \frac{dy}{dt} \\ \frac{dz}{dt} \end{bmatrix} = \begin{bmatrix} C_\theta C_\psi & S_\phi S_\theta C_\Psi - C_\phi S_\psi & C_\phi S_\theta C_\Psi + S_\phi S_\psi \\ C_\theta S_\psi & S_\phi S_\theta S_\Psi + C_\phi C_\psi & C_\phi S_\theta S_\Psi - S_\phi C_\psi \\ -S_\theta & S_\theta C_\psi & C_\theta C_\psi \end{bmatrix} \begin{bmatrix} u \\ v \\ w \end{bmatrix}$

2.2 Small Disturbance Theory for the Decoupled Analysis

The equation developed in the can be linearized by using the small disturbance theory. This theory cannot be applied to problems in which large amplitude motions are to be expected, for example spinning and stalling flight. The study of responses of the aircraft to small disturbance theory is based further on the following assumptions. The Earth rotation about its axis as well as its orbital motion around the sun is ignored. The aircraft has a vertical plane of symmetry and the motion of the aircraft consists of small disturbance about a steady flight condition. The effects of spinning rotors are negligible. This is the case when the aircraft is in gliding flight with power off, when the symmetrical engines have opposite rotation, or when the rotor angular momentum is small and the wind velocity is zero.

It is assumed that the aircraft is in a steady, unaccelerated flight before it encounters a disturbance, i.e. both the net force and net moment on the aircraft is zero. For convenience, the reference flight conditions are assumed to be symmetric and the propulsive forces are assumed to remain constant. Furthermore, in the study of aircraft dynamics, it is customary to use the stability axes system. This implies that in the equilibrium flight conditions prior to encountering the disturbance, the body axes system coincides with the stability axes system. The longitudinal and lateral equation of motions for elevator control can be seen in Table 2.2. The full derivation of this equation can be found in Appendix B.

These equations can be written as a set of first-order differential equations, called the state-space or state variable equations and represented mathematically as

$$\dot{X} = AX + BU \tag{2.33}$$

where

$$X = \begin{bmatrix} u \\ \Delta\alpha \\ q \\ \Delta\theta \end{bmatrix} \qquad A = \begin{bmatrix} a_{11} & a_{12} & a_{13} & a_{14} \\ a_{21} & a_{22} & a_{23} & a_{24} \\ a_{31} & a_{32} & a_{33} & a_{34} \\ a_{41} & a_{42} & a_{43} & a_{44} \end{bmatrix} \qquad B = \begin{bmatrix} b_{11}\, b_{12} \\ b_{21}\, b_{22} \\ b_{31}\, b_{32} \\ b_{41}\, b_{42} \end{bmatrix} \tag{2.34}$$

The X vector is the state vector, while the U Vector is the control vector. The control vector consists of the control system on the aircraft. In the longitudinal equation, the author will only be concern with the elevator, while for the lateral equation; the author will take into consideration of the deflection of aileron and rudder.

Similarly the linearized lateral equations from equation can be represented in state form can be expressed in the following matrices:

$$\dot{X} = AX + BU \tag{2.35}$$

where

$$X = \begin{bmatrix} V \\ p \\ r \\ \Delta\phi \end{bmatrix} \quad A = \begin{bmatrix} a_{11} & a_{12} & a_{13} & a_{14} \\ a_{21} & a_{22} & a_{23} & a_{24} \\ a_{31} & a_{32} & a_{33} & a_{34} \\ a_{41} & a_{42} & a_{43} & a_{44} \end{bmatrix} \quad B = \begin{bmatrix} b_{11} & b_{12} \\ b_{21} & b_{22} \\ b_{31} & b_{32} \\ b_{41} & b_{42} \end{bmatrix} \tag{2.36}$$

The matrix A and B contains the aircraft dimensional stability derivatives. It should be noted that the matrix A is the stability matrix. The elements of matrix A depends on the stability derivatives of the aircraft which influence the design of the aircraft. The equations for obtaining the stability derivatives are also included in Appendix A.

Table 2.2: The linearized small disturbance longitudinal and lateral rigid boy equation of motion

Longitudinal Equation

$$\left(m_1\frac{d}{dt}-C_{xu}\right)u-\left(C_{x\dot{\alpha}}c_1\frac{d}{dt}+C_{x\alpha}\right)\Delta\alpha-\left(C_{xq}c_1\frac{d}{dt}+C_{x\theta}\right)\Delta\theta=C_{x\delta_e}\Delta\delta_e+C_{x\delta_t}\Delta\delta_t$$

$$-C_{zu}u+\left[\left(m_1\frac{d}{dt}-C_{z\dot{\alpha}}c_1\frac{d}{dt}\right)-C_{z\alpha}\right]\Delta\alpha-\left(m_1\frac{d}{dt}+C_{zq}c_1\frac{d}{dt}+C_{z\theta}\right)\Delta\theta=C_{z\delta_e}\Delta\delta_e++C_{x\delta_t}\Delta\delta_t$$

$$-C_{mu}u-\left(C_{m\dot{\alpha}}c_1\frac{d}{dt}+C_{m\alpha}\right)\Delta\alpha+\frac{d}{dt}\left(I_{y1}\frac{d}{dt}-C_{mq}c_1\right)\Delta\theta=C_{m\delta_e}\Delta\delta_e++C_{x\delta_t}\Delta\delta_t$$

Where, $m_1=\dfrac{2m}{\rho US}$ $c_1=\dfrac{\bar{c}}{2U}$ $I_{y1}=\dfrac{I_y}{\frac{1}{2}\rho U^2S\bar{c}}$

Lateral Equation

$$\left(m_1\frac{d}{dt}-b_1C_{y\dot{\beta}}\frac{d}{dt}-C_{y\beta}\right)\Delta\beta-\left(b_1C_{yp}\frac{d}{dt}+C_{y\Phi}\right)\Delta\Phi+\left(m_1\frac{d}{dt}-b_1C_{yr}\frac{d}{dt}\right)\Delta\Psi=C_{y\delta_r}\Delta\delta_r+C_{y\delta_a}\Delta\delta_a$$

$$\left(-C_{l\beta}-b_1C_{l\dot{\beta}}\frac{d}{dt}\right)\Delta\beta+\left(-b_1C_{lp}\frac{d}{dt}+I_{x1}\frac{d^2}{dt^2}\right)\Delta\Phi+\left(-b_1C_{lr}\frac{d}{dt}-I_{xz1}\frac{d^2}{dt^2}\right)\Delta\Psi=C_{l\delta_r}\Delta\delta_r+C_{l\delta_a}\Delta\delta_a$$

$$\left(-C_{n\beta}-b_1C_{n\dot{\beta}}\frac{d}{dt}\right)\Delta\beta+\left(-b_1C_{np}\frac{d}{dt}-I_{xz1}\frac{d^2}{dt^2}\right)\Delta\Phi+\left(-b_1C_{nr}\frac{d}{dt}+I_{xz1}\frac{d^2}{dt^2}\right)\Delta\Psi=C_{n\delta_r}\Delta\delta_r+C_{n\delta_a}\Delta\delta_a$$

Where, $\dfrac{d\Phi}{dt}=p$ $\dfrac{d\psi}{dt}=r$ $b_1=\dfrac{b}{2U}$ $I_{x1}=\dfrac{I_x}{\frac{1}{2}\rho U^2Sb}$ $I_{z1}=\dfrac{I_z}{\frac{1}{2}\rho U^2Sb}$ $I_{xz1}=\dfrac{I_{xz}}{\frac{1}{2}\rho U^2Sb}$

2.3 Small Disturbance Theory for Coupled Analysis

The traditional Euler angle formulation of the rigid-body six degree of freedom equations of motion can be easily modified to account for the effects of longitudinal-lateral coupling. The weight transformation of co-ordinate system is also introduced as the weight and body axis cannot be assumed to coincide for this case. The 12 first-order differential equations that govern the motion of a rigid aircraft can be written as:

$$\frac{W}{g}\begin{Bmatrix}\dot{u}\\ \dot{v}\\ \dot{w}\end{Bmatrix}=\begin{Bmatrix}X\\ Y\\ Z\end{Bmatrix}+W\begin{Bmatrix}-S_\theta\\ S_\phi C_\theta\\ C_\phi C_\theta\end{Bmatrix}+\frac{W}{g}\begin{Bmatrix}rv-qw\\ pw-ru\\ qu-pv\end{Bmatrix} \tag{2.37}$$

$$\begin{bmatrix}I_{xx} & -I_{xy} & -I_{xz}\\ -I_{xy} & I_{yy} & -I_{yz}\\ -I_{xz} & -I_{yz} & I_{zz}\end{bmatrix}\begin{Bmatrix}\dot{p}\\ \dot{q}\\ \dot{r}\end{Bmatrix}=\begin{Bmatrix}l\\ m\\ n\end{Bmatrix}+\begin{bmatrix}0 & -h_z & h_y\\ h_z & 0 & -h_x\\ -h_y & h_x & 0\end{bmatrix}\begin{Bmatrix}p\\ q\\ r\end{Bmatrix}+\begin{Bmatrix}(I_{yy}-I_{zz})qr+I_{yz}(q^2-r^2)+I_{xz}pq-I_{xy}pr\\ (I_{zz}-I_{xx})qr+I_{xz}(r^2-p^2)+I_{xy}qr-I_{yz}pq\\ (I_{xx}-I_{yy})qr+I_{xy}(p^2-q^2)+I_{yz}pr-I_{xz}qr\end{Bmatrix} \tag{2.38}$$

$$\begin{Bmatrix}\dot{x}_f\\ \dot{y}_f\\ \dot{z}_f\end{Bmatrix}=\begin{bmatrix}C_\theta C_\psi & S_\phi S_\theta C_\Psi - C_\phi S_\psi & C_\phi S_\theta C_\Psi + S_\phi S_\psi\\ C_\theta S_\psi & S_\phi S_\theta S_\Psi + C_\phi C_\psi & C_\phi S_\theta S_\Psi - S_\phi C_\psi\\ -S_\theta & S_\theta C_\psi & C_\theta C_\psi\end{bmatrix}\begin{Bmatrix}u\\ v\\ w\end{Bmatrix}+\begin{Bmatrix}V_{wx}\\ V_{wy}\\ V_{wz}\end{Bmatrix} \tag{2.39}$$

$$\begin{Bmatrix}\dot{\phi}\\ \dot{\theta}\\ \dot{\psi}\end{Bmatrix}=\begin{bmatrix}1 & S_\phi\tan\theta & C_\phi\tan\theta\\ 0 & C_\phi & -S_\phi\\ 0 & S_\phi\sec\theta & C_\phi\sec\theta\end{bmatrix}\begin{Bmatrix}p\\ q\\ r\end{Bmatrix} \tag{2.40}$$

where the dot indicates a time derivative.

To obtain the classical dynamical modes from these 12 equations, the system must be linearized relative to an equilibrium flight condition. The equilibrium flight condition commonly chosen for this purpose is the steady climbing flight. This condition is chosen specifically to eliminate the coupling between the longitudinal and lateral modes. However, this is not the most general equilibrium flight condition that can be

used to linearize the equations of motion, if the longitudinal-lateral coupling is to be introduced in the final results.

The most common cause of longitudinal-lateral coupling is a simple turning flight as shown in Philips [42]. The equation of motions is usually linearized relative to a flight path having both the equilibrium bank angle and azimuth angle set to zero. Because there is no force in the body-fixed coordinate that depends on azimuth angle, the equilibrium azimuth angle is arbitrary and has no effect on the disturbance equations. On the other hand, allowing for a nonzero-equilibrium bank angle will significantly affect the disturbance equation, introducing longitudinal-lateral coupling.

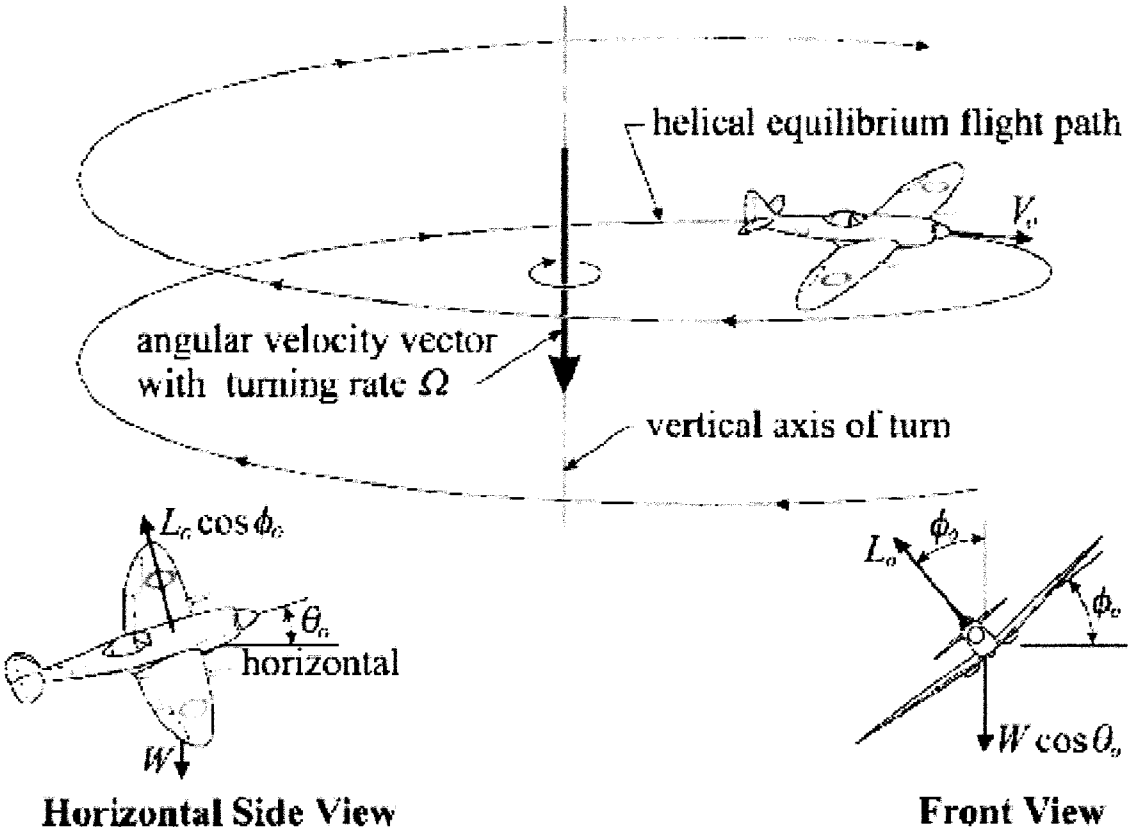

Figure 2.5 Equilibrium flight conditions for a steady coordinated turn

Source: Philips, Warren F. *Mechanics of Flight*, 2nd Edition

In a steady coordinated turn as shown in Figure 2.5, the ailerons, elevators, and rudder are coordinated to maintain a constant airspeed and angular acceleration while eliminating the side force. The equilibrium angular velocity is aligned with the Earth-fixed z-axis and the equilibrium translational velocity is aligned in the body-fixed x-axis. The equilibrium angular velocity vector in the body-fixed coordinate system can be determined by applying the usual Earth-fixed to body-fixed transformation matrix to the angular velocity vector in the Earth-fixed coordinates,

$$\begin{Bmatrix} p \\ q \\ r \end{Bmatrix}_0 = \begin{bmatrix} C_\theta C_\psi & C_\theta S_\psi & -S_\theta \\ S_\phi S_\theta C_\Psi - C_\phi S_\psi & S_\phi S_\theta S_\Psi + C_\phi C_\psi & S_\phi C_\theta \\ C_\phi S_\theta C_\Psi + S_\phi S_\psi & C_\phi S_\theta S_\Psi - S_\phi C_\psi & C_\phi C_\theta \end{bmatrix} \begin{Bmatrix} 0 \\ 0 \\ \Omega \end{Bmatrix}$$

$$= \Omega \begin{Bmatrix} -S_{\theta_0} \\ S_{\phi_0} C_{\theta 0} \\ C_{\phi_0} C_{\theta_0} \end{Bmatrix} \tag{2.41}$$

where the 0 subscript shall indicated evaluation at the equilibrium reference state. The translational velocity vector, in the body-fixed coordinate system, for this equilibrium flight condition can be defined as,

$$\begin{Bmatrix} u \\ v \\ w \end{Bmatrix}_0 = \begin{Bmatrix} V_0 \\ 0 \\ 0 \end{Bmatrix} \tag{2.42}$$

From equation 2.37, constant airspeed and zero side force requires

$$\frac{W}{g}\begin{Bmatrix} 0 \\ 0 \\ 0 \end{Bmatrix} = \begin{Bmatrix} X \\ 0 \\ Z \end{Bmatrix} + W\begin{Bmatrix} -S_\theta \\ S_\phi C_\theta \\ C_\phi C_\theta \end{Bmatrix} + \frac{W}{g}\begin{Bmatrix} rv - qw \\ pw - ru \\ qu - pv \end{Bmatrix} \tag{2.43}$$

substituting the equilibrium flight conditions into the equations,

$$\begin{Bmatrix} 0 \\ 0 \\ 0 \end{Bmatrix} = \begin{Bmatrix} X_0 \\ 0 \\ Z_0 \end{Bmatrix} + W\begin{Bmatrix} -S_{\theta_0} \\ S_{\phi_0} C_{\theta_0} \\ C_{\phi_0} C_{\theta_0} \end{Bmatrix} + \frac{W\Omega V_0}{g}\begin{Bmatrix} 0 \\ -C_{\phi_0} C_{\theta_0} \\ S_{\phi_0} C_{\theta_0} \end{Bmatrix} \tag{2.44}$$

From row 2 of the equation 2.44, it can be determined the equilibrium turning rate as a function of airspeed and bank angle,

$$\Omega = \frac{g \tan \phi_0}{V_0} \tag{2.45}$$

From the above equation, the net equilibrium aerodynamic force required to maintain a steady coordinate turn is

$$\begin{Bmatrix} X \\ Y \\ Z \end{Bmatrix}_0 = W \begin{Bmatrix} S_{\theta_0} \\ 0 \\ \dfrac{C_{\theta_0}}{C_{\phi_0}} \end{Bmatrix} \tag{2.46}$$

From equation, the equilibrium Euler angle rates are readily found to be

$$\begin{Bmatrix} \dot{\phi} \\ \dot{\theta} \\ \dot{\psi} \end{Bmatrix}_0 = \begin{Bmatrix} 0 \\ 0 \\ \Omega \end{Bmatrix} \tag{2.47}$$

Integrating equation 2.47 subject to the initial conditions of zero azimuth angles at t=0, the equilibrium Euler angles for a steady coordinate turn can be found are

$$\begin{Bmatrix} \phi \\ \theta \\ \psi \end{Bmatrix}_0 = \begin{Bmatrix} \phi_0 \\ \theta_0 \\ \Omega t \end{Bmatrix} \tag{2.48}$$

From the equation, the equilibrium position for the steady coordinate turn is

$$\begin{Bmatrix} \dot{x}_f \\ \dot{y}_f \\ \dot{z}_f \end{Bmatrix}_0 = \begin{bmatrix} C_\theta C_\psi & S_\phi S_\theta C_\Psi - C_\phi S_\psi & C_\phi S_\theta C_\Psi + S_\phi S_\psi \\ C_\theta S_\psi & S_\phi S_\theta S_\Psi + C_\phi C_\psi & C_\phi S_\theta S_\Psi - S_\phi C_\psi \\ -S_\theta & S_\theta C_\psi & C_\theta C_\psi \end{bmatrix} \begin{Bmatrix} V_0 \\ 0 \\ 0 \end{Bmatrix} + \begin{Bmatrix} V_{wx} \\ V_{wy} \\ V_{wz} \end{Bmatrix}$$

$$\begin{Bmatrix} \dot{x}_f \\ \dot{y}_f \\ \dot{z}_f \end{Bmatrix}_0 = \begin{Bmatrix} V_0 C_\theta C_\psi \\ V_0 C_\theta S_\psi \\ -V_0 S_\theta \end{Bmatrix} + \begin{Bmatrix} V_{wx} \\ V_{wy} \\ V_{wz} \end{Bmatrix} \tag{2.49}$$

Integrating the equation 2.49 subject to the initial conditions, the equilibrium position can be found to be

$$\begin{Bmatrix} x_f \\ y_f \\ z_f \end{Bmatrix}_0 = \begin{Bmatrix} \dfrac{V_0 C_{\theta_0} S_{\Omega t}}{\Omega} \\ \dfrac{V_0 C_{\theta_0} S_{\Omega t}}{\Omega} \\ -V_0 S_{\theta_0} \end{Bmatrix} + \begin{Bmatrix} V_{wx} t \\ V_{wy} t \\ V_{wz} t \end{Bmatrix} \tag{2.50}$$

Upon expanding the aircraft flight variables relative to this equilibrium state, the equations can be re-written

$$\begin{Bmatrix} u \\ v \\ w \end{Bmatrix} = \begin{Bmatrix} V_0 + \Delta u \\ \Delta v \\ \Delta w \end{Bmatrix} \tag{2.51}$$

$$\begin{Bmatrix} p \\ q \\ r \end{Bmatrix} = \begin{Bmatrix} \dfrac{-gT_{\phi_0} S_{\theta_0}}{V_0} + \Delta p \\ \dfrac{gT_{\phi_0} S_{\phi_0} C_{\theta_0}}{V_0} + \Delta q \\ \dfrac{gS_{\phi_0} C_{\theta_0}}{V_0} + \Delta r \end{Bmatrix} \tag{2.52}$$

$$\begin{Bmatrix} X \\ Y \\ Z \end{Bmatrix} = \begin{Bmatrix} WS_{\theta_0} + \Delta X \\ \Delta Y \\ \dfrac{-WC_{\theta_0}}{C_{\phi_0}} \Delta Z \end{Bmatrix} \tag{2.53}$$

$$\begin{Bmatrix} l \\ m \\ n \end{Bmatrix} = \begin{Bmatrix} l_0 + \Delta l \\ m_0 + \Delta m \\ n_0 + \Delta n \end{Bmatrix} \tag{2.54}$$

$$\begin{Bmatrix} x_f \\ y_f \\ z_f \end{Bmatrix} = \begin{Bmatrix} \dfrac{V_0 C_{\theta_0} S_{\Omega t}}{\Omega} + V_{wx} t + \Delta x_f \\ \dfrac{V_0 C_{\theta_0} S_{\Omega t}}{\Omega} + V_{wy} t + \Delta y_f \\ -V_0 S_{\theta_0} + V_{wz} t + \Delta z_f \end{Bmatrix} \tag{2.55}$$

$$\begin{Bmatrix} \phi \\ \theta \\ \psi \end{Bmatrix} = \begin{Bmatrix} l_0 + \Delta l \\ m_0 + \Delta m \\ n_0 + \Delta n \end{Bmatrix} \tag{2.56}$$

Using the equilibrium values in Equation 2.48, the general equations of motions can now be linearized and represented in a state space format for mathematical manipulation as shown in Equation 2.57 as defined in Philips [26],

$$\begin{bmatrix} [B]_m & [n] & [n] & [n] \\ [B]_{iv} & [I] & [n] & [n] \\ [n] & [n] & [I] & [n] \\ [n] & [n] & [n] & [I] \end{bmatrix} \begin{Bmatrix} \Delta\dot{u} \\ \Delta\dot{v} \\ \Delta\dot{w} \\ \Delta\dot{p} \\ \Delta\dot{q} \\ \Delta\dot{r} \\ \Delta\dot{x} \\ \Delta\dot{y} \\ \Delta\dot{z} \\ \Delta\dot{\phi} \\ \Delta\dot{\theta} \\ \Delta\dot{\psi} \end{Bmatrix} = \begin{bmatrix} [A]_{fv} & [A]_{fw} & [n] & [A]_w \\ [A]_{mv} & [A]_{mw} & [n] & [n] \\ [A]_{pv} & [n] & [n] & [A]_{pe} \\ [n] & [A]_{ew} & [n] & [A]_{ee} \end{bmatrix} \begin{Bmatrix} \Delta u \\ \Delta v \\ \Delta w \\ \Delta p \\ \Delta q \\ \Delta r \\ \Delta x \\ \Delta y \\ \Delta z \\ \Delta\phi \\ \Delta\theta \\ \Delta\psi \end{Bmatrix} + \begin{bmatrix} [C]_f \\ [C]_m \\ [n] \\ [n] \end{bmatrix} \begin{Bmatrix} \Delta\delta_a \\ \Delta\delta_e \\ \Delta\delta_r \end{Bmatrix} \tag{2.57}$$

2.4 Controller Design

The role of the controller is to help relieve the operators in handling the aircraft. These controllers assist the operators in controlling the aircraft to follow the desired commanded motions. A simple approach is to analyze the eigenvalues of the aircraft and use an open loop controller, where the poles in the mathematical model are merely cancelled by compensator zeros and the compensator poles are used to define the desired

aircraft dynamics. The main problem is that the control system performance deteriorates rapidly if the aircraft dynamic mathematical model changes or the aircraft experiences disturbances.

Feedback control is the solution to this problem as it dramatically reduces the sensitivity of the system to modeling uncertainties and provides disturbance rejection to those quantities that detract from the desired aircraft motions. The fundamental task in controlling an aircraft is to control roll, pitch and yaw attitudes with respect to the body axis of the UAV. The attitude must be controlled because it essentially provides a feedback and affects the aircraft's acceleration. An example is the bank angle, which determines the centripetal acceleration of the aircraft. Direct control over the aircraft's acceleration is desired because the stabilization effect integrates down into the velocity and position states over time and thus leaves only the reference velocity and position commands to be regulated by outer control loops.

Stability augmentation controllers are responsible for augmenting the natural stability of the higher frequency aircraft modes, by providing artificial damping. The attitude controllers form the lowest level of regulation, and are responsible for regulating the aircraft's pitch and roll angles, effectively controlling the acceleration. Finally, the trajectory controllers form the outer loops that regulate trajectory motion variables such as heading and altitude. These control loops provide commands to the attitude controllers and thus deal with the kinematics of the aircraft more than its natural dynamics.

The few controllers that will be discussed according to the different types of controllers are summarized below first before a summary of the controllers design will be represented.

2.4.1 Stability Augmentation System

Stability augmentation systems (SAS) are another application of automatic flight control systems which provide artificial stability for an aircraft by providing artificial damping. The inherent stability of an aircraft depends on the aerodynamic and stability derivatives. The magnitudes of the stability derivatives affect both the damping and frequency of the longitudinal and lateral motions of the aircraft. Furthermore, it has been

shown that the stability derivatives are a function of the aircraft's aerodynamic and geometrical characteristics.

Stability augmentation involves suppressing the high frequency in the aircraft dynamic model through the artificial damping of the various modes. In the modal analysis, the natural high frequency aircraft modes are the short period mode, the dutch mode and the roll mode. The natural damping of these modes is caused by induced angles of incidence on the aircraft's airfoils during angular rate perturbations. This means that the damping is dependent on the aircraft velocity and center of gravity location, both of which change during flight. The damping is also always relative to the airflow, and not to the inertia space. Thus, it is desired to provide artificial damping, to desensitize the natural damping to changes in flight parameters, and to provide damping wit respect to the inertia space. Damping with respect to inertial space is desired because it is effective at rejecting wind gust disturbance.

In order to provide damping, the aircraft's angular rates need to be sensed by using rate gyroscopes. Although these sensors display significant biases, the feedback control loops like the attitude and trajectory loops will compensate for any steady state errors via the feedback loop. The signals from these gyroscopes can then be fed to the respective actuators to augment the aircraft natural damping.

2.4.2 Attitude Control System

If good sensors and a good aircraft model are available, then all of the aircraft states could either be measured or estimated and used in a Linear Quadratic Regulator (LQR) to solve the entire attitude control problem. However in reality of the situation is such that the aircraft mathematical model has a limited accuracy and only low cost sensors are used in the UAV. These two facts make it desirable to avoid using an estimator based on a low accuracy model, and updated with measurements from low cost sensors, but to rather use directly sensed information to control the aircraft attitude via a feedback control system to provide a full state feedback.

Rate gyroscope used in the UAV are inertial sensors and thus have the advantage of working equally well in all ambient conditions. This quality is desired for the purposes

of autonomous navigation and thus eliminates the use of the infrared and vision based systems.

It is clear that determining the aircraft's attitude using only low cost sensors is a difficult task. However, if the states that are directly related to the aircraft's attitude under common flight conditions can be found, and these states are easily measured using low cost sensors, then they can be used indirectly to control the aircraft's attitude. In this study, the roll angle control will be the main focus since the lateral stability of the UAV is the focus in the study. For example, consider the Figure 2.6 where the aircraft is shown in a steady, constant altitude, banked turn.

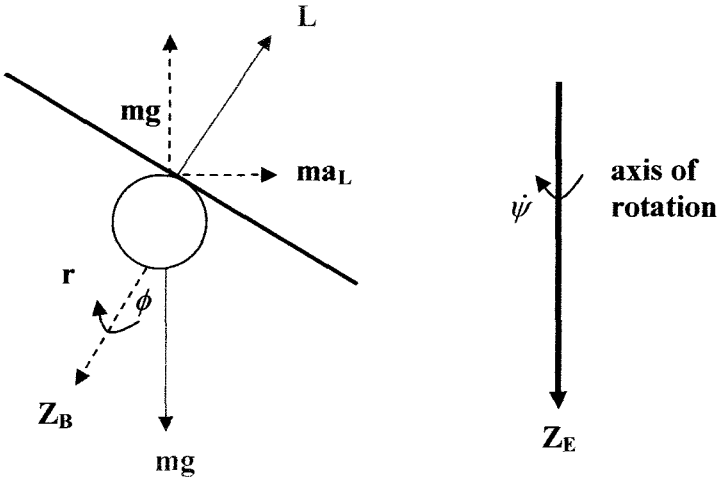

Figure 2.6: Aircraft in a Steady Banked Turn

During the turn maneuver, the lift vector counters the weight of the aircraft and for provides the necessary centripetal acceleration for the turn. Thus, the lateral acceleration can be written as,

$$a = U_0\dot{\varphi} = g\tan\phi \qquad (2.58)$$

If the roll and pitch angles are limited to small angles, then substituting the small angles into equation 2.59 reveals,

$$\phi \approx \frac{U_0}{g}r \qquad (2.59)$$

This means that for small pitch and roll angles, the aircraft's yaw rate is proportional to the roll angles. Thus, the roll angle can be controlled by merely controlling the aircraft's yaw rate.

2.4.3 Trajectory Control System

The trajectory control form the outer most loops of the control system, and are responsible for regulating states like the altitude, heading and track errors. In this section, we will be looking specifically at the heading controller. These controllers are chosen to solve the lateral instability in the UAV. With this controller it is possible for the autopilot to perform conventional lateral maneuver without the user losing control. The heading controller can be effectively implemented by successive loop closure. Heading measurements can be fed to the yaw rate controller to stabilize the extra integrator added to the system by the heading state.

Chapter 3
Estimation of the UAV Aerodynamic Characteristics and the Stability and Control Derivatives

Flight mechanics analysis is an area whereby extensive modeling and simulation technologies and techniques are used. The numerical simulation of the aircraft's dynamic behavior is the most important tool in development and verification of the flight control laws for any aircraft. This is no different in the design processes of an UAV. The availability of special-purpose simulation tools like *Matlab*® [6] and *Simulink*® [7], coupled with the massive computing capabilities at decreased cost, and advances in simulation methodologies have made simulation one of the most widely used and accepted tools in flight operations research and aircraft system analysis. The complete aircraft systems and dynamics model incorporates different subsystem models like the aerodynamics, structures, propulsion, and control subsystems that have interdependent responses to any input. These subsystems also interact with other subsystems within the flight control computer. The dynamical modeling of a UAV is at the heart of its simulation. The response of a UAV system to any input, including commands or disturbance like wind gust can be modeled by a system of ordinary differential equations as discussed previously in the previous chapter. The aerodynamic characteristics and stability and control derivatives are dimensionless values which describes the aircraft in the differential equations. These values are obtained through various techniques, from empirically methods to computational simulation.

The results obtained in this study of the aerodynamic characteristics and stability and control derivatives are discussed in this chapter. They will be generally be grouped under three broad categories, analysis of the results from the experimental techniques obtained from the wind tunnel tests conducted by the manufacturers, semi-empirical analysis methods of the stability and control techniques with *Digital Datcom* [22], and finally the results of the aerodynamic characteristics with and without the propulsion system through computational fluid dynamics with *Fluent* [23] and *SolidWorks FloWorks*.

[24] Following which, the integration of this aerodynamic database into the flight simulation framework is discussed in the subsequent chapters.

3.1 Development of the Aerodynamic Characteristics and Stability and Control Derivatives

The primary elements of the mathematical model are the external forces acting on the airframe, namely the aerodynamic, engine thrust and undercarriage reaction forces. Secondary elements of a model like the control system and the atmosphere contribute significantly to the core. All these features with the primary forces labeled in yellow and secondary forces in blue are summarized in Figure 3.1 below.

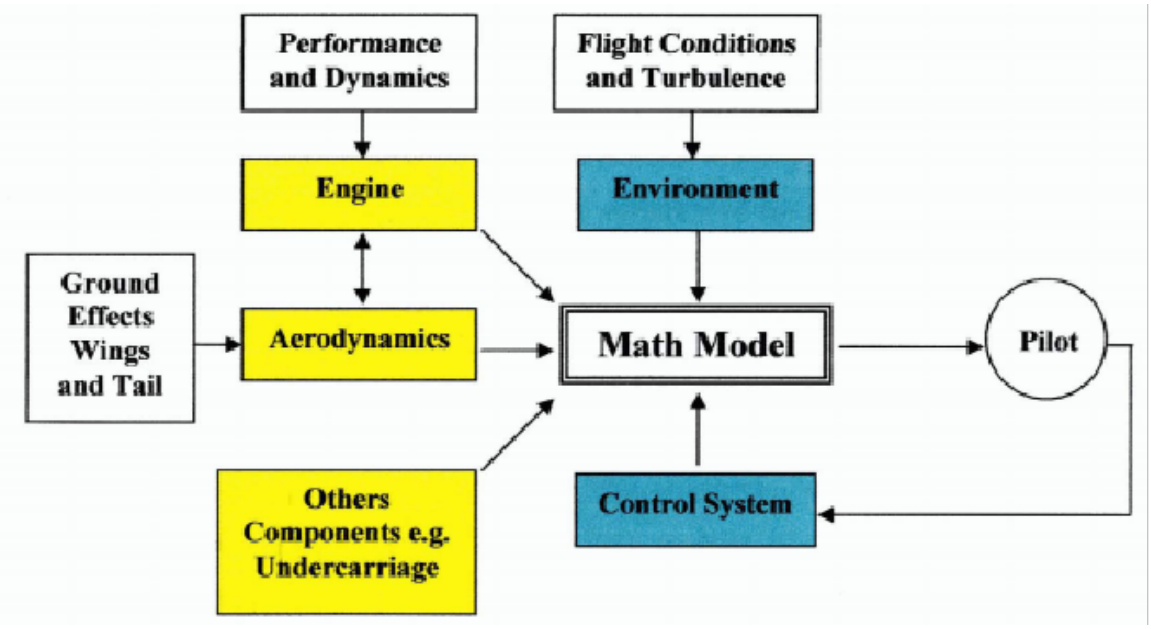

Figure 3.1: Contributions to the aircraft mathematical model

The aerodynamic model computes the aerodynamic forces i.e. the lift and drag, and the aerodynamic moments about all the three axes acting on the UAV. Additional effects like 'ground effects' caused by the influences of the ground forces during take off and landing may be modeled depending on the needs of the simulation model. Ground effects on aerodynamic forces can result in an increased of wing lift and possibility a sharp increase in nose-down pitching moment close to the ground during landing and

take off. Both of these effects are important as they influence the pilot's ability to perform a safe and smooth landing. In the UAV context where the pilot is not present, these effects should be included to enhance the flight controller during sequence of autonomous landing. The aerodynamic models used in analysis are normally defined under static or quasi-static condition. This is based on assumption that the airflow are in a steady flow condition in a time scale which is defined in a much shorter domain in comparison to the time scale of the aircraft maneuver. The simulation framework should be focused in its predefined objectives to suit its scope of work. From the objectives the simulation framework only needs to include the components it require for the specific analysis. For example, if landing and taking off is a requirement in the simulation analysis and is one of the key objectives in the study, considerations have to be taken to include the undercarriage model in the mathematical model, otherwise to simplify the calculation; certain elements can be omitted in the simulation framework.

A full atmospheric model which includes a number of properties needs to be represented in the simulation framework. The variation of the air density and temperature with altitude as defined by the International Standard Atmosphere (ISA) are defined in the forms of lookup tables. Turbulence and wind shear has caused several major accidents and thus is a legitimate item to be simulated. This can either be used for research into aircraft design for training pilots or testing of flight controller to recognize and counter such disturbance it effectively. This is especially so in this case where the pilot are controlling the UAVs remotely. The process of translating the theoretical framework into a graphical model in a simulation framework in *Simulink*®[7] framework are discussed through chapter 3 to 5.

Prior to the construction of the aircraft model using the tools in *Simulink*® [7], there is a need to consolidate the information for the aerodynamic database. The aerodynamic forces and moments depends upon the flight condition (state variable) and external aerodynamic control inputs. These stability and control derivatives can be calculated using analytical techniques, semi empirical formulation, or through experimental methods. The analytical methods based on classical aerodynamic theories can be applied only to idealized wings and bodies. In view of such cases, several

empirical and semi empirical methods have been developed over the years for evaluating the stability and control derivatives of aircraft configurations of practical interest. *Digital Datcom* [22] is one of the most widely used empirical methods for estimating aircraft stability and control derivatives. This is usually done as a first cut estimates during the design phase.

Modern Computational Fluid Dynamics (CFD) methods are capable of providing more accurate estimates of stability and control derivatives. Presently CFD methods are usually used at a later stage in the vehicle design process when the configuration takes its final form. As technology improved over the years, CFD has grown in dominance and it is a commonly used tool for analysis even at the initial phase by engineers. The experimental methods for obtaining dynamic stability derivatives in ground based facilities mainly consist of either forced oscillation or free oscillation technique wherein the test model undergoes oscillatory motions in pitch, roll, or yaw. Another approach that is often used for obtaining dynamic stability derivatives in ground based test facilities is the so called free flight or semi free flight in the viewing area of the test facility. The model motion is recorded in the form of various accelerometer outputs or high speed motion picture records. The dynamic stability derivatives are then obtained implicitly by matching the predicted time history of the model with the observed time history. Because the time and effort involved in fabricating and testing aircraft models in the ground based facilities are considerable large, these approaches are also usually used in the final stages of the vehicle design.

On the other hand, the semi empirical or engineering methods provide quick and cost effective estimates of the static and dynamic stability derivatives, which can be readily used for assessing the vehicle aerodynamic, stability and control derivatives. The predictions based on these engineering methods can be used in the design of flight control and guidance system. The only disadvantage is that the results are not as accurate as CFD and wind tunnel test data. However, this type of information is very useful in the early stages of the design to quickly evaluate several candidate configurations for their suitability in meeting the requirements. As the design matures, these estimates can be replaced by more accurate CFD results or the wind tunnel test data on high fidelity

models as they become available to revise and update the stability and control characteristics as well as the design of flight control and guidance system. The results obtained to defined the control law are based on the linear analysis and calculations has to be verified through a detailed simulation of the system to ensure that the flight control system behaves well over the part of the flight envelope for which it is designed. This often demands solving the nonlinear differential equations which encompassed a wide range of data and flight regime. The results of development of the aerodynamic database using various techniques can be found in this chapter. The development of the database will include a review of the wind tunnel test conducted by the manufactures, empirical estimation of the aerodynamic characteristics using *Digital Datcom,* [22] and computational fluid dynamics using commercial software *Fluent* [23] and *SolidWorks FloWorks*. [24] There is a need to use various techniques as each of the methods has its strengths as well as its constraints. By using various methods, the aerodynamic database can be developed by tapping on the strengths of each techniques and at the same time eliminate their short comings.

3.1.1 Wind Tunnel Data

A wind tunnel test of the UAV has been conducted on a 1:3 scale model of the UAV as reported by Ungar[25]. The test is conducted on the basic configuration supplying longitudinal and lateral data for various flap configurations. The elevator power, rudder power, aileron power, effects of the horizontal tail setting and downwash is also obtained during the wind tunnel tests. A component study of the top antenna, camera capsule, undercarriage, vertical tail, horizontal tails and booms was also completed. The comparative analysis of the wind tunnel test results and the CFD calculations are shown in Figure 3.34. An error is made in the construction of the wind tunnel test model. The wing of the 1:3 model is placed 50mm forward of the actual position. The pressure sensors on the UAV fuselage are also found to be wrongly positioned for most of the test, giving a false reading on the static pressure in the wind tunnel. However in general, the longitudinal and lateral data obtained shows good agreement with the previous database. Anemometric data measured during the test indicated that the plain or clean static port

supplies very large position error which is strongly influenced by angle of attack. These errors are remedied by way of a small strip affixed to the skin slightly aft of the static port. However, the error is very sensitive to the position and angle of the strip. With the wind tunnel test results as the basic framework of the database, various techniques discussed below are completed to build a more comprehensive database.

3.1.2 Empirical Method Estimation of Stability Derivatives with *Digital DATCOM*

The stability and control data compendium, *Datcom* for short, provides a "systematic summary of methods for estimating basic stability and control derivatives." [22] The *Datcom* is over 1500 pages of detailed methodology to determine stability and control characteristics of a wide variety of aircraft and aircraft configurations. "For any given flight condition and configuration the complete set of derivatives can be determined without resort to outside information." [22] Primarily intended for preliminary aircraft design, it is designed to give a first cut estimates at the stability characteristics of an aircraft design based on the geometrical input. However, it is not intended to be used in lieu of wind tunnel or flight test data. In 1979, the *DATCOM* was re-written in *Fortran IV* computer language. Re-named the *USAF Stability and control Digital Datcom* [22], it became an efficient, user-oriented computer program. *Digital Datcom* [22] is used as a first cut analysis in developing the aerodynamic database for this study. The calculations are based on the inputs i.e. flight conditions, aircraft altitudes, physical geometry. *Digital Datcom* [22] treats inputs that represent a traditional wing-body-tail configuration and any control of high lift devices. Some non-standard geometry can be treated as well, especially for non conventional shapes and external apparatus like antenna and landing gear on the aircraft. Due to certain limitation of the program, assumptions are made during the course of using this program.

The fuselage characteristics in the program are based on cylindrical shape, however the UAV is of a non-conventional shape, and certain estimations are used to re-map the fuselage to suit the inputs. The actual model has a trapezium shaped fuselage while the model used in *Digital Datcom* [22] uses a cylindrical shape model. In order to

take into consideration the various external components of the UAV like the landing gear, radar dome and payload capsule, estimation based on overall surface area at each junction is modeled. The inputs to *Digital Datcom* [22] are visualized in Figure 3.2, prior to running the stability and control analysis. This step ensured that the measurements mapped out are close to the UAV configuration. Similarly, to model the vertical twin fin of the tail assembly, certain assumptions are made and taken into consideration. The estimation of this configuration with its dimensions is shown in Figure 3.3. The main difference between the actual geometrical model and the model used in *Digital Datcom* [22] is the orientation of the tail configuration. In the actual model, both tails are inclined inwards, whereas in *Digital Datcom* [22] the tails configuration is taken as vertically perpendicular to the horizontal tail. The inputs only accept the tail component to be vertically upwards, and do not accept an incline input. Thus there are some limitations and the data collected from *Digital Datcom* [22] has to be further enhanced using either other analytical or experimental methods.

Based on the list of inputs as shown in Table 3.1, the calculation done by *Digital Datcom* [22] is completed. The output data are represented using eight different plots depicting different coefficients at various flight conditions.

Table 3.1: Inputs to *Digital Datcom* [22]

Input	**Symbol**	**Value**	**Comments**
Mach	M	0.0 to 0.16	9 sets varied by 0.02 increment
Angle of Attack	A	-2.0 to 24.0	9 sets varied by 2.0 increment
Reference Area	SREF	4.3	Dimension in m^2
Reference Chord	CBARR	0.55	Dimension in m
Reference Span	BLREF	7.648	Dimension in m
x-axis CG	XCG	2.0175	With respect to the front of the fuselage
z-axis CG	XCG	0.01	Center line is the mid section of fuselage
Wing Position	XWING	0.2275	With respect to centerline
Tail Span	VTSPAN	1.34	Dimension in m
Tail Height	VTHT	0.65	With respect to centerline

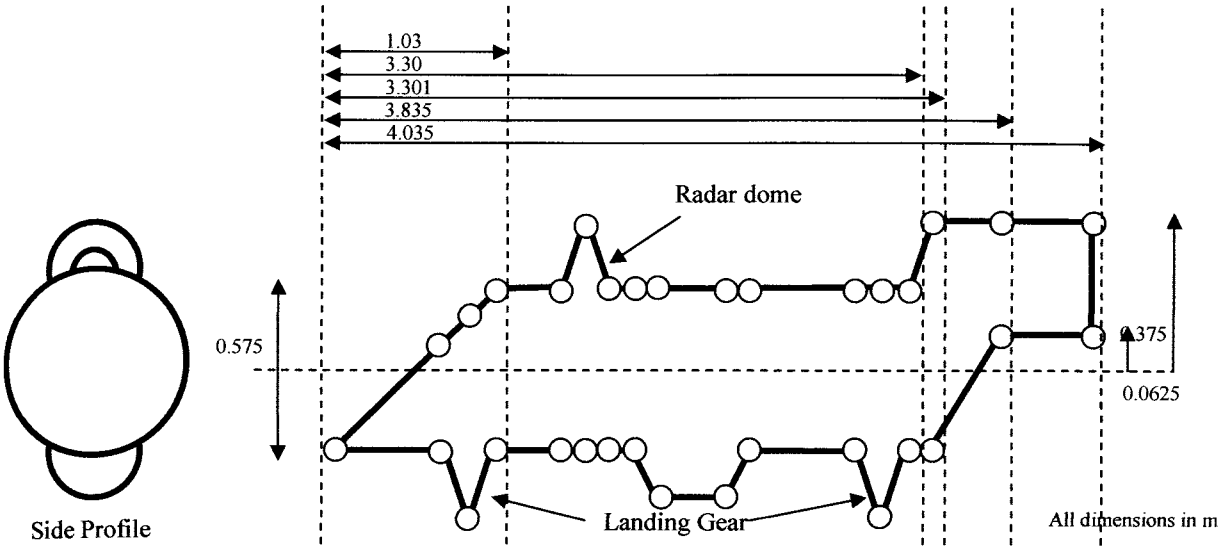

Figure 3.2: Fuselage Sample (Cylindrical Estimates)

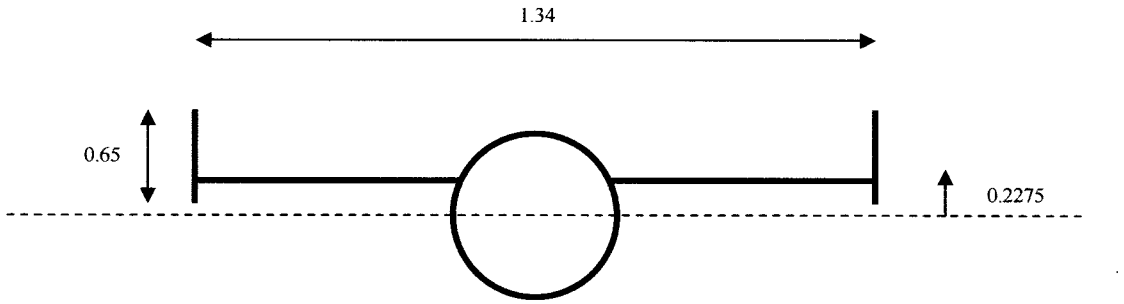

(a)

All dimensions in m

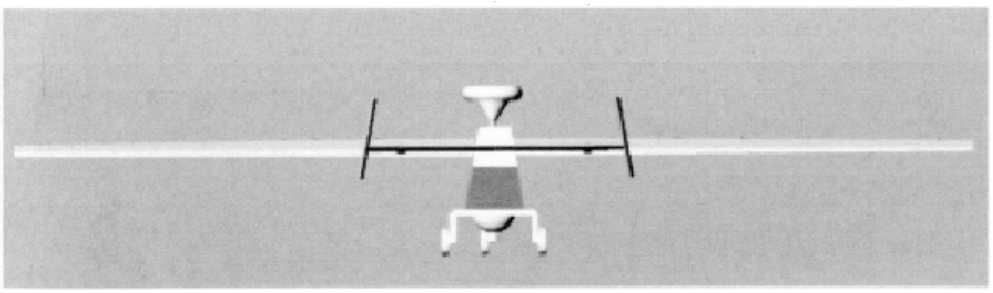

(b)

Figure 3.3: Twin vertical fin Estimation

The data plotted in the Figure 3.4 to 3.11 is obtained from the analysis using *Digital Datcom* [22]. The variation of the lift coefficient plots with angle of attack is shown in Figure 3.4. It can be seen that the stalling angle is within the range of 15 to 17 degrees for the various conditions at different Mach number at different altitude. The variation of the drag coefficient against the angle of attack is shown in Figure 3.5. The drag coefficient ranges from 0.02 to 0.14. This is comparable with the data obtained from the wind tunnel database provided by the OEM of the UAV. The pitching moment variation against the angle attack decreases with increasing angle of attack in a linear manner as seen in Figure 3.6. The normal and axial forces variation with angle of attack are plotted to study the effects of the change in forces when subjected to a variation of the angle of attack variation. The normal forces as seen in Figure 3.7 increases in a similar trend as the lift coefficient while the axial force shown in Figure 3.8 decreases with increasing angle of attack. The derivatives of the coefficient of lift with respect to angle of attack are plotted with respect to the angle of attack in Figure 3.9. The pitching moment derivative is almost consistent with changes to the angle of attack as shown in Figure 3.10. The rolling moment derivatives decreases with increasing angle of attack and the plot of the variation is shown in Figure 3.11.

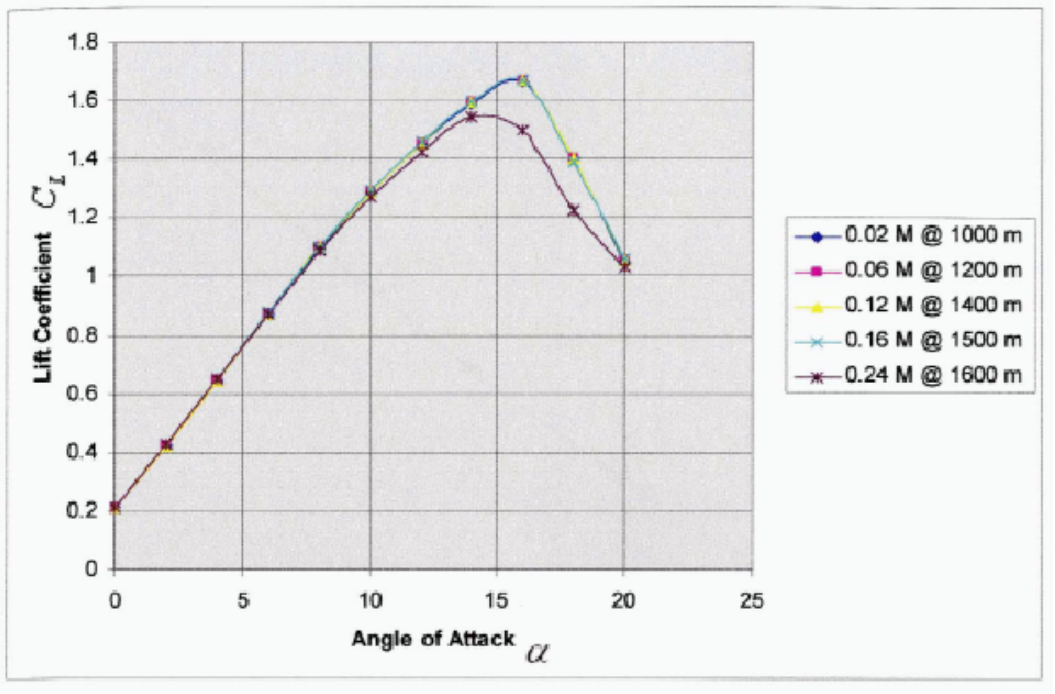

Figure 3.4: Plot of lift coefficient, C_L vs. angle of attack, α

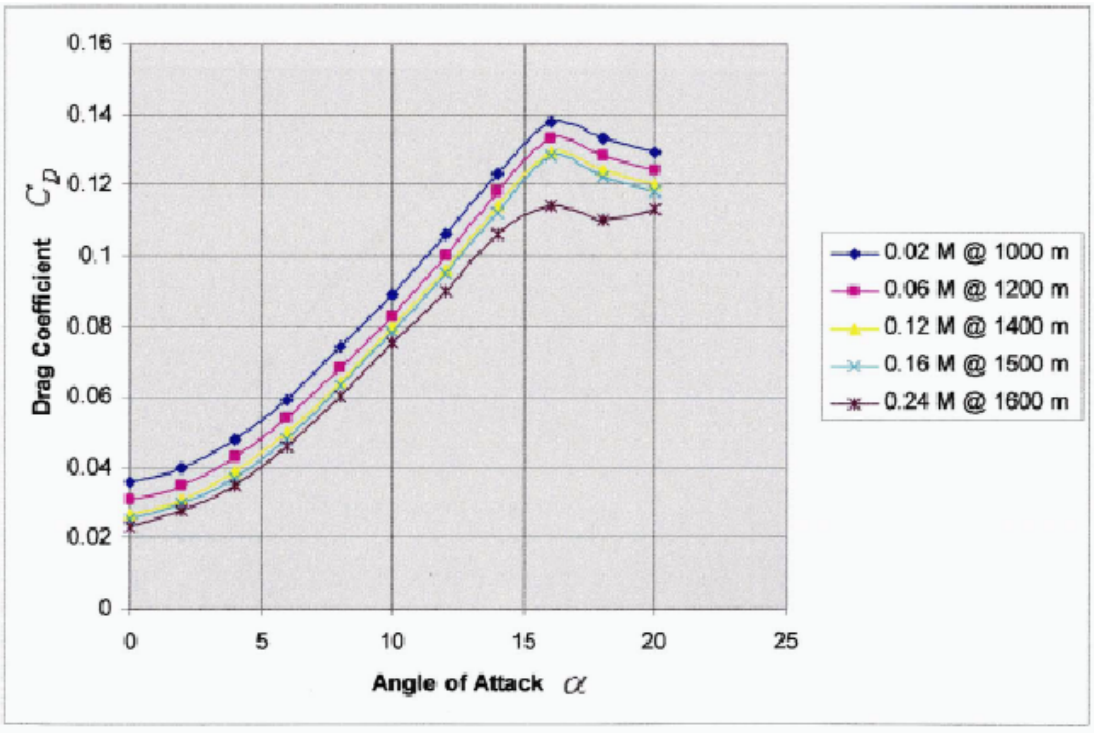

Figure 3.5: Plot of drag coefficient, C_D vs. the angle of attack, α

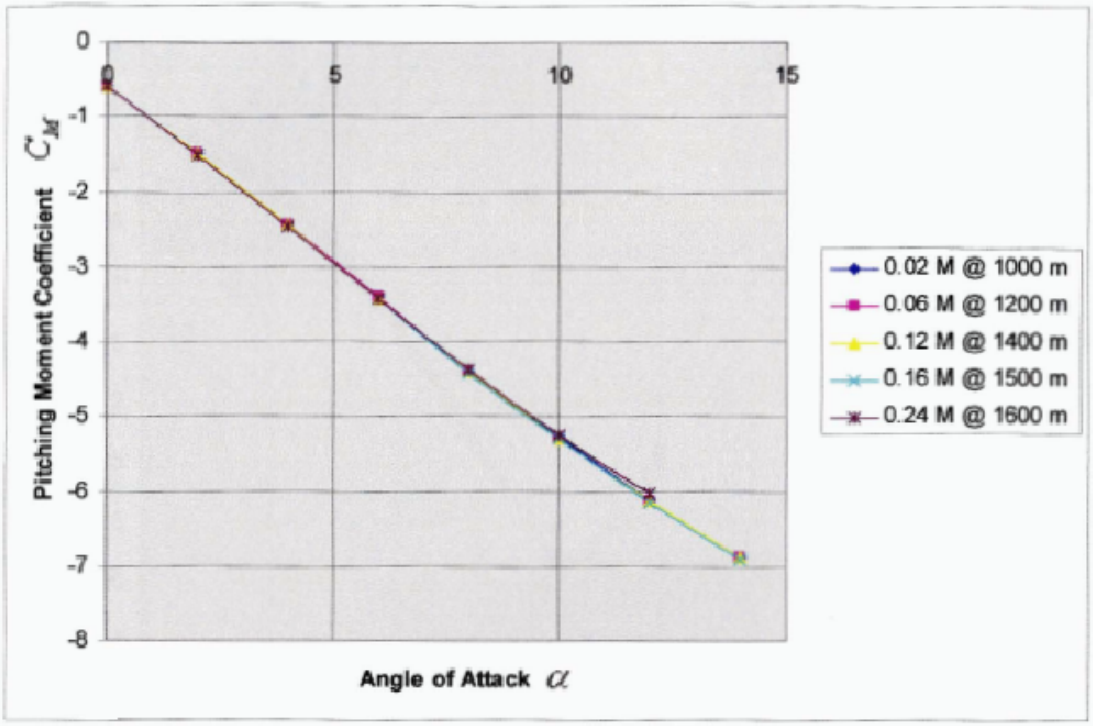

Figure 3.6: Plot of pitching moment coefficient, C_M vs. the angle of attack, α

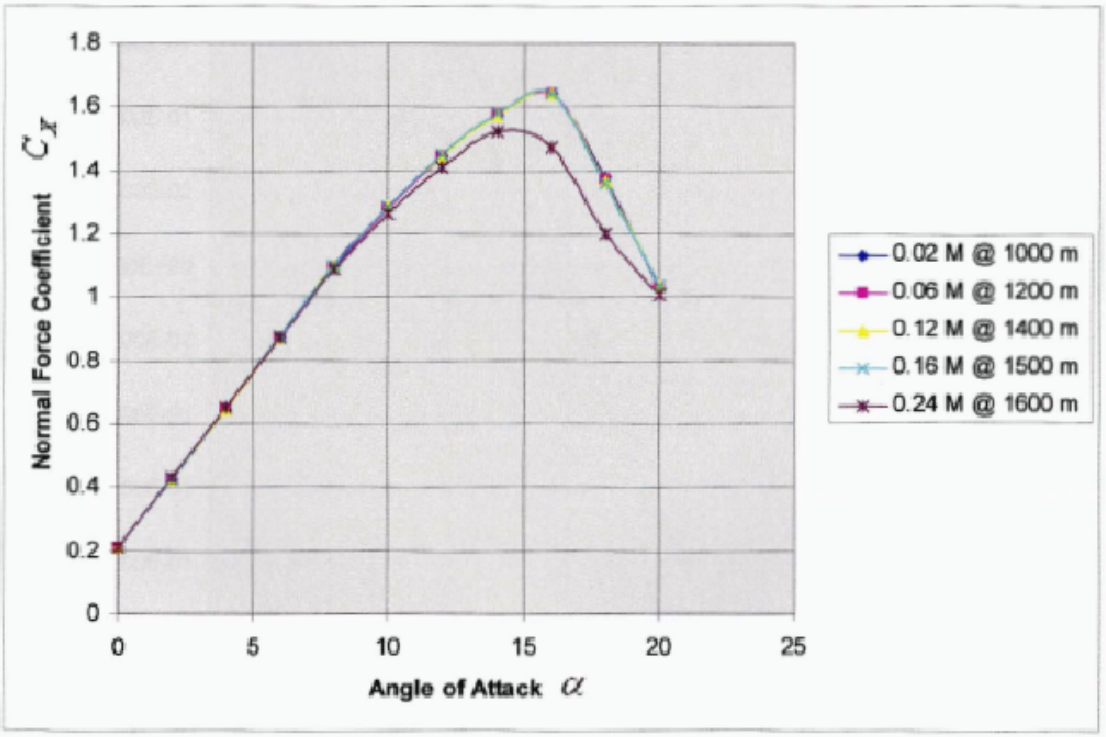

Figure 3.7: Plot of normal force coefficient, C_X vs. the angle of attack, α

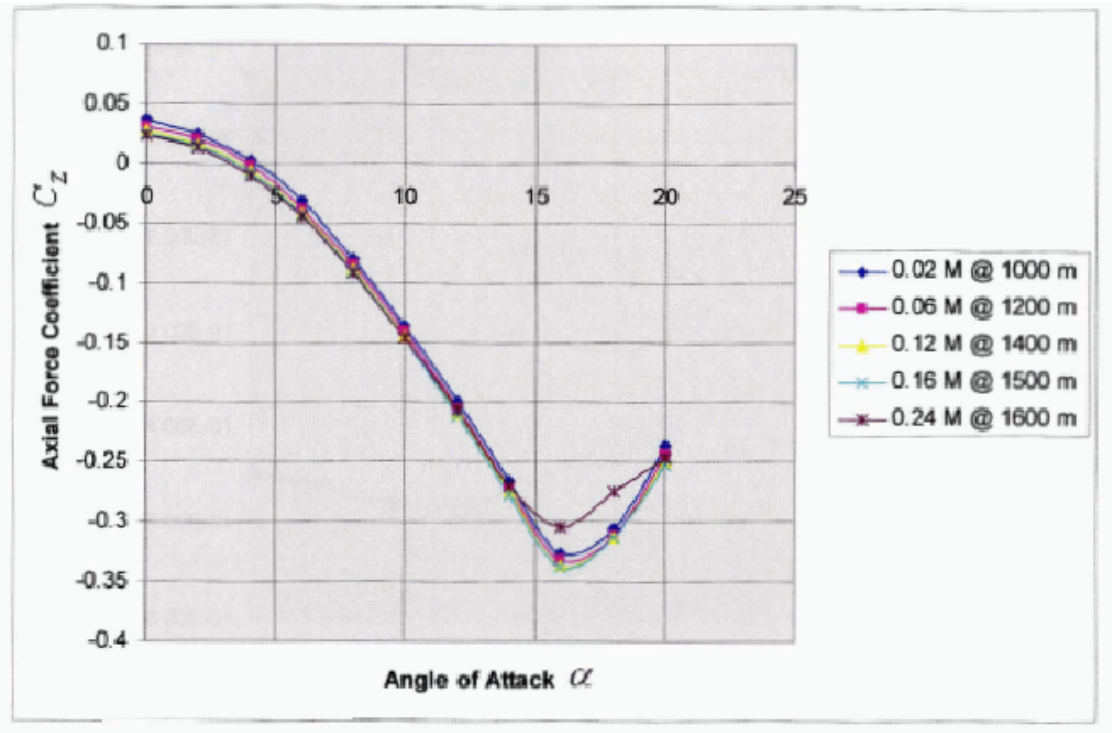

Figure 3.8: Plot of axial force coefficient, C_Z vs. the angle of attack, α

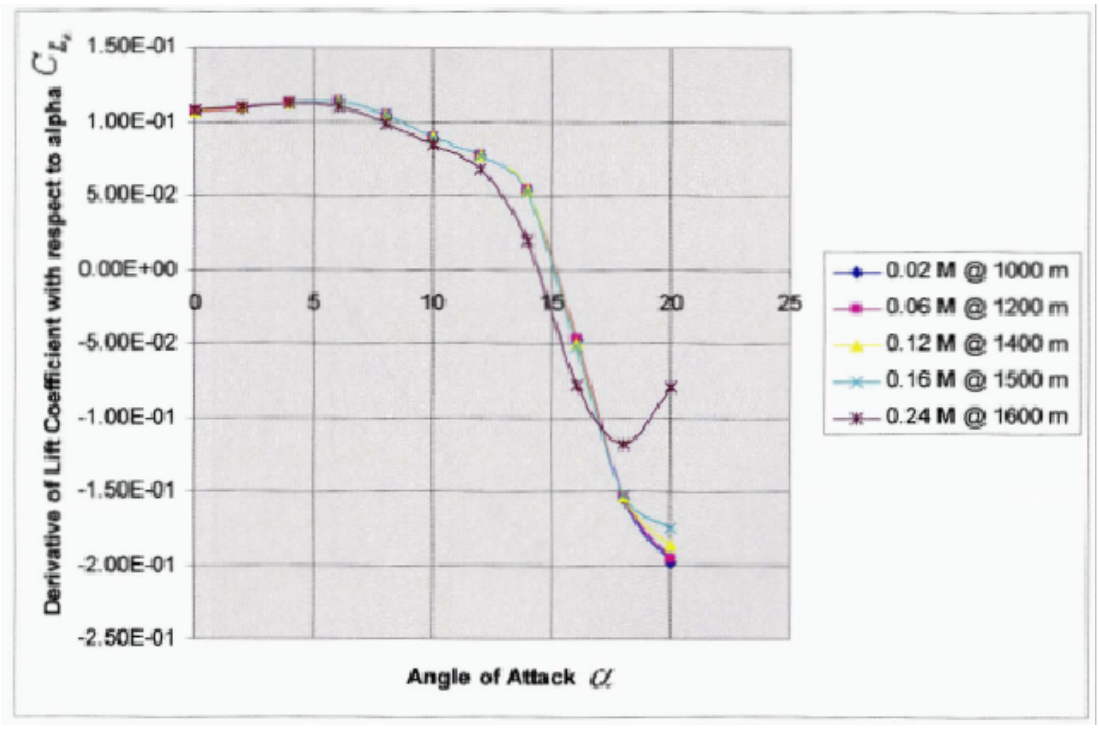

Figure 3.9: Plot of lift coefficient derivative, C_{L_α} vs. the angle of attack, α

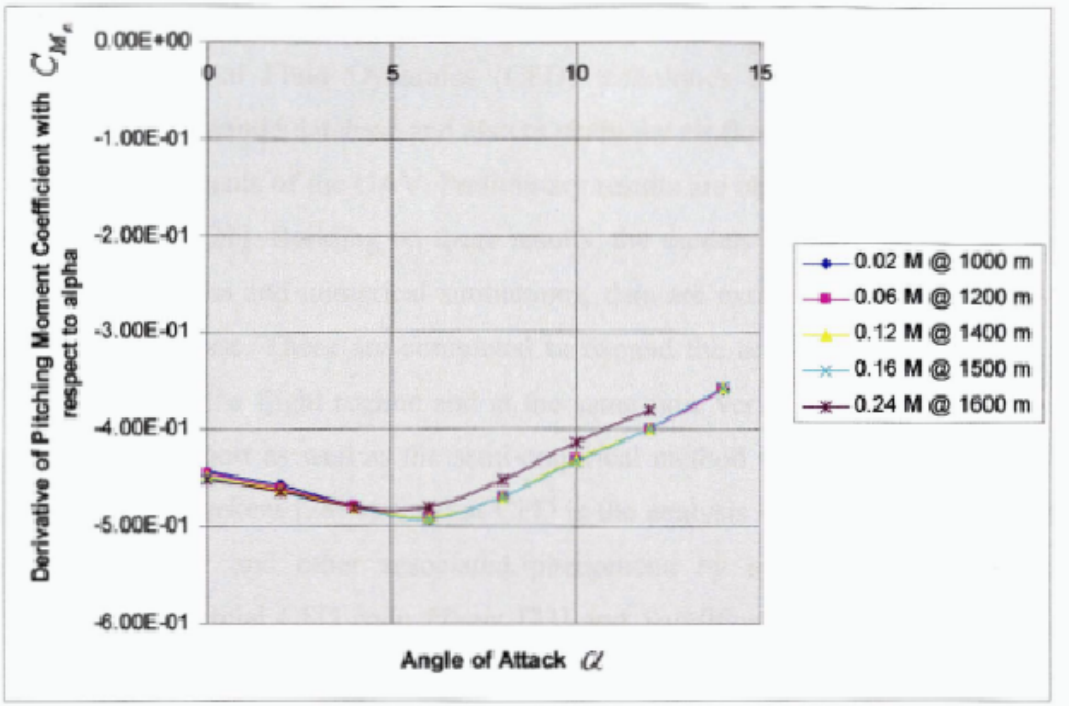

Figure 3.10: Plot of pitching moment coefficient derivative, C_{M_α} vs. the angle of attack, α

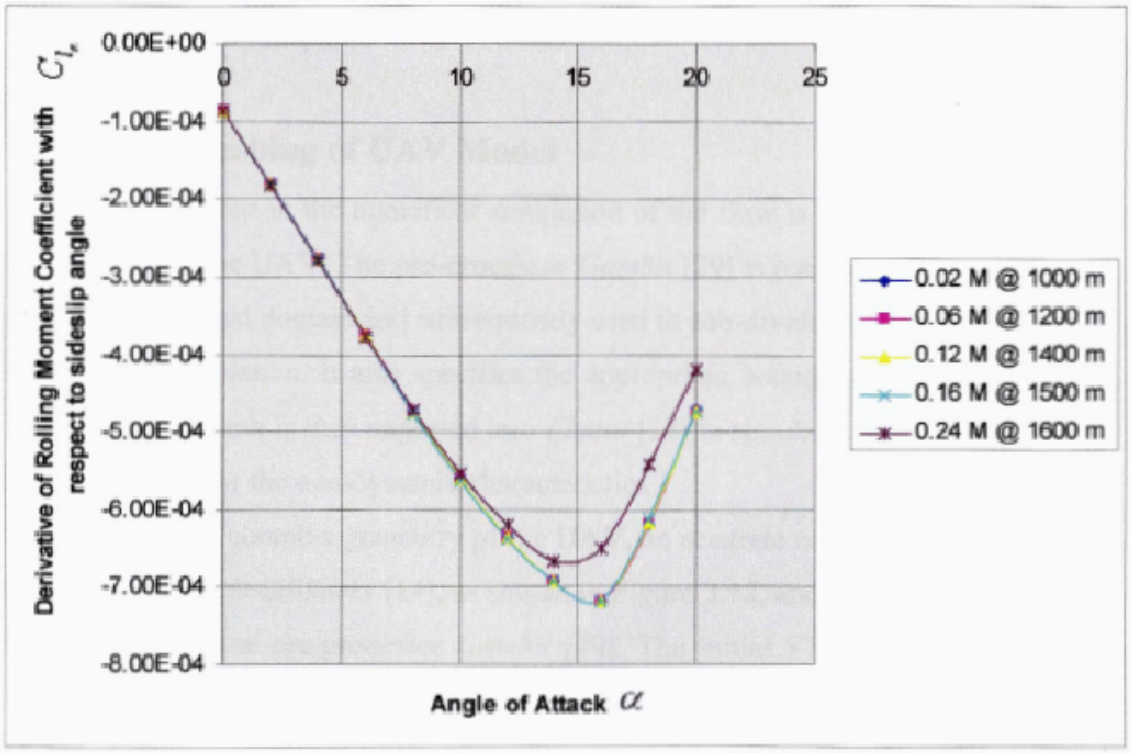

Figure 3.11: Plot of rolling moment coefficient derivative, C_{l_α} vs. the angle of attack, α

3.1.3 Computational Fluid Dynamics with *Fluent*

Computational Fluid Dynamics (CFD) techniques are used in this study to enhance the aerodynamic database and also to study the air flow and effects it has around the various components of the UAV. Preliminary results are obtained from the reports by Chan [26] and Li [27]. Building on these results, the models are enhanced and through further investigations and numerical simulations, data are extracted to be fitted into the aerodynamic database. These are completed to expand the aerodynamic database for a wider spectrum of the flight regime and at the same time verify data obtained from the wind tunnel test report as well as the semi-empirical method with *Digital Datcom* [22]. Versteeg & Malalasekera [28] states that CFD is the analysis of systems involving fluid flow, heat transfer and other associated phenomena by means of computer-based simulation. Commercial CFD code *Fluent* [23] and *SolidWork FloWorks* [24] are used for the analysis. The CFD codes have three main elements: a pre-processor to define the computational domain, a solver to calculate the solution of the governing equations of fluid flow over all the control volumes and a post processor for data visualization through vector plots or path line plots.

3.1.3.1 Meshing of UAV Model

The first step in the numerical simulation of the flow is to generate the mesh for the geometry of the UAV. The pre-processor *Gambit* [29] is used to define the geometry of the computational domain and subsequently used to sub-divide the domain into smaller elements for calculation. It also specifies the appropriate boundary conditions and fluid properties. This mesh is then exported into *Fluent* [23] to simulate the airflow around the model and solve for the aerodynamic characteristics.

Due to the complex geometry of the UAV, an accurate model is first generated in the CAD software *SolidWorks* [14], as shown in Figure 3.12, and exported out as a STEP model for use in the pre-processor *Gambit* [29]. The initial STEP model, as shown in Figure 3.12 is imported into *Gambit* [29] using its "tolerant modeling" option. This tolerant modeling option automatically assigns a tolerance value to each imported vertex and edge to maintain topological integrity for the imported model. The model is then

further cleaned up and simplified to remove unnecessary vertices, duplicate entities and eliminate short edges and small faces. This is necessary to avoid producing highly skewed elements during the mesh generation process.

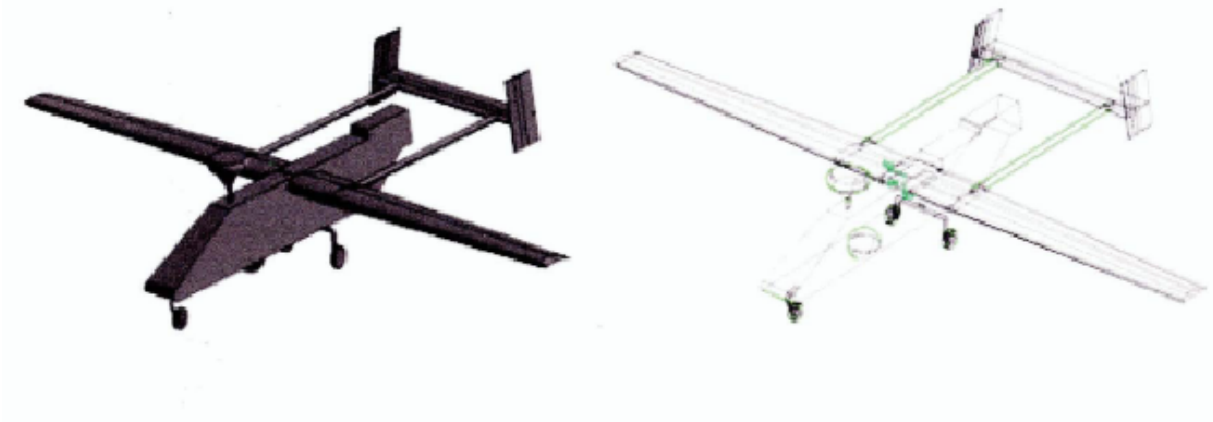

(a) SolidWorks Model (b) Step Model

Figure 3.12: UAV model in Computer domain

A rectangular volume representing the airspace is created around the UAV model. In order to define the faces of the outer volume with pressure far-field conditions, the outer faces of the volume created has to be of a substantial distance with respect to the wing span from the UAV model. Thus the rectangular volume as shown in Figure 3.13 is developed with 20 chord lengths (11.0m) to the side measured from the wingtip, 20 chord lengths (11.0m) away from the fuselage nose and trailing edge of the tail assembly and 15 chord (8.25m) lengths away from the radar dome and landing gears of the UAV. Pressure far field is defined as the free stream condition at infinity unaffected by the disturbance within the flow field. The surfaces of the UAV are defined as a wall where no-slip boundary conditions are enforced on the faces in viscous flow.

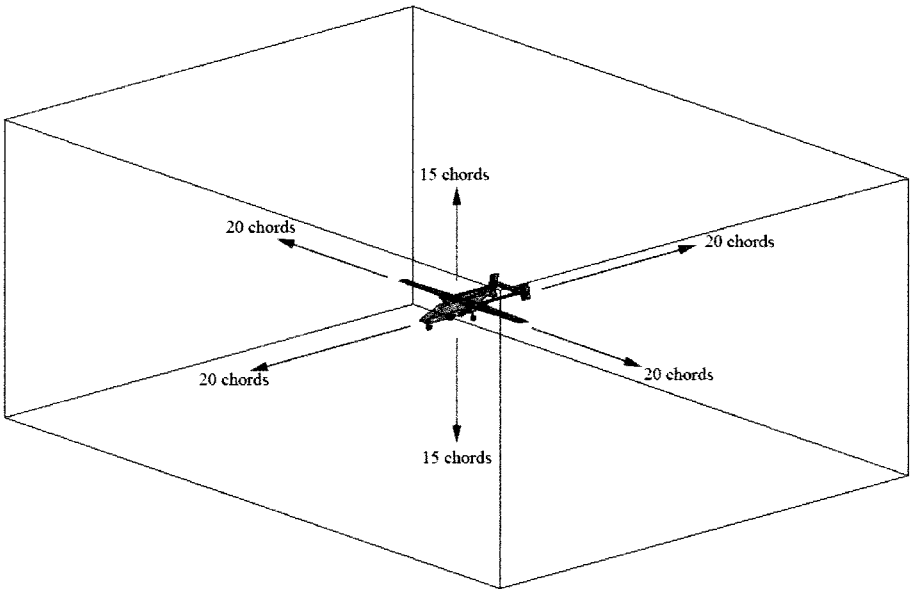

Figure 3.13: Volume grid created for computing external flow field past UAV model

A fine mesh is first generated on the surfaces of the UAV as shown in Figure 3.14. Using this face mesh as the starting condition, the 3-D mesh of the airspace is generated using the Size Function option in *Gambit* [27]. This is to create a mesh with very fine elements near the surface of the UAV, and gradually increase in size with distance from the UAV surfaces, as shown in Figure 3.14. A fine mesh element size near the UAV surface will produce better flow resolution and more accurate data computation. The flow field far away from the UAV surfaces does not change significantly, thus larger and coarser mesh elements are those areas do not affect the results of the simulation as shown in Figure 3.15. The area around the fuselage and near the radar dome has a finer mesh. The mesh around the UAV in the x-z plane can be seen in Figure 3.16. This arrangement of the mesh elements serves to reduce the computational effort in generating the mesh and also make the simulations in *Fluent* [23] computationally more efficient.

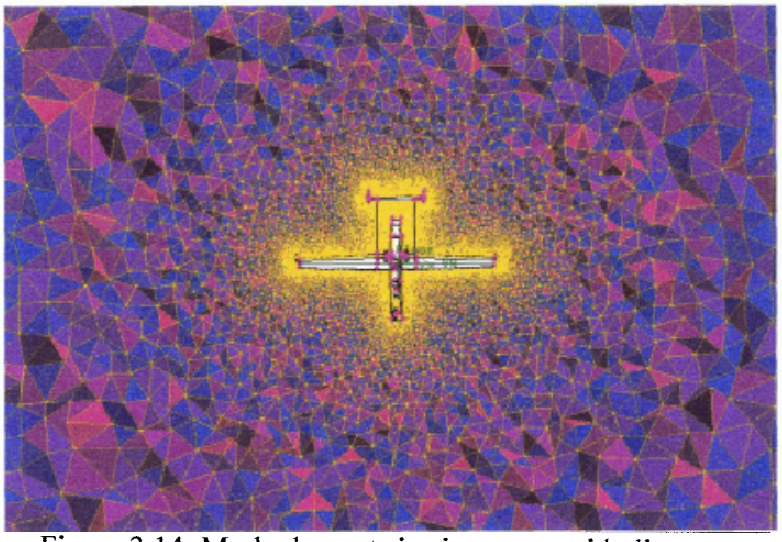

Figure 3.14: Mesh element size increases with distance

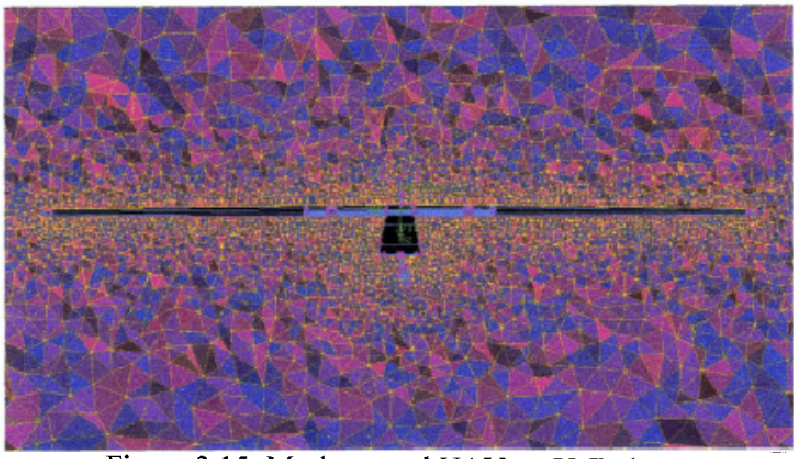

Figure 3.15: Mesh around UAV on Y-Z plane

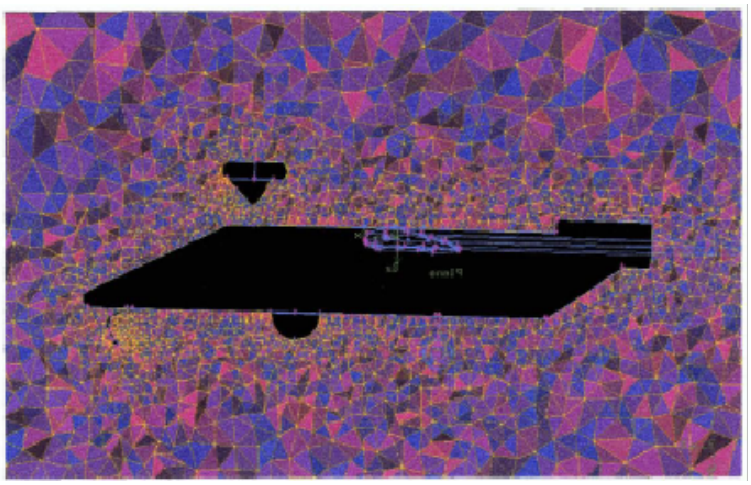

Figure 3.16: Mesh around UAV on X-Z plane

3.1.3.2 Initial and Boundary Conditions

The Navier-Stokes equations describe the motion of fluid substances. These equations establish that changes in momentum in infinitesimal volumes of fluid are simply the sum of the dissipative viscous forces, changes in pressure, and other forces acting inside the fluid: an application of Newton's second law.

The flow simulations of the UAV are computed under two different operational conditions and flight speed. The atmospheric conditions of both sets of simulation are found in the International Standard Atmosphere (ISA) tables. The first set of flow simulations to obtain data similar to the wind tunnel test conditions is set at sea level at the flight speed of 60 m/s with a pressure of 101325 Pa at a temperature of 288.16 K. The second set of flow simulation is computed at the operational cruising conditions of the UAV at an altitude of 1607 m (5000 ft), at a pressure of 89146.57 Pa, with a temperature of 281.21 K at a flight speed of 0.091 Mach.

Pressure far field conditions are used in *Fluent* [23] to model a free stream condition at infinity, with a free stream Mach No. and static conditions being specified. The pressure far-field boundary condition is applicable only when the density is calculated using the ideal gas law and is most appropriate for external aerodynamic flows. To effectively approximate true infinite extent conditions, the far field boundary must be placed far enough from the object of interest. The static pressure, temperature, Mach number and flow direction is defined at the boundary using pressure far-field panel in *Fluent* [23]. The flow direction is defined by setting the components of the direction vectors.

All contact surfaces of the UAV with the flow field are defined as a wall boundary which is used to bind the fluid and solid regions. At wall boundaries, total velocities are set to zero so that there are no forces across those boundaries.

Fluent [23] can compute and store the values of the lift and drag coefficients during the simulations via the use of the force monitor panel. These values are calculated using equation described in the previous section and required the reference area S to be specified. The reference area used for the UAV model comes from the wing platform area which is calculated as 4.463 m^2, while the mean aerodynamic chord (MAC) is

defined as 0.581m. The MAC is used as the reference length in the calculation of the coefficient in *Fluent* [23].

The Spalart-Allmaras model has been used as the turbulent model and is a relatively simple one-equation model that solves a modeled transport equation for the kinematic eddy (turbulent) viscosity. This embodies a relatively new class of one-equation model in which it is not necessary to calculate a length scale related to the local shear layer thickness. The Spalart-Allmaras model was designed specifically for aerospace applications involving wall-bounded flows and has been shown to give good results for boundary layers subjected to adverse pressure gradients.

3.1.3.3 Aerodynamic Characteristics of UAV

Based on the computational simulation results, the pressure plots of the UAV will be used to analyse and calculate the lift and drag forces of the UAV at its routine flight condition. The absolute pressure plot on the top surface of the UAV is shown in Figure 3.17. The regions of high pressure as indicated by the red section occur at the following sections, the leading edge of the fuselage, the frontal area of the dome as well as the leading edges of the wing section. These results from the stagnation points formed due to the effects of the airflow coming into contact with the UAV, obstructing its flow and thus slowing the particles down. As the airflow overcomes the initial disturbances and flows over the surfaces, it began to accelerate over the surfaces. This is predominately visible across the wing section where the region of blue and green regions which indicates an area of low pressure. This creates an upward force which opposed the weight of the UAV, giving the net lift force that keeps the UAV flying.

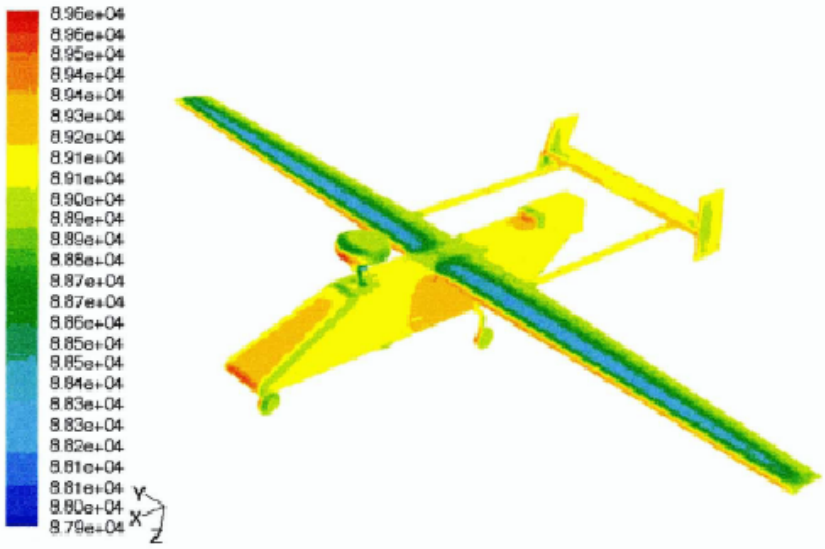

Figure 3.17: Contours of absolute pressure on top surface of UAV

A study on the effects of the angle of attack on the pressure differences is simulated by varying the angle of attack from -8° to 16° while keeping the velocity at its operating speed of approximately 30m/s. The objective is to study the effects of the angle of attack on the lift and drag characteristics of the UAV. The contours of the pressure are shown in Figure 3.18. As the angle of attack is increased, the pressure on the surfaces of the wing increased as the pressure on the bottom of the wing increased. Thus creating a pressure difference between the top and bottom of the wing, generating the lift experienced by the UAV. As the angle of attack increased to 12°, the pressure distribution above the wing begins to change, exhibiting an uneven distribution across the wing surfaces. The air no longer can go around the leading edge of the wing, and separates from the upper wing surface. This phenomenon is called flow separation and it occurs at the top section. Subsequently the UAV will experience stalling of the wing. Flow separation brings along large drag and energy loses. Thus the lift forces experienced by the UAV are reduced and the lift coefficient also decreases after this angle of attack.

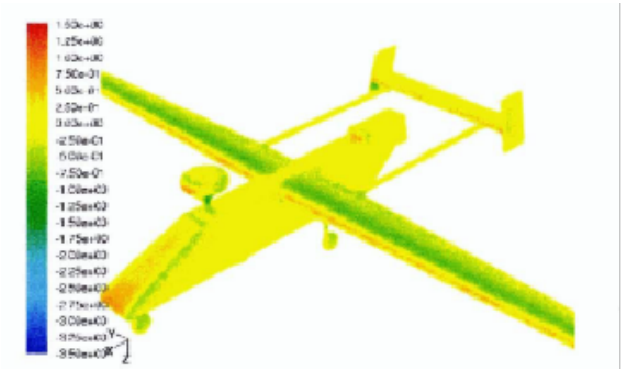

(a) -8 deg AOA

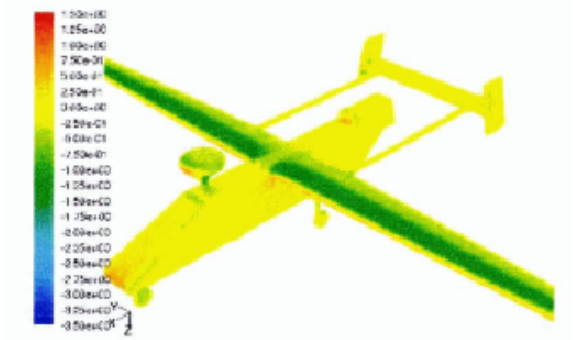

(b) 4 deg AOA

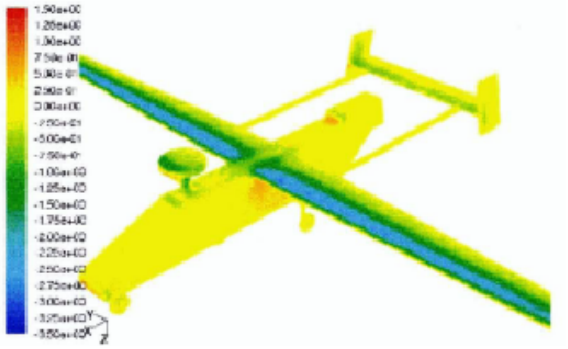

(c) 12 deg AOA

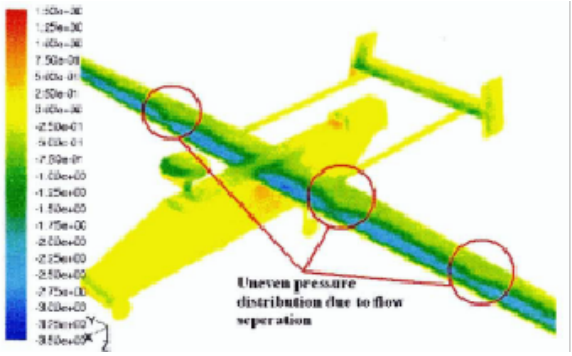

(d) 16 deg AOA

Figure 3.18: Contours of pressure coefficient on UAV surface at different AOA

Similarly the turbulent viscosities are plotted across the centerline of the UAV at the plane of symmetry at the same condition with the pressure contour plots. These plots show the intensity of the turbulence in the airspace around the UAV, giving an overview of the wake development caused by the various components at the different angle of attack. In general, the turbulence region decreases with increasing angle of attack. However the intensity increases through these variations. This is due to the UAV interfering with the airflow, forcing the air to flow round the body. As the angle of attack increases beyond its stalling angle, the area of turbulence is seen to decrease drastically as seen in the last diagram. From the diagrams in Figure 3.19 it can be seen that the turbulence is more profound in the areas behind the front landing gear and at the aft of the UAV, especially at the end of the fuselage.

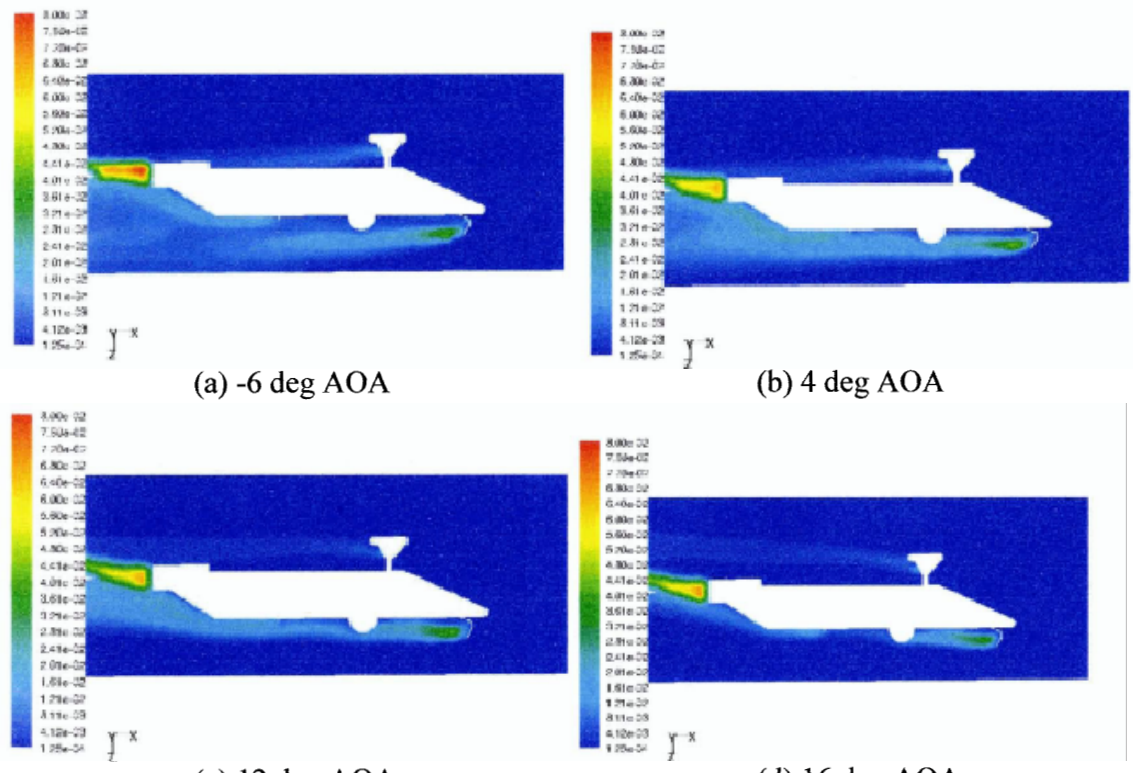

(a) -6 deg AOA (b) 4 deg AOA

(c) 12 deg AOA (d) 16 deg AOA

Figure 3.19: Contours of turbulence viscosity across centerline of UAV at various AOA

3.1.4 Computational Fluid Dynamics analysis with *FloWorks*

SolidWorks FloWorks [23] similarly is based on solving the time-dependent Navier-Stokes equations. The steady state problems are solved through a steady state approach with the method of local (over the computational domain) time steps being employed. A multi-grid method is used for accelerating the solution convergence and suppressing parasitic oscillations. The computational domain is designed as a parallelepiped enveloping model with planes orthogonal to the *SolidWorks* [14] model's Cartesian Global co-ordinate system. The computational mesh is designed by dividing the computational domain into cubic cells whose sides are orthogonal to the Global co-ordinate system's axes. Procedures of refining the computational mesh are used for better resolving the model's features, such as high curvature surfaces in contact with the fluid, thin walls surrounded by fluid, narrow flow passage, and the specific insulator's boundaries. During the subsequent calculations of the problem, the computational mesh can be refined for better resolving the high-gradient flow and solid regions revealed in these calculations.

3.1.4.1 Meshing of UAV Model

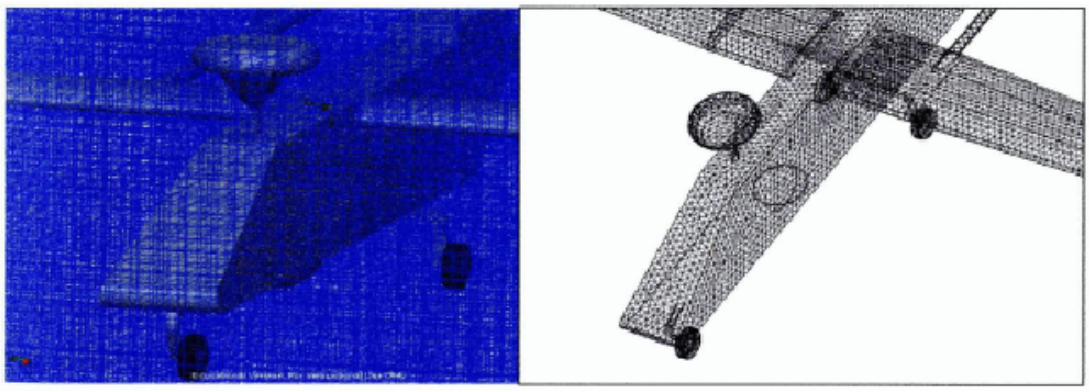

(a) In *SolidWorks FloWorks* [24] (b) In *Fluent* [23]

Figure 3.20: Computational Domain of UAV

SolidWorks FloWorks [24] uses rectangular cells and they are classified into the flowing categories. The fluid and solid cells encompass the fluid and solid respectively. The partial cells are partly in solid and partly in fluid, while the irregular cells are partial cells with undefined normal to the solid face. The blue cells in the Figure 3.20 depict the

fluid cells in the computational domain. In general the differences between the computation domains are shown in the Figure 3.20 above. The red, green and purple blocks which represent the solid, partial and irregular cells respectively are shown in Figure 3.21. The size of the cells is varied according to the complexity of the geometrical shapes of the UAV. The general advantage of this software is the computational time required in obtaining results in comparison with *Fluent* [23]. Computational time is essential in this study especially there is a need to simulate the various component effects at a wide spectrum of atmospheric conditions at varying wind speed at different angles.

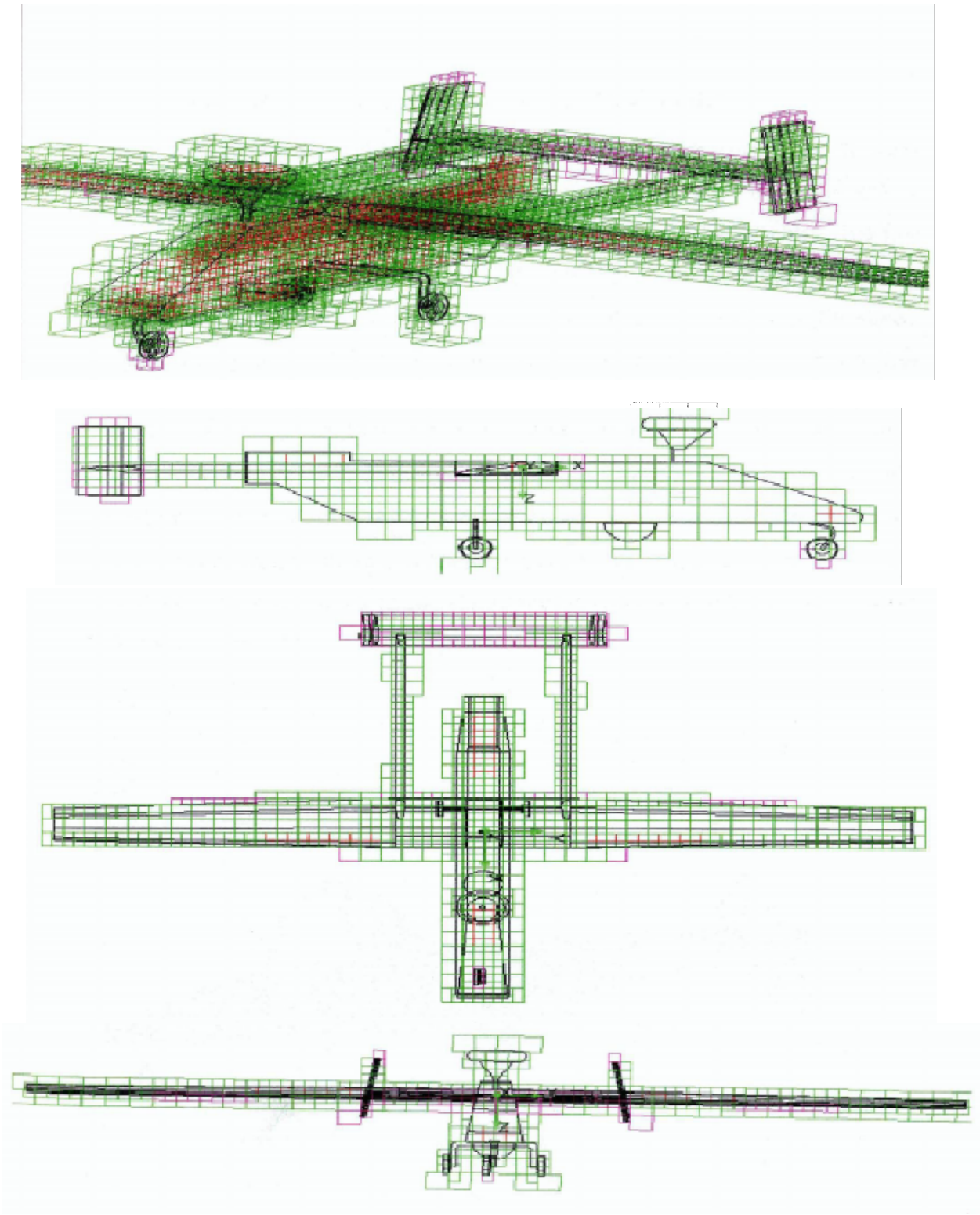

Figure 3.21: Various plots of the mesh of the UAV used in the calculation

3.1.4.2 Aerodynamic Characteristics of UAV model

The flow simulations of the UAV are computed under two different flight conditions. The atmospheric conditions of the three sets are set at sea level with a pressure of 101325 Pa and a temperature of 288.16 K based on the ISA tables. The first set of analysis is completed at 36m/s to simulate the UAV at cruise flight conditions.

The surface pressure on the UAV is shown in Figure 3.22. Similar to the *Fluent* [23] analysis, the region in the front of the fuselage, radar and front of the wing indicates a region of higher pressure. The purpose of this study is to validate the computational model in this suite of software in comparison with the *Fluent* [23] model. With the results in agreement with one another, further study was done to analyse the component effects on the airflow of the UAV and the interaction of the propulsion system with the other components during various flight conditions. Figure 3.23(a) and (b) depicts the pressure contours at the x-z plane and x-y plane. The figures are used to understand the variation of pressure across the UAV.

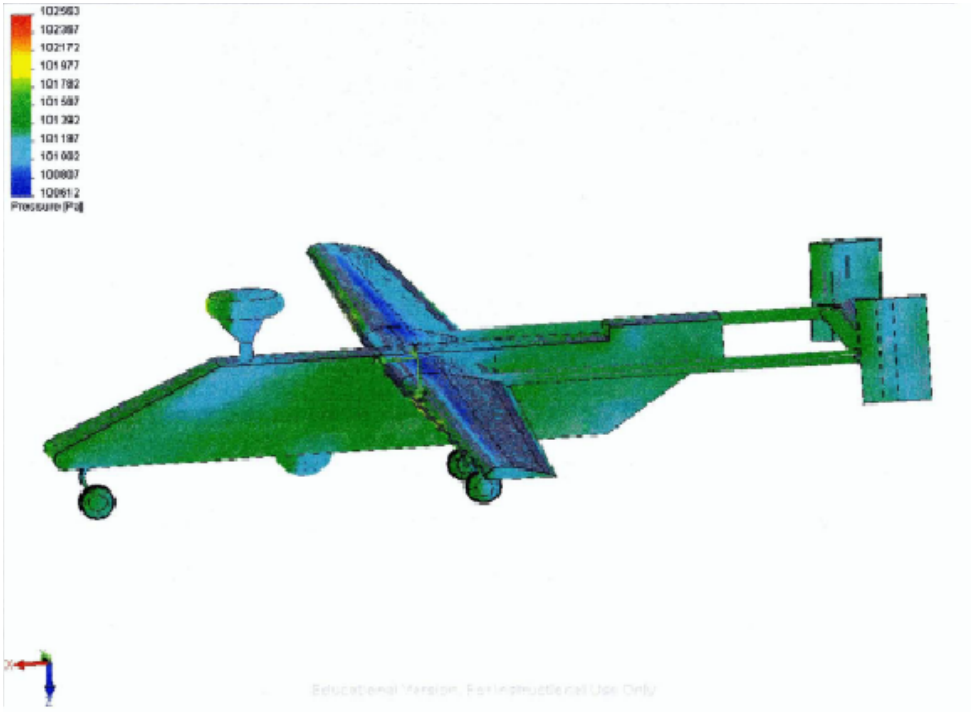

Figure 3.22: Contours of pressure on the surface of the UAV

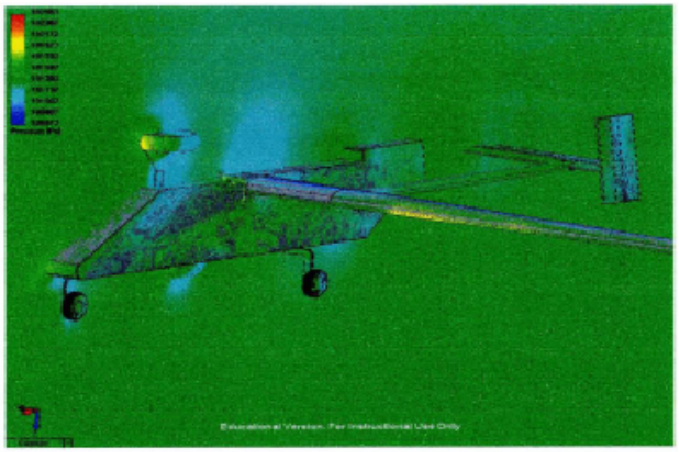

(a) In the x-z plane

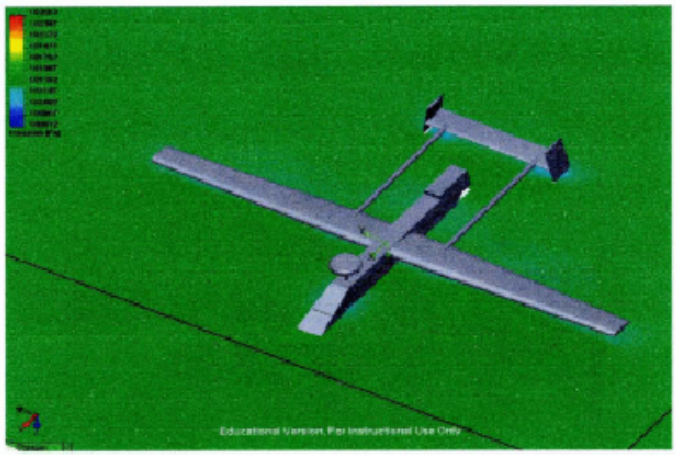

(b) In the x-y plane

Figure 3.23: Contours of pressure coefficient of the UAV

Figure 3.24 displays the contours of the velocity of the UAV under cruise conditions. It can be seen that the velocity varies across the UAV with lower velocity represented by the green and yellow regions in areas behind the radar dome, landing gear as well as the tail. A velocity plot can be seen in Figure 3.25 (a) with a blown up image of the area behind the landing gear shown in Figure 3.25 (b). The figures clearly define the regions of low velocity behind the various components which is indicative of the wake region generated during the cruise flight. This effect is especially more profound at the areas behind the landing gear. Further studies are completed to understand the effects of the aerodynamic characteristics especially for its drag component caused by the external parts of the UAV.

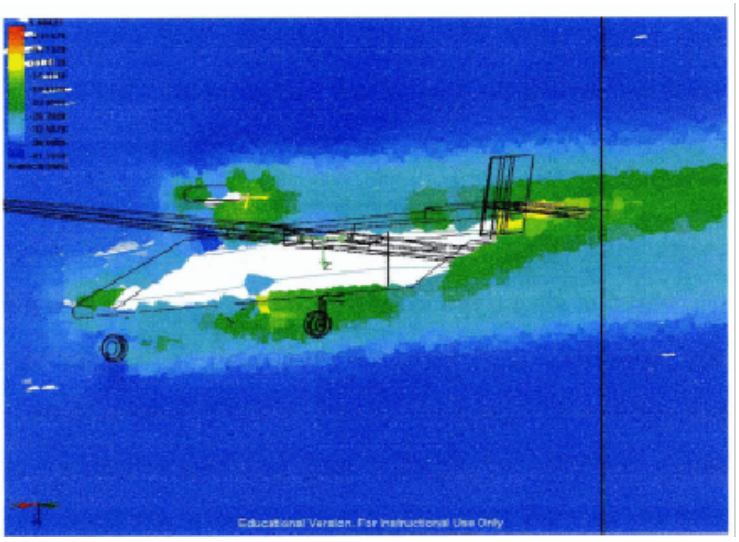

Figure 3.24: Contours of the velocity around the vicinity of the UAV

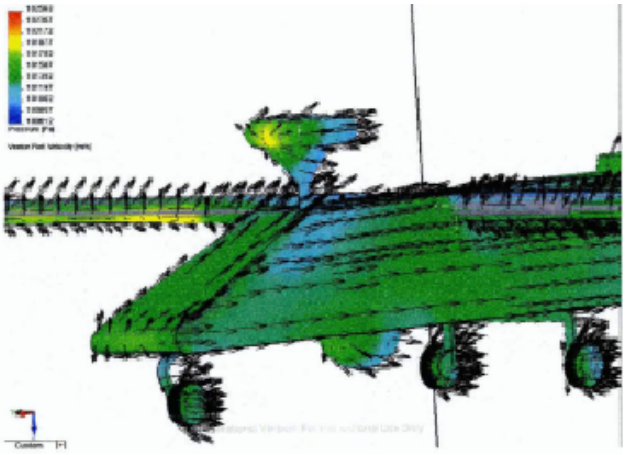

(a) Overview of UAV

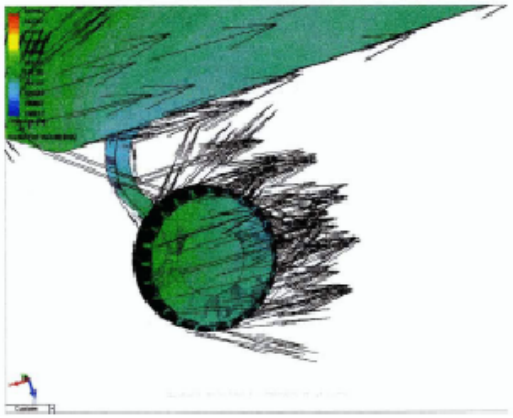

(b) Around the landing gear

Figure 3.25: Contours of the velocity vector around the vicinity of the UAV

The second study is to simulate the UAV under cruise condition at 36m/s subjected to a crosswind vector in the y-axis at a magnitude of 10m/s. The pressure contour plot as shown in Figure 3.26 shows the impact of the crosswind on the UAV. The asymmetrical wind conditions develop a pressure difference across the span of the wing and tail. The region of higher pressure as indicated by the yellow regions shows a build up of force on the region behind the wing. The boom on the left side also experiences an excessive force as indicated by the red region in the figure. However with a predominant airflow from the front of the UAV, it still experience regions of high pressure in the front of the wing. This is clearly shown in Figure 3.26(b) where the red region shows the wing experience a larger pressure in comparison to the other parts of the wing. The sectional view on the x-z axis in Figure 3.26 also indicates the pressure build up in the front part of the fuselage, wing and radar dome.

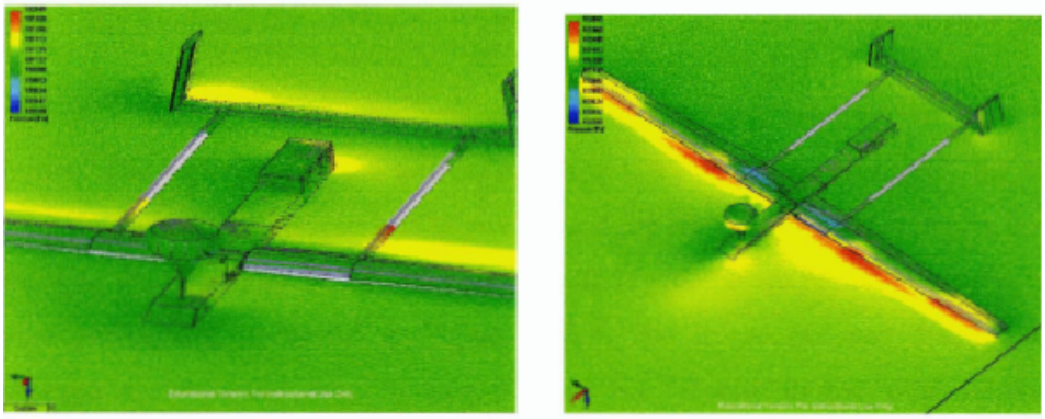

(a) (b)

Figure 3.26: Contours of the pressure coefficient on the surface of the UAV

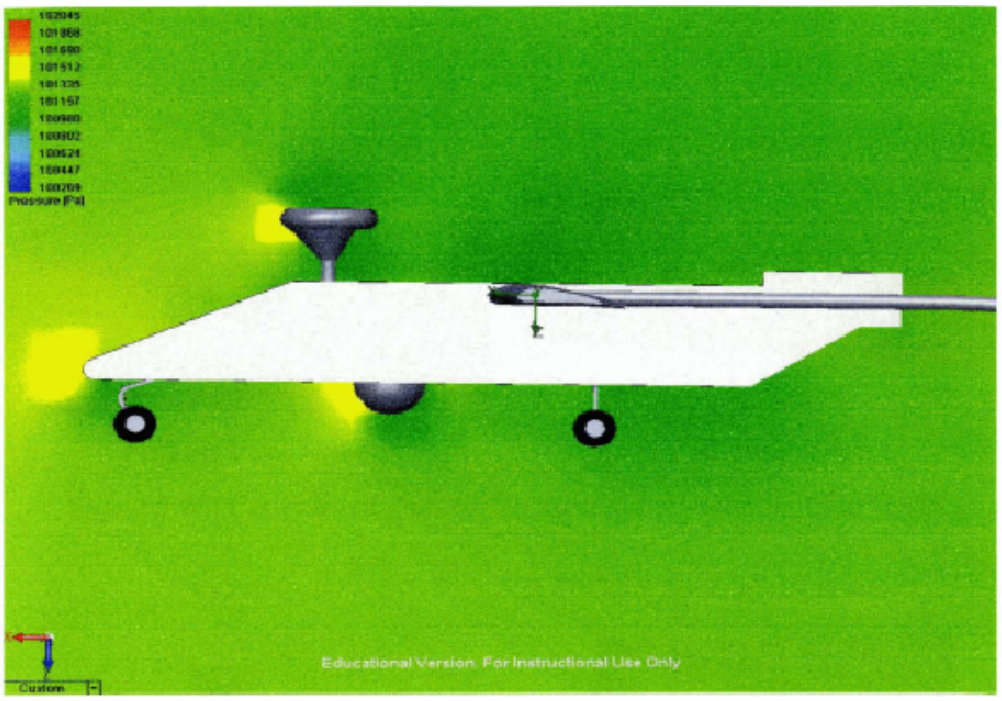

Figure 3.27: Sectional view of the contours of the pressure coefficient on the x-z plane

Figure 3.28(a) shows the velocity variation of the UAV under this flight conditions. The difference in the airflow over the UAV in comparison with the cruise flight is the asymmetrical effects on the aircraft and the slowing down of velocity is more profound on the left region of the UAV as indicated by the green region in the Figure. A different perspective is plotted in Figure 3.28(b) and it can be seen that the UAV experienced a substantial drop to almost 12m/s in velocity in the areas where the propulsion system is supposed to be present as indicated by the light blue region. Taking the reference of the front on the camera capsule and radar dome, the contours of the velocity plot are shown in Figure 3.29 and 3.30 respectively. In Figure 3.28, the velocity column can be seen to come into interaction with the tail vertical tail component of the UAV. The interaction with the control surface may cause complication in the system, as the airflow may degrade its effectiveness under such flight condition.

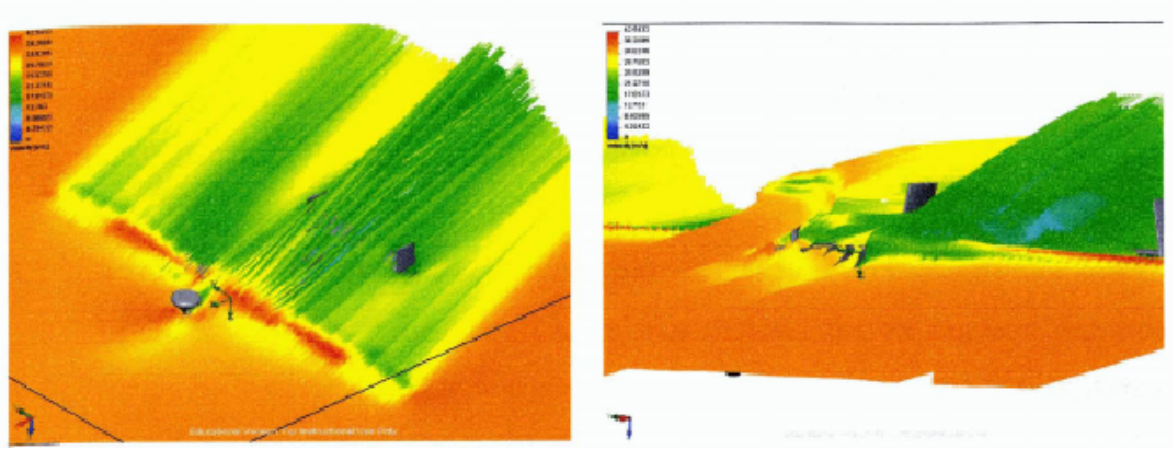

(a) Top View (b) Side View

Figure 3.28: Contours of the velocity around the vicinity of the UAV

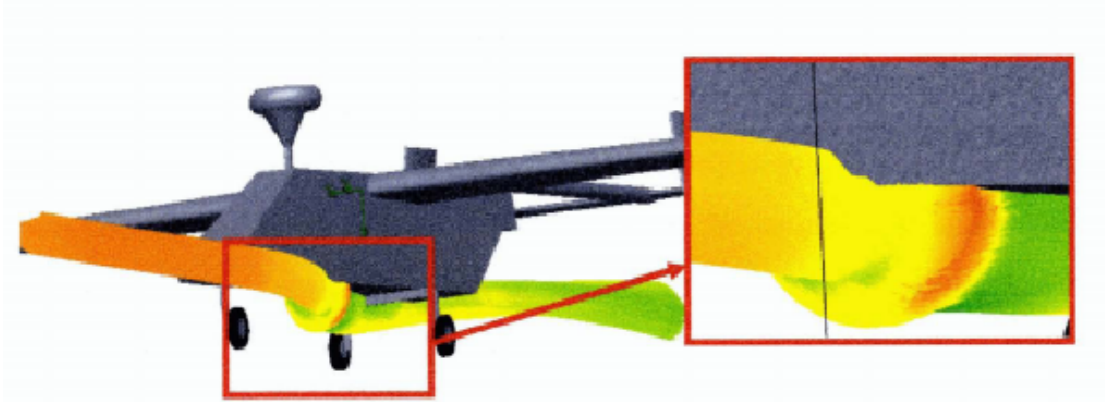

Figure 3.29: Contours of the velocity across the vicinity of the camera capsule

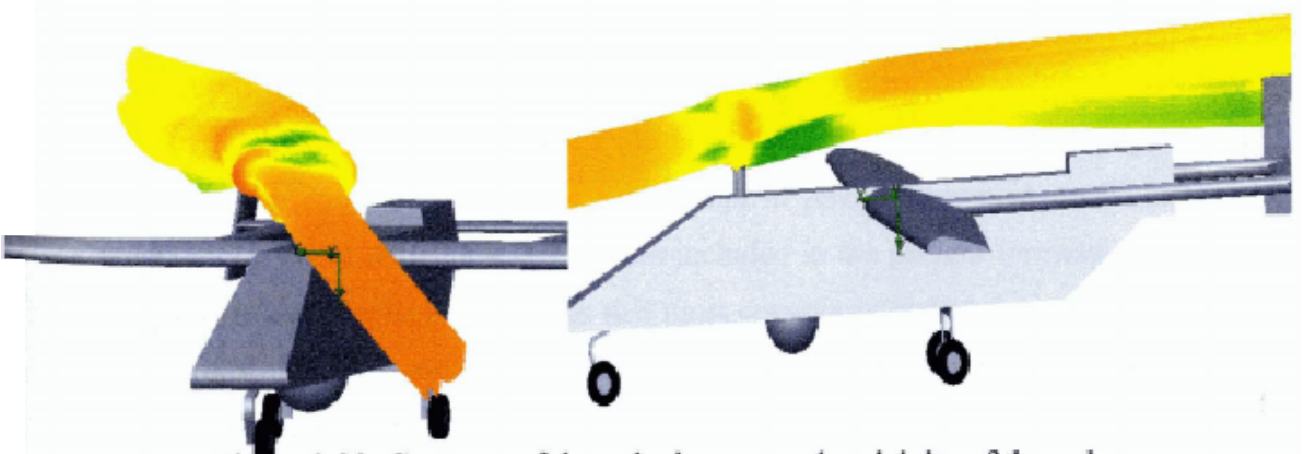

Figure 3.30: Contours of the velocity across the vicinity of the radar

As seen in the second case study, evidence shows that the airflow between components come into interaction with one another, thus this might complicate the airflow and affect the effectiveness of the different control surface.

3.2 Propeller Effects on the Aerodynamic Characteristics of the UAV

In the conventional aircraft flight mechanics analysis, the six degree-of-freedom (6 DOF) rigid body equations of motion are commonly linearized using small disturbance theory. Based on this theory, the lateral equations of motions are uncoupled from the longitudinal equations of motion as a result of imposing the small disturbance approximation whereby assumptions are made to eliminate any interaction between the longitudinal and lateral axis. However in the actual response of a rigid aircraft to a finite lateral disturbance, it involves all 6 DOF.

Based on the formulation in Chapter 2, the UAV is described in a 12 by 12 matrix in a state space format based on the small disturbance theory; the equations are linearized about a coordinated turning flight condition. When the longitudinal-lateral coupling are introduce in the matrix, the net effect of the coupling have to be investigated to see if it does any modest changes to the frequencies and damping rates. At least a small longitudinal-lateral coupling is present in most aircraft. In this study, the aircraft is considered a small aircraft and the propulsion system causes a high thrust to weight ratio, thus there is a need to investigate its effects and make comparison with the decoupled mathematical analysis.

In this analysis, three additional aerodynamic derivatives are included: the change in rolling moment coefficient with angle of attack; the change in yawing moment coefficient with angle of attack, and the change in pitching moment coefficient with sideslip angle. These three derivatives were included in the present formulation because the values are the coupling derivatives that most commonly become significant when an aircraft is flown in an asymmetric configuration. [40] This type of aerodynamic coupling is produced by a rotating propeller. No propeller-driven aircraft can be truly symmetric unless it has an even number of counter rotating propellers symmetrically distributed in the span wise direction. An aircraft with a single rotating propeller as seen in this study

will always display some degree of aerodynamic coupling between the longitudinal and lateral modes. [41]

Figure 3.31 shows a pictorial representation of the effects of the propulsion system on the tail. In this case, it is assumed that the flow field of the propulsion system is not affected by the effects of the wind, i.e. wind direction is in the same direction of the UAV. However, when the wind is not aligned in the same direction of the UAV, the asymmetrical effects might cause some components of the rudder to lose its effectiveness as shown in Figure 3.32 as it falls in the region of its slipstream. Thus there is a need to investigate the effects of the asymmetrical flight due to the propulsion system with and without wind effects.

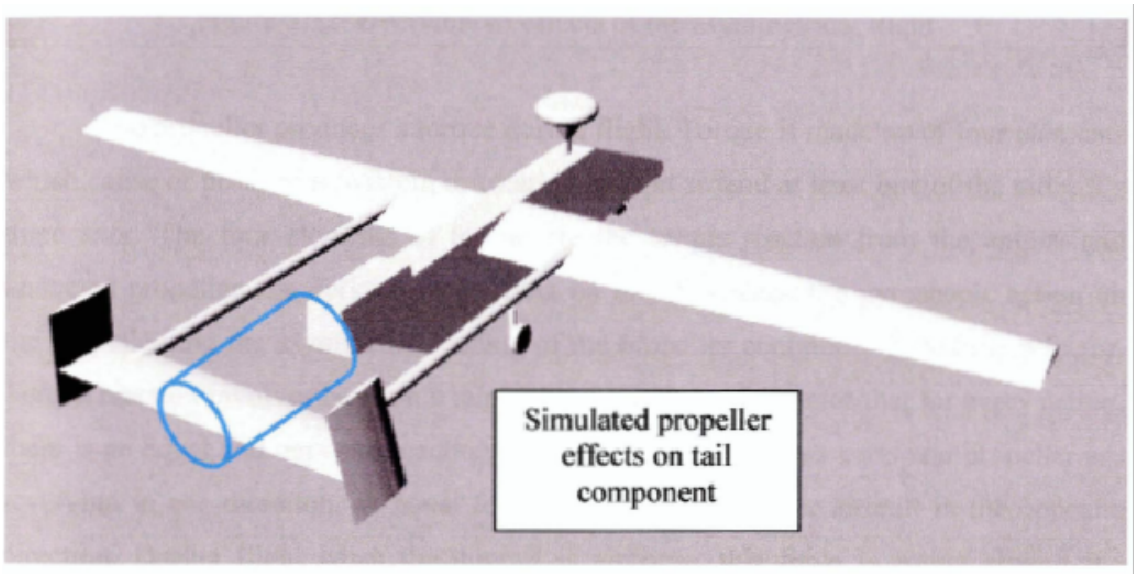

Figure 3.31: Pictorial image of the Effects of the Propeller System

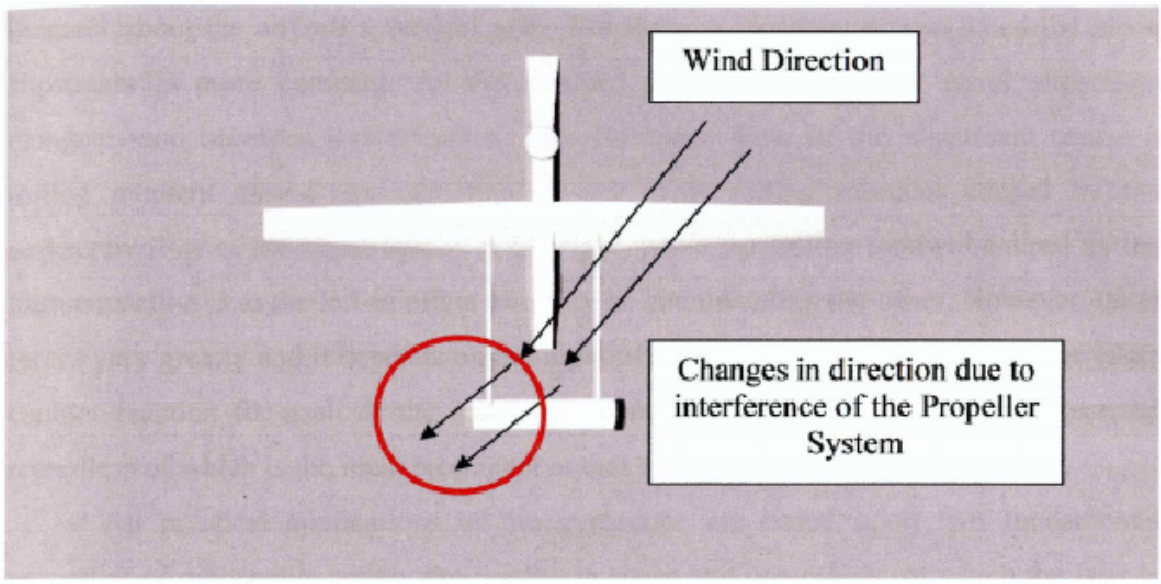

Figure 3.32: Overview of effects of the asymmetrical flight

The propeller produces a torque during flight. Torque is made up of four elements which cause or produce a twisting or rotating motion around at least one of the aircraft's three axes. The four elements of torque are the torque reaction from the engine and unducted propeller, the corkscrewing effect on the slipstream, the gyroscopic action on the propeller and the asymmetric loading of the propeller commonly called the p-factor. Torque reaction involves Newton's third law of motion which states that for every action, there is an equal and opposite reaction. When the internal engine parts and propeller are revolving in one direction, an equal force is trying to rotate the aircraft in the opposite direction. During flight when the aircraft is airborne, this force is acting around the longitudinal axis, tending to make an aircraft roll. To compensate for this, some of the older aircrafts are rigged in a manner to create more lift on the wing that is being forced downwards. The more modern aircraft are designed with engine offset to counter these effects of torque.

The high-speed rotation of an aircraft propeller gives a corkscrew or spiraling rotation to the slipstream. At high propeller speeds and low forward speed, this spiraling rotation is very compact and exerts a strong sideward force on the aircraft vertical surface. When this spiraling slipstream strikes the vertical fin on the left, it causes a left turning

moment about the aircraft's vertical axis. The force is more prominent when the spiral slipstream is more compact. As the forward speed increases, the spiral slipstream elongates and becomes less effective. This corkscrew flow of the slipstream causes a rolling moment around the longitudinal axis. This rolling moment caused by the corkscrew flow of the slipstream is to the right, while the rolling moment caused by the torque reaction is to the left-in effect one may be counteracting the other. However, these forces vary greatly and it depends on the input of the flight controllers to apply the exact counter reaction for each of the rolling moments. These forces must be counteracted regardless of which is the most prominent at that time.

All practical applications of the gyroscope are based upon two fundamental properties of gyroscopic action, the rigidity in space and precession, of which the later is the one of interest in this discussion. Precession is the resultant action, or deflection, of a spinning rotor when a deflecting force is applied to its rim. When a force is applied, the resulting force takes effect 90° ahead of and in the direction of the force. The rotating propeller of an aircraft makes a very good gyroscope and thus has similar properties. Any time a force is applied to deflect the propeller out of its rotation; the resulting force is 90° ahead of and in the direction of rotation and in the direction of the application, causing a pitching moment, a yawing moment, or a combination of the two depending upon the point at which the force was applied. The change in pitch attitude has the same effect as applying a force to the top of the propeller's plane of rotation. The resultant force acting 90° ahead causes a yawing moment to the left around the vertical axis. The magnitude of this moment depends on several variables, one of which is the abruptness with which the tail is raises. However, precession, or gyroscopic action occurs when a force is applied to any point on the rim of the propeller's plane of rotation; the resultant force still be 90° from the point of application in the direction of rotation. Depending on where the force is applied, the aircraft is caused by the yawing left or right, to pitch up or down or a combination of pitching and yawing. As a result, the gyroscopic action - any yawing around the vertical axis results in a pitching moment and any pitching around the lateral axis results in a yawing moment. To correct for the effect of the gyroscopic action, it is

necessary for the pilot or the flight controller system to properly use the elevator and rudder control surface to prevent undesired pitching and yawing.

When an aircraft is flying with a high angle of attack, the bite of the downward moving blade is greater than the bite of the upward moving blade; thus moving the center of thrust to the right of the propeller disc area - causing a yawing moment towards the left around the vertical axis. The asymmetric loading is caused by the resultant velocity, which is generated by the combination of the velocity of the propeller blade in its plane of rotation and the velocity of air passing horizontally through the propeller 'disc'. With the aircraft being flown at positive angles of attack, the right viewed from the pilot perspective or down swinging blade, is passing through an area of resultant velocity which is greater than that affecting the left or up swinging blade. Since the propeller blade is an airfoil, increased velocity means increased lift. Therefore, the down swinging blade have more 'lift' tends to pull (yaw) the aircraft's nose to the left.

Simply stated, when the aircraft is flying at a high angle of attack, the downward moving blade has a higher resultant velocity; therefore creating more lift than the upward moving blade. This might be easier to visualize if the propeller shaft was mounted perpendicular to the ground like a helicopter. If there were no air movement at all, except that generated by the propeller itself, identical sections of each blade would have the same airspeed. However, with air moving horizontally across this vertically mounted propeller, the blade proceeding forward into the flow of air will have a higher airspeed than the blade retracting with the airflow. The blade proceeding into the horizontal airflow is creating more lift, or thrust, moving the center of thrust towards the blade. Visualize rotating vertically mounted propeller shaft to shallower angles relative to the moving air as on the aircraft. Their unbalanced thrust then becomes proportionately smaller and continues getting smaller until it reaches the value of zero when the propeller shaft is exactly horizontal in relation to the moving air.

Each of these four elements of torque effects vary with changes in flight situations. In one phase of flight, one of these elements may be more prominent than another whereas in another phase of flight another element may be more prominent. The

relationship of these values to each other will vary with different aircraft depending on the configuration of the aircraft

3.2.1 CFD analysis of the UAV with the Propeller System

The propeller system plays an important role in causing additional aerodynamic forces and moments. This will increase the complexity of the airflow around the system. Therefore, a study to simulate the UAV under cruise flight conditions of 36m/s with the propulsion system included is completed. The propulsion system is modeled as a fan with a differential pressure drop between the disc stations based on the actuator disc theory. The objective is to study the flow over the propulsion system and the impact it has on the components like the tail. It is assumed that the modeling in actuator disc theory will give a good representation of the reaction with the tail, thus the full model is not completed.

Figure 3.33 shows the velocity profile of the UAV under crosswind conditions, and the velocity difference between the actuator discs. The sudden jump in velocity before and after the disc is shown by the blue and green region in the figure. The complexity of airflow over the propulsion system can be further analyzed by the side profile of the velocity profile shown in Figure 3.34. There is also a sudden increase in velocity before and after the propulsion disc. The difference in the velocity and subsequently the pressure creates a force and thus thrust for the UAV. The pressure profile of the actuator disc is presented in Figure 3.35. The drop in pressure over the disc and the flow around the tail component shows impact the propulsion has on the tail. The effectiveness of the elevator at certain flight situation might be compromise and not work as effectively as it will be under normal conditions without the propeller interference. Figure 3.35 depicts the pressure differences at the propulsion disc from the side perspective of the UAV, and the difference in pressure developed is the thrust force that propels the UAV in the forward direction.

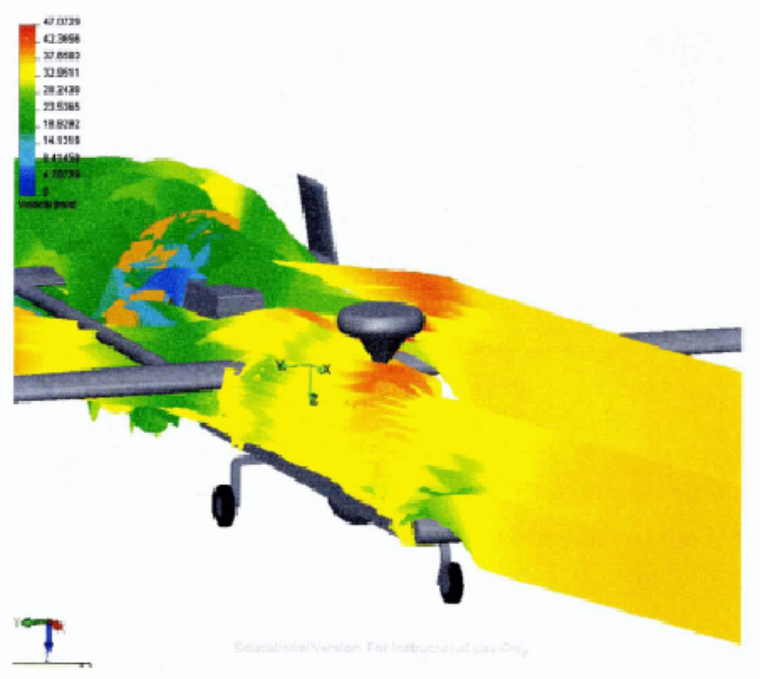

Figure 3.33: Contours of the velocity of the UAV under crosswind conditions

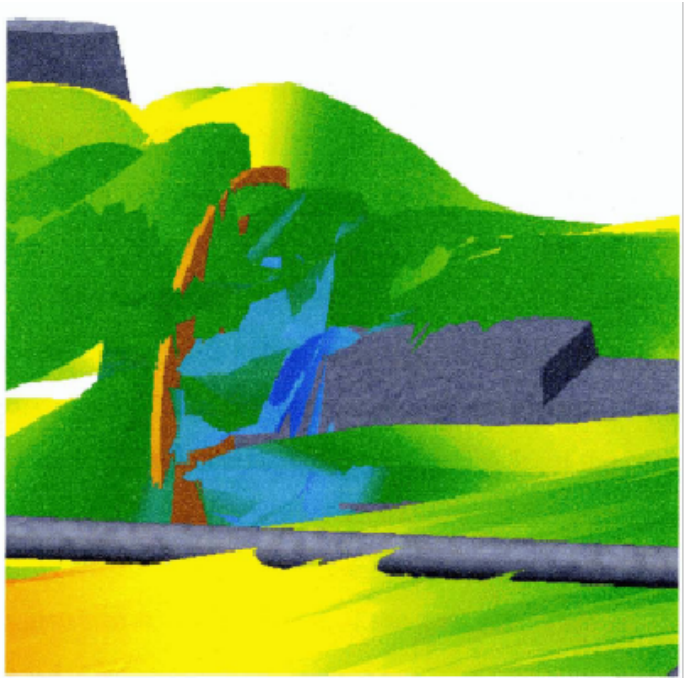

Figure 3.34: Contours of the velocity in the vicinity of the propeller system

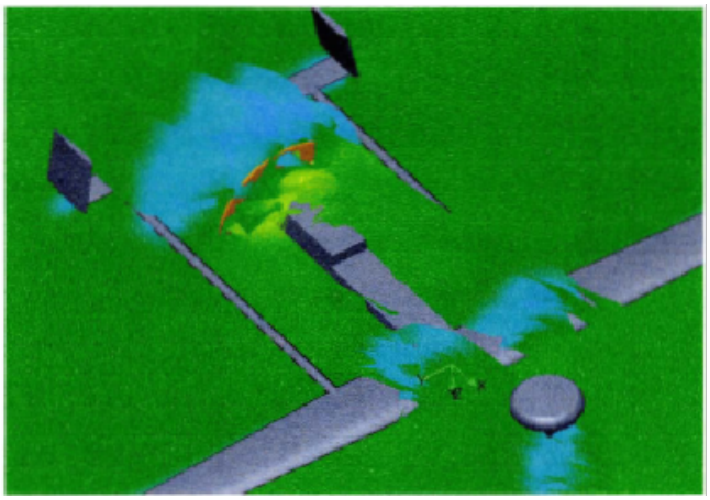

Figure 3.35: Sectional plot of the pressure contours of the UAV

3.3 Development of Aerodynamic Characteristics

The quality of the mesh generated greatly affects the end results obtained from the simulations. Coarse mesh elements give large errors in the data computed and poor flow resolution, while very fine mesh elements increases the accuracy but requires much more computational effort and time. The only way to eliminate errors due to the coarseness of a grid is to perform a grid dependence study, which is a procedure of successive grid refinement of an initially coarse grid until certain key results do not change. The simulation is then grid independent defined in Verteeg [28]. The number of grid cells is varied through the use of the Size Function option in *Gambit* [29] when generating the mesh. Using a coarse grid of 173791 cells as the starting point, the number of cells is gradually increased up to 911003 cells. A plot in figure 3.36 of the convergences shows a converging trend, approaching a horizontal asymptote as the number of mesh elements increases. The study showed that a mesh of approximately 800000 elements is sufficiently fine to give results independent of the grid size. This grid will be used for all simulation of the full UAV model in basic configuration.

The results of the numerical simulation in CFD for both *Fluent* [23] and *SolidWorks FloWorks* [24] on the UAV are compared with the results of the wind tunnel data as reported by Ungar [25]. A plot comparing the lift coefficients against the angle of

attack is shown in Figure 3.37. The results shows similar trends for both the lift and drag coefficients but with significant differences.

In general, the plots of the CFD analysis for both *Fluent* [23] and *SolidWorks FloWorks* [24] shows that the lift coefficient against angle of attack varies linearly from the angles from -8° to 10°. The graph becomes parabolic with a further increase in the angle of attack, reaching a maximum lift coefficient of approximately 1.6 at 14° angle of attack, after which the lift coefficient decreases with increasing angle of attack, indicating stalling of the UAV. The major differences of the plots are the difference in the zero lift angle of attack and stalling angle. The zero-lift angle of attack for both the CFD simulation is higher than that for the wind tunnel test by approximately 2°. The lift coefficients obtained from the CFD simulation for the angle of attack below 2° are higher than the wind tunnel test results. The trend with the wind tunnel results higher are reversed above 2° angle of attack. The wind tunnel test revealed a max lift coefficient of 1.94 at an angle of attack of 12°, while the CFD simulation yields a lower lift coefficient of 1.57 an angle of attack of 13°. The lift vs. drag plot of the CFD simulation and the wind tunnel test exhibit similar parabolic trends, with the CFD simulation yielding higher drag coefficients as compared to the wind tunnel test data. The minimum drag coefficient C_{Do} occurs at the same lift coefficient of about 0.47 for both, with a lower C_{Do} for the wind tunnel test at about 0.054.

These discrepancies in the results obtained for both the wind tunnel and CFD simulation is due to errors in the numerical simulation and the inaccuracy of the wind tunnel test data as indicated at the start of the chapter. The CFD model might also yield some inaccuracies. Due to the complex nature of the UAV, the grid might not be sufficiently developed and the truncation error may arise from the change in cell volume between adjacent cells, affecting the solution to the flow variables calculated by the CFD simulation.

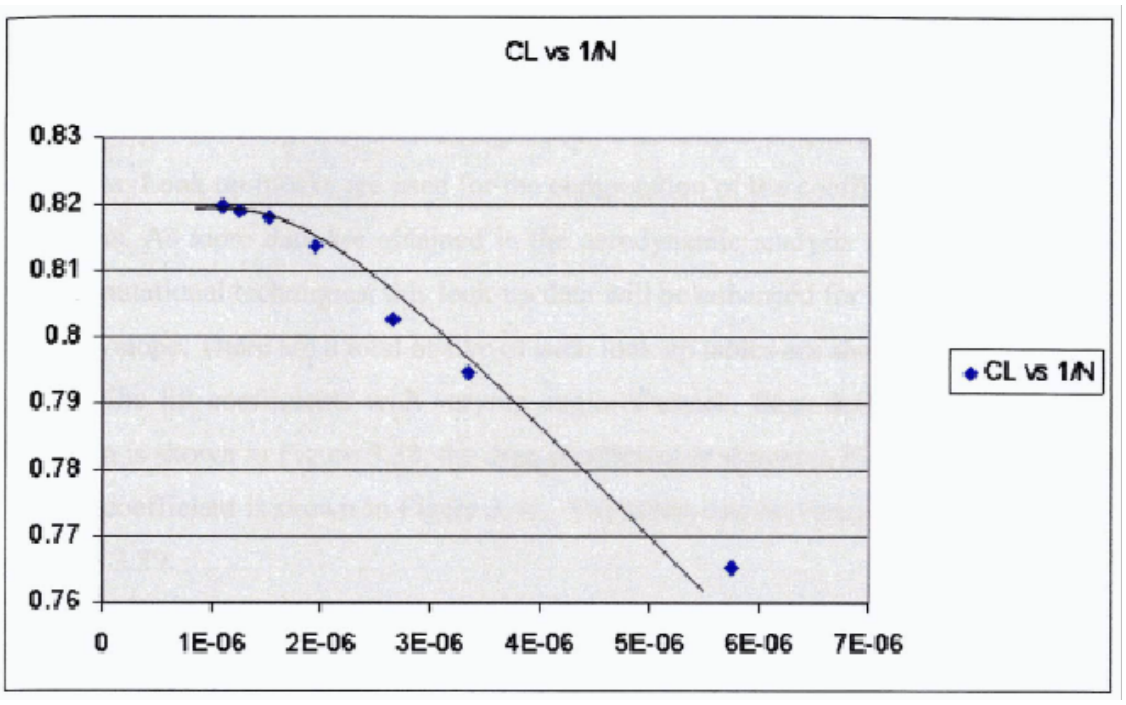

Figure 3.36: Graph of lift coefficient vs. reciprocal of number of mesh cells

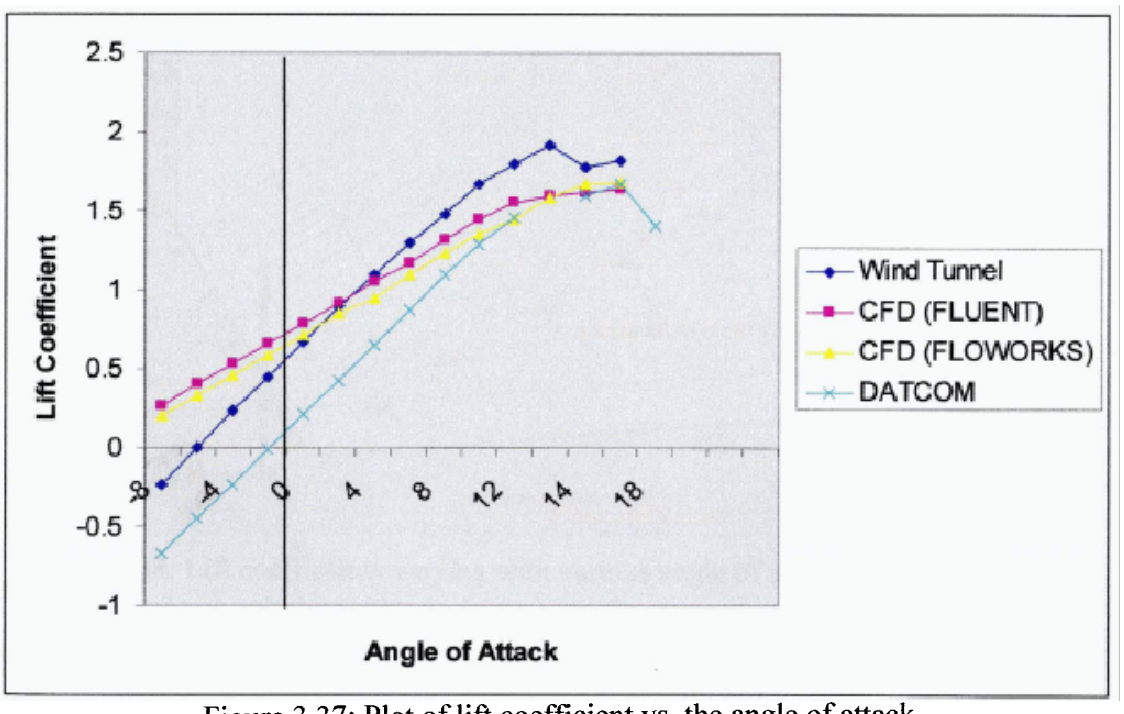

Figure 3.37: Plot of lift coefficient vs. the angle of attack

These aerodynamic data gathered from the various methods as indicated in the above sections are tabulated in a database. Tapping on the strengths of the individual methods and combining them into a single database, several plots are developed with the given data. Look up blocks are used for the computation of the coefficients at the various conditions. As more data are obtained in the aerodynamic analysis through engineering and computational techniques, this look-up data will be enhanced for a wider scope of the flight envelope. There are a total of five of such look up tables are shown in the following figures. The lift coefficients with varying angle of attack, flaps deflection and elevator deflection is shown in Figure 3.38, the drag coefficient is shown in Figure 3.40, while the moment coefficient is shown in Figure 3.41. The tables can be viewed in excel as shown in Figure 3.39.

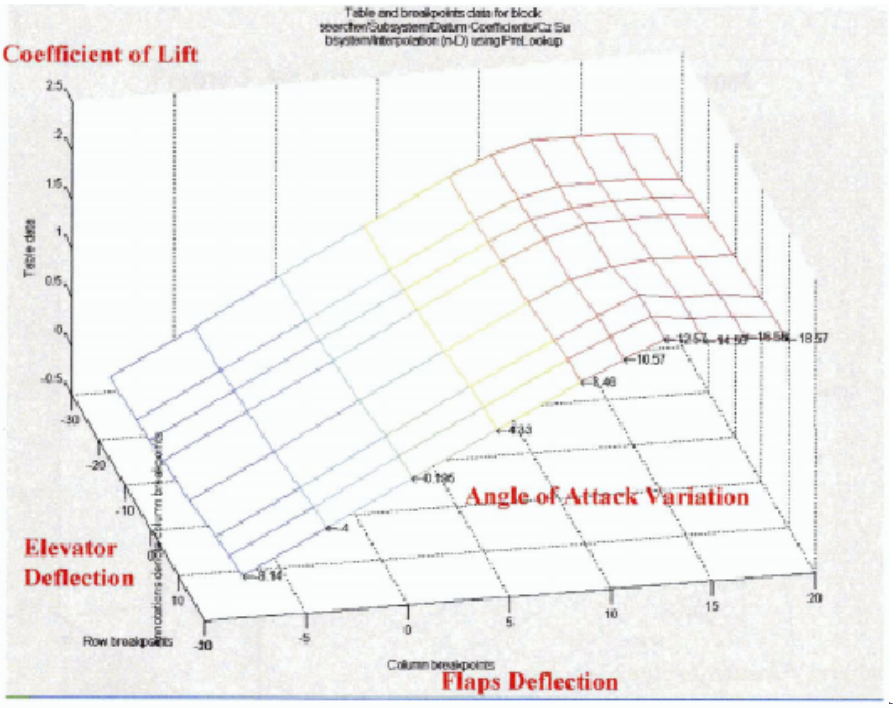

Figure 3.38: Lift coefficients varying with various angle of attack, flaps and elevator deflection

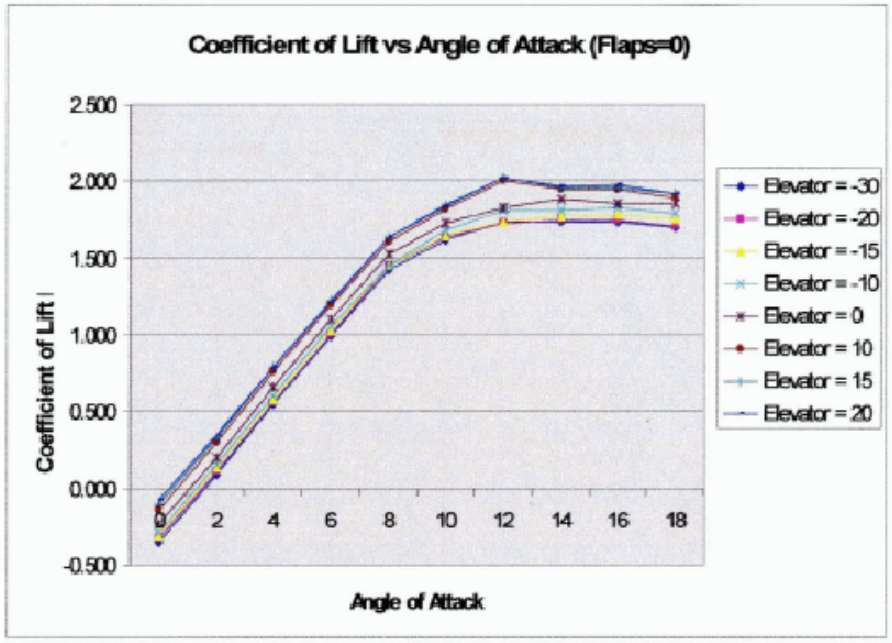

Figure 3.39: Lift coefficient data in excel format

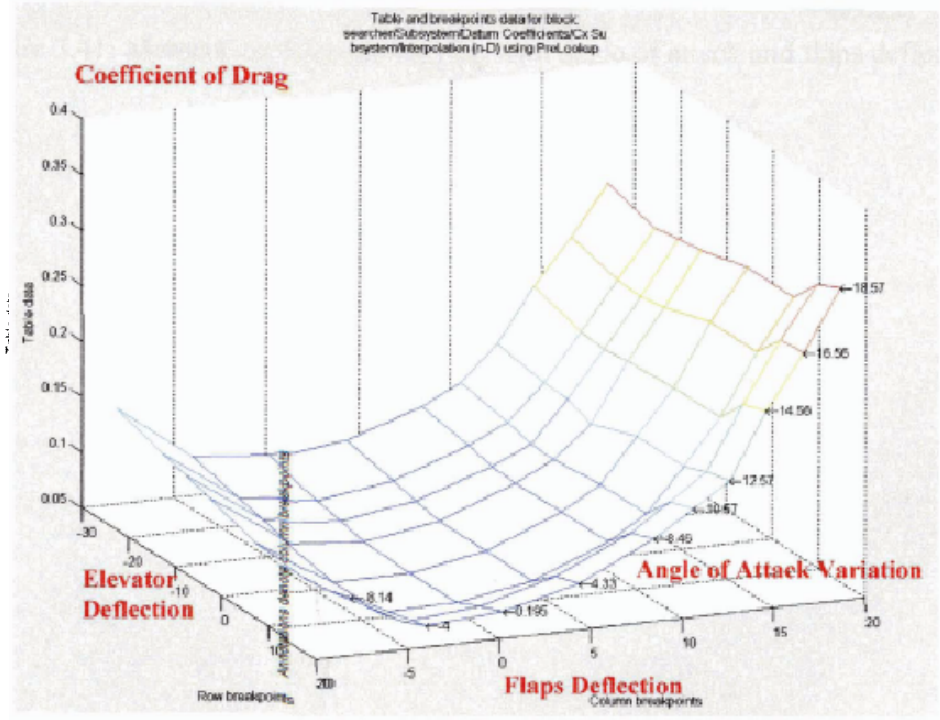

Figure 3.40: Drag coefficients varying with various angles of attack, flaps and elevator deflation

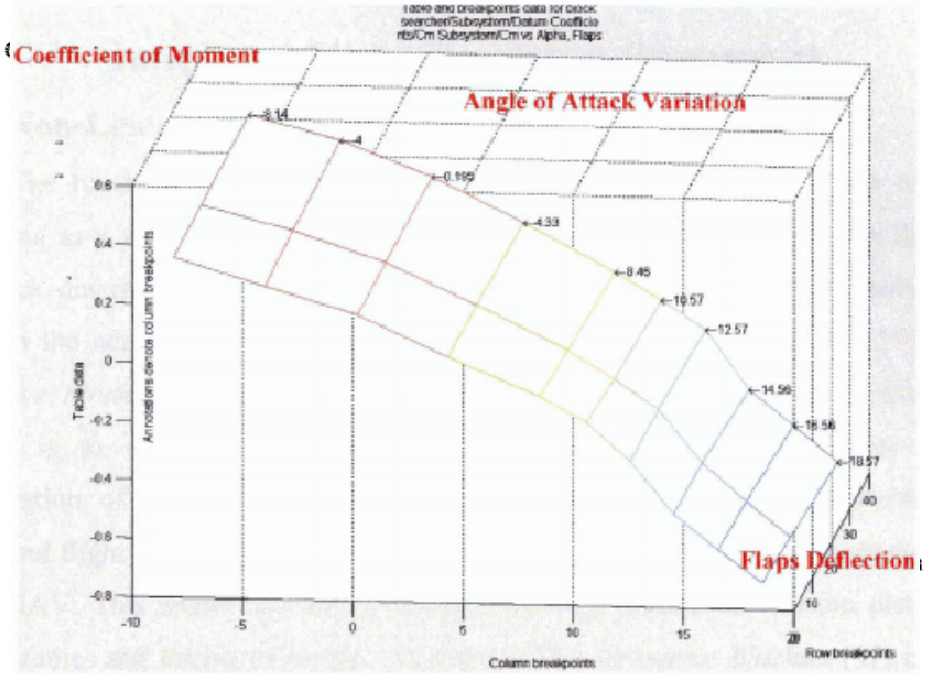

Figure 3.41: Moment coefficients varying with angle of attack and flaps deflection

Chapter 4

Integrated Flight Simulation Framework

4.1 Non-Linear Simulation

The block diagram simulator and graphical simulator to study the non-linear simulation as a verification of the linear simulation results are developed in this study. The block diagram simulator was built using the *Simulink*® [7] suite of software and based on the non-linear aircraft model developed in Chapter 2. *Simulink*® [7] and the *Aerospace Blockset* [17] are used for the modeling of the UAV aircraft model. The purpose is to create a modular simulation framework, which includes the full configuration of the UAV including the aerodynamic characteristics, environmental effects and flight controller, to assess and evaluate the stability and control characteristics of the UAV. This model can also be used as an experimental simulation platform for further studies and testing of control algorithms. The *Aerospace Blockset* [17] is used to rapidly assemble portion of the UAV system. The other portions like the calculation of aerodynamic coefficients were modeled in *Simulink* [7]. An alternative product is the *Aerosim Blockset* that sits on the *MATLAB*® [16] and *Simulink* [7] framework which provides components for rapid development of non-linear 6-DOF aircraft dynamic models. In addition to aircraft dynamics the Blockset also includes environment models such as standard atmosphere, wind disturbance, turbulence and Earth models. *Aerospace Blockset* [17] is designed as a generic library which contains blocks commonly used in aeronautical and space vehicle dynamics, guidance, and control. The library provides 49 blocks in total. As for the *AeroSim Blockset* [18], it is focused only on aircraft dynamics; there are no guidance or control blocks in the product. With more than 100 blocks, the *AeroSim Blockset* [18] goes into more detail on the subject of aircraft dynamics. Both blockset were used together to develop the UAV model in this study.

The advantage of the block diagram simulator over the graphical simulator lies in the structure. It gives good visual insight on how the complete aircraft model interacts with the other subsystems like the environmental blocks and flight controller. The block diagram also allows the user to manipulate and change the values of the various

components manually without a need to change any part of the code. The graphical simulator used the same non-linear flight dynamics equation as the block diagram simulator, but is written in an extensible markup language (XML) format in the *JSBSim* [35] framework which is written in C++ programming language and uses *FlightGear* [8] to visually display the aircraft as it moves through the virtual surroundings. The major advantage with this type of simulator lies in its visual interface. The interface allows for the real time interaction with the aircraft and for the autopilot to be visually scrutinized. In order to tap on the strengths of both the simulator, a third framework is built based on the block diagram simulator and tapping on the graphical simulator characteristics to give the users the opportunity to change the elements of the input real time to visual the effects of the changes and its impact on the UAV. Each of the three different types of simulators is discussed in more details with the emphasis on the specific implementation and the problems that it can solve.

4.1.1 Block Diagram Simulator

The UAV is modeled with several assumptions made. It is assumed that the airframe is rigid and has constant mass and centre of gravity. It is also assumed that the UAV is laterally symmetric, and the compressibility effects are neglected. The typical airframe model consists of a number of components such as, equations of motions, environment models and modules for the calculation of aerodynamic coefficients, forces and moments. A systematic analysis of the calculation process will be discussed in this section.

The UAV airframe consists of a total of six main blocks. They are as indicated in Figure 4.1 and the blocks are labeled as, six degree-of-freedom (Euler angles), environment block, angle of attack, sideslip angle and Mach No. block, aerodynamic coefficients block, force and moment block and thrust input block. The differential equations based on the Newton's law of motion are automatically calculated within the block based on the aerodynamic forces and moment inputs. The block automatically generates the aircraft velocity, altitude and attitude based on the Euler angles transformation definition.

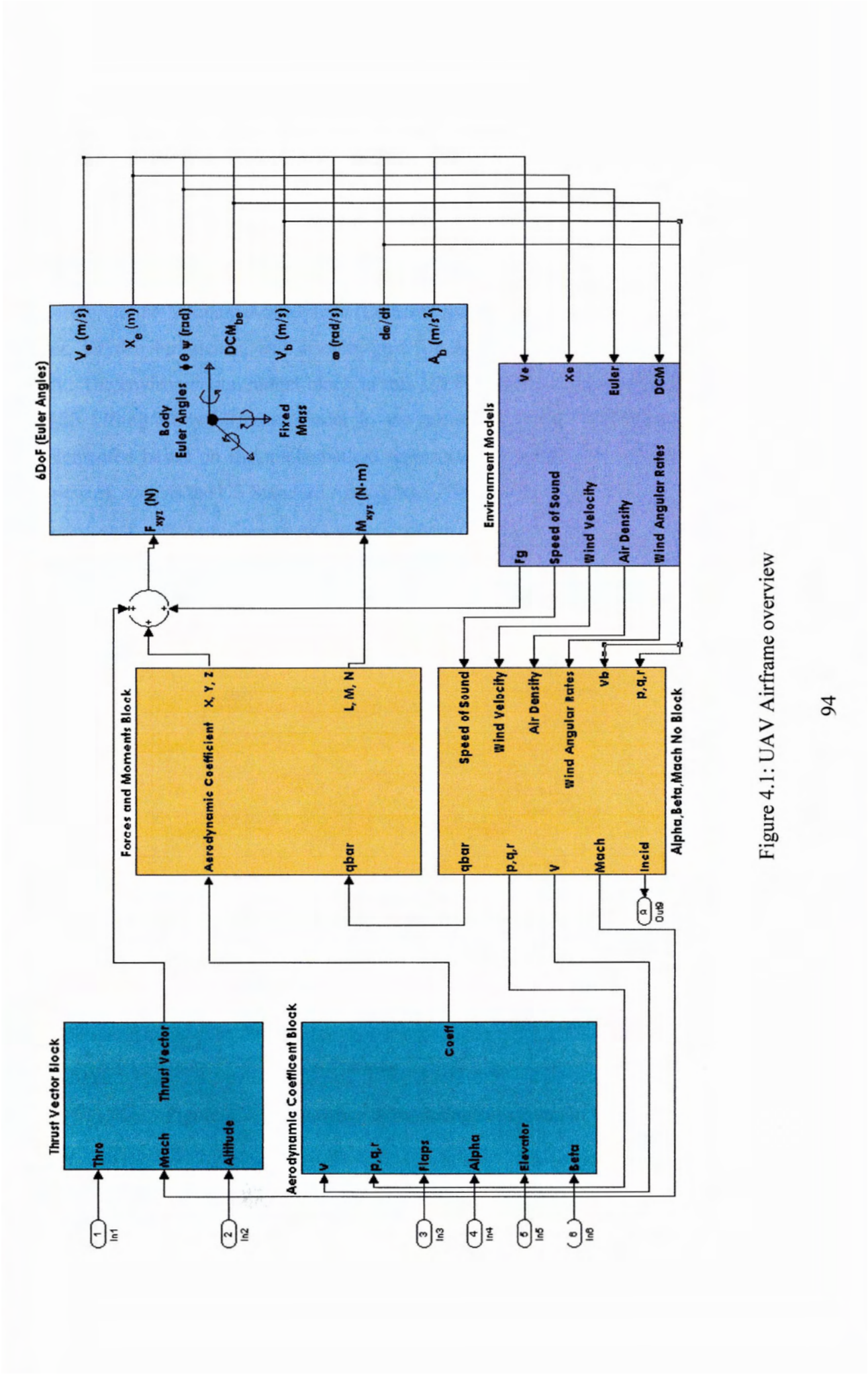

Figure 4.1: UAV Airframe overview

The next block as shown in Figure 4.2 used in the UAV system is the environment model. This model used the following subsystem available in *Aerospace Blockset* [17] to calculate the environment effects on the UAV during flight. It consist of the World Geotactic System of 1984 (WGS 84) for gravity calculation, Committee Extension to the Standard Atmosphere (COESA) model for data on the atmosphere, wind shear, Dryden turbulence, and discrete gust for the environmental wind effect on the UAV. The environmental model block in this UAV model was adapted from the NASA HL-20 Lifting Body airframe model in the article by Gage [34]. These models are implemented based on the mathematical representation within the standard references framework such as the US Standard Atmosphere, 1976.

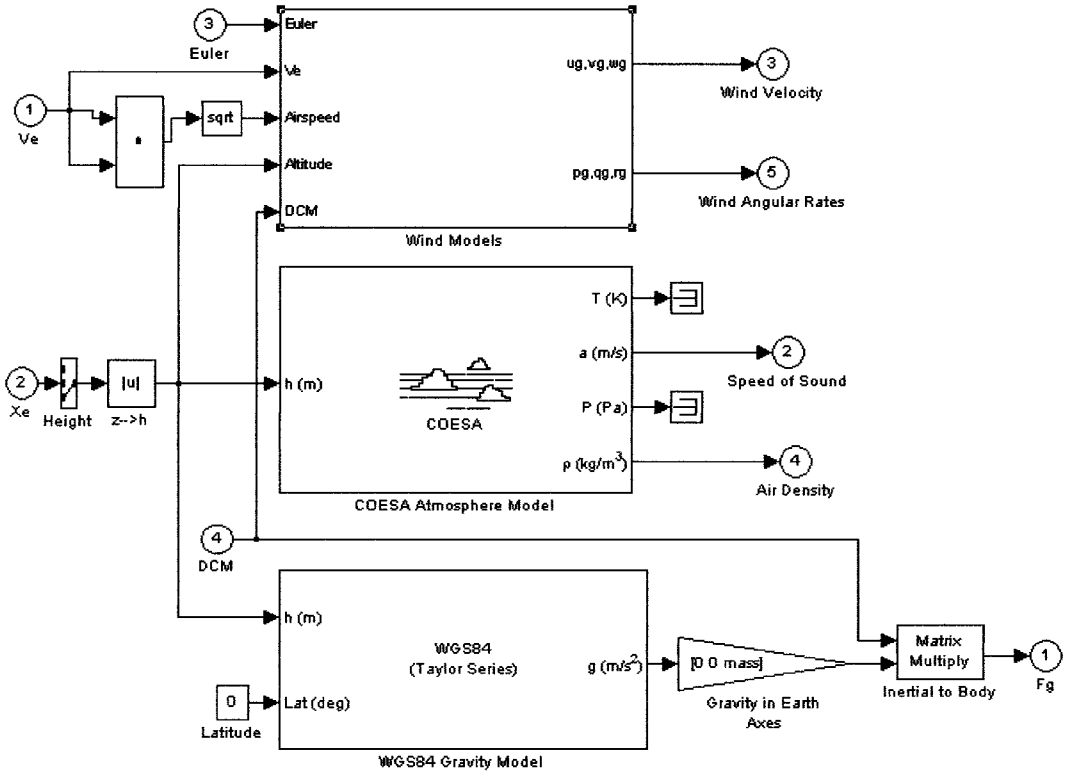

Figure 4.2: Environmental modeling subsystem in UAV

The next system shown in Figure 4.3 is the angle of attack, sideslip angle, Mach No. subsystem. This system includes the calculated parameter such as the dynamic

pressure that will be needed for the computation of the aerodynamic coefficients in a separate sub system. In addition to the calculation of the Mach No. and incidence angles based on the velocity calculated from the incidents, sideslip and airspeed blocks, the total velocity and dynamic pressure are also computed. The wind velocities from the environmental model and angular acceleration computed previously are added to the body velocity and body rates respectively.

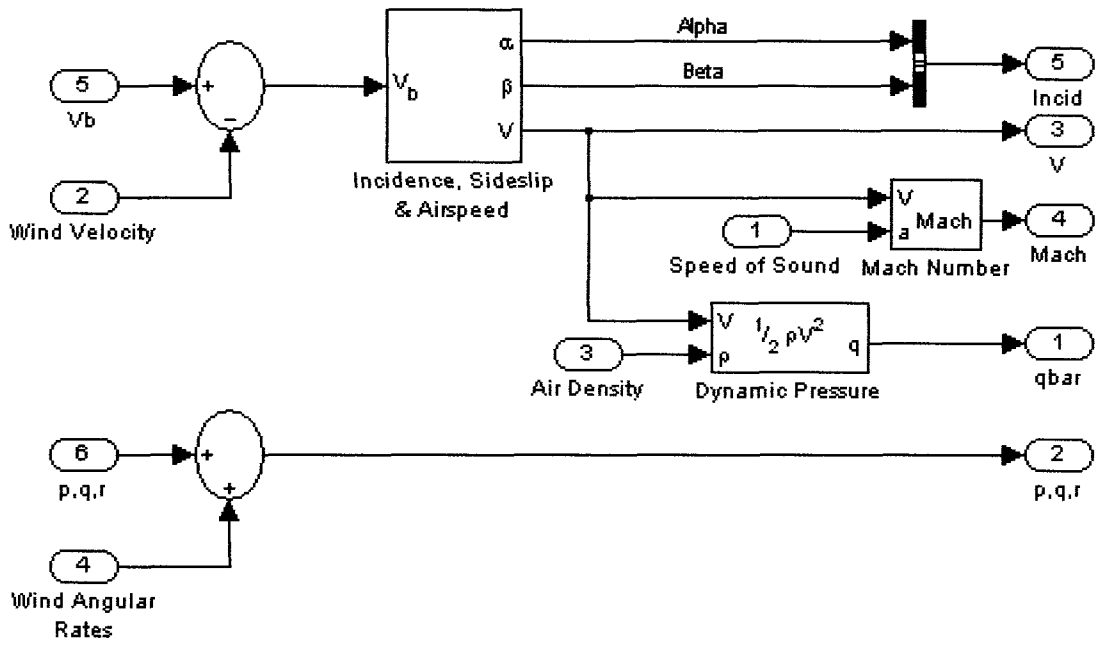

Figure 4.3: Angle of Attack, Sideslip angle and Mach No. subsystem

With this calculated data from this subsystem, the outputs are used to extract the aerodynamic coefficient data from the aerodynamic coefficient block. The equations for calculating the six aerodynamic coefficients are divided into two subsystems: static and dynamic derivatives of the UAV. The static derivative calculation subsystem is shown in Figure 4.4. It uses the inputs to obtain the static derivatives of the UAV. These are dependent on the incidence angles of the aircraft with respect to the axis. Since the data given in the database includes the control deflection, the author has placed them together in this system. Different control surface like the wing flaps, elevator and rudder deflections are the control surface input, and together with the angle of attack and sideslip

angle inputs, the aerodynamic characteristics are read off from the look up tables defined in the previous chapter. The dynamic derivatives are similarly retrieved in the dynamic derivative subsystem as shown in Figure 4.5.

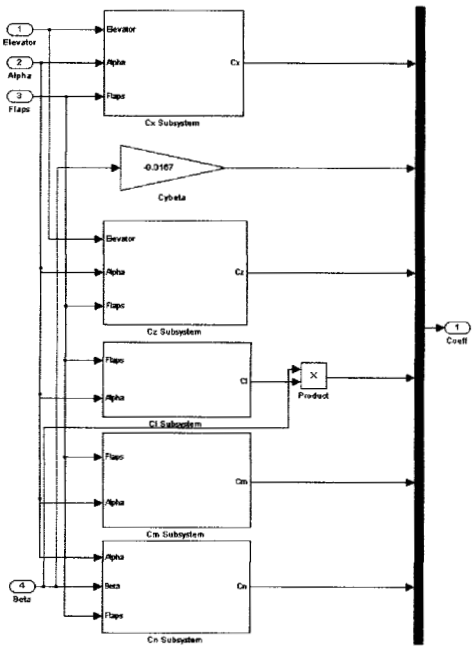

Figure 4.4: Static Stability Derivatives of the UAV

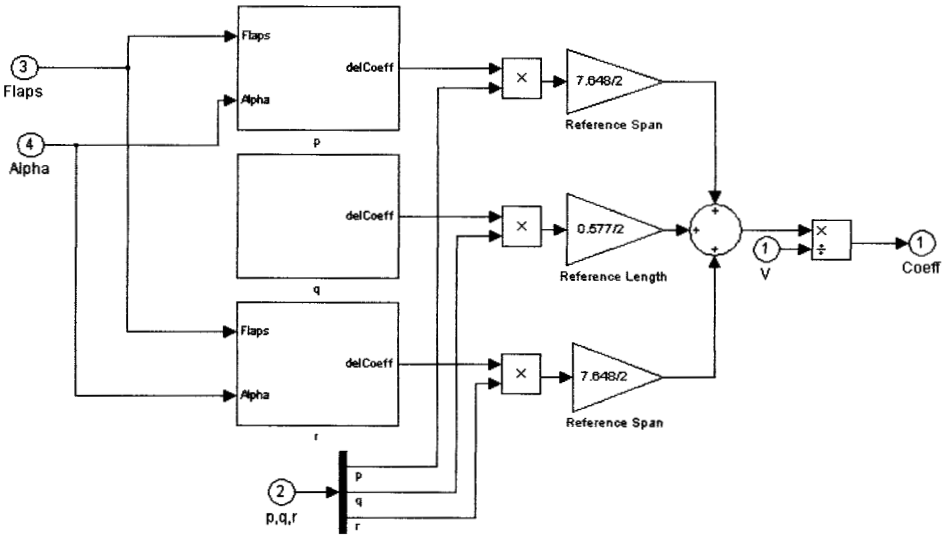

Figure 4.5: Dynamic Stability Derivatives of the UAV

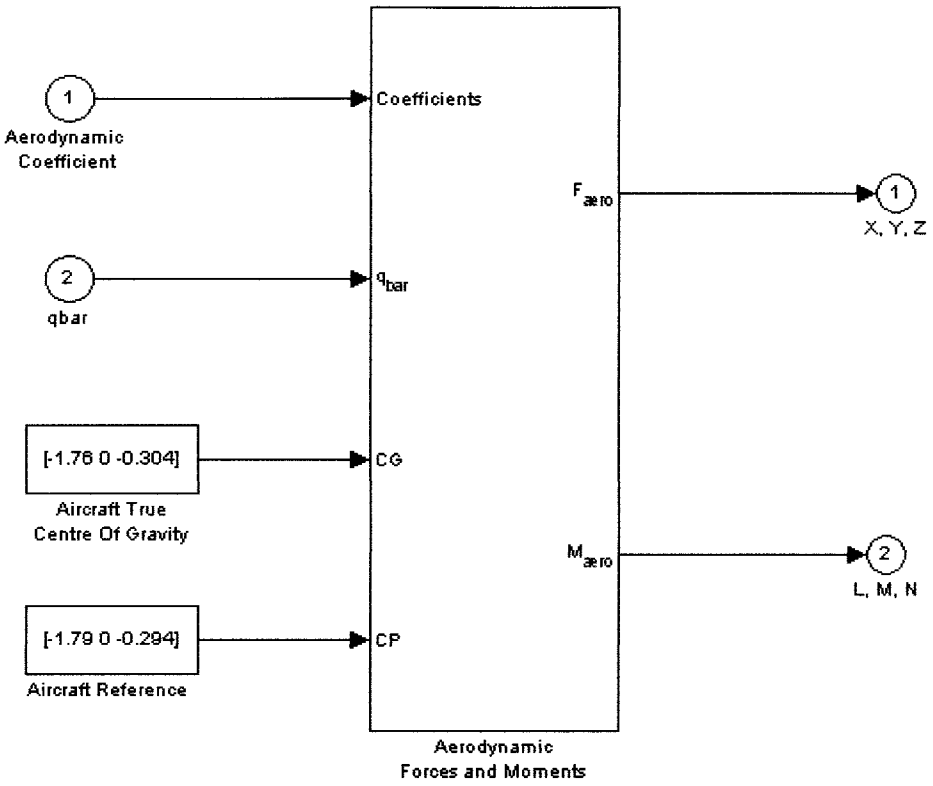

Figure 4.6: Aerodynamic Forces and Moments Block

Summing the static and dynamic stability derivatives, the author will get the six aerodynamic coefficients that are used to calculate the airframe forces and moments. The aerodynamic data are input into the force and moment block. This block will calculate the body forces and moments about the centre of gravity acting in the airframe. These forces and moments are dependent on the aerodynamic coefficients, thrust from the propulsion plant, dynamic pressure, and reference airframe parameters. The propulsion subsystem is shown in Figure 4.7. The thrust varies accordingly to the various conditions, i.e. the throttle, Mach No. and altitude. All this data are plotted in a table form for data retrieval, and this is shown in Figure 4.8.

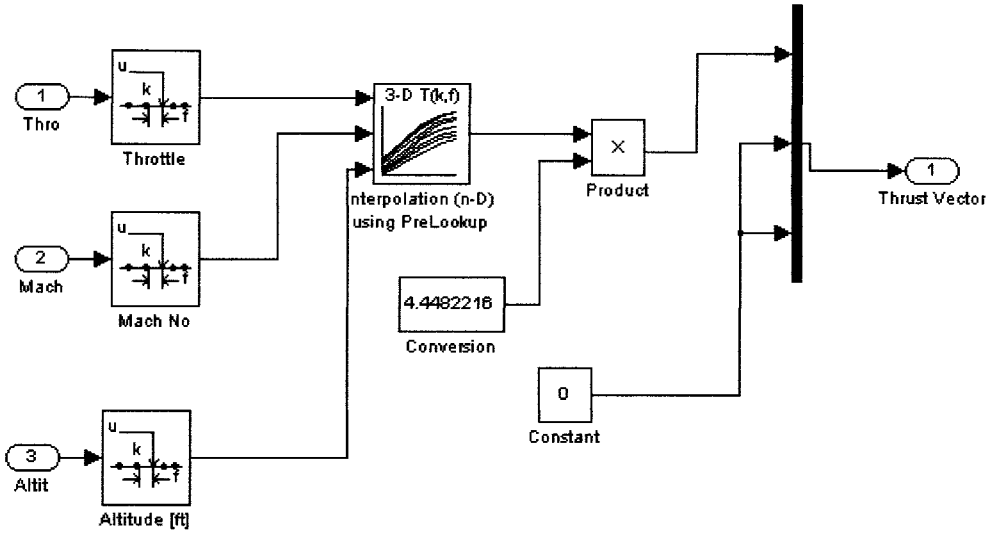

Figure 4.7: Propulsion System

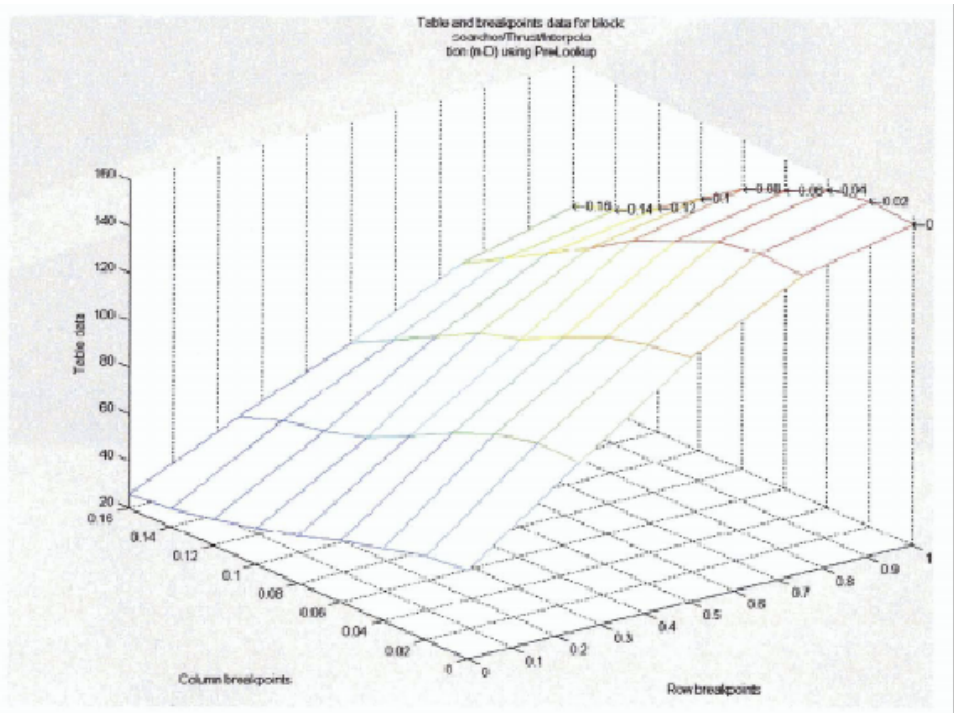

Figure 4.8: Thrust Variation with Throttle, Mach No. and Altitude

This model, which represents the UAV in the computer domain, is used as the heart of the simulation framework. By incorporating the flight controller to the simulation framework, the design of the flight controller for example a yaw damper or autonomous landing system can be analyzed and its effects can be evaluated. This simulation framework can be linked to a virtual reality environment via graphical representation to evaluate the UAV response when subjected to various disturbances. Figure 4.9 shows a screen shot of the UAV captured in a virtual reality backdrop.

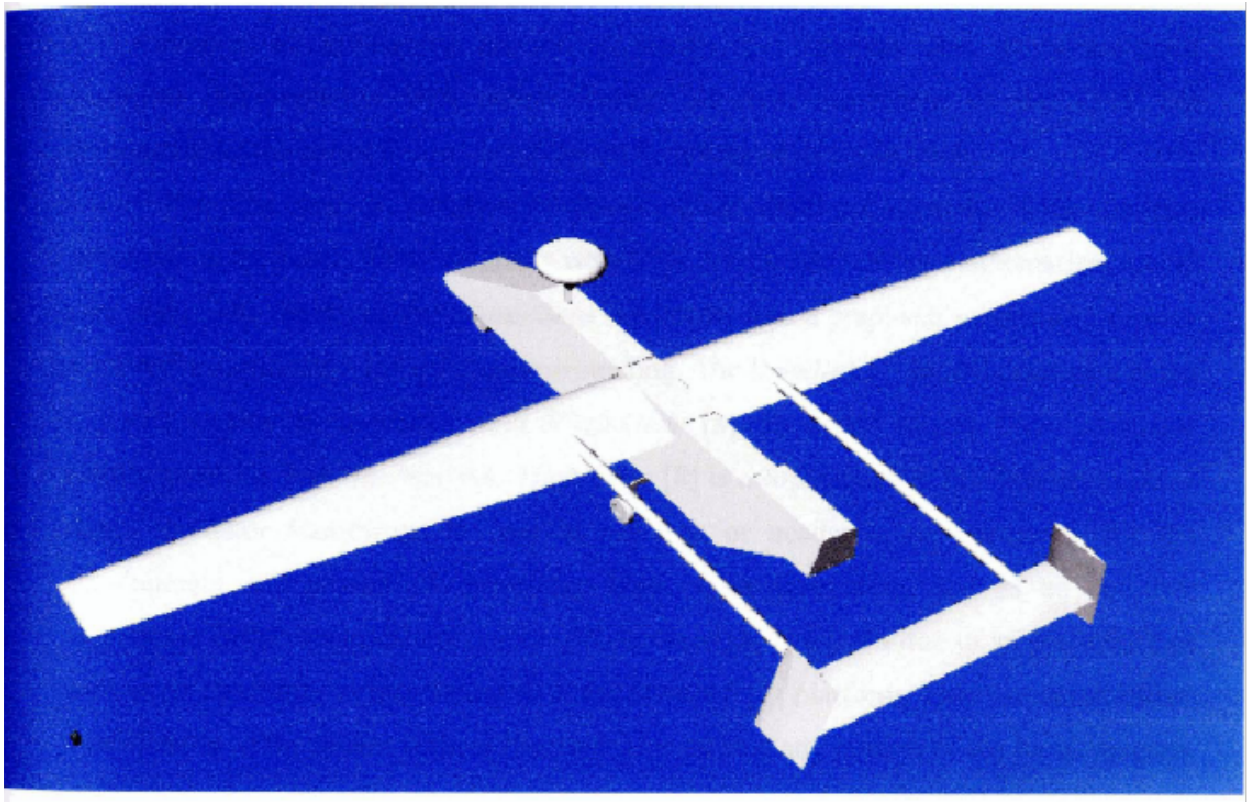

Figure 4.9: Overview of the UAV

4.1.2 Graphical Model

The graphical simulator developed in this study comprises two different types of variations. For both variations, the key advantage of the graphical simulator over the block diagram simulator is the interface. The interface makes it possible for the users to interact with the aircraft in real time. At the same time the responses will be presented in a graphical mode instead of the conventional graphs responses. The virtual world makes it possible for the users to operate the UAV from taking off to landing the UAV at the designated airport. This makes the simulator a very useful tool for further development and evaluation of autonomous controllers. Finally, the simulator also provides a good graphical representation with actual footage of each movement of the UAV for demonstrating the controllers at the different instances of its application.

The first type of variation of the graphical simulator uses the block diagram simulator as the heart of the simulator where the calculations of the mathematical model take place. The results of the calculations are output into a graphical platform to display the UAV's motion through a virtual surrounding. The *Simulink* [7] model discussed in the previous section is interfaced with *FlightGear* [8], an opens source flight simulator readily available from the internet. *FlightGear* [8] is a sophisticated, full-feature, desktop flight simulator framework for use in research or academic environments, for the development and pursuit of interesting flight simulation ideas, and as an end-user application for aeronautical enthusiast. *Flight Gear* [8] is chosen due to its portability as well as its flexibility in interfacing with the *Simulink* [7] platform. This simulator allows modification of the model without the need of re-coding any portion of the block diagram which represents the aircraft model. As the model is developed in a modular block diagram, it can be setup to allow real time changes to be inputted during the simulation process. However a disadvantage of this simulator is the amount of computer resources that it utilized. Two separate programs are needed to be run concurrently; thus it requires a powerful computer to run the simulator on a single platform. An alternative is to setup a network of computers to run the two programs in parallel on different stations to minimize the computer resources on each of the stations.

A screen shot of the UAV model with its scopes can be seen in Figure 4.10. This model shows a screen which represents the UAV at every instances of the simulation, and three smaller screens to represent the scopes of the data obtained from the mathematical calculations from the block diagram. The time histories of the airspeed, pitch angle and angle of attack are plotted real time as the simulation takes place. The model of the UAV in the graphical screen is represented through *FlightGear* [8]. It reciprocates the real time data obtained from the calculations from the block diagram. A sequential screen shot of the responses of the UAV at various instances of the simulation is shown in Figure 4.11. The UAV is cruising at 36 m/s at t=0 as shown in Figure 4.11 (a). A disturbance which represents a gust in the z-axis to simulate an upward wind disturbance is initiated. The UAV responses to the disturbance and through a sequence of damping effects and autopilot input reaction to the disturbances, the UAV regain its initial heading position and stabilize to return to its cruising position. Notice the similarity of the representation of the UAV in the history plot and graphical representation shown in the screen shots at the various time steps.

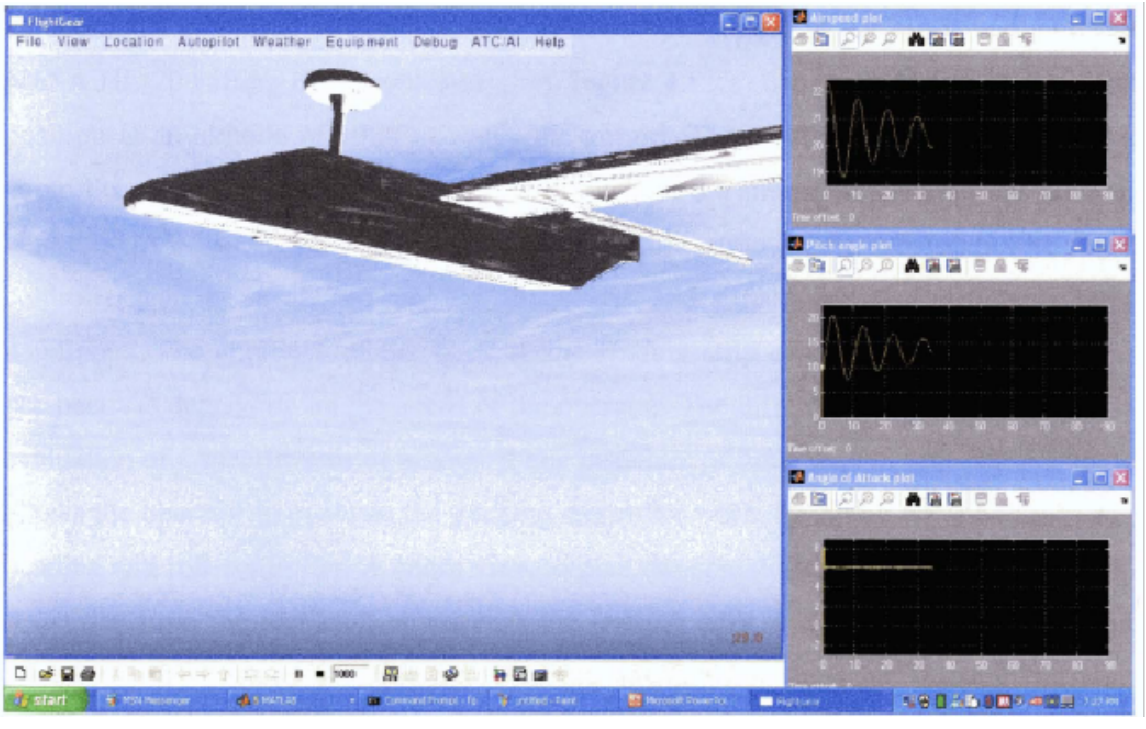

Figure 4.10: Flight Gear Screen shot with the real time readings

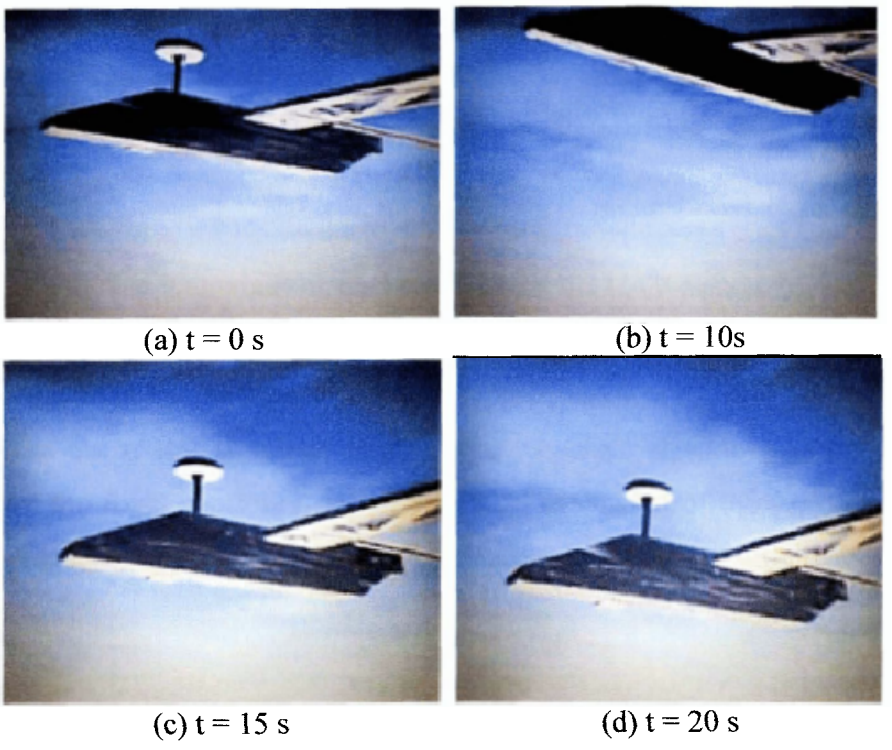

(a) t = 0 s (b) t = 10s

(c) t = 15 s (d) t = 20 s

Figure 4.11: Screen Shots of the UAV at different time frames during the simulation

Similarly using the same concept as the first variation of the graphical simulation, an automatic controller is developed for autonomous landing of the UAV based on the NASA HL-20 Lifting Body controller [34]. Figure 4.12(a) depicts the UAV in its initial position at an altitude of 1000 m above the airport. The controller is activated and the controller commands the UAV to react accordingly to the atmospheric conditions input to land the UAV. By varying the wind conditions in the atmospheric subsystem, the flight controller can be evaluated on the robustness and effectiveness at different flight conditions. The approach of the UAV to the landing strip can be viewed from various perspectives depending on the needs of the operator. The different perspectives allow the evaluation of a specific axis of motion at any instances of time, for example the side view allows the operator to evaluate the pitching controller while the chase view evaluates the heading and roll controller. A chase view to give the operator a perspective of the UAV responses from the rear as it approaches the landing strip in the airport can be seen in Figure 4.12(b). Figures 4.13 (a) and (b) depict the UAV in the same instance but with different perspective, one from the side view to evaluate the pitching effects and the other

from the cockpit view to evaluate the heading and rolling responses. The video extract of this simulation can be found in the CD-ROM clip title Autonomous Landing. The cockpit view can be offset depending on the position of the pilot or in this case, depending on where the operators want to place the "eyes" on the UAV. It can be modeled to be placed at the payload which is at the belly of the UAV or from the front of the UAV. As the UAV approaches the landing strip, the UAV orientation can be viewed from the back in Figure 4.14(a) or from the side perspective as shown from the screen capture in Figure 4.14(b). With this graphical representation in the simulation framework, engineers can utilize this simulator to study the responses at various gust disturbances and approve the flight controller design based on evaluation of the various simulation case studies implemented.

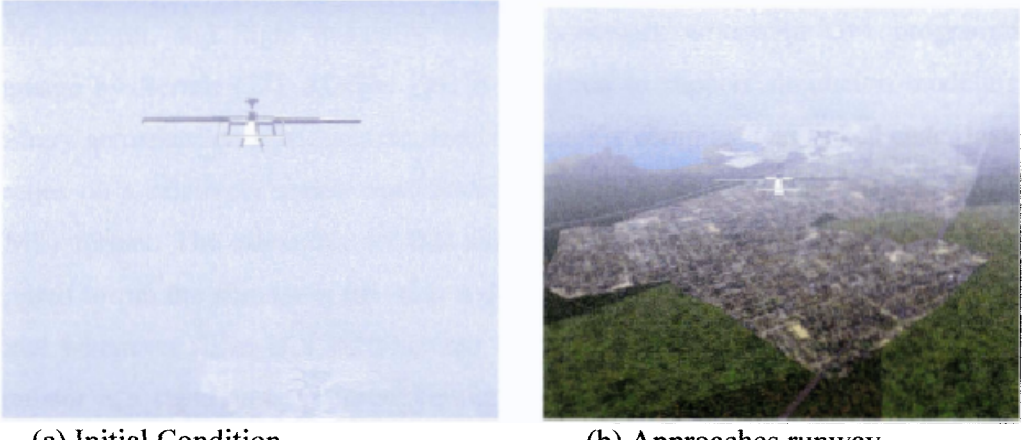

(a) Initial Condition (b) Approaches runway

Figure 4.12: Screenshot of UAV as controller is activated (in graphical simulator)

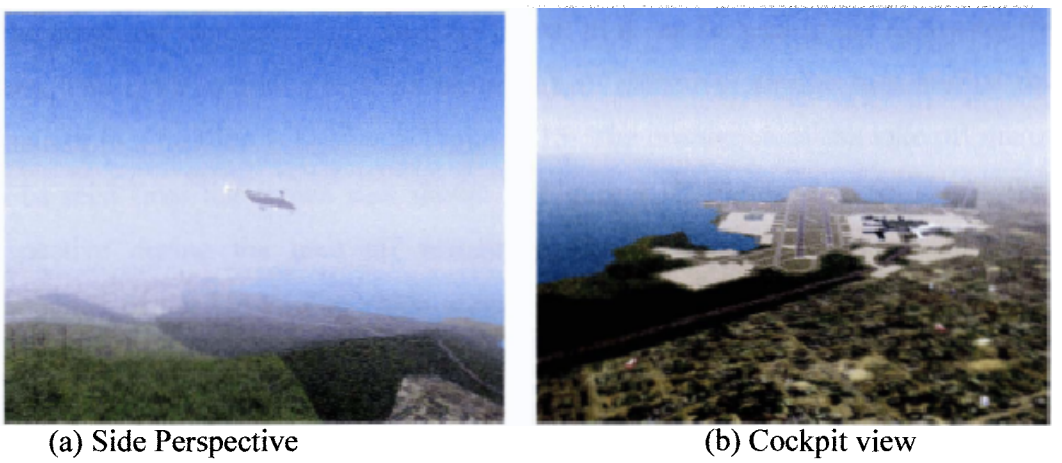

(a) Side Perspective (b) Cockpit view

Figure 4.13: Various perspective of the UAV orientation during approach

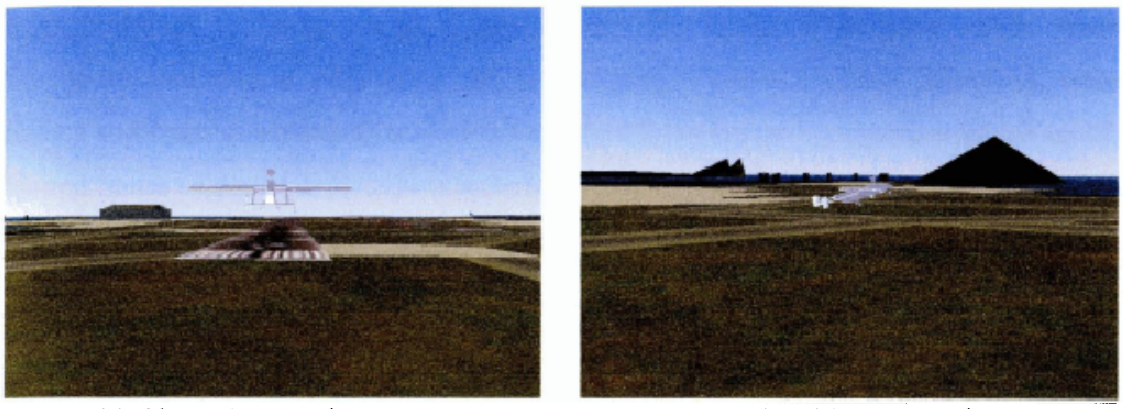

(a) Chase Perspective (b) Side Perspective

Figure 4.14: Various view of the UAV prior to landing

In the second variation of the graphical simulator, the internal aircraft model is modeled similar to the block diagram simulator but coded in *JSBSim* [35], an open source, multi-platform, and flight dynamics model framework written in C++ programming language by Berndt [37]. *JSBSim* [35] is designed to support simulation modeling of arbitrary aerospace craft without the need for specific compiled and linked code. Instead, it relies on a relatively simple specification written in an extensible markup language (XML) format. The advantage of this simulator is the amount of computer resources required to run the simulator, however a disadvantage is the need to re-code the aircraft model whenever there is a modification made to the aircraft systems. This graphical simulator is a stand alone program similar to the computer games like *Microsoft Flight Simulator X* [36]. It allows the user to utilize keyboard to control the aircraft or stick input to represent the actual controller of the UAV. Some screen shots of this variation of the graphical simulator with the UAV flown in it can be seen in the following figures below. The UAV is flown in a commanded turn maneuver similar to a normal routine maneuver in a mission is shown in Figure 4.15. The evaluation of the take off maneuver can be seen from the screen shot shown in Figure 4.16. Figure 4.16 (a) shows the side perspective during the take off maneuver while Figure 4.16 (b) shows the front perspective of the UAV. The video extract of this simulation can be found in the CD-ROM clip title Take-off. The UAV is flown in a 3-D world, where bridges and buildings can be modeled to depict the original environment. Depending on the availability of the graphical models of the surroundings, the 3-D world can be modeled to minor details

from buildings to bridges with a city setting. The current data base which covers Singapore available in *FlightGear* [8] is currently limited to merely grassland, water bodies and basic structures as shown in Figure 4.16. However the database which covers United States of America is quite comprehensive as shown in Figure 4.17, thus most case studies done in this study are completed against the United States of America backdrop.

Figure 4.15: UAV in a turning maneuver as commanded through an external pilot

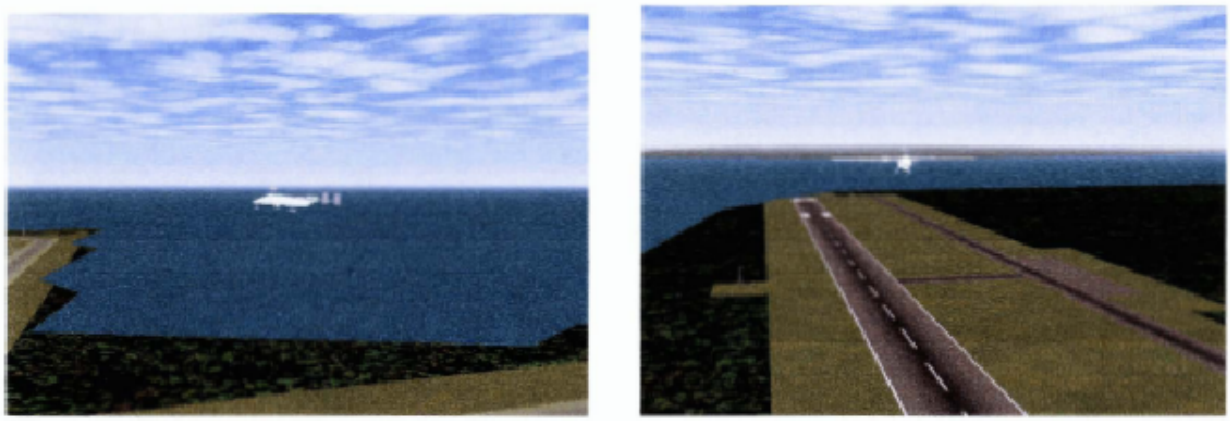

(a) Side Perspective (b) Front Perspective

Figure 4.16: Various perspective of the UAV taking off from the airport

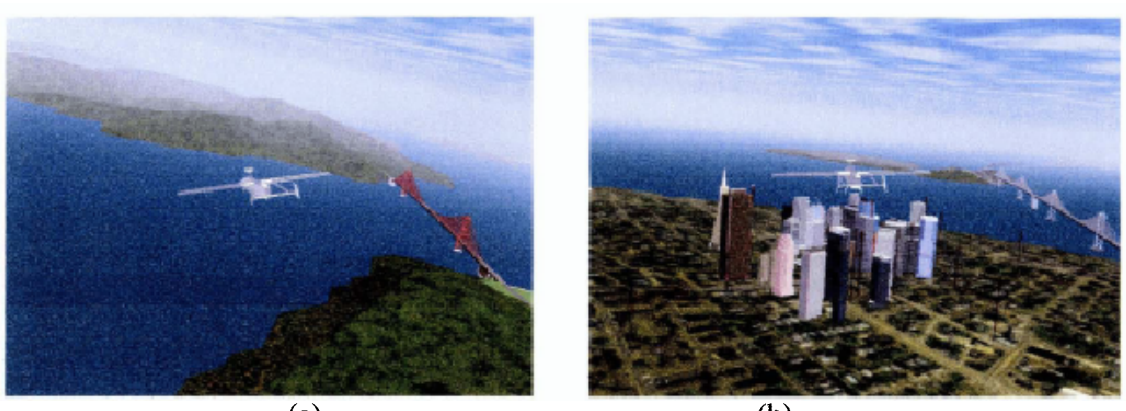

(a) (b)

Figure 4.17: UAV flying in a 3-D virtual world background

By incorporating all the data obtained from the aerodynamic study, the complete system can be tested via this graphical and modular simulation framework to simulate the results of the flight controllers developed. The data can be visually scrutinized through the incorporation of the flight model in *FlightGear* [8]. Moreover with the modular simulation framework, modification of the UAV system can be developed and completed quickly and effectively. The whole process depending on the modification of the systems can be completed within a shorter frame of time in comparison to experimental study.

Chapter 5
Results and Discussion

5.1 De-Coupled Open Loop Response of the UAV

The equations of motion for an aircraft are nonlinear and fully coupled. In general, because of these nonlinearities, no closed form solution exists and a steady state solution can be found by using a numerical method. Therefore, many researchers simplify these equations when accomplishing a preliminary flight control system design. Two basic techniques for the simplification of the nonlinear, fully coupled equations of motions are linearization and decoupling. They may be applied individually or simultaneously. Decoupling may be applied on the state variable or on the aerodynamic forces. The linearized equations of motion are valid only for small perturbation about the reference trim condition i.e. when the perturbed motion is very close to the steady state motion of the trim conditions. Decoupling is also valid when the interaction between the longitudinal motion and lateral-directional motion is small.

In the conventional aircraft flight mechanics analysis, the six degree-of-freedom (6 DOF) rigid body equations of motion are commonly linearized using small disturbance theory. Based on this theory, the lateral equations of motions are uncoupled from the longitudinal equations of motion as a result of imposing the small disturbance approximation whereby assumptions are made to eliminate any interaction between the longitudinal and lateral axis. However in the actual response of a rigid aircraft to a finite lateral disturbance, it involves all 6 DOF. Furthermore, inertia and gyroscopic effects can produce coupling between the lateral and longitudinal equations, even in the framework of small disturbance theory. Inertial coupling occurs whenever the aircraft's mass is not completely asymmetrical about the x-z plane and the so called gyroscopic coupling occurs as a result of any net angular momentum associated with rotor spinning relative to the body-fixed coordinate system. Aircraft asymmetry can also give rise to the aerodynamic coupling because aerodynamic derivatives such as $C_{l,\alpha}, C_{n,\alpha}$, and $C_{m,\beta}$ can become non-zero. The occurrence of such first order coupling between the

longitudinal and lateral DOF is not unusual. In this second section the author will look at the de-coupled modes first prior to the investigation of the coupled model.

The equations of motion with the stability derivatives representation have been formed in chapter two under the assumption of small disturbance theory. The equations are decoupled based on the assumption that the interaction of the longitudinal motion and lateral-directional motion is small. To automate the process of calculating the linear model for the UAV, the *Matlab*® [16] program utilized the aircraft's physical parameters and trim conditions to calculate the desired longitudinal and lateral models and represent them in the state space format. All the data used in this chapter is based on the trim flight velocity of 36m/s, and the stability derivatives are defined in Appendix A.

The longitudinal and lateral aircraft models, specific to the UAV, are presented and analyzed in detail using the modal decomposition techniques. Modal decomposition involves using an eigenvector transformation matrix to convert the current system model to model form. This representation provides maximum insight into the aircraft's natural modes of motion. The detail summary of the theory of modal decomposition is presented in Appendix C. The information developed in the first section based on the decoupled equation of motion is used to verify the aircraft model develops as well as to assist in the design of an effective controller in the later chapter.

5.1.1 Longitudinal Aircraft Model

The longitudinal model can be written as,

$$\dot{X} = AX + BU \tag{5.1}$$

where

$$X = \begin{bmatrix} u \\ \Delta\alpha \\ q \\ \Delta\theta \end{bmatrix} \quad A = \begin{bmatrix} -0.0812 & 0.0214 & 0 & -9.81 \\ -0.4978 & -2.1367 & 36 & 0 \\ 0.0223 & -0.0202 & -3.078 & 0 \\ 0 & 0 & 1 & 0 \end{bmatrix} \quad B = \begin{bmatrix} 0 & 1 \\ -1.1704 & 0 \\ -0.0247 & 0 \\ 0 & 0 \end{bmatrix}$$

The state vector $\boldsymbol{X}$ and control input vector $\boldsymbol{U}$ are defined in the previous chapter respectively. The attitude, longitudinal position errors and throttle states have not been

augmented to the longitudinal state space of equation (5.1), because their dynamics are trivial and only complicate the analysis of the core longitudinal dynamics.

The units of u are in meters per second (m/s), $\Delta\alpha$, $\Delta\theta$ and δe are in degrees (deg), q in degrees per second (deg/s), and δ_t in specific force (m/s^2). The units were chosen such that one unit has roughly the same physical significance to the aircraft motion.[30] There are a few approaches to choosing units that produce well scaled variables. A maximum deviation approach was adopted in this study. This approach involves comparing the maximum deviation of each motion and control variables from the trim conditions, and then setting the units of each variable such that their maximum deviations are of a similar magnitude.

The maximum deviations of the variables in the longitudinal state vector are discussed in Table 5.1 and the maximum allowed control deflections are listed in Table 5.2. The tables define the maximum values that the model is valid under the small disturbance theory. Beyond this boundary condition, other methods are required to obtain a better representation of the dynamic response.

Table 5.1: Longitudinal State Vector Maximum Derivatives

Variable	**Description**	**Max**	**Units**
u	With a trim velocity of 36m/s, it is estimated that the maximum deviation from this trim condition will be approximately 10m/s	10	m/s
α	At the trim velocity of 36m/s, the maximum stalling angle of attack is defined at 12 deg, thus the maximum deflection will be defined at 12 deg.	12	deg
q	The maximum pitch rate disturbance during conventional flight is estimated to be 20 deg/s	20	deg/s
θ	The maximum pitch angle deviation during conventional flight is estimated to be 15 deg	15	deg

Table 5.2 Longitudinal Control Vector Maximum Deflections

Variable	Description	Max	Units
δ_e	The maximum elevator deflection is limited to 10 deg	10	deg
δ_T	From the engine database, the maximum specific force deviation is 5m/s^2	5	m/s^2

With the values of the longitudinal state space variables defined and calculated, the focus turns to gaining insight into the natural motions of the longitudinal state space system. This is done using the modal decomposition techniques. The modal transformation matrix that converts the system of equation (5.1) to modal form is shown below,

$$\begin{bmatrix} u \\ \Delta\alpha \\ q \\ \Delta\theta \end{bmatrix} = \begin{bmatrix} 0.9945 & 0 & -0.0212 & 0.0159 \\ -0.1003 & 0.0009 & -0.9993 & 0 \\ 0.0079 & -0.0007 & 0.0131 & -0.0194 \\ -0.0055 & -0.0280 & -0.0065 & 0.0056 \end{bmatrix} \begin{bmatrix} z_{l_1} \\ z_{l_2} \\ z_{l_3} \\ z_{l_4} \end{bmatrix} \tag{5.2}$$

where the original state vector is shown on the left and the corresponding modal state vector on the right. The modal transformation matrix has the real and imaginary parts of each eigenvector as its columns. Transforming the longitudinal state space model of equation (5.1) reveals,

$$\dot{z}_l = F_l z_l + G u_l \tag{5.3}$$

where,

$$z_l = \begin{bmatrix} z_{l_1} & z_{l_2} & z_{l_3} & z_{l_4} \end{bmatrix}^T$$

$$F_l = \begin{bmatrix} -0.0288 & 0.2759 & 0 & 0 \\ -0.2759 & -0.0288 & 0 & 0 \\ 0 & 0 & -2.6191 & 0.7065 \\ 0 & 0 & -0.7065 & -2.6191 \end{bmatrix} \qquad G_l = \begin{bmatrix} -0.0079 & 0.9979 \\ 0.1433 & -0.1049 \\ 1.1721 & -0.1002 \\ 2.0569 & 0.3415 \end{bmatrix}$$

The longitudinal system matrix in modal form clearly shows the two sets of complex poles that define the natural modes of the primary longitudinal system. The

higher frequency pole set is known as the short period mode while the lower frequency set is know as the phugoid mode. Each of these modes is now discussed in more detail with specific focus on the shapes and the relative control of the longitudinal actuators over each mode.

5.1.1.1 Phugoid Mode

The phugoid mode poles are summarized below,

$$\lambda = -0.0288 \pm 0.276i \tag{5.4}$$

$$\varsigma = 0.104 \tag{5.5}$$

$$w_n = 0.277 rad/s \tag{5.6}$$

These poles form a stable, low frequency, lightly damped oscillatory mode with an exponential decay of approximately 34.7s. The eigenvector corresponding to the phugoid mode is displayed in phasor form below,

$$\begin{bmatrix} u \\ \Delta\alpha \\ q \\ \Delta\theta \end{bmatrix} = \begin{bmatrix} 0.9945\angle 0 \\ 0.1003\angle -0.5 \\ 0.0079\angle -5.1 \\ 0.0285\angle 78.0 \end{bmatrix} \tag{5.7}$$

where the phasor angles are shown in degrees. The eigenvector indicates that the magnitude and phase contribution of each element of the original state vector to the specific mode of motion. From the vector, it can be seen that the mode is dominated by the change in axial velocity with very small changes in the pitch rate.

The phugoid mode can be visualized as a sinusoidal exchange of the aircraft's potential and kinetic energy, damped by the aerodynamic drag. Consider a disturbance that leaves the aircraft with a negative pitch angle, flying slightly downwards, as the aircraft moves downwards it builds speed, which at constant angle of attack, translate directly into an increased in lift. The eigenvector shows that the change in airspeed leads to a change in the pitch angle by approximately 78° which means that the speed is a

maximum around the lowest point of the motion. The kinetic energy then carries the aircraft up to the next peak and the motion continues in a sinusoidal fashion.

A time history response of pure phugoid mode motion, obtained by initializing the system state vector with the real parts of the phugoid mode eigenvector, is plotted in Figure 5.1. It is clear from the plot that the phugoid mode motion is well observed in the axial velocity and angle of attack.

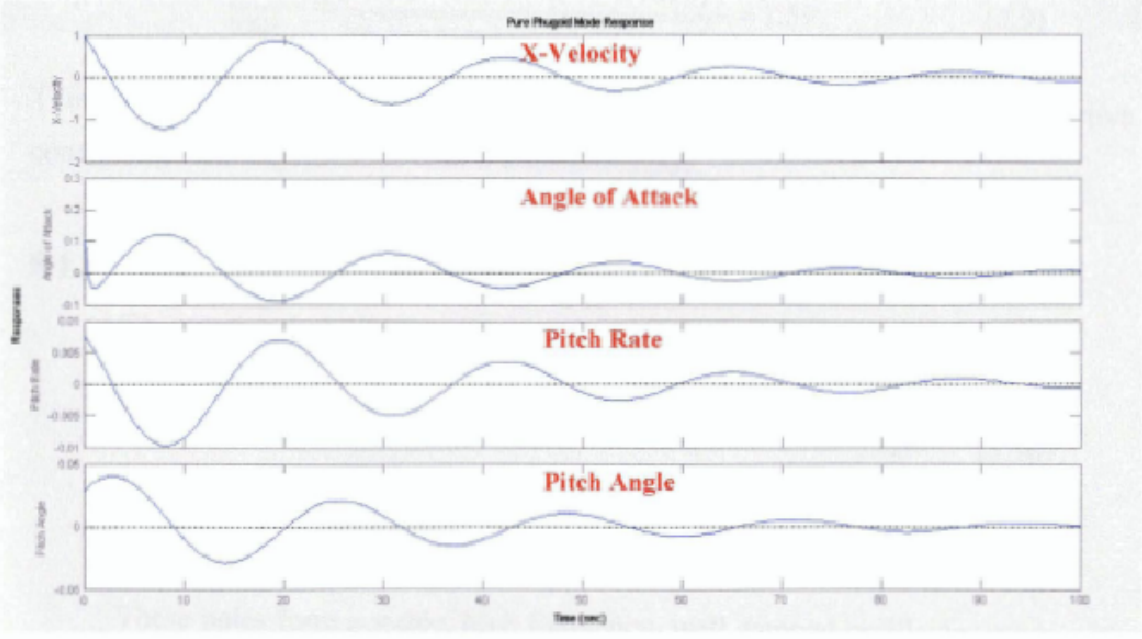

Figure 5.1: Pure Phugoid Mode Response

An extract of the lateral modal input matrix (G_t) of equation (5.3), pertinent to the phugoid mode, is shown below,

$$G_{t_{ph}} = \begin{bmatrix} -0.0079 & 0.9979 \\ 0.1433 & -0.1049 \end{bmatrix} \tag{5.8}$$

The magnitude of the first column vector of G_{tph} indicates the control gain from the elevator to the phugoid mode states. Similarly, the magnitude of the second column vector indicates the control gain from the throttle to the phugoid modes states. Before the magnitudes of the columns can be directly compared, the values of G_{tph} must be scaled such that the elevator and throttle states have units of full scale deflection. The elevator and throttle full scale deflection quantities are listed in Table 5.2. Although the current

elevator and throttle units are reasonably well scaled for a relative analysis, the scaling is still carried out because, unlike the state vector maximum deviations, the actuator maximum deflections are user defined values set within the capabilities of the actuator. Thus, the accuracy of the analysis is improved by carrying out the scaling. Calculating the relative magnitude of the scaled columns of G_{tph} gives,

$$\frac{Elv}{Thr} = \frac{\sqrt{(-0.0079x10)^2 + (0.1433x10)^2}}{\sqrt{(0.1433x5)^2 + (-0.1049x5)^2}} = 1.59 \qquad (5.9)$$

This result indicates that the elevator is approximately 1.6 times more effective at controlling the phugoid mode than the throttle mode.

5.1.1.2 Short Period Mode

The short period modes poles are summarized below,

$$\lambda = -2.26 \pm 0.707i \qquad (5.10)$$

$$\varsigma = 0.965 \qquad (5.11)$$

$$w_n = 2.71 rad/s \qquad (5.12)$$

These poles form a stable, high frequency, well damped oscillatory mode with an exponential decay of 0.44s. The short period mode eigenvector is displayed in phasor form below,

$$\begin{bmatrix} u \\ \Delta\alpha \\ q \\ \Delta\theta \end{bmatrix} = \begin{bmatrix} 0.0265\angle -41.86 \\ 0.9930\angle 180 \\ 0.0234\angle -55.97 \\ 0.0086\angle -40.74 \end{bmatrix} \qquad (5.13)$$

The eigenvector indicates that the mode is observed mainly in the angle of attack with smaller corresponding changes to the axial velocity and pitch rate. The short period mode can be compared to the torsional mass spring damper system, where the aircraft is restrained about the O-Y axis. During a disturbance the aircraft plays the major role in producing the spring and damper forces. The spring effect arises from the natural weathercock tendency of the aircraft to align itself with the incident flow. This effect is

quantified by the pitching moment due to the normal velocity disturbance derivatives (C_{Mw}). The damping is due to the induced angle of incidence on the aircraft as it oscillates through the oncoming airflow. This effect is quantified by the pitch rate damping stability derivatives (C_{Mq}).The large component of the tail in this study explains the good natural damping of the short period mode.

A time history plot of the pure short period mode motion is shown in Figure 5.2, where the longitudinal system (5.1) has been initialized with the real part of the short period mode eigenvector.

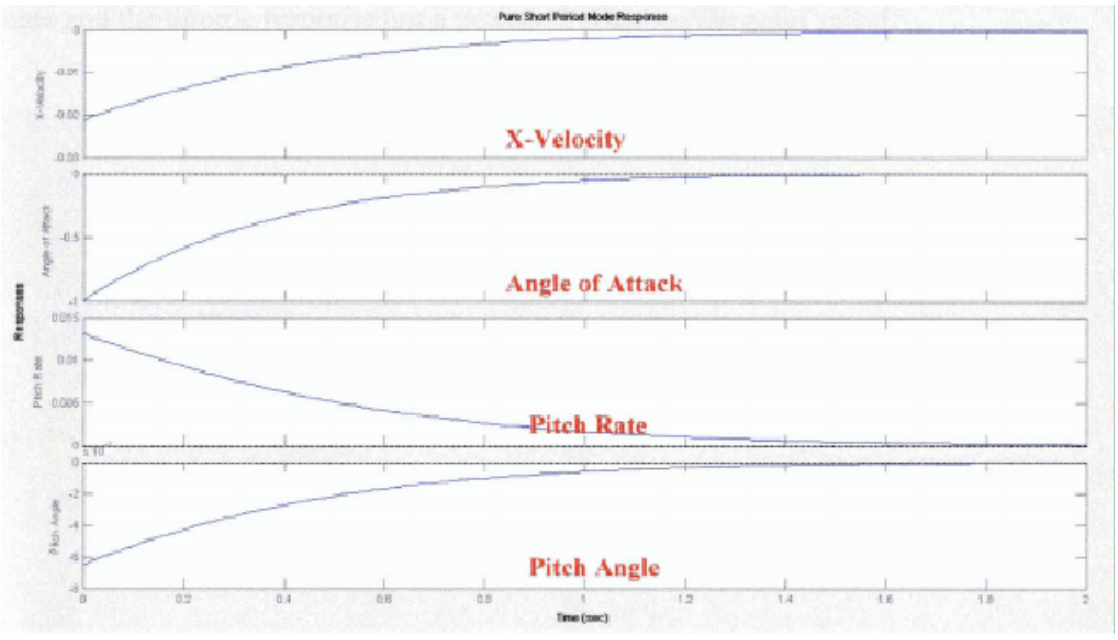

Figure 5.2: Pure Short Period Mode Responses

An extract of the lateral modal input matrix (G_t) of equation (5.3), pertinent to the short period mode, is shown below,

$$G_{t_{sp}} = \begin{bmatrix} 1.1721 & -0.1002 \\ 2.0569 & 0.3415 \end{bmatrix} \tag{5.14}$$

Continuing in a similar fashion to the analysis of the phugoid mode input matrix, the calculation of the relative magnitudes of the local scaled columns of G_{tsp} gives,

$$\frac{Elv}{Thr} = \frac{\sqrt{(1.172x10)^2 + (2.056x10)^2}}{\sqrt{(2.0569x5)^2 + (0.3415x5)^2}} = 2.26 \tag{5.15}$$

The above results make it clear that the short period mode is 2.26 times better controlled by the elevator than the throttle.

A time history response of the longitudinal state space system was obtained by initializing the system state vector with the real parts of the control eigenvector is plotted in Figure 5.3. The impulse input, which is indicative of the change in the respective control surface, can be used to analyze its effects on the on the axial velocity, angle of attack, pitch angle and rate when subjected to changes. From the plots, it can be seen that the inputs are generally stable and the elevator control surface has an effect on the pitch angle and the throttle response has a profound effect on the axial velocity.

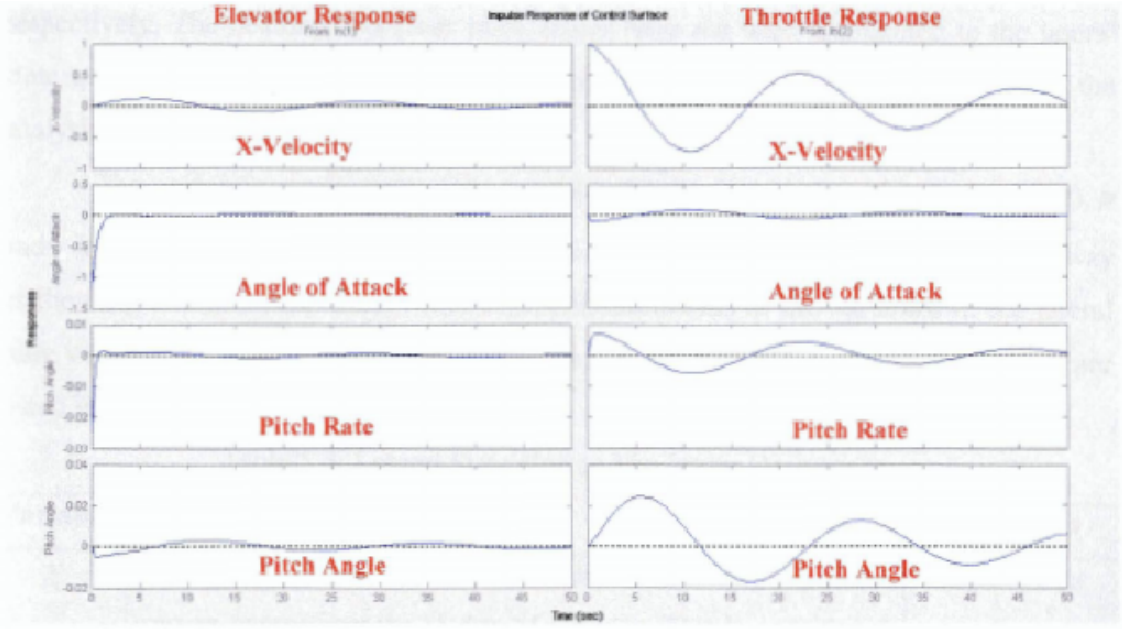

Figure 5.3: Impulse Response of the Control Surfaces on UAV

5.1.2 Lateral Aircraft Model

The lateral model can be written as,

$$\dot{X} = AX + BU \tag{5.16}$$

where

$$X = \begin{bmatrix} v \\ p \\ r \\ \phi \end{bmatrix} \quad A = \begin{bmatrix} -0.210 & 0 & -1.000 & 0.327 \\ -15.11 & -8.400 & 3.18 & 0 \\ 3.611 & -0.411 & -0.821 & 0 \\ 0 & 1 & 0 & 0 \end{bmatrix} \quad B = \begin{bmatrix} 0 & 0.04 \\ 20.06 & -4.5 \\ -0.076 & -2.27 \\ 0 & 0 \end{bmatrix}$$

The state vector $\boldsymbol{X}$ and control input vector $\boldsymbol{U}$ are defined in the previous chapter respectively. The heading and cross track errors have not been augmented to the lateral state space of equation (5.16), because their dynamics are trivial and only complicate the analysis of the core lateral dynamics.

The units of v are in meters per second (m/s), ϕ, δ_a and δ_r are in degrees (deg), p and r in degrees per second (deg/s). The lateral mode units were chosen in the same way as the longitudinal model units. The maximum deviations of the variables in the lateral state vector are discussed in Table 5.3 and the maximum allowed control deflections are listed in Table 5.4.

Table 5.3: Lateral State Vector Maximum Derivatives

Variable	**Description**	**Max**	**Units**
v	With a trim velocity of 36m/s, a lateral velocity of 10m/s causes approximately 15 deg of sideslip. This is considered the maximum angle of sideslip.	10	m/s
p	The maximum roll rate disturbance during conventional flight is estimated to be 20 deg/s	20	deg/s
r	The maximum yaw rate disturbance during conventional flight is estimated to be 20 deg/s	20	deg/s
ϕ	The maximum roll angle deviation during conventional flight is estimated to be 15 deg	15	deg

Table 5.4 Lateral Control Vector Maximum Deflections

Variable	Description	Max	Units
δ_a	The maximum aileron deflection is limited to 10 deg	10	deg
δ_r	The maximum rudder deflection is limited to 10 deg	10	deg

Proceeding in a similar fashion to the analysis of the longitudinal system, modal decomposition is used to gain insight into the primary lateral aircraft model. The model transformation matrix that converts the system of equation to the modal form is shown below,

$$\begin{bmatrix} v \\ p \\ r \\ \phi \end{bmatrix} = \begin{bmatrix} 0.0093 & -0.0537 & 0.3239 & 0.0473 \\ 0.9917 & -0.0079 & -0.6190 & -0.0049 \\ 0.0494 & 0.6572 & 0 & 0.2119 \\ -0.1183 & -0.2693 & 0.0684 & 0.9761 \end{bmatrix} \begin{bmatrix} z_{t_1} \\ z_{t_2} \\ z_{t_3} \\ z_{t_4} \end{bmatrix} \tag{5.17}$$

where the original state vector is shown on the left and the corresponding modal state vector on the right. Transforming the lateral state space model of equation reveals

$$\dot{z}_l = F_l z_l + G_l u_l \tag{5.18}$$

where,

$$z_l = \begin{bmatrix} z_{t_1} & z_{t_2} & z_{t_3} & z_{t_4} \end{bmatrix}^T$$

$$F_l = \begin{bmatrix} -8.287 & 0 & 0 & 0 \\ 0 & -0.5211 & 2.1662 & 0 \\ 0 & -2.1662 & -0.5211 & 0 \\ 0 & 0 & 0 & -0.005 \end{bmatrix} \qquad G_l = \begin{bmatrix} 19.922 & -4.024 \\ -2.207 & -2.737 \\ -0.477 & 0.884 \\ 1.831 & -1.305 \end{bmatrix}$$

The lateral system matrix in modal form clearly shows the two real poles and the set of complex poles that define the natural modes of motion of the primary lateral system. The set of complex poles is known as the dutch roll mode while the low frequency real pole is known as the spiral mode and the high frequency pole as the roll mode. Each of these modes is now discussed in more detail with specific focus on the modes shapes and the relative control of the lateral actuators over each mode.

5.1.2.1 Roll Mode

The roll mode is at,

$$\lambda = -8.38 \tag{5.19}$$

This corresponds to a fast first order exponential response with a time constant of 0.109s. The roll eigenvector is displayed in phasor form below,

$$\begin{bmatrix} v \\ p \\ r \\ \phi \end{bmatrix} = \begin{bmatrix} 0.0013\angle 0 \\ 0.9917\angle 0 \\ 0.0494\angle 0 \\ 0.1183\angle 180 \end{bmatrix} \tag{5.20}$$

The eigenvector indicates that the roll mode is strongly observed in roll rate with a smaller corresponding amount of roll angle. The lateral velocity and yaw rate perturbations are negligible during this motion.

In order to visualize the mode, the aircraft is assumed to be constrained to one degree of freedom in the roll axis. If a roll moment is disturbance occurs, the aircraft will begin to roll in accordance with Newton's second law. However, as the aircraft will rolls, the angle of attack on the down going wing is increased and the angle of attack on the up going wing is decreased. The differential angle of attack across the wing produces differential lift and thus an exponentially increasing roll moment in opposition to the disturbing moment. The interaction manifests itself in a first order roll rate response with a time constant dependent on the roll damping stability derivative (C_{Lp}) and the roll axis moment of inertia (I_y). The fast roll mode time constant is due to the low roll inertia of the model aircraft in this study.

A time history plot of the pure roll mode motion is shown in Figure 5.4, where the lateral state space system in equation (5.16) has been initialized with the roll mode eigenvector. The lateral velocity and yaw rate motion fluctuates and stabilized in within a period of 4s, while the roll rate and bank angle stabilized to a steady state value within the first second of the response. The video extract of the roll hold controller can be found in the CD-ROM clip title Roll hold Controller.

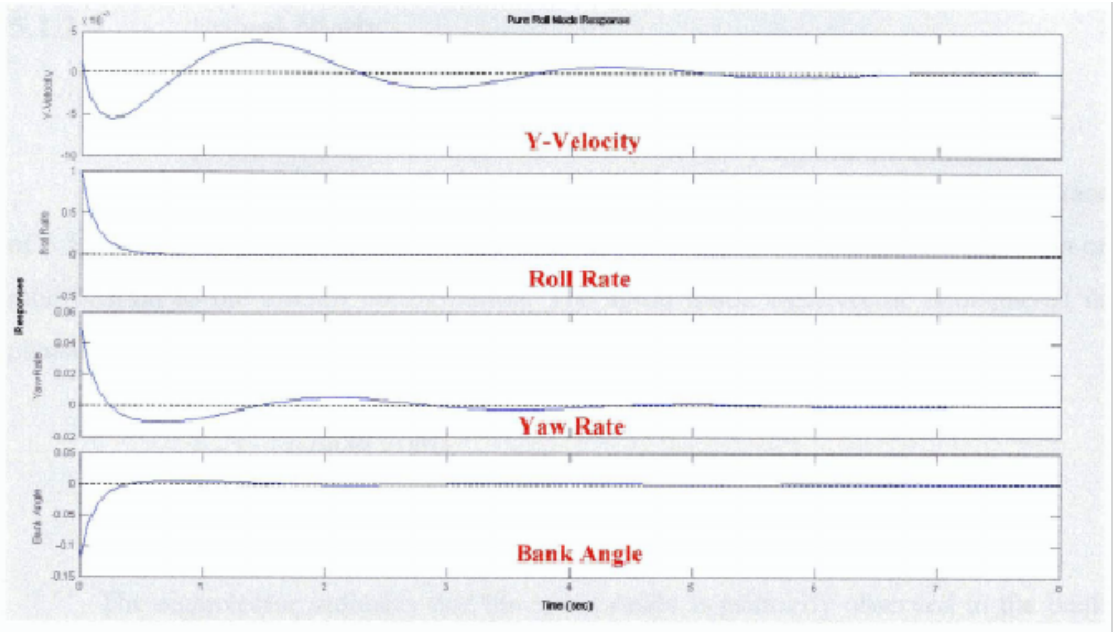

Figure 5.4: Pure Roll Mode Response

An extract of the lateral modal input matrix (G_t) of equation (5.18), pertinent to the roll mode, is shown below,

$$G_{t_r} = \begin{bmatrix} 19.923 & -4.024 \end{bmatrix} \tag{5.21}$$

With reference to Table, the maximum deflection of both aileron and rudder are set at 10^o. This means that the relative magnitudes of the elements of the G_t can be directly compared without the need for scaling. Comparing the column magnitudes of G_t reveals,

$$\frac{Ail}{Rud} = \frac{|19.923|}{|-4.024|} = 4.95 \tag{5.22}$$

which implies that the roll mode is almost 4.95 times better controlled by the ailerons than by the rudder.

5.1.2.2 Spiral Mode

The spiral mode pole is at,

$$\lambda = -0.005 \tag{5.23}$$

This corresponds to a slow, first order exponential response with a time constant of 6.54s. The mode is unstable and could be stabilized using either a feedback system or modification to the aircraft configuration. The spiral mode eigenvector is displayed in phasor form below,

$$\begin{bmatrix} v \\ p \\ r \\ \phi \end{bmatrix} = \begin{bmatrix} 0.0473\angle 0 \\ 0.0049\angle 180 \\ 0.2119\angle 0 \\ 0.9761\angle 0 \end{bmatrix} \tag{5.24}$$

The eigenvector indicates that the spiral mode is primarily observed in the bank angle. With such a long time constant, the bank angle will translate into a slow turn which will make the spiral mode very well observed in heading angle.

The spiral mode describes the tendency of the aircraft to resettle to or diverges from a wing level position after a disturbance. The forces involved arise from a complex interaction of roll, yaw and sideslip motions. Assume the aircraft has been disturbed from its wings level position by a small positive bank angle ϕ. Left unchecked, the disturbance will result in positive sideslip which will cause the aircraft to yaw right as a result of the weather cock effect (C_{N_v}). The yaw rate motion causes an increase in airflow velocity over the left wing and a decrease in airflow velocity over the right wing. The differential airflow velocity results in a positive roll moment that tends to further increase the bank angle disturbance and cause a diverging motion. However, dihedral and quarter chord sweep back effects of the wing (C_{L_v}), produce a negative roll moment in response to the sideslip that tends to restore the wings to level condition. These opposing forces are usually very similar in magnitude which gives rise to the long time constant of the spiral mode.

A time history plot of the pure spiral mode is shown in Figure 5.5, where the lateral system in equation (5.16) has been initialized with the spiral mode eigenvector.

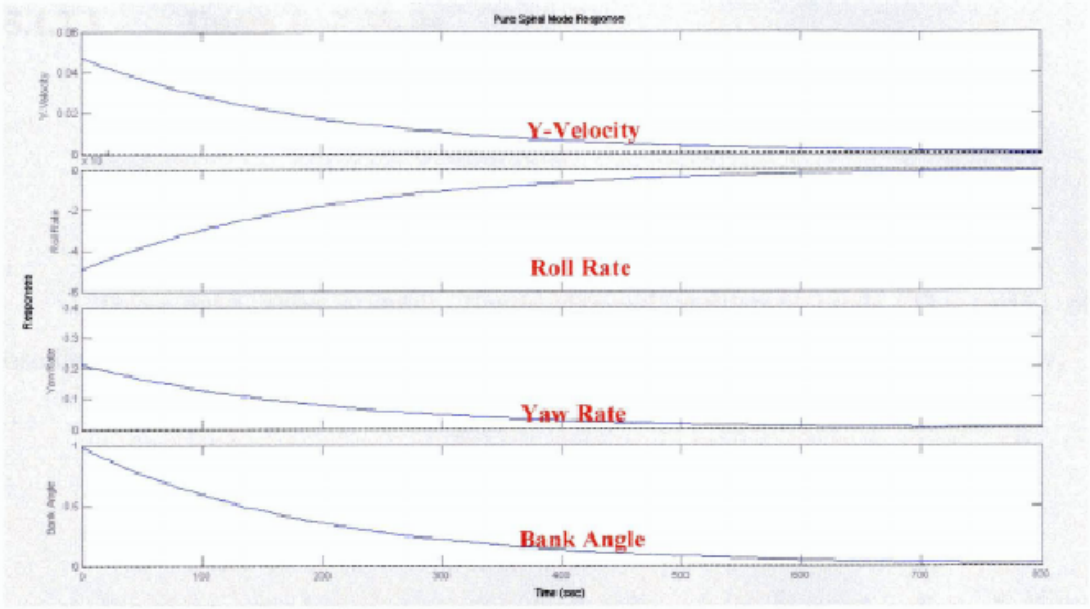

Figure 5.5: Pure Spiral Mode Response

An extract of the lateral modal input matrix (G_t) of equation (5.18), pertinent to the spiral mode, is shown below,

$$G_{t_r} = \begin{bmatrix} 1.839 & -1.305 \end{bmatrix} \tag{5.25}$$

With reference to Table 5.4, the maximum deflection of both aileron and rudder are set at 10^o. This means that the relative magnitudes of the elements of the G_t can be directly compared without the need for scaling. Comparing the column magnitudes of G_t, reveals,

$$\frac{Ail}{Rud} = \frac{|1.839|}{|-1.305|} = 1.41 \tag{5.26}$$

which implies that the spiral mode is almost 1.41 times better controlled by the ailerons than by the rudder.

5.1.2.3 Dutch Roll Mode

The dutch roll modes are summarized below,

$$\lambda = -0.521 \pm 2.1662i \tag{5.27}$$

$$\zeta = 0.234 \tag{5.28}$$

$$w_n = 2.23 rad/s \tag{5.29}$$

These poles form a stable, lightly damped oscillatory mode. The period of oscillation is 1.92s. The dutch roll mode eigenvector is displayed in phasor form below,

$$\begin{bmatrix} v \\ p \\ r \\ \phi \end{bmatrix} = \begin{bmatrix} 0.328\angle 80.6 \\ 0.619\angle 89.3 \\ 0.657\angle 0 \\ 0.278\angle -1.78 \end{bmatrix} \tag{5.30}$$

The eigenvector indicates that the dutch roll mode is observed well in all of the lateral states but predominately in the yaw rate and lateral velocity. Note that the yaw rate motion less the roll rate motion by approximately 90° which is a classic feature in this mode.

Fundamentally, the dutch roll mode is the lateral equivalent of the short period mode with the fin causing the spring and damper forces. However, since the fin is usually less aerodynamically effective than the tail plane, the mode tends to be lightly damped. The mode can be visualized by initially considering the aircraft to be restrained about the O-Z axis in the body axis frame. This is then the lateral equivalent of the short period mode setup, with the weather cock stability derivative (C_{Nv}) primarily determining the frequency of oscillation after a disturbance, and the yaw damping stability derivative (C_{Nr}) primarily determining the damping. However, the yaw rate oscillation causes differential airflow across the wings and thus induces a rolling motion that lags the yaw rate motion by approximately 90°. This phase difference between the yawing and rolling motion means that the forward going wing is low and the aft moving wing is high. The dutch roll mode motion can be well visualized as a rhythmic lateral motion of the aircraft, where the wing tips trace the ellipses in the O-XZ plane in the body axis configuration.

A time history of pure dutch roll mode is shown in Figure 5.6, where the lateral state space system in equation (5.16) has been initialized with the real part of the dutch roll mode eigenvector. Note the 90° lag of roll rate from yaw rate.

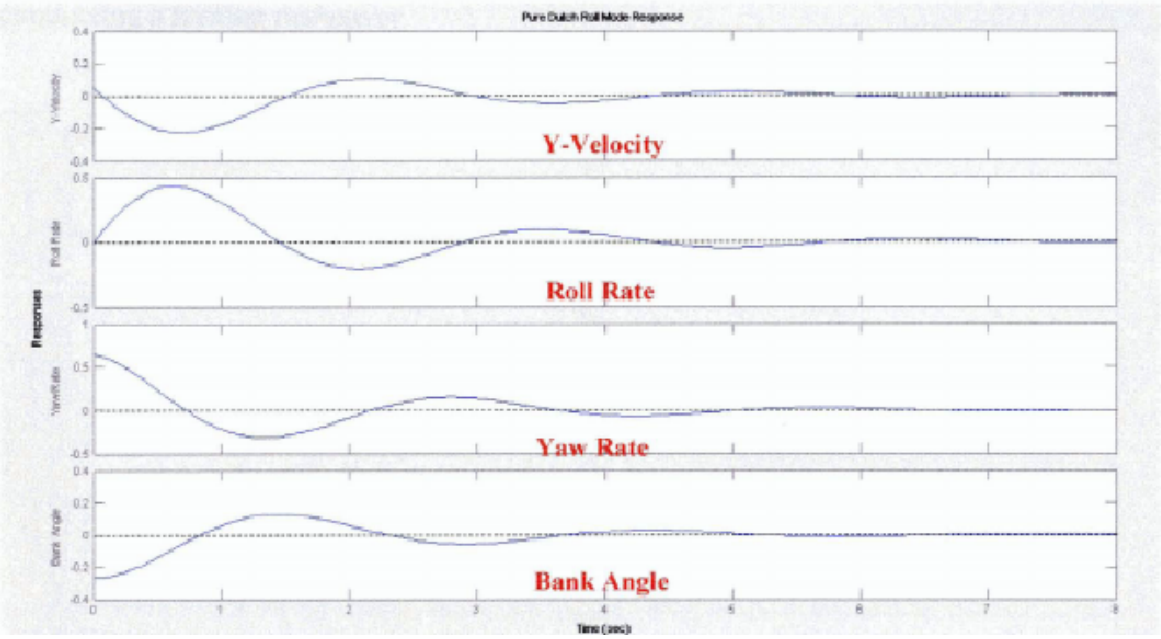

Figure 5.6: Pure Dutch Roll Mode Response

An extract of the lateral modal input matrix (G_t) of equation (5.18), pertinent to the spiral mode, is shown below,

$$G_{t_r} = \begin{bmatrix} -2.2072 & -2.7309 \\ -0.4769 & 0.8838 \end{bmatrix} \tag{5.31}$$

The relative magnitude of the columns of (Gt) reveals,

$$\frac{Ail}{Rud} = \frac{\sqrt{(-2.2072)^2 + (-0.4769)^2}}{\sqrt{(-2.7309)^2 + (0.8838)^2}} = 0.7867 \tag{5.32}$$

which implies that the dutch roll mode is almost 1.27 times better controlled by the rudder than by the aileron.

A time history response of the lateral state space system was obtained by initializing the system state vector with the real parts of the control eigenvector is plotted in Figure 5.7. The impulse input, which is indicative of the change in the respective control surface, can be used to analyze its effects on the on the lateral velocity, roll rate,

yaw rate and bank angle when subjected to changes. From the plots, it can be seen that the inputs are generally stable and the aileron and rudder control surface on the bank angle has stabilized to a non-zero steady state value. This is indicative that the aircraft is conducting a turning maneuver.

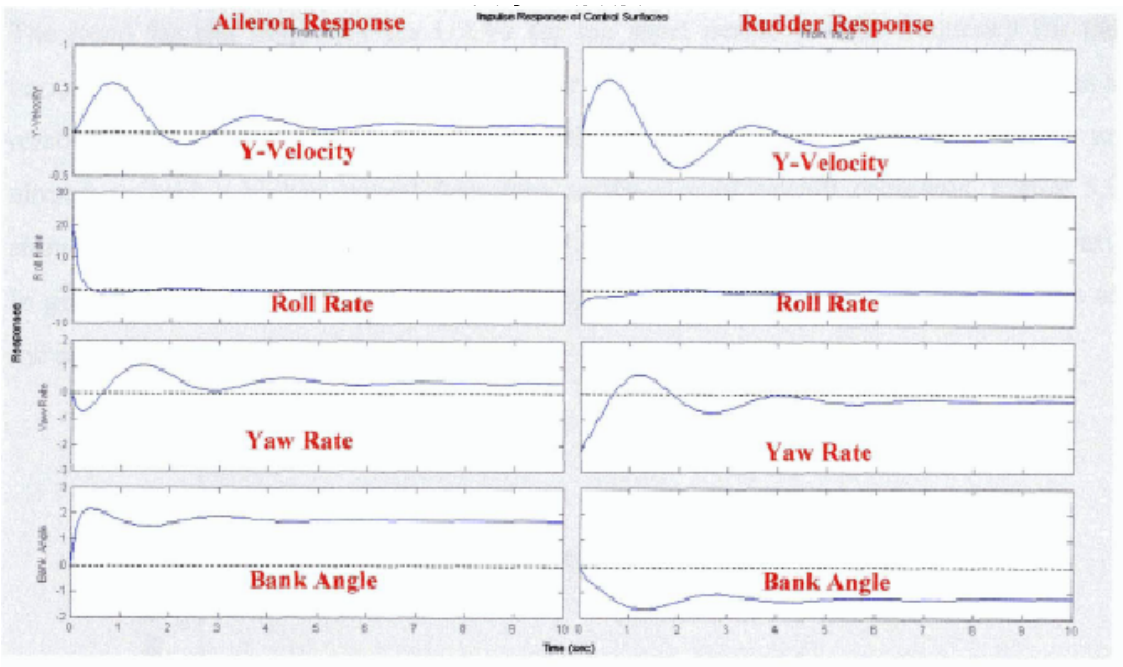

Figure 5.7: Impulse Response of the Control Surfaces on UAV

5.2 Dynamic Stability and Handling Qualities Comparison

In the previous section, the longitudinal and lateral aircraft modes of the UAV are presented. The modes of motions are analyzed, showing which states are dominant in each mode, and what control surface actuators are most effective at controlling each of the modes. The information gained on the mode shape and control surface actuator effectiveness is used later in the aid in the design of the controller. These data obtained can be further used to analyze the dynamic stability and handling qualities of the UAV.

There are no articles discussing the dynamic stability and handling qualities for UAV. Williams [31] called for a new standard for UAV handling qualities based on the current military standards because of the significant differences in requirements for UAV

and conventional aircraft performance. The use of "Froude" scaling to relate the natural frequencies of large vehicles to the UAV are discussed in several articles [32].

The dynamic behaviors of large and small aircrafts are very similar, but the smaller masses and inertias as well as the slower speed of UAV tend toward higher natural frequencies in comparison with the conventional aircraft in some of the modes. The trend for the frequency for UAVs for the short period natural frequency for the various spans can be seen in Figure 5.8. For the short period mode, the searcher has a relative similar frequency in comparison with the Cessna. It shows the trend for an aircraft to have a higher natural frequency as the size of aircraft decreases. Figure 5.9 shows the results of the dutch roll frequency in comparison with the span of the aircraft. In general in can be seen that the natural frequency for the dutch roll mode increases as the aircraft size decreases.

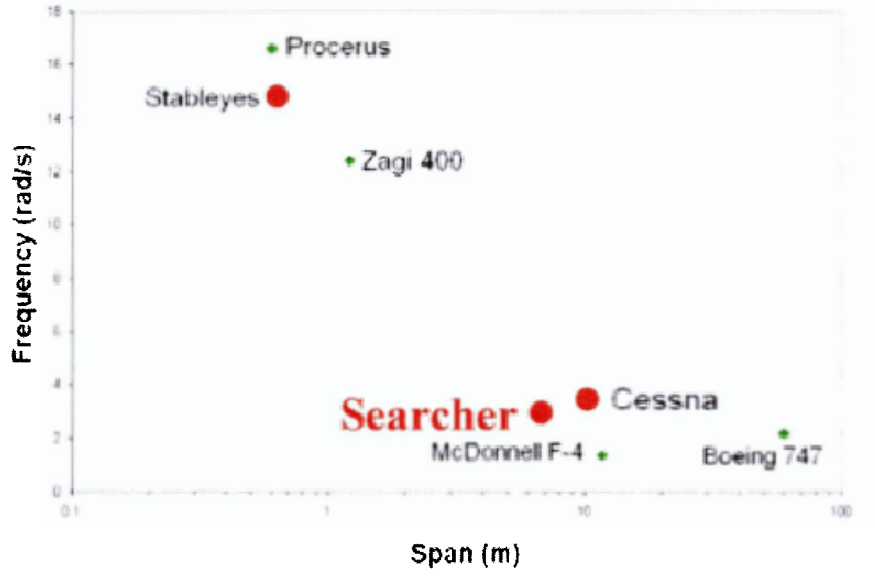

Figure 5.8: Short Period natural frequency plotted versus span for various aircrafts

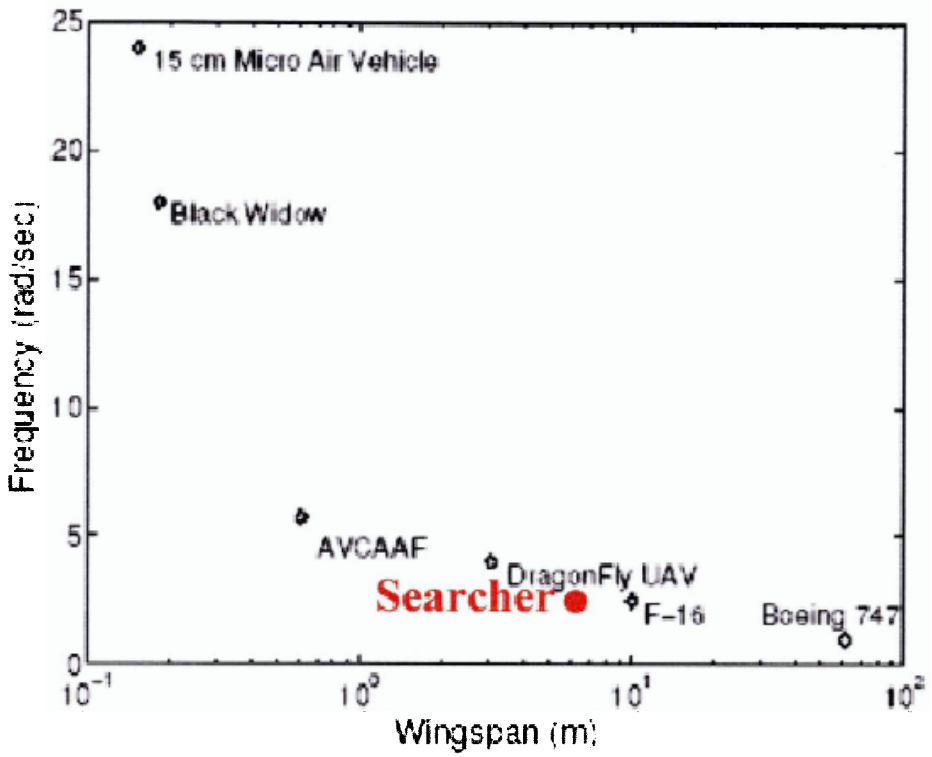

Figure 5.9: Dutch-roll mode natural frequency plotted versus span for various aircrafts

The higher natural frequencies of oscillation present in UAV compared to larger aircraft cause their handling qualities to fall outside the current standards given in MIL-F-8785C [32]. In order to analyze the difference in handling qualities, a comparison is made between StablEyes, a 0.61m wing span mini UAV, the Cessna-182 and the Searcher, the UAV in the study. Table 5.5 contains the mass and moments of inertia data for the various aircrafts. Both the short period and dutch-roll natural frequencies have a strong inverse relation to the moments of inertia about the respective axes of oscillation. Smaller inertia leads to lager dimensional derivatives which cause higher natural frequencies in both the short and duct-roll modes. For the case of the phugoid mode, the natural frequencies are higher because of the inverse relation between the natural frequency and velocity. According to the calculation, the lower flight speeds of the UAV yield higher phugoid natural frequencies then the larger faster aircrafts.

When the characteristics of the dynamic modes are quantified, the difference caused by the smaller moments of inertia and lower flight speed is apparent. Table 5.6 shows a comparison of the dynamic modes taken from Tyler [33] and methods stated previously. The values of the natural frequency for the phugoid and dutch-roll mode of the aircraft increases as the size of the aircraft decreases in size, while the damping ratio of the aircraft moves in the opposite direction, i.e. it increases with as the aircraft is smaller. These it is important to note that UAV and conventional aircraft have different dynamic stability and thus handling qualities, thus the handling qualities cannot be used directly in evaluating the controllability of UAV.

Table 5.5 Comparison of mass and inertia data

	Cessna-182	**Searcher (UAV)**	**Ratio**	**StablEyes (MUAV)**	**Ratio**
m (kg)	1200	380	3:1	0.445	2700:1
I_{xx} (kg*m^2)	700	150	5:1	0.002	350,000:1
I_{yy} (kg*m^2)	1000	450	2:1	0.004	250,000:1
I_{zz} (kg*m^2)	1450	550	3:1	0.005	290,000:1

Table 5.6: Comparison of the predicted natural frequencies and damping ratio for the oscillatory modes of motions

		Cessna-182	**Searcher (UAV)**	**StablEyes (MUAV)**
Short Period	w_n (rad/s)	3.6	2.7	14.9
	ζ	0.89	0.97	1.00
Phugoid	w_n (rad/s)	0.21	0.28	0.90
	ζ	0.08	0.10	0.16
Dutch Roll	w_n (rad/s)	2.0	2.23	9.0
	ζ	0.30	0.24	0.16

5.3 Coupled Open Loop Response of the UAV

Based on the formulation in Chapter 2, the matrix to represent the coupled analysis can be seen in Figure 5.10. A summary of the effects of the coupling components are included below the matrix. The values in yellow are the data which represents the longitudinal components while the values in orange represent the lateral components.

Velocity	Sideslip Angle	Angle of Attack	Roll Rate	Pitch Rate	Yaw Rate	X	Y	Z	Roll Angle	Pitch Angle	Yaw Angle
-0.00071	0	0.0008	0	0	0	0	0	0	0	-0.00278	0
0	1	0	0	0	-0.99	0	0	0	0.01614	0	0
-0.00566	0	-0.03151	0	0.97309	0	0	0	0	0	0	0
0	-0.1481	0	-0.8099	0	0.2074	0	0	0	0	0	0
0	0	-0.0022	0	-0.03212	0	0	0	0	0	0	0
0	0.079	0	-0.0325	0	-0.0705	0	0	0	0	0	0
1	0	0	0	0		0	0	0	0	0	0
0	1	0	0	0	0	0	0	0	0	0	1
0	0	1	0	0		0	0	0	0	-1	0
0	0	0	1	0	0	0	0	0	0	0	0
0	0	0	0	1	0	0	0	0	0	0	0
0	0	0	0	0	1	0	0	0	0	0	0

Coupling due to translational velocity due to Coriollis forces	Coupling due to roll rates	Na	Weight Orientation
Coupling due to asymmetry	Rotational Coupling as a results of the gyroscopic effects	Na	Na
Coupling in position	Na	Na	Coupling in position
Na	Orientation	Na	Orientation

Figure 5.10: Matrix depicting the effects of the coupling analysis

In the matrix above, the coupling effects can be split into four main components. The coupling due to the translational velocity caused by the propulsion vortex, the coupling due to the roll rates, the coupling due to the asymmetrical effects introduced by the propulsion system and the gyroscopic effects similar in the analysis of rolling and spinning. With the introduction of such coupling effects the matrix have to be re-orientated and thus the introduction of the other components which includes the weight orientation. The data obtained through computation fluid dynamics described in Chapter 3 are inputted in the matrix to obtain the responses of the coupled model.

5.3.1 Longitudinal-Lateral Coupled Model

Based on the above matrix, three plots to compare the coupled and de-coupled analysis are developed and it can be seen from figures below. Each of the plots represents different values with Figure 5.11 representing the velocity variation, Figure 5.12 represents sideslip angle and Figure 5.13 represents the variation of pitch rate. In general, the three plots show that the both coupled and decoupled analysis tends to a similar equilibrium position but with different path lines. The only difference is the amplitude oscillation prior to tending to its equilibrium position. Coupled analysis tends to exaggerate the effects and have a larger effect in terms of amplitude than the decoupled analysis. This is because certain effects and data were assumed to be constant and were omitted in the de-coupled analysis and have been included in the coupled analysis which introduces more variables. Thus depending on the overall effects, the coupling effects may introduce undesirable disturbances which should not be neglected as the coupled model will represent a more realistic model compared to the de-coupled model. When the coupling effects are taken into considerations, it represents a better modeled system if the results agree with flight test data.

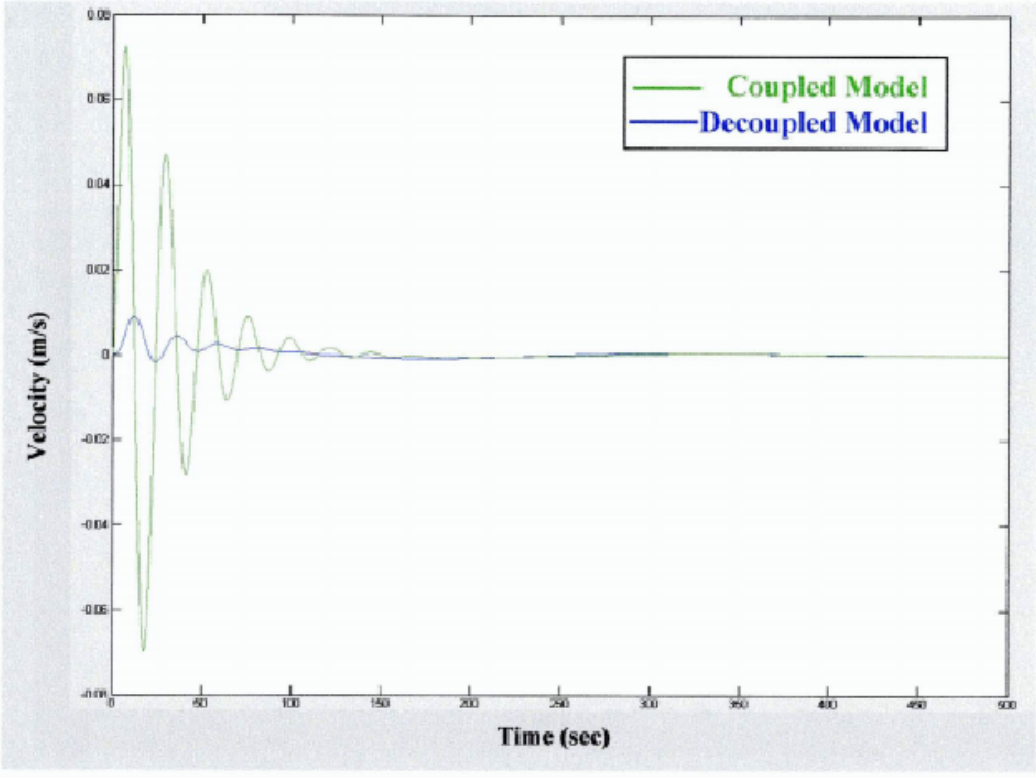

Figure 5.11: Velocity variation of coupled and decoupled analysis

Figure 5.11 shows the decoupled and coupled analysis plot of the velocity variation when an initial input to simulate a disturbance was introduced in the state space matrix. Both plots of the velocity variation in the decoupled and coupled model show a similar trend, but the coupled model oscillates at more profound amplitude as compared to the decoupled model. The coupled model takes about 150s to stabilize while the decoupled model only takes approximately 80s.

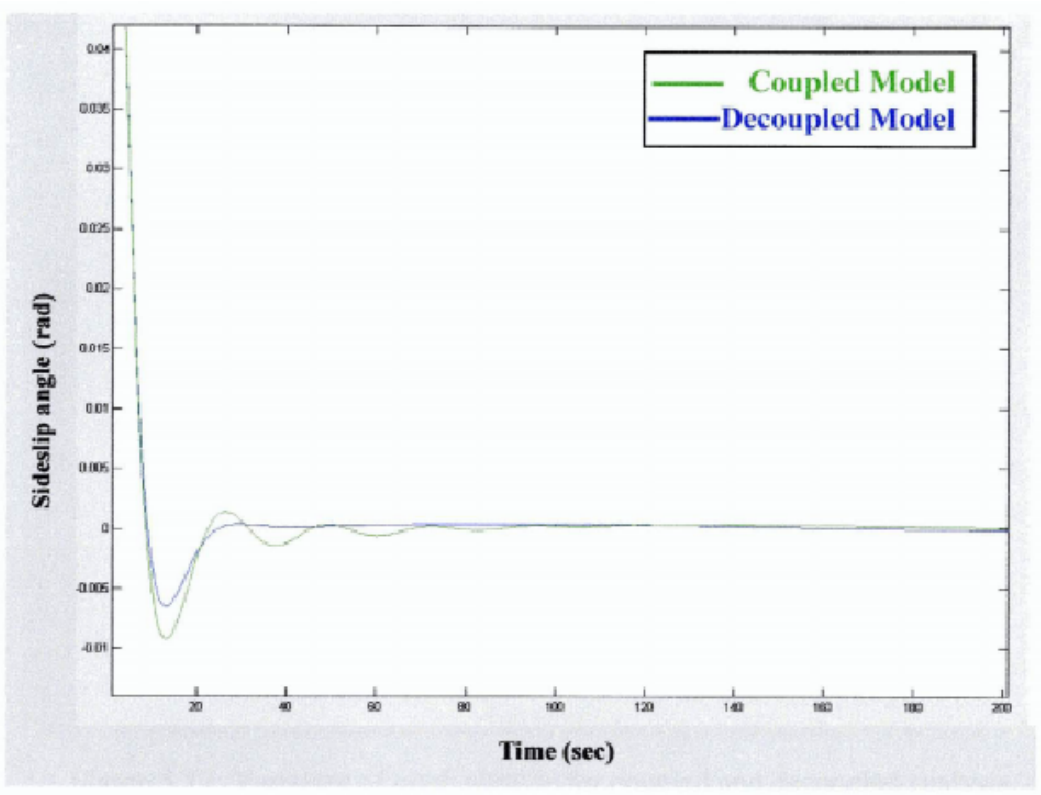

Figure 5.12: Sideslip angle variation of coupled and decoupled analysis

Beside the velocity plot, the plot of the change of sideslip angle can be seen in Figure 5.12. This is crucial in coupled analysis as this is the element which causes the aircraft to move in an asymmetrical flight. Both data follows similar trends; both decrease from an initial value to a negative value before decaying off to an equilibrium position. In comparison, the coupled analysis oscillates to slightly higher amplitude although the absolute value is not profound for this case. Further, the coupled analysis has a more significant and distinct amplitude change during the course of the variation, whereas the decoupled analysis is effectively damped off within the first 30 seconds.

Of all the analysis, the variation of the pitch attitude has the most drastic variation between the coupled and decoupled analysis. Similar to the side slip variation, the aircraft exhibits a quicker damping rate for the decoupled analysis and the decoupled analysis tends to oscillates at a higher variation. In the plot in Figure 5.13, it can be seen that the amplitude oscillates with a larger number of cycle than the decoupled analysis, thus it can be seen that there is a need to investigate the coupling effects.

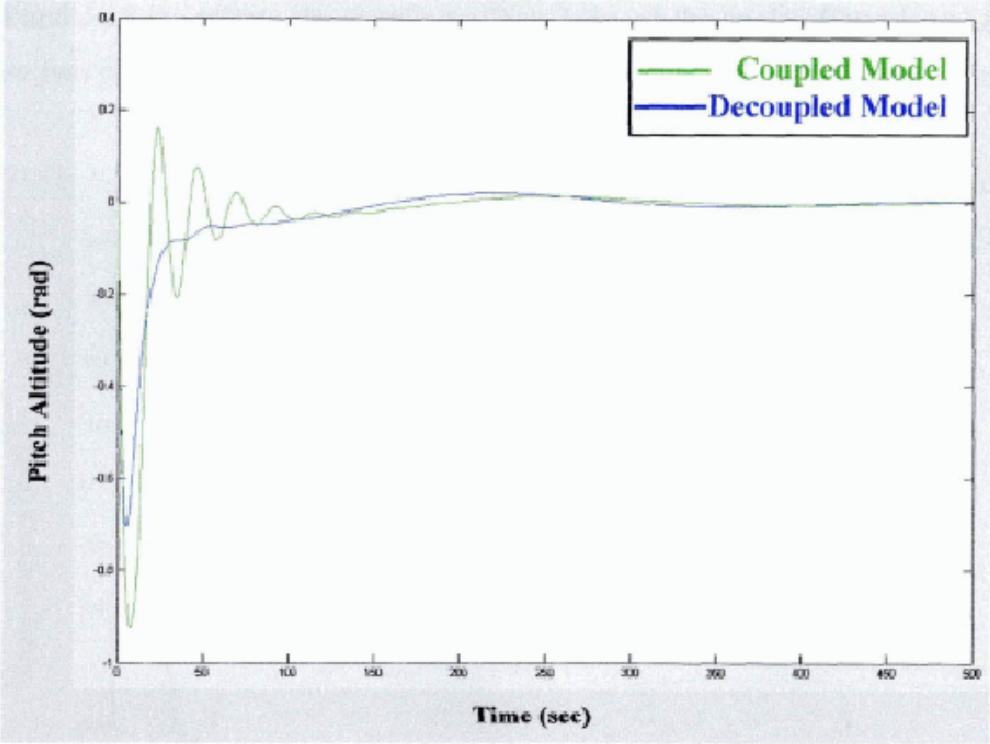

Figure 5.13: Variation of pitch altitude for coupled and decoupled analysis

In general, although the variation between coupled and decoupled analysis is considered significant, it is necessary to look at the whole system holistically. This is because the data changes as seen in the plot are significantly smaller, and if the formulation permits, this data might not have any significant effects on the system. For example, if the objective is to design a flight control system, a decoupled data analysis might be sufficient as both the coupled and decoupled analysis provide similar trends. However, if there is a need to investigate the aerodynamic and stability of the individual part of the aircraft, the coupled analysis has to be used as it creates the coupling phenomena which change the dynamics of flight. This is especially so for UAV where the high thrust to weight ratio is significant.

Similar to the above analysis, the author also includes the study of the effects that the UAV will response to with and without the inclusion of the propulsion effects. This study is done by including Cn_{α} and Cm_{β} caused by the propulsion system. The data introduced is estimation based on CFD analysis above and it can be seen from Figures

5.14 and 5.15 the effects the coupling effects have on the angle of attack and pitch rate. These two plots were selected as they show the most significant difference in the analysis.

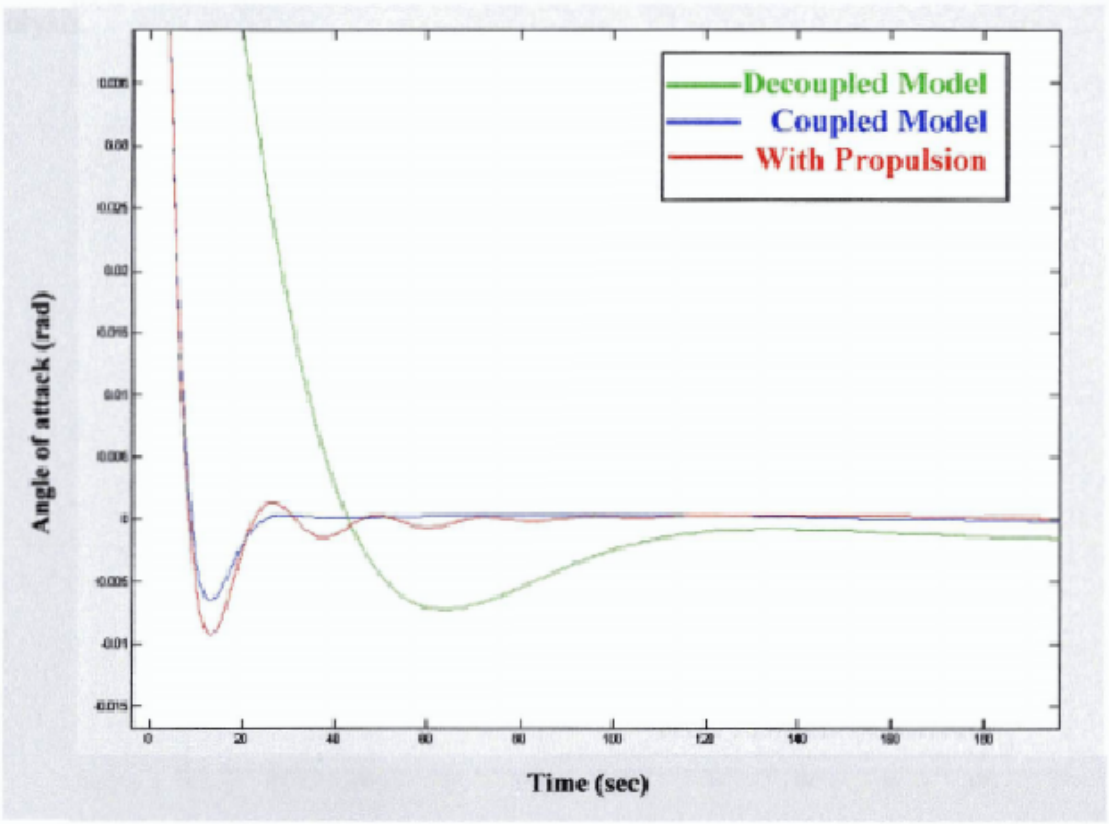

Figure 5.14: Variation of coupling effects with and without propulsion effects on angle of attack

The variation of the pitch rate is more significant as seen in Figure 5.15. Although both tend to a similar equilibrium value, it moves through a very different path prior to equilibrium. In the coupled analysis, the data drops to a lower negative value before moving up to a positive value, whereas the decoupled analysis does not have such a significant drop, the values are much more gentle. This can be due to several reasons, the first being the fact that the propulsion data are based on a rough estimation and are based on raw data which might not predict the actual behavior. Secondly, the effects of the propulsion system might cause such phenomena, thus there is a need to investigate this further by comparing this results with flight statistics and data. At the present moment,

the results are based on several assumptions; further studies have to be done to get a more accurate model to investigate the problem further. However it can be seen that coupling has an effect on the whole system and has to be taken into consideration when doing the analysis.

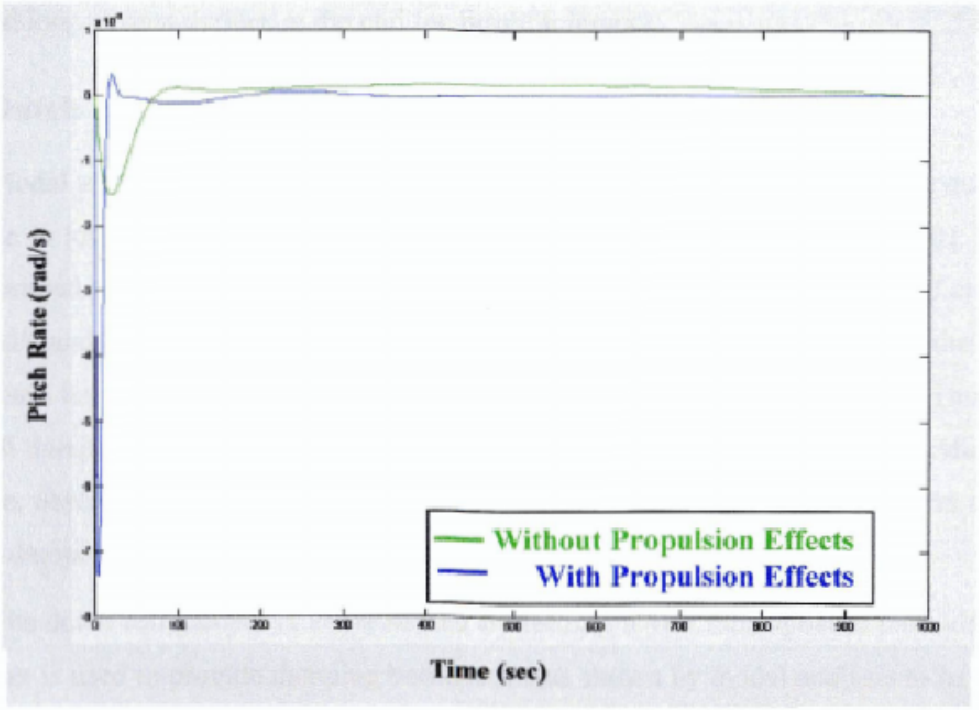

Figure 5.15: Variation of coupling effects with and without propulsion effects on pitch rate

5.4 Overview of Controller

The design and simulation of the aircraft controllers are considered in this section. In view of the case study spelled out in the first chapter, the controller design will focus on the implementation and design of the lateral controllers. The stability augmentation, attitude and trajectory controllers are discussed in the previous three sections, the lateral controller that will be discussed in this study is the Dutch Roll Damper based on the stability augmentation system.

The controller design begins with description of the concept of the controller, followed by the discussion of the design approach before the details of the controller are considered and the results are verified by linear simulation. All controller designs are carried out using root locus methods in *Matlab*® [16] while simulations are performed in *Simulink* [7]. The open loop system is merely referenced at the onset of the design and the closed loop system defined at the end for future reference.

5.4.1 Dutch Roll Damper

Modal analysis in the above section showed that the natural damping of the dutch roll mode is low. With a cruise speed of 36m/s at an altitude of 1068m (3500 ft), the lightly damped poles called the dutch roll mode is given with a natural frequency of close to 1.1 rad/s and damping ratio at 0.0351. This natural damping is dependent on the fin moment arm length (l_F) and the aircraft velocity, both of which vary during flight. Thus a dutch roll damper is implemented in order to suppress the natural dynamics of the dutch roll mode, desensitizes the overall yawing damping to variation in flight parameters and provides damping with respect to the inertial space for wind gust disturbance.

The dutch roll damper is implemented by feeding a yaw rate signal to the rudder. The rudder is used to provide damping because it was shown by modal analysis to be 1.3 times more effective at controlling the dutch roll mode than the ailerons are. The yaw rate signal must however, be high pass filtered before it is fed to the rudder so that the damper does not counter constant turn rate motions. A secondary advantage of the high pass filter is that it negates the bias effects of low cost rate gyroscopes.

5.4.2 Controller Design

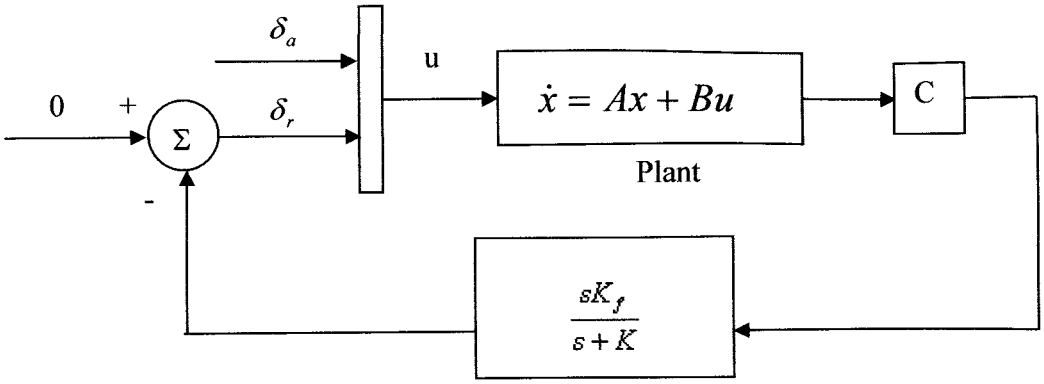

Figure 5.16: Dutch Roll Damper Block Diagram

The control system is summarized in the block diagram in Figure 5.16 where the plant dynamics are taken from the de-coupled lateral equation. The stability derivatives of the UAV are represented in the plant dynamics based on the specific flight conditions. The output matrix C is set to extract the yaw rate state in degrees per sec (deg/s). This yaw rate moves through a washout filter before being fed back to the rudder in a proportional fashion. A washout filter is required to prevent the over stabilizing of the spiral mode as shown in the design process below.

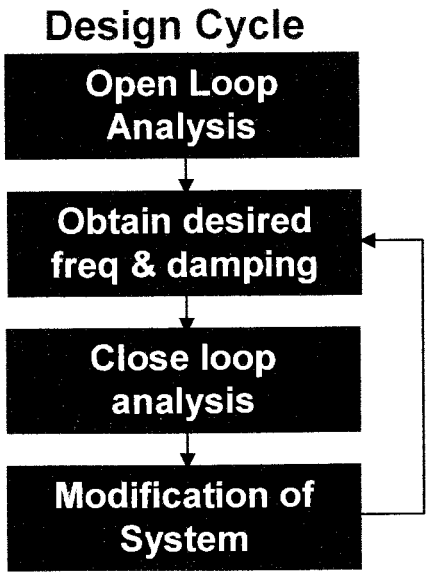

Figure 5.17: Design Cycle of the Control System

The design cycle of the control system is shown in Figure 5.17. Starting with the analysis of the dutch roll mode to obtain the open loop data, a pole zero map of the poles are plotted as shown in Figure 5.18. These data are obtained by computing the eigenvalues of the UAV dynamics model. It shows that this model has a pair of lightly damped poles as indicated by the red circles in the pole-zero maps. The objective is to design a compensator that increases the damping of these poles, so that the resulting complex poles have a damping ratio $\zeta \geq 0.35$ with natural frequency $w_n \leq 1 rad/\sec$.

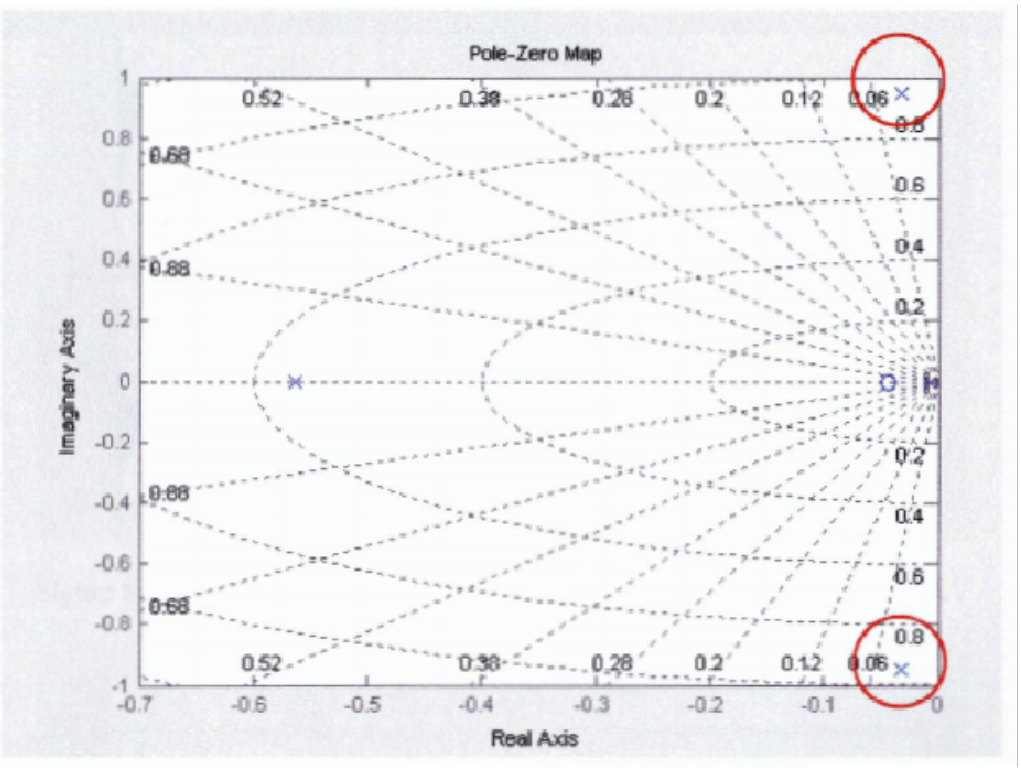

Figure 5.18: Pole-Zero Mapping of the Lateral State Space Model

The open loop response based on the impulse input for both the control surface for the state space model is shown in Figure 5.19. This response is indicative of the effects of the control surface deflection on the UAV. In Figure 5.19, four plots are shown. The first row shows the response of the yaw rate in response to the impulse input of the rudder and aileron. Similarly, the second row shows the response of the bank angle with respect to the two control surfaces. The impulse response confirms that the system is lightly damped and the time frame for it to settle is too long for comfort. In the figure, the

response settles in approximately 400s for both the yaw and bank angle. It can also be seen that the values varies substantially in the first 100s after the input function was initiated. In order to understand the effects over the first 20s, separate plots of the same response are shown in Figure 5.20. This is the time frame which the controller will be targeted to suit the required handling qualities of the UAV. It can also be seen that the impulse effects on the yaw and bank angle are predominately controlled by the rudder response.

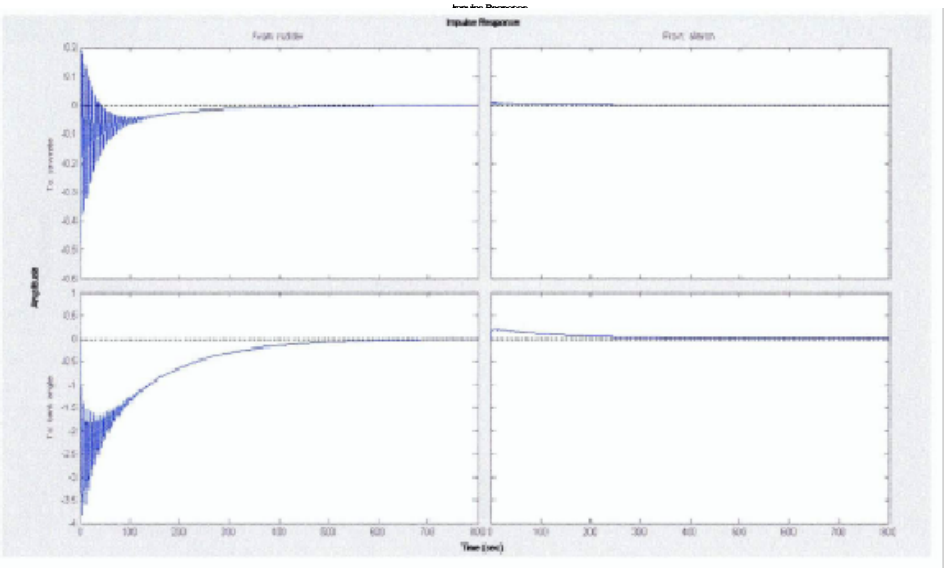

Figure 5.19: Multi input multi output (MIMO) impulse response on the UAV

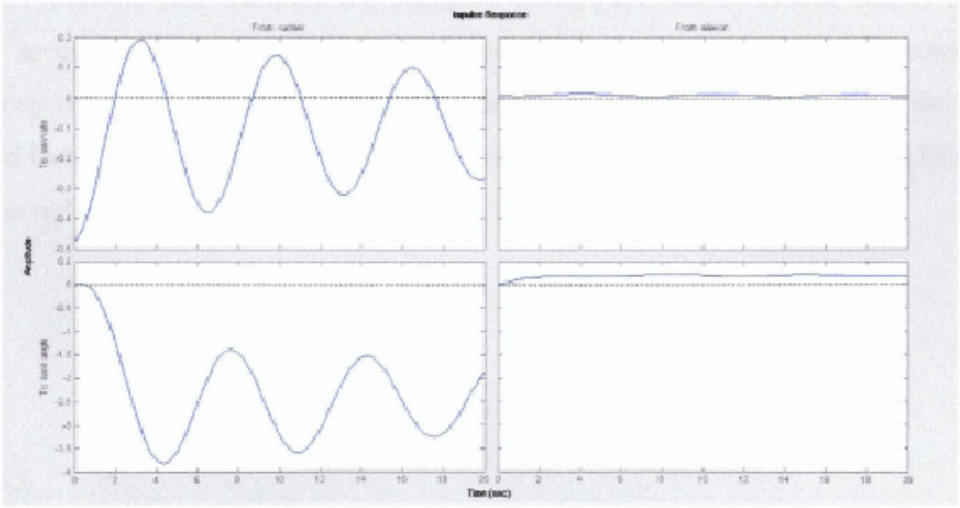

Figure 5.20: MIMO impulse response on the UAV over 20s time frame

By closer inspection of the various responses in the Figure 5.20, it can be seen that the aircraft oscillating around a nonzero bank angle. A blown-up view of the response can be seen in Figure 5.21. This is the usual response expected when an aileron deflection is introduced to the UAV: the UAV is turning in response to an aileron impulse input. This behavior will have an effect in the modification to the close loop feedback system and it will be discussed later.

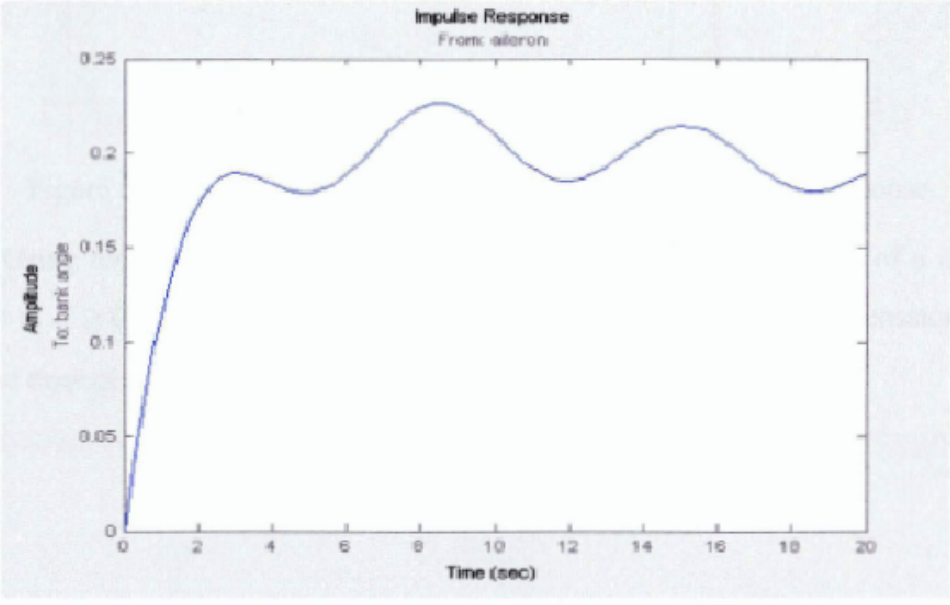

Figure 5.21: Impulse Response of the aileron input to the bank angle

Typically, yaw dampers are designed using yaw rate as sensed output and the rudder as control input as shown in the block diagram. Looking at the corresponding frequency response, we can see that the rudder has a significant effect around the lightly damped Dutch Roll Mode around the region when the frequency is 1 rad/s. The Bode plot with the red line indicative of the response at 1 rad/s is shown in Figure 5.22.

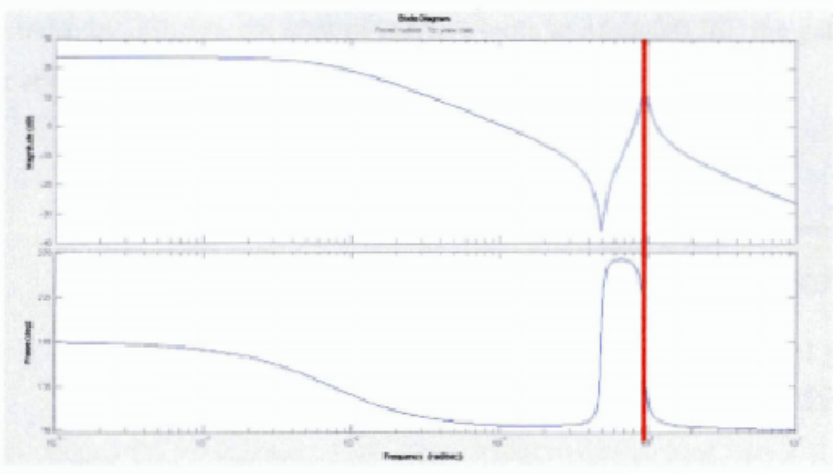

Figure 5.22: Bode diagram of the rudder input to the yaw rate response

Using root locus design methodology, with the objective function of a damping ratio set at $\zeta \geq 0.35$ with natural frequency $w_n \leq 1 rad/\sec$, a simple compensator can be designed through the gains determined by this technique.

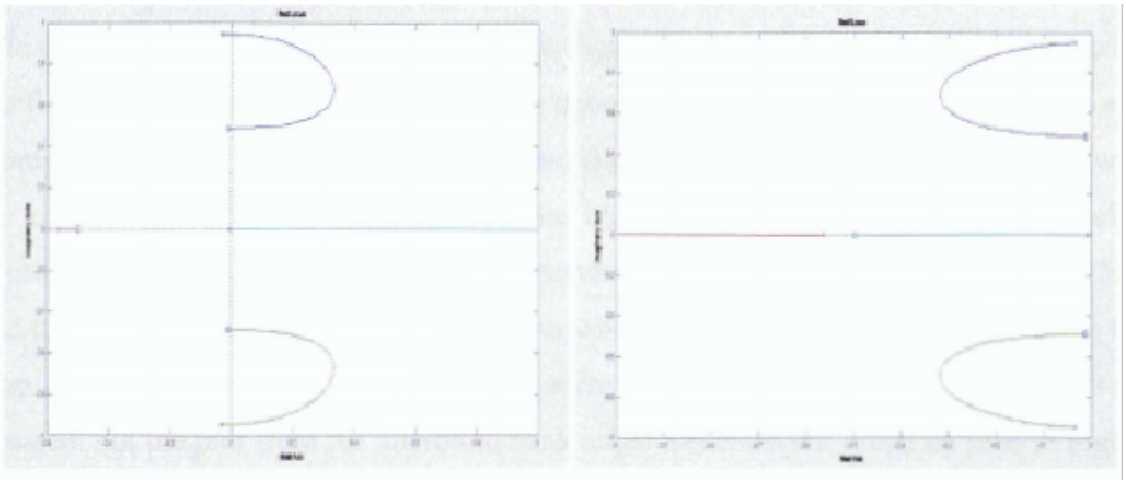

(a) Negative Feedback (b) Positive Feedback

Figure 5.23: Root Locus Design

Figure 5.23 (a) depicts the root locus for a negative feedback controller, and the value goes unstable almost immediately, thus it is not suitable for the system. With a modification to the positive feedback as shown in Figure 5.23(b), it can achieve a damping ratio of $\zeta = 0.45$ as required by the objective function. In order to achieve such

a damping ratio, by utilizing the control toolbox tools in *Matlab*® [6], the gain k can be obtained at about 2.85 as shown in Figure 5.24.

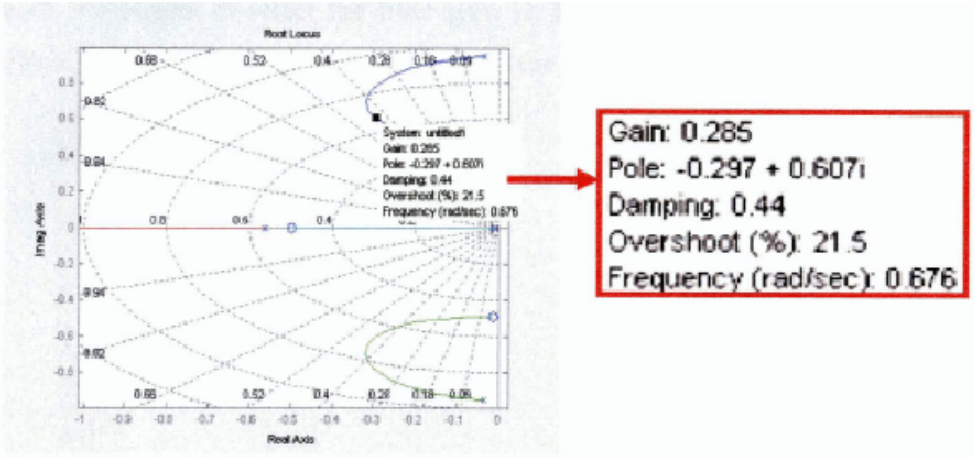

Figure 5.24: Root Locus Diagram

Using the value k=2.85, in the third step in the design phase, it is necessary to close the Single input single output (SISO) feedback loop to understand the effects of the gain on the various response. It can see from Figure 5.25 that the impulse response during the first 20 seconds is must better than the open loop response. The close loop response represented by the red line settles quickly and does not oscillate much in comparison with the open loop response represented by the blue line. The close loop response takes approximately 15 sec to settle with its maximum amplitude approximately 0.05 at t=2sec and this is substantially lower in comparison with the open loop response. By closing the loop on the full MIMO model, it can be seen that the yaw rate response is now well damped, but the plot from the aileron to bank angle has changed. It can be seen in Figure 5.26 that when the aileron is moved, the system no longer continues to bank like a normal aircraft. In this case the spiral mode has been over stabilized. The spiral mode is typically a very slow mode and allows the aircraft to bank and turn without constant aileron input. In order to ensure the spiral mode does not move further into the left half plane when the loop is closed a washout filter k_w $H(s)$ has to be designed. The equation is of the gain is shown below,

$$H(s) = \frac{s}{s+k} \qquad (5.33)$$

The washout filter places a zero at the origin, which constraints the spiral mode to remain near the origin. By considering k =0.2 for a time constant of five seconds and use the root locus techniques to select the filter gain H. Similarly using the tools from the control toolbox, the gain can be obtained to modify the original gain.

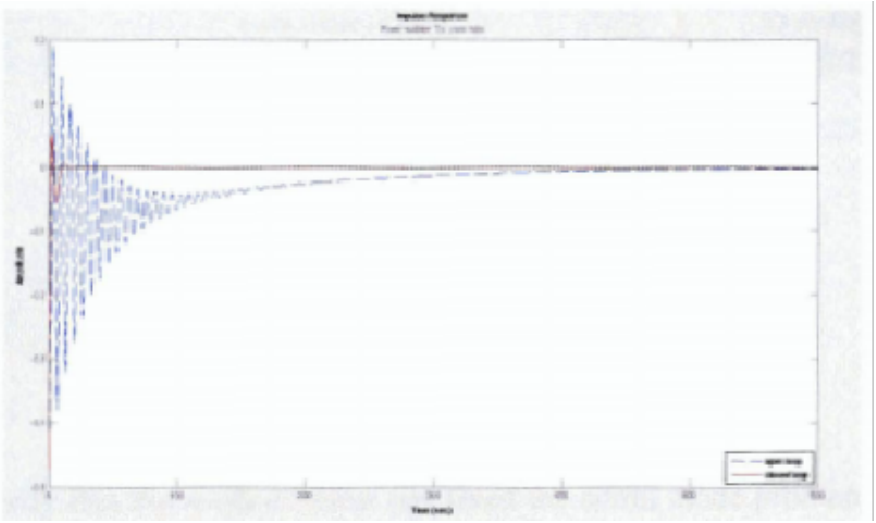

Figure 5.25: SISO response of the rudder to yaw rate

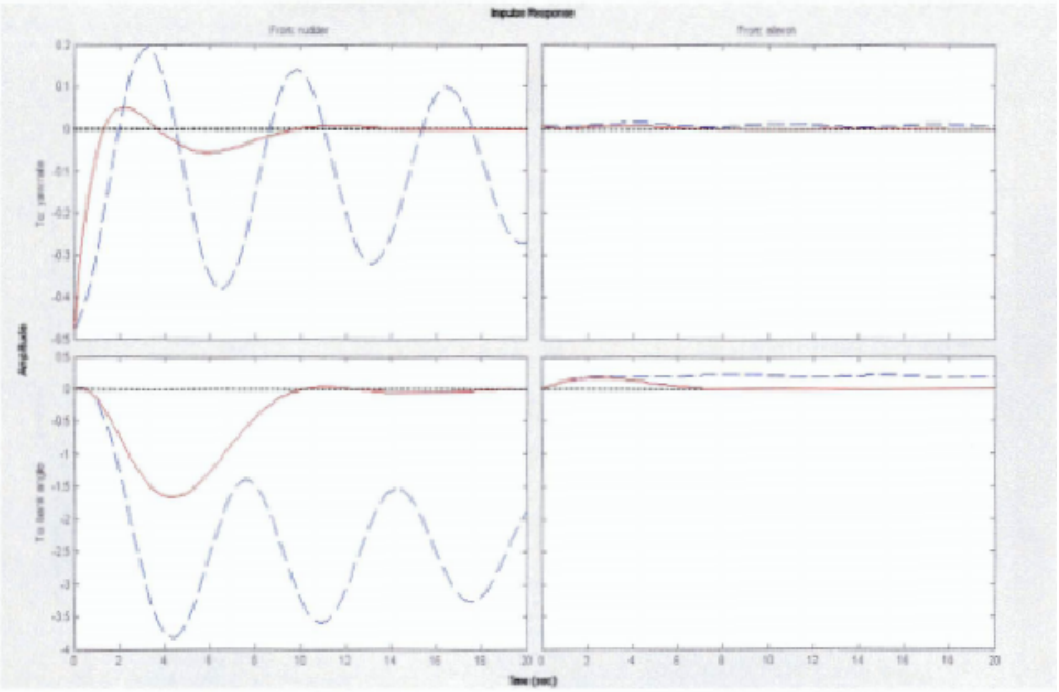

Figure 5.26: MIMO response of the impulse input

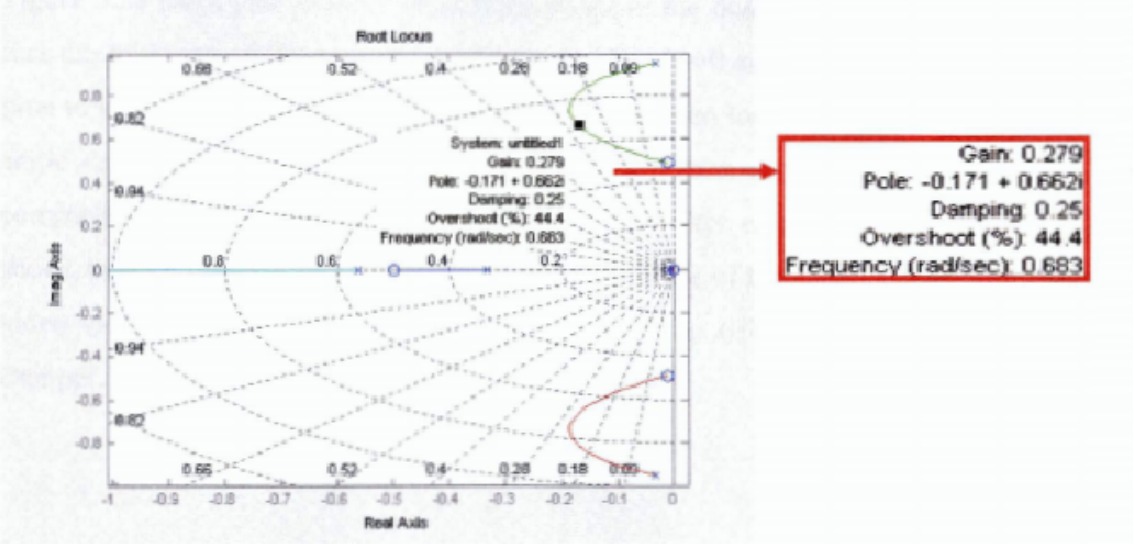

Figure 5.27: Root Locus Diagram for washout filter

To verify that the washout filter has fixed the spiral mode problem, the complete washout filter $k_w H(s)$ (washout+gain) can be represented by

$$WashoutFilter = -K_w \times H \tag{5.34}$$

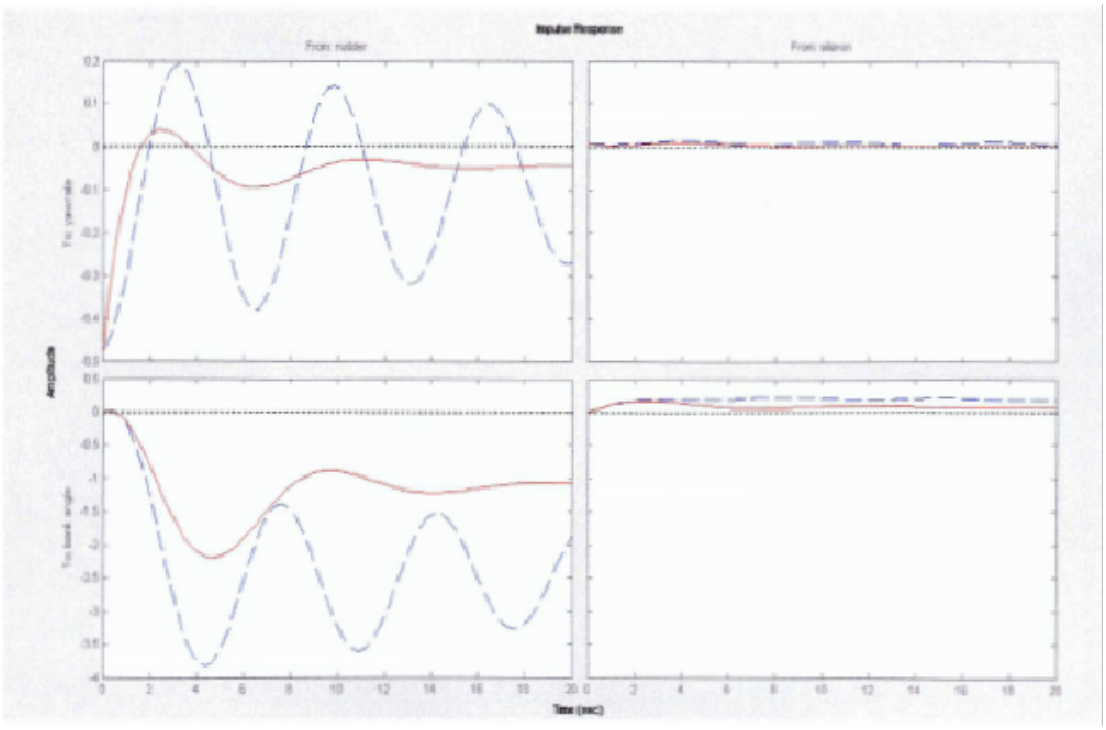

Figure 5.28: MIMO response with washout filter

Figure 5.28 shows the MIMO impulse response of the dutch roll damper. It can be seen that the response of the yaw rate and bank angle is well suppressed by the damper. The time to settle is much better in comparison with the open loop system. Moreover the bank angle response due to an aileron impulse now has a desired constant behavior in comparison with the system without the washout filter over this short time frame. It shows that the damper has not affected the performance of the other control surfaces. The video extract of this simulation can be found in the CD-ROM clip title Dutch Roll Damper.

Chapter 6
Conclusion and Further Work

6.1 Conclusion

From the analysis of the case studies provided, three key areas have been identified and addressed. Firstly, due to its light weight characteristic in comparison to a conventional aircraft, the UAV is affected by small changes to the atmospheric inputs during flight. Secondly, with a single propeller system, the UAV is subjected to an asymmetrical flight condition about its x-axis which is oriented along the direction of flight. Thirdly, the slipstream caused by the pusher propulsion system located aft of the UAV can cause aerodynamic interference with the UAV tail assembly. This is evident in the situation where the wind approaches the UAV at a sideslip angle. The rudder and elevator control surface will fall in the wind slipstream and this will cause the rudder and elevator to lose up to approximately 30% of its effectiveness.

Therefore, the goal of this study is to develop an integrated flight simulation framework to investigate the key areas identified earlier in the case study in Chapter 1. A modular simulation framework has been developed and implemented in the study. This model attempts to integrate the aerodynamic, stability and control derivatives data obtained by using the various computational modeling techniques that are readily available in the market.

This framework has been developed to depict the actual responses of the UAV under various inputs either from the external pilot or flight computer. The heart of the simulate ion model is based on the principles of flight dynamics as presented in Chapter 2. A block diagram model for modularity and reusability has been constructed in *Simulink*. These modularity characteristics allow the user to integrate new modules easily without the need to change architecture drastically. Lessons have been learnt during the process of modeling of the aircraft simulation framework. Initially, a sequential approach was adopted in developing the model. However, this approach was not time efficient and effective for the project. Hence, the modular approach was then adopted for this project.

Modular blocks representing the aerodynamic database, thrust models, environmental models and sample flight controllers were developed based on the available and calculated data. Due to its modularity characteristic, additional data can be incorporated at later stages. Furthermore, based on the needs of the users, the architecture allows results to be presented in various configurations such as graphical analysis in the *FlightGear* domain and block diagram analysis in *Simulink.*

With limited experimental and flight data provided by the operators of the UAV, additional analysis is required to enhance the aerodynamic database in the integrated flight simulation framework. The aerodynamic database was then developed through semi-empirical calculations and CFD. Each of these techniques has its own advantages as well as limitations. Starting with the experimental data obtained from a wind tunnel test provided by the manufacturers of the UAV, *Digital Datcom,* a computer program which provides a systematic summary of empirical methods for estimation of basic stability and control, is used to estimate the stability and control derivatives of the UAV. This program itself has certain limitations in the modeling of the aircraft. The aircraft fuselage can only be modeled in cylindrical shapes, and since the UAV considered in this study has a trapezoidal shape fuselage, the UAV geometry has to be estimated through similarity to enable the estimation of the stability and control derivatives. The results obtained provide a reasonably good estimation when compared with the experimental data. Computational fluid dynamics using commercial software like *Fluent* and *SolidWorks FloWorks,* has been used to compute the aerodynamic flow fields from which the pertinent stability and control derivatives are estimated. In order to establish the aerodynamic database of the UAV, certain assumptions have been made to simplify the geometry of the UAV. As the main goal is to calculate the global aerodynamic flow field around the UAV configuration, the geometric model only considers its external shape. The flow interaction between the control surfaces and wings and other details like flow through propeller blades are assumed to remain constant throughout the system. The modeling of the propeller system has been simplified using the actuator disc theory model to avoid using extensive computer resources. As the main objective of the study is to understand the propulsive forces on the UAV, the optimization methods of the blades in the

propulsion system are not explored in this study. Thus, the actuator disc theory techniques are used instead of modeling the full propeller system. A subsystem within the aircraft block was created by integrating the data obtained into look up tables. This block can be modified easily in future to cater for potential growth in data when more information is made available.

To understand and investigate the flight characteristics of the UAV, calculations in *Matlab* ® have been done for both the de-coupled longitudinal and lateral mathematical models. Both the longitudinal and lateral equations are solved independently on the assumption that there are no interactions between these equations. The coupled longitudinal – lateral equations, where the coupling effects like the aerodynamic coupling caused by the propeller system, have been solved to obtain the flight dynamic responses based on the respective controller inputs. Although the de-coupled modes presented define a reasonably stable aircraft, the settling time and natural frequency can be further enhanced for more favorable handling qualities. The coupled analysis shows profound differences when the coupling effects caused by the propeller system have been incorporated. A controller design process has been initiated to develop and design a controller to enhance the damping ratio and natural frequency for the dutch-roll mode. This mode was identified as one of the focal points in the study. Through the process, it is evident that the coupling effects are present and it cannot be neglected during the design of the flight controller. A roll hold controller was also developed for the project, to maintain a specific roll attitude regime even when subjected to atmospheric disturbance. The controller was tested using the linear simulation model, and the results shows that it has enhanced the settling time of the UAV through introducing a damper as a feedback loop controller.

Subsequently it is necessary to implement the controller into a non-linear simulation environment for verification and validation purposes. This simulation model will depict the actual response as it considers all the forces acting on the UAV. Two methods, namely the block diagram simulation model and graphical simulation model, are developed for the project, each having its own advantages and disadvantages. The modular structure of the block diagram model allows changes to be made to the aircraft

model at any point of time during the course of the simulation and for future modification to the system. The visual model allows the user to mimic the actual ground response in the computer domain and gives the user a better understanding of the behavior of the UAV. In addition, the visual effects allow the operators to view the UAV from different perspectives after the completion of the flight simulator. In the past, the operators could only view the UAV from a cockpit perspective. The view is also offset as the payload is located at the belly of the airframe. However with the simulator, from a third party perspective, the operators can view the UAV under disturbance from the rear to the front of the UAV. This allows the operators to have a better picture of the response of the UAV when subjected to atmospheric disturbance. Although the data obtained for the aerodynamic and stability and control characteristic database are compared across various software, and the dynamics modes are cross-checked with similar aircraft models, there is a need to verify the data with actual flight test cases. The aircraft model in the computer domain presented in this report requires further validation through verification against real flight test data so that the enhanced model can be used to test new flight control systems.

In conclusion, the integrated flight simulation model, as presented in the project, allows the study and evaluation of the three key areas identified earlier in the case study. These key areas namely i) effects of the light weight nature of the UAV as compared to other aircrafts, ii) coupled analysis due to the propeller system and iii) interference of the wind slipstream with control surfaces, conclude that the UAV is unable to control itself effectively without the aid of a system to enhance its stability and control. The damping need to isolate the disturbances is of a higher magnitude and nature. The UAV design does not have sufficient characteristics to have an inherent stability to cater for such atmospheric disturbances. A flight controller is essential in controlling the UAV when subjected to atmospheric disturbance, especially when the UAV is subjected to high speed wind in sideslip conditions. Results shows that with a damper embedded in the aircraft system for each of its mode, the UAV can be controlled more effectively by the operators. As seen in the case studies, the flight computer system is unable to cater for such disturbance currently. Thus the database in the current system has to be further

upgraded to expand the scope of control for the UAV over a wider spectrum of the flight envelope.

6.2 Future Work

In general, the following areas can be further enhanced. The testing methods and verification techniques are areas which need to be more robust to cater for actual testing of new systems. In addition, the aerodynamic characteristics can be further enhanced via advanced analysis and techniques. Currently, the full system has not been incorporated; more flight controller systems based on the actual UAV system should be included to allow the system to mimic the actual aircraft. With this flight controller integrated into the model, this model can be used for pilot training.

The development of an automated testing system across the different components in the simulation framework for verification of data obtained in the model through actual flight testing should be the item that needs to be enhanced in the next phase. The model should be inputted with actual flight test cases, and results can be verified with the actual responses in flight to validate the model. As new models are added or when systems are optimized through new controllers, the automated testing will alert the developer to any errors introduced during the modification. The modularity of the system allows for future modification and enhancement to cater for future development. More advanced functions and blocks can be added to provide more accurate flight dynamics over a greater range of flight conditions and regime.

Advanced analysis and techniques on the aerodynamics can be included in future studies. Studies to the flow analysis between the control surface deflection and its effectiveness during atmospheric disturbance can be incorporated and simulated in the six-degree-of freedom simulation framework. A study on the propeller system and ways of optimizing the blade design to enhance performance can be completed and tested with this framework. The additional data obtained through CFD analysis can be incorporated into the aerodynamic database for a wider range of flight regime and the model can be used to analyze the UAV at higher angle of attack, to study spinning phenomenon and to recover the UAV at such a flight condition.

This system also allows the user to test out different flight algorithms for different flight regimes, especially new codes for autonomous flight and navigational controls for future applications. This includes waypoint navigation, loitering commands and return home functions. This modular system can incorporate the various control systems required to be tested and verified before testing them in the field.

A future goal for this project is to develop a flight simulator test system for pilot training, where the pilot can train in an environment which mimics the actual responses and behavior of the UAV. The system will form the heart of the simulation test setup which can include other components like flight control stick and mission computers.

References

[1]Blazakis, J *Border Security and Unmanned Aerial Vehicles*, CRS Report for Congress, 2004.

[2] Nelson, R.C., *Flight Stability and Automatic Control*, 2nd Edition, McGraw Hill International Editions, 1998.

[3] Draper, C.S. *Flight Control* in the Journal of the Royal Aeronautical Society, Vol 59, July 1955.

[4] Richardson K. I. T, *The Gyroscopic Applied*, The Philosophical Library, New York, pp. 261-264, 1954.

[5] Blakelock, John H, *Automatic control of Aircraft and Missile*, 2nd Edition, John Wiley and Sons Inc. 1991.

[6] The MathWorks, Inc. 3 Apple Hill Drive Natick, MA 01760-2098, United States of America. www.mathworks.com

[7] *Simulink* Version 6, The MathWorks, Inc. 3 Apple Hill Drive Natick, MA 01760-2098 United States of America, 2005. www.mathworks.com

[8] *FlightGear* Version 0.9.8, Project FlightGear, 2006. www.flightgear.org

[9] Scans, N.S & Barnes, A.G, *Fifty years of success and failures in flight simulation*, in the Report in fifty years of flight simulations, London: Royal Aeronautical Society, 1979.

[10] Davis, D. P *Approval of flight simulator flying quantities* in The Aeronautical Journal 79, 1975, pp. 281-298.

[11] Shannon, R. E. *Systems Simulation: the art and science*, Englewood Cliffs: Prentice Hall, 1975.

[12] Prophet, W.W., Caro, P.W. & Hall, E, R *Some current issues in the design of flight training devices* in the 25th Anniversary Commemorative Technical Journal, US Naval Training Devices Center, Orlando, Florida. 1971.

[13] Kertesx Rony, *Six Degree of Freedom Manual Version 1*, Manual and data of the UAV, 1990.

[14] *SolidWorks* Version 2006, SolidWorks Corporation, 300 Baker Avenue Concord, MA 01742, United States of America, 2006. www.solidworks.com

[15] *Rhinoceros* Version 3.0, McNeel North America 3670 Woodland Park Ave N Seattle, WA 98103, United States of America, 2003. www.rhinocad.co.uk

[16] *MATLAB®* Version 7, The MathWorks, Inc. 3 Apple Hill Drive Natick, MA 01760-2098, United States of America, 2005. www.mathworks.com

[17] *Aerospace Blockset* Version 1.6 Release 14, for use with Simulink ® User Guide version 1, The MathWorks Inc. 3 Apple Hill Drive Natick, MA 01760-2098, United States of America, 2005. www.mathworks.com

[18] *Aerosim Blockset* Version 1.1, U-dynamics LLC, Unmanned Dynamics, User Guide, 2005. www.u-dynamics.com

[19] Thomas, H. H. B.M, *Some thoughts on mathematical models for flight dynamics* in the Aeronautical Journal 88, No 875, 1984, pp. 169-178.

[20] Etkin Bernard and Lloyd Duff Reid. *Dynamics of Flight: Stability and Control*, 3rd Edition, John Wiley and Sons Inc, 1996.

[21] Philips, Warren F. *Mechanics of Flight*, 2nd Edition, John Wiley and Sons Inc, 2004.

[22] USAF Stability and Control DATCOM, Flight Control Division, Air Force Flight Dynamics Laboratory Wright Patterson Air Force, Fairborn, OH, Vol 1, User Manual, Updated by Public Domain Aeronautical Software, Santa Cruz CA98061, 1999.

[23] *FLUENT* Version 6.2, Fluent Inc. 10 Cavendish Court, Lebanon, NH 03766, United States of America, 2005. www.fluent.com

[24] *COSMOS FloWorks*, SolidWorks Corporation, 300 Baker Avenue Concord, MA 01742, United States of America, 2006. www.solidworks.com

[25] Ungar Steve, *A/F Searcher 1:3 Scale Model Test Report*, IAI TASHAN Engineering Centre, Aircraft Division, Israel Aircraft Industries Ltd., June 3, 1991.

[26] Chan Su Ling, *Computational Study of the Aerodynamic Characteristics of an Unmanned Aerial Vehicle*, Final Year Project Report, School of the Mechanical & Production Engineering, Nanyang Technological University, 2006.

[27] Li Guo Hao, *Computational Aerodynamic of an Unmanned Aerial Vehicle*, Final Year Project Report, School of the Mechanical & Aerospace Engineering, Nanyang Technological University, 2007.

[28] Versteeg H. K. & Malalasekera W., *An Introduction to Computational Fluid Dynamics, The Finite Volume Method*, Prentice Hall, England. 1995.

[29] *GAMBIT* Version 2.0, Fluent Inc. 10 Cavendish Court, Lebanon, NH 03766, United States of America, 2005. www.fluent.com

[30] Arthur E. Bryson. Jr., *Control of Spacecraft and Aircraft*, Princeton University Press, 1994.

[31] Williams, W. *UAV handling Qualities.....You must be joking*, Aerospace Sciences Corporation Pte Ltd, 2003.

[32] Mettler, B. Tischler, M.B. Kanade T. *System Identification of small sized Unmanned helicopter dynamics*, Final Year Report, Carnegie Mellon University, 2002.

[33] Tyler M. Foster and Jerry Bowman, *Dynamic Stability and Handling qualities of small Unmanned Aerial Vehicle*, Brigham Young University, Utah, in the 43rd AIAA Aerospace Science Meeting and Exhibit, Reno, Neveda , AIAA 2005-1023, 10 to 13 Jan 2005.

[34] Gage Stacy, *NASA HL-20 Lifting Body Airframe Modeled with Simulink and Aerospace Blockset*, The MathWorks, Inc. 3 Apple Hill Drive Natick, MA 01760-2098 United States, 2006.

[35] Berndt, Jon. *JSBSim, The open source flight simulator in C++*, 2000. www.jsbsim.org

[36] *Microsoft Flight Simulator X*, Microsoft Corporation, 2006. www.microsoft.com/games/flightsimulatorx

[37] Berndt, Jon. "*JSBSim: An open source Flight Dynamics Model in C++*", JSBSim Project, League City, TX, in the AIAA Modeling and Simulation Technologies Conference and Exhibit, Providence, Rhode Island, AIAA 2004-4923, 16 to 19 August 2004.

[38] E. Bruce Jackson, Bruce L. Hildreth, *"Flight Dynamic Model Exchange Using XML"*, in the Modeling & Simulation Technologies Conference, Paper Number AIAA-2002-4482, August, 2002.

[39] Phillips, W. F., Hailey, C. E., and Gebert, G. A., "*A Review of Attitude Representations Used for Aircraft Kinematics*," in the Journal of Aircraft, Vol. 38, No. 4, 2001, pp. 718–737.

[40] Phillips, W. F., and Anderson, E. A., "*Predicting the Contribution of Running Propellers to Aircraft Stability Derivatives*," AIAA Paper 2002-0390, 2002.

[41] Goldstein, S., "*On the Vortex Theory of Screw Propellers*," in the proceedings of the Royal Society, Series A: Mathematical and Physical Sciences, Vol.123, 1929, pp. 440–465.

[42] Phillips, W. F., and Santana B.W., "*Aircraft Small Disturbance Theory with Longitudinal-Lateral Coupling*," in the Journal of Aircraft, Vol. 39, No. 6, 2002, pp. 973-980.

Lists of Appendices

Appendix A
UAV Characteristics

Figure A.1: UAV model used in study

The UAV described in this study is a fixed-wing, 7.648m wingspan aircraft as shown in the photograph Figure A.1. The UAV is made of composite materials, characterized by low weight and high strength. The advantage of composite material, in addition to its optimal weight-strength ratio is low radar reflection that reduces detection probability during a mission. The aeronautical design and large wing surface area provide the UAV with stabilized flight properties and low fuel consumption. The UAV structure consists of the following major components, a fuselage assembly, a wing assembly, a tail and boom assembly and a landing gear assembly which consist of a main landing gear, a nose landing gear and the arresting hook system. The UAV fuselage houses the propulsion system and payload of the craft. Various compartments have been designed to place the various equipment and system. The weight without any payload is 222.0 kg and the maximum take off weight is approximately 381.0 kg. The wing assembly has two booms that connect to the tail assembly which consists of a twin vertical tail and a horizontal platform. The pusher propulsion system is placed at the end of the aft fuselage.

Table A.1 Basic Specification of UAV

Length	5.07 m
Wingspan	7.648 m
Wing Area	4.3 m^2
Aerodynamic chord	0.577 m
Weight	380 N

Table A.2 The aerodynamic stability derivatives of the UAV

Longitudinal Aerodynamic derivatives		**Lateral Aerodynamic derivatives**	
C_L	0.64	$C_{y\beta}$	-0.9568
C_D	0.055	$C_{l\beta}$	-0.0126
$C_{L\alpha}$	6.119	$C_{n\beta}$	0.0427
$C_{D\alpha}$	0.368	C_{lp}	-0.624
$C_{m\alpha}$	-2.14	C_{np}	-0.0725
$C_{L\dot{\alpha}}$	2.1	C_{lr}	0.335
$C_{m\dot{\alpha}}$	-9.4	C_{nr}	-0.834
C_{Lq}	6.8	$C_{l\delta a}$	0.16
C_{mq}	-30.5	$C_{n\delta a}$	-0.0055
C_{Lm}	0	$C_{y\delta r}$	0.16
C_{Dm}	0	$C_{l\delta r}$	-0.01
C_{mm}	0	$C_{n\delta r}$	-0.054
$C_{L\delta e}$	0.005632		
$C_{m\delta e}$	-0.0248		

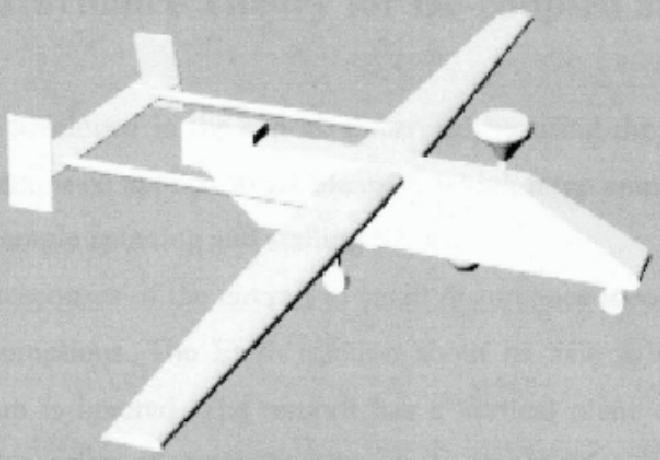

Center of Gravity and Mass Characteristics

W = 380.0 kg
CG at 42.0% MAC
I_x = 150 kg m^2
I_y = 450 kg m^2
I_z = 550 kg m^2
I_{xy} = -22.5 kg m^2

Reference Geometry

S = 4.3 m^2
b = 7.648 m
c = 0.577 m

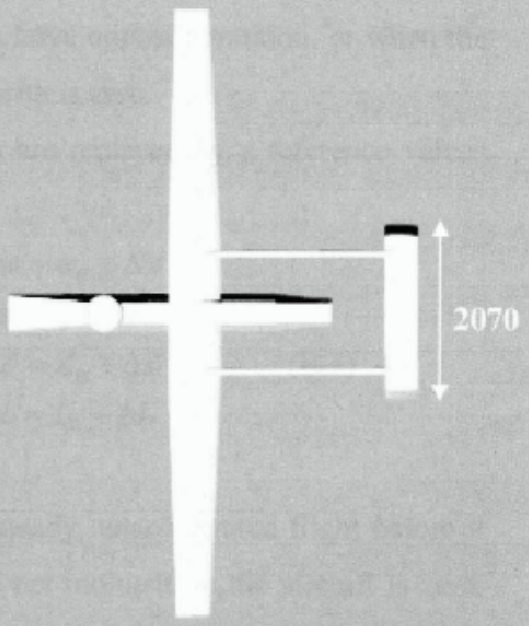

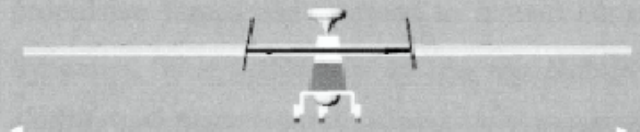

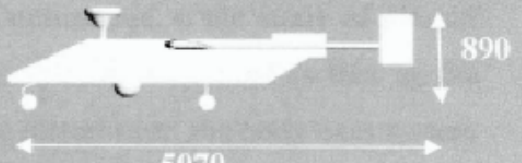

All Dimensions in mm

Appendix B

Small Disturbance Theory for De-coupled analysis

The equation developed in the can be linearized by using the small disturbance theory. This theory cannot be applied to problems in which large amplitude motions are to be expected, for example spinning and stalling flight.

The study of responses of the aircraft to small disturbance theory is based further on the following assumptions. The Earth rotation about its axis as well as its orbital motion around the sun is ignored. The aircraft has a vertical plane of symmetry. The motion of the aircraft consists of small disturbance about a steady flight condition. The effects of spinning rotors are negligible. This is the case when the aircraft is in gliding flight with power off, when the symmetrical engines have opposite rotation, or when the rotor angular momentum is small. And the wind velocity is zero.

All the variables in the equations of motion are replaced by a reference values plus a perturbation or disturbance.

$$
\begin{aligned}
&u = u_0 + \Delta u \qquad v = v_0 + \Delta v \qquad w = w_0 + \Delta w \\
&p = p_0 + \Delta p \qquad q = q_0 + \Delta q \qquad r = r_0 + \Delta r \\
&X = X_0 + \Delta X \qquad Y = Y_0 + \Delta Y \qquad Z = Z_0 + \Delta Z \\
&M = M_0 + \Delta M \qquad N = N_0 + \Delta N \qquad L = L_0 + \Delta L \\
&\delta = \delta_0 + \Delta\delta
\end{aligned}
\tag{B.1}
$$

The author assumed that the aircraft is in a steady, unaccelerated flight before it encounters a disturbance, i.e. both the net force and net moment on the aircraft is zero. For convenience, the reference flight conditions are assumed to be symmetric and the propulsive forces are assumed to remain constant. Furthermore, n the study of aircraft dynamics, it is customary to use the stability axes system. This implies that in the equilibrium flight conditions prior to encountering the disturbance, the body axes system coincides with the stability axes system. This implies that

$$v_0 = p_0 = q_0 = r_0 = \phi_0 = \psi_0 = 0 \tag{B.2}$$

Furthermore, if the aircraft is aligned along the direction of the aircraft's velocity vector, then $w_0 = 0$.

Now, if the small disturbance notation is introduced into the equations of motions, the equation can be simplified. Considering the X force equations

$$X = m(\dot{u} + qw - rv) \tag{B.3}$$

Substituting the small disturbance variables into this equations yields

$$X_0 + \Delta X = m[\frac{d}{dt}(u_0 + \Delta u) + (q_0 + \Delta q)(w_0 + \Delta w) - (r_0 + \Delta r)(v_0 + \Delta v)] \tag{B.4}$$

If the product of disturbance are neglected and assume that

$$v_0 = w_0 = p_0 = q_0 = r_0 = \phi_0 = \psi_0 = 0 \tag{B.5}$$

Then the X equation becomes

$$X_0 + \Delta X = m\Delta\dot{u} \tag{B.6}$$

If all the disturbance quantities are set equal to 0 in these equation, the reference flight conditions is

$$X_0 = 0 \tag{B.7}$$

This reduces the X-force equation to

$$\Delta X = m\Delta\dot{u} \tag{B.8}$$

Similarly for the other equations, it can be reduced to the following,

$$\Delta Y = m(\Delta\dot{v} + ru_0) \tag{B.9}$$

$$\Delta Z = m(\Delta\dot{w} - qu_0) \tag{B.10}$$

$$\Delta L = \dot{p}I_x - \dot{r}I_{xz} \tag{B.11}$$

$$\Delta M = \dot{q}I_y \tag{B.12}$$

$$\Delta N = \dot{r}I_z - \dot{p}I_{xz} \tag{B.13}$$

The aerodynamic forces are defined in terms of dimensionless coefficients, the flight dynamic pressure and a reference area S as follows:

$$\Delta X = \frac{1}{2}\rho u_0^2 S\Delta C_x \tag{B.14}$$

$$\Delta Y = \frac{1}{2}\rho u_0^2 S\Delta C_y \tag{B.15}$$

$$\Delta Z = \frac{1}{2}\rho u_0^2 S \Delta C_z \tag{B.16}$$

In a similar manner, the moments on the aircraft can be divided into moments created by the aerodynamic load distribution and the thrust force not acting through the centre of gravity. The components of the aerodynamic moment also are expressed in terms of dimensionless coefficients, flight dynamic pressure, reference area and a characteristic length as follows:

$$\Delta L = \frac{1}{2}\rho u_0^2 S b \Delta C_l \tag{B.17}$$

$$\Delta M = \frac{1}{2}\rho u_0^2 S \bar{c} \Delta C_m \tag{B.18}$$

$$\Delta N = \frac{1}{2}\rho u_0^2 S b \Delta C_n \tag{19}$$

Here U_o is the flight velocity, S is the reference (wing) area, $\bar{c}$ is the mean aerodynamic chord, and b is the wing span. Note that the reference length used for defining the rolling and yawing moment coefficients C_l and C_n is the span b and that for pitching moment; coefficient C_m is the mean aerodynamic chord $\bar{c}$.

$$\tan\alpha \cong \Delta\alpha = \frac{w}{u_0} \tag{B.20}$$

$$\sin\beta \cong \Delta\beta = \frac{v}{u_0} \tag{B.21}$$

So that

$$\Delta\alpha \cong \frac{\Delta w}{u_0} = w \tag{B.22}$$

$$\Delta\beta \cong \frac{\Delta v}{u_0} = v \tag{B.23}$$

Then Equation 2.41-2.46 takes the following form:

$$\Delta C_x = \frac{m u_0}{\frac{1}{2}\rho U_0^2 S}\dot{u} \tag{B.24}$$

$$\Delta C_y = \frac{mu_0}{\frac{1}{2}\rho U_0^2 S}(\Delta\dot{\beta} + r) \tag{B.25}$$

$$\Delta C_z = \frac{mu_0}{\frac{1}{2}\rho U_0^2 S}(\Delta\dot{\alpha} - q) \tag{B.26}$$

$$\Delta C_l = \frac{1}{\frac{1}{2}\rho U_0^2 Sb}(\dot{p}I_x - \dot{r}I_{xz}) \tag{B.27}$$

$$\Delta C_m = \frac{mu_0}{\frac{1}{2}\rho U_0^2 S\bar{c}}\dot{q} \tag{B.28}$$

$$\Delta C_n = \frac{1}{\frac{1}{2}\rho U_0^2 Sb}(\dot{r}I_z - \dot{p}I_{xz}) \tag{B.29}$$

B.1 Estimation of Aerodynamic Forces and Moments

The next task is to estimate the aerodynamic coefficients ΔC_x, $\Delta C_y, \Delta C_z, \Delta C_l, \Delta C_m, \Delta C_n$ in the disturbed motion. For this purpose, Bryan's method [21] is used, based on two principal assumptions: 1) the instantaneous aerodynamic forces and moments depend on the instantaneous values of the motion variables and 2) the aerodynamic forces and moments vary linearly with motion variables. The longitudinal aerodynamic forces and moments are also assumed to be only influenced only by the longitudinal variables u, α and q. It is assumed that the lateral-directional variables like β, p and r do not influence the longitudinal aerodynamic force and the pitching moment. Similar assumptions are made for the lateral directions; it is thus assumed that there is no-aerodynamic coupling between the longitudinal and lateral directional variables, forces and moments. These assumptions are valid for small angles of attack and sideslip when the aerodynamic coefficients vary linearly with the angle of attack and sideslip angle. At high angle of attack, these assumptions are not valid because of flow separation, vortex shredding and stall where the aerodynamic coefficient varies non-linearly. The study of the coupled analysis due to asymmetrical flight conditions as well

as the study of stability and control at nonlinear conditions will be discussed in the later part of this chapter.

With these assumptions and remembering the disturbance variables are assumed to be small, the change of aerodynamic and propulsion force in the x-direction and can be expressed by means of a Taylor series in terms of the perturbation variables. It is assumed that ΔC_x is a function only of u, α, δ_e and δ_T, then ΔC_x can be expressed as

$$\Delta C_x = \frac{\partial C_x}{\partial u} u + \frac{\partial C_x}{\partial \alpha} \Delta\alpha + \frac{\partial C_x}{\partial \theta} \Delta\theta + \frac{\partial C_x}{\partial \dot{\alpha}} \Delta\dot{\alpha} + \frac{\partial C_x}{\partial q} q + \frac{\partial C_x}{\partial \delta_e} \Delta\delta_e + \frac{\partial C_x}{\partial \delta_T} \Delta\delta_T \tag{B.30}$$

$$\Delta C_y = \frac{\partial C_y}{\partial \beta} \Delta\beta + \frac{\partial C_y}{\partial \phi} \Delta\phi + \frac{\partial C_y}{\partial \dot{\beta}} \Delta\dot{\beta} + \frac{\partial C_y}{\partial p} p + \frac{\partial C_y}{\partial r} r + \frac{\partial C_y}{\partial \delta_a} \Delta\delta_a + \frac{\partial C_y}{\partial \delta_r} \Delta\delta_r \tag{B.31}$$

$$\Delta C_z = \frac{\partial C_z}{\partial u} u + \frac{\partial C_z}{\partial \alpha} \Delta\alpha + \frac{\partial C_z}{\partial \theta} \Delta\theta + \frac{\partial C_z}{\partial \dot{\alpha}} \Delta\dot{\alpha} + \frac{\partial C_z}{\partial q} q + \frac{\partial C_z}{\partial \delta_e} \Delta\delta_e + \frac{\partial C_z}{\partial \delta_T} \Delta\delta_T \tag{B.32}$$

$$\Delta C_l = \frac{\partial C_l}{\partial \beta} \Delta\beta + \frac{\partial C_l}{\partial \phi} \Delta\phi + \frac{\partial C_l}{\partial \dot{\beta}} \Delta\dot{\beta} + \frac{\partial C_l}{\partial p} p + \frac{\partial C_l}{\partial r} r + \frac{\partial C_l}{\partial \delta_a} \Delta\delta_a + \frac{\partial C_l}{\partial \delta_r} \Delta\delta_r \tag{B.33}$$

$$\Delta C_m = \frac{\partial C_m}{\partial u} u + \frac{\partial C_m}{\partial \alpha} \Delta\alpha + \frac{\partial C_m}{\partial \theta} \Delta\theta + \frac{\partial C_m}{\partial \dot{\alpha}} \Delta\dot{\alpha} + \frac{\partial C_m}{\partial q} q + \frac{\partial C_m}{\partial \delta_e} \Delta\delta_e + \frac{\partial C_m}{\partial \delta_T} \Delta\delta_T \tag{B.34}$$

$$\Delta C_n = \frac{\partial C_n}{\partial \beta} \Delta\beta + \frac{\partial C_n}{\partial \phi} \Delta\phi + \frac{\partial C_n}{\partial \dot{\beta}} \Delta\dot{\beta} + \frac{\partial C_n}{\partial p} p + \frac{\partial C_n}{\partial r} r + \frac{\partial C_n}{\partial \delta_a} \Delta\delta_a + \frac{\partial C_n}{\partial \delta_r} \Delta\delta_r \tag{B.35}$$

Where $\partial C_x / \partial u$ and $\partial C_x / \partial w$ are called stability derivatives and terms such as $\partial C_x / \partial \delta_e$ and $\partial C_x / \partial \delta_T$,called control derivative, that are evaluated at the reference flight conditions from which the aircraft is supposed to be disturbed. The variable δ_e and δ_T are the change in elevator angle and throttle setting, respectively.

In the literature on aircraft stability and control, it is customary to use short hand notation to denote the stability and control derivatives. For example,

$$C_{xu} = \frac{\partial C_x}{\partial u} \qquad C_{x\alpha} = \frac{\partial C_x}{\partial \alpha} \qquad C_{m\alpha} = \frac{\partial C_m}{\partial \alpha}$$

$$C_{y\beta} = \frac{\partial C_y}{\partial \beta} \qquad C_{l\beta} = \frac{\partial C_l}{\partial \beta} \qquad C_{n\beta} = \frac{\partial C_n}{\partial \beta} \qquad \text{(B.36)}$$

And so on. However, the partial derivatives with respect to variables such as $\dot{\alpha}$, $\dot{\beta}$, p, q, and r are defined somewhat differently as follows:

$$C_{L\dot{\alpha}} = \frac{\partial C_L}{\partial\left(\frac{\dot{\alpha}\bar{c}}{2u_0}\right)} \qquad C_{Lq} = \frac{\partial C_L}{\partial\left(\frac{q\bar{c}}{2u_0}\right)} \qquad C_{mq} = \frac{\partial C_m}{\partial\left(\frac{q\bar{c}}{2u_0}\right)}$$

$$C_{y\dot{\beta}} = \frac{\partial C_y}{\partial\left(\frac{\dot{\beta}b}{2u_0}\right)} \qquad C_{l\dot{\beta}} = \frac{\partial C_l}{\partial\left(\frac{\dot{\beta}b}{2u_0}\right)} \qquad C_{n\dot{\beta}} = \frac{\partial C_n}{\partial\left(\frac{\dot{\beta}b}{2u_0}\right)}$$

$$C_{yp} = \frac{\partial C_y}{\partial\left(\frac{pb}{2u_0}\right)} \qquad C_{lp} = \frac{\partial C_l}{\partial\left(\frac{pb}{2u_0}\right)} \qquad C_{np} = \frac{\partial C_n}{\partial\left(\frac{pb}{2u_0}\right)}$$

$$C_{yr} = \frac{\partial C_y}{\partial\left(\frac{rb}{2u_0}\right)} \qquad C_{lr} = \frac{\partial C_l}{\partial\left(\frac{rb}{2u_0}\right)} \qquad C_{nr} = \frac{\partial C_n}{\partial\left(\frac{rb}{2u_0}\right)} \qquad \text{(B.37)}$$

This form of definition of stability derivatives involving time derivatives and angular components is necessary to make these derivatives non dimensional like all the other stability and control derivatives. The stability and control derivatives with respect to variables like $\dot{\alpha}$ and $\dot{\beta}$ are called acceleration derivatives, and those with respect to p, q and r are called rotary derivatives. Together they are called dynamic stability and control derivatives.

Using short hand notation, the equation can be rewritten in non dimensional form in the force and moment expression are as follows:

The longitudinal equation of motions [21] for elevator control is given by the following equation:

$$\left(m_1\frac{d}{dt}-C_{xu}\right)u-\left(C_{x\dot{\alpha}}c_1\frac{d}{dt}+C_{x\alpha}\right)\Delta\alpha-\left(C_{xq}c_1\frac{d}{dt}+C_{x\theta}\right)\Delta\theta=C_{x\delta_e}\Delta\delta_e+C_{x\delta_t}\Delta\delta_t$$

(B.38)

$$-C_{zu}u+\left[\left(m_1\frac{d}{dt}-C_{z\dot{\alpha}}c_1\frac{d}{dt}\right)-C_{z\alpha}\right]\Delta\alpha-\left(m_1\frac{d}{dt}+C_{zq}c_1\frac{d}{dt}+C_{z\theta}\right)\Delta\theta=C_{z\delta_e}\Delta\delta_e++C_{x\delta_t}\Delta\delta$$

(B.39)

$$-C_{mu}u-\left(C_{m\dot{\alpha}}c_1\frac{d}{dt}+C_{m\alpha}\right)\Delta\alpha+\frac{d}{dt}\left(I_{y1}\frac{d}{dt}-C_{mq}c_1\right)\Delta\theta=C_{m\delta_e}\Delta\delta_e++C_{x\delta_t}\Delta\delta_t$$

(B.40)

Where,

$$m_1=\frac{2m}{\rho US}\qquad c_1=\frac{\bar{c}}{2U}\qquad I_{y1}=\frac{I_y}{\frac{1}{2}\rho U^2S\bar{c}}$$

(B.41)

Similarly the lateral-directional equations of motion for small disturbance are as follows:

$$\left(m_1\frac{d}{dt}-b_1C_{y\dot{\beta}}\frac{d}{dt}-C_{y\beta}\right)\Delta\beta-\left(b_1C_{yp}\frac{d}{dt}+C_{y\Phi}\right)\Delta\Phi+\left(m_1\frac{d}{dt}-b_1C_{yr}\frac{d}{dt}\right)\Delta\Psi=C_{y\delta_r}\Delta\delta_r+C_{y\delta_a}\Delta\delta_a$$

(B.42)

$$\left(-C_{l\beta}-b_1C_{l\dot{\beta}}\frac{d}{dt}\right)\Delta\beta+\left(-b_1C_{lp}\frac{d}{dt}+I_{x1}\frac{d^2}{dt^2}\right)\Delta\Phi+\left(-b_1C_{lr}\frac{d}{dt}-I_{xz1}\frac{d^2}{dt^2}\right)\Delta\Psi=C_{l\delta_r}\Delta\delta_r+C_{l\delta_a}\Delta\delta_a$$

(B.43)

$$\left(-C_{n\beta}-b_1C_{n\dot{\beta}}\frac{d}{dt}\right)\Delta\beta+\left(-b_1C_{np}\frac{d}{dt}-I_{xz1}\frac{d^2}{dt^2}\right)\Delta\Phi+\left(-b_1C_{nr}\frac{d}{dt}+I_{xz1}\frac{d^2}{dt^2}\right)\Delta\Psi=C_{n\delta_r}\Delta\delta_r+C_{n\delta_a}\Delta\delta_a$$

(B.44)

Where,

$$\frac{d\Phi}{dt}=p\qquad\frac{d\psi}{dt}=r\qquad b_1=\frac{b}{2U}\qquad I_{x1}=\frac{I_x}{\frac{1}{2}\rho U^2Sb}\qquad I_{z1}=\frac{I_z}{\frac{1}{2}\rho U^2Sb}\qquad I_{xz1}=\frac{I_{xz}}{\frac{1}{2}\rho U^2Sb}$$

(B.45)

B.2 State Variable Representation of the Equations of Motion

The motion of an aircraft in free flight can be extremely complicated. The aircraft has three translational motions (vertical, horizontal and transverse), three rotational motions (pitch, yaw, and roll), and numerous elastic degrees of freedom. There are some simplifying assumptions which can reduce the complexity of the motions of an aircraft.

First, assume that the aircraft's motions consist of small deviation from its equilibrium flight conditions. Second, assume that the motion of the aircraft can be analyzed by separating the equations into two groups. The X-force, Z-force, and pitching moment equations embody the longitudinal equations, and the Y-force, rolling, yawing moments of equation form the lateral equations. To separate the equations in this manner, the longitudinal and lateral equations must not be coupled. These are all reasonable assumptions provided the aircraft is not undergoing a large-amplitude or very rapid maneuver. [3]

The linearized longitudinal equations, equations are simple, ordinary linear differential equations with constant coefficients. These equations can be written as a set of first-order differential equations, called the state-space or state variable equations and represented mathematically as

$$\dot{X} = AX + BU \tag{B.46}$$

where

$$X = \begin{bmatrix} u \\ \Delta\alpha \\ q \\ \Delta\theta \end{bmatrix} \qquad A = \begin{bmatrix} a_{11} & a_{12} & a_{13} & a_{14} \\ a_{21} & a_{22} & a_{23} & a_{24} \\ a_{31} & a_{32} & a_{33} & a_{34} \\ a_{41} & a_{42} & a_{43} & a_{44} \end{bmatrix} \qquad B = \begin{bmatrix} b_1 \\ b_2 \\ b_3 \\ b_4 \end{bmatrix} \tag{B.47}$$

The X vector is the state vector, while the U Vector is the control vector. The control vector consists of the control system on the aircraft. In the longitudinal equation, the author will only be concern with the elevator, while for the lateral equation; the author will take into consideration of the deflection of aileron and rudder.

And

$$a_{11} = \frac{C_{xu} + \xi_1 C_{zu}}{m_1} \qquad a_{12} = \frac{C_{x\alpha} + \xi_1 C_{zu}}{m_1}$$

$$a_{13} = \frac{C_{xq} c_1 + \xi_1 (m_1 + C_{zq} c_1)}{m_1} \qquad a_{14} = \frac{C_{x\theta} + \xi_1 C_{z\theta}}{m_1}$$

$$a_{21} = \frac{C_{zu}}{m_1 - C_{z\dot{\alpha}} c_1} \qquad a_{22} = \frac{C_{z\alpha}}{m_1 - C_{z\dot{\alpha}} c_1}$$

$$a_{23} = \frac{m_1 + C_{zq} c_1}{m_1 - C_{z\dot{\alpha}} c_1} \qquad a_{24} = \frac{C_{z\theta}}{m_1 - C_{z\dot{\alpha}} c_1}$$

$$a_{31} = \frac{C_{mu} + \xi_2 C_{zu}}{I_{y1}} \qquad a_{32} = \frac{C_{m\alpha} + \xi_2 C_{z\alpha}}{I_{y1}}$$

$$a_{33} = \frac{C_{mq} c_1 + \xi_2 (m_1 + C_{zq} c_1)}{I_{y1}} \qquad a_{34} = \frac{\xi_2 C_{z\theta}}{I_{y1}}$$

$$a_{41} = 0 \qquad a_{42} = 0 \qquad a_{43} = 1 \qquad a_{44} = 0$$

$$b_1 = \frac{C_{x\delta e} + \xi_2 C_{z\delta e}}{m_1} \qquad b_2 = \frac{C_{z\delta e}}{m_1 - C_{z\dot{\alpha}} c_1}$$

$$b_3 = \frac{C_{m\delta e} + \xi_2 C_{z\delta e}}{I_{y1}} \qquad b_4 = 0$$

$$\xi_1 = \frac{C_{x\dot{\alpha}} c_1}{m_1 - C_{z\dot{\alpha}} c_1} \qquad \xi_2 = \frac{C_{m\dot{\alpha}} c_1}{m_1 - C_{z\dot{\alpha}} c_1}$$

$$m_1 = \frac{2m}{\rho U S} \qquad c_1 = \frac{\bar{c}}{2U}$$

$$I_{y1} = \frac{I_y}{\frac{1}{2}\rho U^2 S \bar{c}} \qquad \text{(B.48)}$$

Similarly the linearized lateral equations from equation can be represented in state form can be expressed in the following matrices:

$$\dot{X} = AX + BU \qquad \text{(B.49)}$$

where

$$X = \begin{bmatrix} \Delta\beta \\ \Delta\phi \\ p \\ \Delta\psi \\ r \end{bmatrix} \quad A = \begin{bmatrix} a_{11} & a_{12} & a_{13} & a_{14} & a_{15} \\ a_{21} & a_{22} & a_{23} & a_{24} & a_{25} \\ a_{31} & a_{32} & a_{33} & a_{34} & a_{35} \\ a_{41} & a_{42} & a_{43} & a_{44} & a_{45} \\ a_{51} & a_{52} & a_{53} & a_{54} & a_{55} \end{bmatrix} \quad B = \begin{bmatrix} b_{11} & b_{12} \\ b_{21} & b_{22} \\ b_{31} & b_{32} \\ b_{41} & b_{42} \\ b_{51} & b_{52} \end{bmatrix} \quad \text{(B.50)}$$

The matrix A and B contains the aircraft dimensional stability derivatives. It should be noted that the matrix A is the stability matrix. The elements of matrix A depends on the stability derivatives of the aircraft which influence the design of the aircraft. Stability derivatives are obtained from the aerodynamic force and moments estimates during the initial design of the aircraft. These stability derivatives determine the dynamic stability of the aircraft and under design. The formulae for the Equation are as follows:

$$a_{11} = \frac{C_{y\beta}}{m_1 - C_{y\dot{\beta}} b_1} \qquad a_{12} = \frac{C_{y\phi}}{m_1 - C_{y\dot{\beta}} b_1}$$

$$a_{13} = \frac{C_{yp} b_1}{m_1 - C_{y\dot{\beta}} b_1} \qquad a_{14} = 0$$

$$a_{15} = -\left(\frac{m_1 - C_{yr} b_1}{m_1 - C_{y\dot{\beta}} b_1} \right) \qquad a_{21} = 0$$

$$a_{22} = 0 \qquad a_{23} = 1$$

$$a_{24} = 0 \qquad a_{25} = 0$$

$$a_{31} = C_{l\beta} I'_{z1} + C_{n\beta} I'_{xz1} b_1 + \xi_1 b_1 a_{11} \qquad a_{32} = \xi_1 b_1 a_{12}$$

$$a_{33} = C_{lp} b_1 I'_{z1} + C_{np} I'_{xz1} b_1 + \xi_1 b_1 a_{13} \qquad a_{34} = 0$$

$$a_{35} = C_{lr} b_1 I'_{z1} + C_{nr} I'_{xz1} b_1 + \xi_1 b_1 a_{15}$$

$$a_{41} = a_{42} = a_{43} = a_{44} = 0 \qquad a_{45} = 1$$

$$a_{51} = I'_{x1} C_{n\beta} + I'_{xz1} C_{l\beta} + \xi_2 b_1 a_{11} \qquad a_{52} = \xi_2 b_1 a_{12}$$

$$a_{53} = b_1 (C_{np} I'_{x1} + C_{lp} I'_{xz1} + \xi_2 a_{13}) \qquad a_{54} = 0$$

$$a_{55} = b_1 (C_{nr} I'_{x1} + C_{lr} I'_{xz1} + \xi_2 a_{15})$$

$$b_{11} = \frac{C_{y\delta a}}{m_1 - C_{y\dot{\beta}} b_1} \qquad b_{12} = \frac{C_{y\delta r}}{m_1 - C_{y\dot{\beta}} b_1}$$

$$b_{21} = 0 \qquad b_{22} = 0$$

$$b_{31} = C_{l\delta a} I'_{z1} + C_{n\delta a} I'_{xz1} b_1 + \xi_1 b_1 b_{11} \qquad b_{32} = C_{l\delta r} I'_{z1} + C_{n\delta r} I'_{xz1} b_1 + \xi_1 b_1 b_{12}$$

$$b_{41} = 0 \qquad b_{42} = 0$$

$$b_{51} = I'_{x1} C_{n\delta a} + I'_{xz1} C_{l\delta a} + \xi_2 b_1 b_{11} \qquad b_{52} = I'_{x1} C_{n\delta r} + I'_{xz1} C_{l\delta r} + \xi_2 b_1 b_{12}$$

$$\xi_1 = C_{l\dot{\beta}} I'_{z1} + C_{n\dot{\beta}} I'_{xz1} \qquad \xi_2 = C_{n\dot{\beta}} I'_{x1} + C_{n\dot{\beta}} I'_{xz1}$$

$$b_1 = \frac{b}{2U} \qquad I_{x1} = \frac{I_x}{\frac{1}{2}\rho U^2 Sb}$$

$$I_{z1} = \frac{I_z}{\frac{1}{2}\rho U^2 Sb} \qquad I_{xz1} = \frac{I_{xz}}{\frac{1}{2}\rho U^2 Sb}$$

$$I'_{x1} = \frac{I_{x1}}{I_{x1} I_{z1} - I_{xz1}^2} \qquad I'_{z1} = \frac{I_{z1}}{I_{x1} I_{z1} - I_{xz1}^2}$$

$$I'_{xz1} = \frac{I_{xz1}}{I_{x1} I_{z1} - I_{xz1}^2} \qquad \text{(B.51)}$$

Appendix C

Formulation of Solution of Stability Matrix

C.1 Form of solution and stability

The results of the free response and forced responses will be discussed in this section. For the free response, the elevator is assumed to be held fixed (stick-fixed) and for the forced responses, the elevator is moved in a specified manner to a new position i.e. by inputting a step response to the system.

For free response, U=0 so that,

$$\dot{X} = AX \tag{C.1}$$

A solution to equation (3.1) can be obtained in the usual way

$$X = X_0 e^{\lambda t} \tag{C.2}$$

So that

$$\dot{X} = X_0 \lambda e^{\lambda t} \tag{C.3}$$

And

$$X_0 \lambda e^{\lambda t} - A X_0 e^{\lambda t} = 0 \tag{C.4}$$

Giving

$$(\lambda I - A) X_0 = 0 \tag{C.5}$$

For non trivial solutions, the determinant must be equals to zero

$$|\lambda I - A| = 0 \tag{C.6}$$

An expansion of the determinant in the above equation results in a fourth order algebraic equation of the form

$$A_\delta \lambda^4 + B_\delta \lambda^3 + C_\delta \lambda^2 + D_\delta \lambda + E_\delta = 0 \tag{C.7}$$

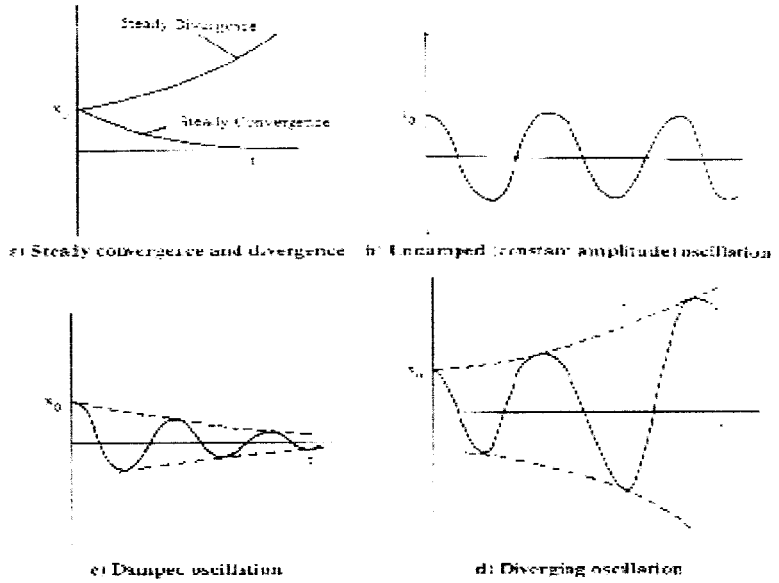

Figure C.1 Typical dynamic motions

Equation C.1 is called the characteristic equation of the longitudinal motion and gives four values of the roots. The nature of the free response can be a combination of the typical free responses shown in Figure C.1. A steady convergence corresponds to a real negative root, a steady divergence if the real root is positive, and an oscillatory motion of constant amplitude if the root is zero, a damped oscillatory motion if the real part of a complex root is negative, and a divergent oscillatory motion is the real part of the complex root is positive. Thus for dynamic stability, the roots of the characteristics equation must be negative if real or must have negative real parts if complex.

The other parameters need for the study of handling qualities of the UAV are the period, time to double if unstable situation and time to half if it shows stable characteristics. When the roots are real, there is no period. The only parameter of concern is the time to double or half. When the modes are oscillatory, it is the envelop ordinate that doubles or halves. The envelope may be regarded as an amplitude modulation and the doubling of halving as applied to the variable amplitude. These parameters mentioned are important in determining how fast the disturbance can be reduced.